LOUISE O.V. EDWARDS

Line Emission in Brightest Cluster Galaxies:
The Nature of Recent Activity

Thèse présentée
à la Faculté des études supérieures de l'Université Laval
dans le cadre du programme de doctorat en Physique
pour l'obtention du grade de Philosophiae Doctor (Ph.D.)

FACULTÉ DES SCIENCES ET DE GÉNIE
UNIVERSITÉ LAVAL
QUÉBEC

DECEMBRE 2007

Résumé

Cette thèse est présentée en deux parties. Premièrement, je vais examiner les propriétés de la galaxie la plus brillante au sein d'amas (GBA) sélectionnée à partir de deux grands relevés systématiques, le National Optical Astronomy Observatory Fundamental Plane Survey (NFPS) et le Sloan Digital Sky Survey Data Release 3 (SDSS-DR3). Mon but est de mieux comprendre les raies d'émission du visible des GBA en fonction des propriétés de la galaxie et de son amas. Dans cette analyse, je compare les raies des GBA avec celles d'un échantillon de contrôle qui est constitué d'autres galaxies brillantes situées près du centre des amas. Pour les deux échantillons du NFPS et du SDSS, on voit une fraction modeste ($\sim$15%) de GBA avec des raies d'émission. Il n'y a pas de relation entre la fraction des GBA avec des raies d'émission et la masse de la galaxie ou la dispersion des vitesses dans l'amas. Par contre, environ 70% des GBA qui se trouvent dans des amas de type "cooling flow" ont des raies d'émission. De plus, si on considère seulement les GBA qui se trouvent dans un rayon de 50 kpc du centre de l'émission des rayons X du cooling flow, la fraction des galaxies avec raies d'émission est près de 100%. En excluant les amas de type cooling flow, seulement $\sim$10% des GBA ont des raies d'émission, un nombre comparable à celui des galaxies de contrôle. Je montre que l'origine physique de l'émission varie: dans certains cas l'émission est plutôt charactéristique de celle des LINERs, et dans d'autres cas, elle ressemble à l'émission due à un mélange de LINERs et de formation stellaire. Je conclus que la présence des raies d'émission des GBA est reliée directement au refroidissement des rayons X dans le centre des amas. Dans la deuxième partie de cette thèse, j'explore plus en détails les propriétés de l'émission en utilisant des données de spectroscopie de champs intégral pour un sous-échantillon de GBA. J'examine la morphologie de l'émission dans les raies au centre de GBA dans 9 amas cooling flow et non-cooling flow. Je déduis la source d'ionisation qui est a l'origine des raies. L'ionisation par les étoiles jeunes est présente dans deux cas alors que l'ionisation par un AGN est requise dans les autres cas. De plus, je constate que les GBA des amas cooling flow ne sont pas les seules à montrer des raies. Tout ça pour conclure que le processus d'ionisation dans les GBA n'est pas universel. Différents processus sont plus ou moins importants selon le cas.

Abstract

This thesis is presented in two parts. First, I examine the optical emission line properties of Brightest Cluster Galaxies (BCGs) selected from two large, homogeneous datasets, the National Optical Astronomy Observatory Fundamental Plane Survey (NFPS) and the Sloan Digital Sky Survey Data Release 3 (SDSS-DR3). My goal is to better understand the optical line emission in BCGs with respect to properties of the galaxy and the host cluster. Throughout the analysis I compare the line emission of the BCGs to that of a control sample made of the other bright galaxies near the cluster center. Overall, both the NFPS and SDSS show a modest fraction of BCGs with emission lines ($\sim$15%). No trend in the fraction of emitting BCGs as a function of galaxy mass or cluster velocity dispersion is found. However I find that, for those BCGs located in cooling flow clusters, about 70% have optical emission. Furthermore, considering only BCGs within 50 kpc of the X-ray center of a cooling flow cluster, the emission-line fraction rises to nearly 100%. Excluding the cooling flow clusters, only $\sim$10% of BCGs are line emitting, comparable to the control sample of galaxies. I show that the physical origin of the emission line activity varies: in some cases it has LINER-like line ratios, whereas in others it is a composite of star formation and LINER-like activity. I conclude that the presence of emission lines in BCGs is directly related to the cooling of X-ray gas at the cluster center. In the second part of this thesis, I explore the detailed properties of this emission using integral field spectroscopy on a select subsample of BCGs. I examine the morphology of the line emission at the center of BCGs in 9 clusters, both cooling flow and non-cooling flow. I discriminate between gas ionized by hot stars and that ionized by a harder source, such as an AGN. There are two cases for which ionization by hot stars is convincing, however, for the rest the emission mechanism appears to be associated with AGN. Furthermore, it is not always cooling flow BCGs which show emission, and non-cooling flow BCGs which do not. The conclusion is that the emission mechanism is not universal among BCGs. Different processes are more or less important for each specific system.

Preface

Chapter 2 of this thesis includes an article published in volume 397 of the journal *Monthly Notices of the Royal Astronomical Society* in July, 2007 by Blackwell Publishing and the Royal Astronomical Society (Edwards et al. 2007). This article, "Line Emission in the Brightest Cluster Galaxies of the NOAO Fundamental Plane and Sloan Digital Sky Surveys", was written by L. O. V. Edwards, Michael J. Hudson, Michael L. Balogh, and Russell J. Smith. During a six month work term at the University of Waterloo, Department of Physics and Astronomy, and under the supervision of Michael Hudson and Michael Balogh, I reworked the cluster properties based on galaxies in the two surveys, and created a table of BCGs and control galaxies from these clusters. I analyzed the properties of the BCGs and Controls and wrote the paper. Russell Smith, presently at Durham University was instrumental in completing the observations of the NFPS galaxy sample, and derived the Hβ line strengths while working as a post-doc with Michael Hudson. Chapter 3 includes several tests and specifics on how the final BCG and controls lists and properties were chosen. This information was not included in the article, but is included here for completeness and clarity.

Chapter 4 presents the data and analysis of a sample of BCGs that were observed using integral field spectroscopy. L. O. V. Edwards and Carmelle Robert developed the project goals and submitted the observing proposals together. Mercedes Mollá was the principal investigator on the proposals for the OASIS data, as this was not possible for a Canadian astronomer; however, I conducted the observations of the OASIS sample with the help of Jorge Iglesias and Samantha Rix, the observing assistant. I also spent 2 months at Gemini South, where I participated in the queue mode observations of Abell 1060, and where I started the data reduction and analysis. Shortly, L.O.V. Edwards and Carmelle Robert will be submitting this project for publication in a refereed journal.

I would like to thank my supervisor Dr. Carmelle Robert for her support over the last four years. I always felt uplifted after our meetings. She was also very open to sending me on observation runs, local and international conferences, and supporting

new collaborations. In turn, I thank Dr. Michael Balogh and Dr. Michael Hudson who made me feel at home during my stay at the University of Waterloo.

I have had lots of interesting science discussions with the professors, the postdocs and the students at Laval, especially helpful were discussions with Dr. Laurent Drissen, Dr. Sylvie Beaulieu as well as Dr. Mat Pieri. I'd like to highlight the Thursday meetings of Dr. Hugo Martel's cosmology group as being beneficial as well. Simon Cantin and Véronique Petit were very nice in lending their expertise in data reduction and analysis techniques.

Thank you to my good friend Sean McGee and his love of Astrophysics which has been an inspiration to me since I started graduate school. Also essential to the completion of this thesis was mid-afternoon coffee with (the very soon to be Dr.) Medini Ghodgaonkar.

I dedicate this thesis to my father, William Edwards, who encouraged me to push further on in my scholastic education and to my mother, Karen, who is able to share this time with me.

Credits

Several publicly available routines were used in order to complete the reduction and analysis in this thesis. These include:

- The NASA/IPAC Extragalactic Database (NED), which is operated by the Jet Propulsion Laboratory, California Institute of Technology, under contract with the National Aeronautics and Space Administration
- The NASA Extragalactic Data System Abstract Service (ADS)
- The Sloan Digital Sky Survey (SDSS). Funding for the SDSS and SDSS-II has been provided by the Alfred P. Sloan Foundation, the Participating Institutions, the National Science Foundation, the U.S. Department of Energy, the National Aeronautics and Space Administration, the Japanese Monbukagakusho, the Max Planck Society, and the Higher Education Funding Council for England. The SDSS Web Site is http://www.sdss.org/
- Two Micron All Sky Survey, which is a joint project of the University of Massachusetts and the Infrared Processing and Analysis Center/California Institute of Technology, funded by the National Aeronautics and Space Administration and the National Science Foundation
- The Canadian Astronomical Data Center (CADC)
- Gemini Science Archive, which is operated by the Association of Universities for Research in Astronomy, Inc., under a cooperative agreement with the NSF on behalf of the Gemini partnership: the National Science Foundation (United States), the Particle Physics and Astronomy Research Council (United Kingdom), the National Research Council (Canada), CONICYT (Chile), the Australian Research Council (Australia), CNPq (Brazil) and CONICET (Argentina)
- High Energy Astrophysics Science Archive Research Center (HEASARC), provided by NASA's Goddard Space Flight Center

Contents

List of Figures

List of Tables

Chapter 1

Introduction

1.1 Activity in Galaxy Clusters

Galaxy clusters are the largest gravitationally bound systems known in the Universe, and consequently are host to a number of exciting astrophysical phenomena which influence the evolution of the galaxies within. Observers and theorists alike have been kept busy for decades pursuing the discovery and understanding the nature of the often complex activity at play in these massive clusters. Galaxies interacting with each other, the activity of the central galaxy, the detection of large reservoirs of X-ray emitting gas between these galaxies, and the interactions between the cluster members and the hot intracluster gas are some of the topics that have been given considerable study (Rosati et al. 2002; Phillipps 2005). The objective of this thesis is to find out how common such activity is in nearby bright cluster galaxies, to identify and describe the sites of this activity in these galaxies, in order to better understand its origin.

Poor galaxy clusters, or groups, are host to a few dozen galaxies and stretch $\sim$1.5 Mpc across. On the other hand, their rich counterparts host up to thousands of galaxies within a diameter of $\lesssim$ 10 Mpc, for a typical total mass of $\sim 10^{15}\,M_{\odot}$ (Carroll & Ostlie 1996), about 90% of which is in the form of dark matter (Sarazin 1988). Rich clusters come in two varieties: irregular clusters such as Virgo are composed of all galaxy types, whereas regular clusters are spherical in shape, centrally concentrated, and, as in Coma, dominated by S0 and elliptical galaxies at the center (Sparke & Gallagher 2000; Carroll & Ostlie 1996).

For the most part, regular rich clusters are host to the galaxies and processes which will be studied in this thesis. Often they are Bultz-Morgan type BM I or II clusters, that is, they are dominated by a giant elliptical galaxy surrounded by an extended halo (a cD) which lies at the bottom of the gravitational potential of the cluster (Bautz & Morgan 1970; Sarazin 1988). In the tightly concentrated center galaxy harassment, ram pressure stripping, and even mergers have likely occurred. In fact, one explanation for the lower fraction of spirals in regular rich clusters is that the galaxy's gas has been removed and compressed by such processes and the spiral subsequently evolves to

become an elliptical. In areas of lower local galaxy density, away from the center of a regular rich cluster, a higher fraction of star-forming (spiral) galaxies exists (Postman & Geller 1984).

Also playing a key role in the evolution of a galaxy cluster is the hot gas emitting thermal bremsstrahlung in X-rays that is found in these massive systems (see Section 1.5). Hierarchical models of structure formation predict that the smallest objects form first (Navarro et al. 1994; Springel et al. 2005). Therefore, the clusters would have formed last, and are probably still in some stage of formation. Unless the processes that caused the galaxies to collapse were extremely efficient, it is natural to expect that some of the primordial gas did not make it into stars and galaxies. This is the likely nature of the hot X-ray gas found in clusters (Phillipps 2005). Because of its diffuse nature, the intracluster gas reaches staggeringly high temperatures of 10^7 K, and is thus observed in X-rays. This primordial gas has a surprisingly high metallicity, suggesting pollution from the galaxies of the cluster. The mass of gas emitting in X-rays is several times that of the visible galaxies in the cluster (Rosati et al. 2002).

1.2 The Brightest Cluster Galaxy

Of the three main types of galaxies - irregulars, spirals, and ellipticals, it is the most massive of the latter type, the giant ellipticals, which are of interest in this thesis. In contrast to spiral galaxies, which are characterized by a large population of young, bright, massive blue stars in a disk and much H I and molecular gas, and irregular galaxies which are smaller and have little symmetry in their structure, but resemble spirals in their content, the ellipticals do not usually host young stars and gas (van den Bergh 1998). The massive, bright O and B type stars found in young stellar populations are not usually present here as they would have exploded long ago, and in general, there is a deficit of molecular gas. Rather, elliptical galaxies are red in colour due to an old stellar population.

The galaxy formation process is not perfectly understood. It is possible that galaxies could form either top-down within a monolithic collapse (Eggen et al. 1962), or in conjunction with a bottom-up process where hierarchical merging is involved (Larson 1969). The importance of hierarchical merger scenarios is underlined and exploited by many authors (Schweizer & Seitzer 2007; Goudfrooij et al. 2007; Berrier et al. 2006; Nagashima et al. 2005; De Lucia et al. 2004) as it fits well into the cold dark matter scheme. In this regime, larger systems result from the merging of the smaller systems that are already in place. The large fraction of ellipticals found within the centers of rich clusters supports this scenario.

The Brightest Cluster Galaxy (BCG) is typically a giant elliptical, and often a cD, located at the center of the gravitational potential of a rich cluster, as illustrated in Figure 1.1. The cD class of galaxy is the most luminous class of galaxy known (excluding

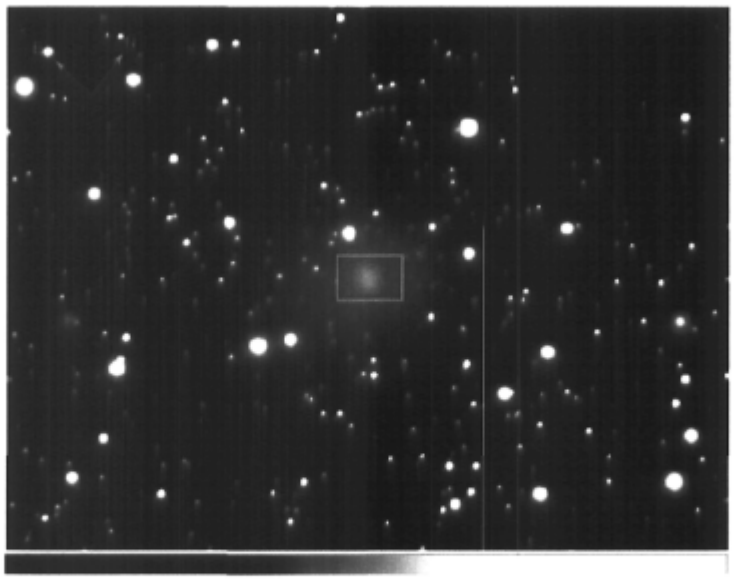

Figure 1.1: **The Ophiuchus galaxy cluster.** *The image was taken through the r-filter using the GMOS instrument in imaging mode at the Gemini North telescope. A massive galaxy cluster is seen though the foreground stars and a giant cD galaxy, the brightest cluster galaxy, is marked with a rectangle. This rectangle is $5 \times 7''$, the size of the IFU field discussed in Chapter 4.*

nuclear sources), and is characterized by an extended low surface brightness halo which surrounds a giant elliptical galaxy (Matthews et al. 1964). These galaxies are more luminous than they would be if they were simply the bright end of the elliptical galaxy luminosity function (Dressler 1978), suggesting that they are a special class of galaxy which could be subject to their own formation and evolutionary history. Close pairs, and multiple nuclei are common in cD galaxies, and hence it has been hypothesized that mergers and galactic cannibalism (Ostriker & Hausman 1977) create these galaxies (see also Section 2.1). Because cDs are often found at the peak of the cluster's X-ray surface brightness, where the hot intracluster gas may cool to form molecular clouds, an additional relationship between the stellar and gaseous content of the cD and cooling intracluster gas is thought plausible.

1.3 Emission Lines in Elliptical Galaxies

In this thesis, the origin of line emission in cluster elliptical galaxies will be studied. Events of star formation generate emission lines; but detection of emission lines does not imply a simple straightforward sequence such as the collapse from a molecular cloud to the formation of young stellar population. The line emission may be related to interactions and mergers (see Section 1.4) which can modify the spatial distributions

of the gas in a galaxy and trigger starbursts (Kennicutt 1998). But the presence of emission lines may also be related to the cooling intracluster medium (Crawford et al. 1999), which can be a source of molecular gas (as described in Section 1.5). The ionization of molecular clouds from a harder source, such as an active galactic nucleus (AGN) can produce emission lines as well (Osterbrock & Ferland 2006). Type 2 AGNs, which are observed through an obscuring dusty nucleus can produce strong emission lines from photoionization by the light escaping from the unobscured regions. The ratios of [N II] λ 6584/Hα and [O III] λ 5007/Hβ can then be placed on Baldwin et al. (1981, hereafter BPT) diagrams to discriminate between this ionization and that of photoionization by H II regions. The BPT diagram was first defined empirically, as objects known to be star forming regions were found to be separated from harder spectra best by using the aforementioned ratios. However, there is a theoretical reason behind why the ratios of recombination to forbidden lines unveil the form of the ionizing source spectrum. The Hα and Hβ lines are a result of recombination, and so their strength is proportional to that of the ionizing luminosity. The [N II] λ 6584 and [O III] λ 5007 lines however are forbidden transitions. Forbidden lines occur only in low density gas where the it is possible for the transitions to occur before the atom is de-excited via collisional processes. The strength of such transitions are dependent on not only the ionizing luminosity strength, but also the ion abundance and the form of the ionization field. The ratio of these two types of transition lines therefore is sensitive only to the metallicity of the gas and the hardness of the ionizing source. There is an area on the BPT diagnostic diagram where objects are a composite of the two sources, and Kauffmann et al. (2003) have shown that there is a connection between the presence of an AGN and young stellar populations. Using a large sample from the Sloan Digital Sky Survey (SDSS), they found that the hosts of AGNs have younger central mean stellar ages than galaxies of the same mass and at the same redshift which do not have AGN. This includes merging and interacting galaxies, blue cDs, and isolated barred spirals. Kewley et al. (2006) have also shown using galaxies from the SDSS that AGN and current star formation are coupled in that the stronger AGN (parameterized by the strength of the [O III] λ 5007 line) have more star formation.

Despite the complications listed above, if careful study of the spectral characteristics of a galaxy, or a region of a galaxy, is effected, it is nevertheless possible to pinpoint the dominant emission mechanisms, and the dominant population of stars. If one examines properties such as kinematics, morphology, and chemical composition much more information can be obtained about the system as a whole. There may be many populations following the evolutionary history of the galaxy. However, a clear picture (age, metallicity, star formation rate, initial mass function, and mechanical energy) for the stellar populations can be deduced using evolutionary synthesis codes, such as Starburst99 (Leitherer et al. 1999) combined with observations of high spatial and spectral quality. Additionally, a comparison of diagnostic line ratios can be invoked to

discriminate between emission lines originating from starbursts versus AGN (Kewley & Dopita 2002). With the above tools and an understanding of the history of mergers and interactions between galaxies, the effect of the intracluster gas can be inferred.

1.4 Galaxy Interactions

Interactions manifest themselves in dichotomous ways as they can cause not only a quenching of star formation from the loss of molecular gas in the galaxy (Balkowski et al. 2001; Fujita & Nagashima 1999), but also an increase in star formation by allowing for a compression of the gas (Fujita & Nagashima 1999; Bridge et al. 2007). Mergers, galaxy harassment, and ram pressure stripping are amongst the most common and well studied processes and are reviewed in the following sections.

Mergers have been found to occur in many clusters. These are thought to be the result of more direct gravitational interactions whereby only one perturbed galaxy survives; the other(s) is (are) absorbed. For example, Sakai et al. (2002) find star forming knots near the large spiral galaxies in the nearby cluster Abell 1367 which they attribute to strong tidal interactions or mergers. In their high resolution HST images, Oemler et al. (1997) find that for clusters at high redshift ($z = 0.4$), the fraction of galaxies involved in interactions/mergers is 19% for clusters with blue colours and 12% for those with red. They classify galaxies involved in interactions morphologically; as having tidal arms or isophotal distortions, and those undergoing mergers as showing features such as outer shells and tails. Interactions are often thought to have the effect of creating starbursts which should result in making galaxies both brighter and bluer. However, at the redshift of the study of Oemler et al. (1997), no tendency is found for galaxies with particularly close neighbors to have bluer colours, and the conclusion is made that although mergers and interactions are common, they are not responsible for the blue colours of most of the galaxies. In other words, most blue galaxies are just normal late-type (spirals and irregulars).

Initially, mergers provide a natural explanation for the Butcher-Oemler effect, as less are occuring presently, and the spiral galaxy population is currently smaller. Nevertheless, according to Oemler et al. (1997), there are two reasons why galaxy mergers are not the ideal process to create the rapid disappearance of spiral galaxies prescribed by the Butcher-Oemler effect. First of all, their signatures should be visible for a few crossing times (on the order of a few hundred million years) and second, the local ellipticals and lenticulars would be much bluer than observed, since starbursts would follow. Another problem with attributing the Butcher-Oemler effect to mergers is that the dynamics of rich clusters are not favorable since the velocity dispersions are too high (Oemler et al. 1997).

For some cluster galaxies star formation is unusual as it is concentrated in the galaxy center. Recall that star formation in disc galaxies is normally spread throughout the

disc, and does not appear concentrated in the central regions. The central concentration of the emission is another factor which suggests that the star formation has been from a burst, and not from the truncation of normal disc star formation. A process is now needed that can either drive the gas into the center of the galaxy to provoke star formation, or that can remove the gas from the outer regions, and then produce a starburst which terminates at the center (Rose et al. 2001). In addition, many emission line galaxies in nearby clusters have disturbed morphologies. These non-spiral disturbances are observed to be concentrated into knots and ripples, which is also suggestive of tidal interactions (Miller & Owen 2002).

One of two well studied possibilities for a less dramatic gravitational interaction still able to produce central starbursts, knots and ripples, is galaxy harassment. This is defined as high speed encounters between the galaxies within the cluster (Lake & Moore 1999). Simulations have shown that such encounters can first produce barred spirals, then starbursts, and finally galaxies exhibiting a prolate morphology (Oemler et al. 1997).

A second possibility for weaker gravitational interactions is ram pressure stripping. Ram pressure stripping occurs due to the interaction of the intracluster medium (ICM) with a galaxy in the cluster (Gunn & Gott 1972). When a galaxy moves rapidly within the hot intra-cluster gas, it is left with a disturbed disk and an H I deficiency from the stripping caused by the ICM. For example, the galaxy cluster Pegasus I has no X-ray emission, which is a sign of an unimportant ICM gas mass. It shows a low velocity dispersion and no evidence for systematic depletion of H I in the spiral galaxies. As a result of this moderate cluster environment, ram pressure stripping is not a likely effect to explain the central starburst of the galaxy NGC 7648 in this cluster (Rose et al. 2001).

Interactions with the ICM however, have remained a popular explanation of some of the properties of the Butcher-Oemler population in general (Poggianti et al. 1999), for the simple reason that a removal of H I gas would reduce the amount of star formation in the galaxy clusters at low redshift. A large fraction of the spirals in moderate redshift clusters are k or k+a type (Poggianti et al. 1999). This means that they have little or no asymmetry and suggests that whatever process is ending star formation, it cannot affect their morphology in any great sense. The effects of mergers, and to some extent galaxy harassment, last a fairly long time and therefore do not present a good case. The fact that ram pressure stripping acts exclusively on the gas content of the galaxy is another reason it could be linked to the Butcher-Oemler effect (Poggianti et al. 1999), and remains an important process for galaxy evolution.

1.5 Cool Cores and Cooling Flows

The discovery of large amounts of hot gas that permeates rich clusters has been key in understanding the nature of galaxy clusters. The properties of this X-ray emitting gas have been studied with vigor for several decades. In the 1970's, a central spike in the X-ray emitting gas density profiles of certain clusters of galaxies was first observed, and these spikes were seen continually to occur at the center of optically rich clusters, often within a few tens of kiloparsecs of the brightest cluster galaxy. And so began the effort to understand any interplay between the BCG and the hot intracluster medium. A model was soon put forth, in which a cooling flow forms when the internal pressure of the cooling X-ray gas drops below the gravitational potential of the cluster (Cowie & Binney 1977; Fabian & Nulsen 1977). As the ICM cools through bremsstrahlung radiation, the gas becomes more dense, succumbs to the gravitational potential of the cluster, and flows towards the center. A cooling flow cluster is therefore identified observationally as one with an excess central X-ray flux (as the radiation is due only to collisional processes and therefore proportional to the electron density of the gas).

1.5.1 The Mass Deposition Rate

For gas emitting below 10^7 K, the presence of strong iron L lines near 1 keV becomes more prominent, and the metallicity and temperature of the gas can be determined. After deprojection, a process which assumes spherical symmetry of the cluster gas, spectra are extracted from representative annuli to which model spectra are fit (White 2000). The surface brightness at intermediate radii can be fit to the so-called β-model, which is derived for isothermal collisional processes, and used to characterized the electron density. The following equation (Fabian & Nulsen 1977; McNamara & Nulsen 2007) shows how the cooling time, t_{cool}, falls as the electron and proton density increase (n_e and n_H, respectively):

$$t_{cool} = \frac{P}{[(\gamma - 1)\, n_e\, n_H\, \Lambda(T)]}, \tag{1.1}$$

where P is the gas pressure, $(\gamma - 1)$ is the ratio of specific heats, and $\Lambda(T)$ is the cooling function.

This leads to short cooling times, $< 10^9$ yr, at the cluster center where the high surface brightness spikes are seen. Assuming the luminosity, L_{cool}, from within the cooling region (r_{cool} - the radius with which t_{cool} is less than the time from the last major heating event) arises only from the thermal radiation of the gas and the work done on the gas as it flows into r_{cool}, the mass deposition rate (MDR) can be calculated from the equation below (Fabian 1994):

$$\mathrm{MDR}\,[M_\odot\,\mathrm{yr}^{-1}] = \frac{2}{5}\,\frac{\mu\, m_H}{k\,T}\,L_{cool}, \tag{1.2}$$

where μ is the mean molecular weight, m_H is the hydrogen mass, T is the temperature, and k is the Boltzmann's constant ($8.617 \times 10^{-5}\,\mathrm{eV\,K^{-1}}$).

In the absence of an additional heat source, the gas must condense out of the hot phase. If the cooling flow deposits huge reservoirs of molecular hydrogen, this gas could potentially give birth to stars which would then ionize the hydrogen gas. However, the process is certainly not so simple. For example, Bertoldi & McKee (1992) calculate the Jean's mass for several molecular gas clumps inside giant molecular clouds of the Galaxy and find that several are too small to be gravitationally supported, and instead are being confined by the ambient medium. As such, and unless otherwise stimulated, these clumps never undergo the collapse required for subsequent star formation (Elmegreen 2000).

Nonetheless, and beginning early on, evidence of star forming regions, including the observations of small scale Hα emission line luminosities (Cowie et al. 1983) and excessively blue colours (McNamara & O'Connell 1989; Johnstone et al. 1987) were reported. Edge et al. (2002), found that whenever there are detections of molecular hydrogen in a cooling flow cluster, there are also detections of Hα emission. Crawford et al. (1999) found that 27% of their 256 X-ray selected BCGs have optical spectra similar to those seen in cooling flow clusters. Regardless of the fact that the implied levels of star formation were too low, its discovery encouraged an almost teleological hypothesis which was argued for several years - that the hot gas would condense into clouds of molecular hydrogen, at the prescribed rates, of order 100-1000 $\mathrm{M_\odot\,yr^{-1}}$, and subsequently form a new generation of stars (Fabian 1994).

New Complexity in the Cooling Flow Hypothesis

Despite the many convincing observations of nearby cooling flow clusters which show that star formation does happen at some level (which I discuss below in Section 1.5.2), that these observations are the evidence supporting the cooling flow phenomenon is controversial, and debate over this issue has remained strong even until the writing of this thesis. Historically, the problem had been a discrepancy between the mass deposition rates, how much cool gas drops out of the ICM per year, and the star formation rates inferred in the central galaxies from ultraviolet excess or Hα emission (McNamara 2004).

Recently, high resolution X-ray observatories have been launched, and the simple view of the cooling flow producing molecular clouds which directly produce a new burst of star formation has become obsolete. The more recent problem with cooling flows is that although newer X-ray observatories such as *Chandra* and *ASCA* still show temperature drops towards the center of the cluster (Bauer et al. 2005), the strong iron L lines that describe gas much cooler than $\sim$2 keV do not exist (Peterson et al. 2003; Böhringer et al. 2002). Even though the theoretical values for mass deposition rates are no longer much too large as compared to the observed star formation rates,

questions remain as to why so little of the gas is cooling. The implication is that the gas must be continually reheated by some mechanism such as thermal conduction from the surrounding ICM, shocks, hot stars, or an AGN (Böhringer et al. 2002), and therefore the details of how the star formation takes place are more complicated than the mere drop-out from the ICM.

Most prominently featured in the current literature, is the discussion of the importance of AGN feedback (Pizzolato & Soker 2005), and the radio relics that are often seen around the BCG (McNamara & Nulsen 2007). By measuring the extent of X-ray cavities, which have been created by radio jets, the radio power expelled by the AGN can be deduced (Bîrzan et al. 2004), and this is enough to offset the cooling flow. These AGNs are also potential sinks for the cooling gas as well, and can contribute to the ionization of hydrogen gas clouds. In fact, molecular hydrogen observations by Edwards (2004) of Abell 1795 using the Canada France Hawaii Telescope's infrared detector showed an H_2(2-1) flux higher than that expected from direct cooling of the ICM, as well as a rather condensed morphology suggesting that perhaps the molecular hydrogen is being reheated by an AGN, as already suggested by Donahue et al. (2000) for NGC 1275.

There is more observational work to be done as well. Optical line emission ratios can elucidate much about the state and excitation source of the emitting gas, but it is rare that these properties are studied in great detail in cooling flow BCGs. As well, several X-ray clusters at low redshift are missing the high quality *Chandra* and *XMM-Newton* observations. In terms of the X-ray properties of the cooling flow itself, there are the seminal papers describing cluster X-ray properties (Fabian 1994; White 2000; Peres et al. 1998; Chen et al. 2007), but these all derive parameters such as the mass deposition rate from *ROSAT* data, which is known to be of too low a resolution to constrain cooling models adequately. In this thesis we are interested in the optical properties which might suggest a clear link between the cooling X-ray gas and interesting activity at the center of the BCG such as AGN emission, or a younger generation of stars, but again the current data is not overabundant. Cowie et al. (1983), Crawford et al. (1999), Donahue et al. (2000), Conselice et al. (2001) and recently, Crawford et al. (2005a), Wilman et al. (2006), and Hatch et al. (2007) discuss the morphology of Hα emission at the center of cooling flow BCGs. Fabian et al. (2001), Edge et al. (2002), and Edwards (2004) have looked at molecular hydrogen in some well known cases, but again this makes up only a small subset of the total number of observable systems.

1.5.2 Activity in Cooling Flows

The evidence put forth for recent star formation in cooling flow clusters is plentiful. A trend exists between cooling flows and the occurrence and amplitude of blue colour excesses associated with star formation in central cluster galaxies. Observations from the *Chandra* telescope have shown that the regions of star formation are associated with

bright lumps and filaments of gas whose radiative cooling times approach ~300 Myr (Fabian et al. 2001). In Abell 1795 for example, blue light is detected in excess to what is expected from the underlying central dominant galaxy. This suggests a population of hot young stars (McNamara et al. 1996). Also, not only have many rotationally excited transitions of CO been detected, but the O VI line has been seen as well, which shows that gases at a range of temperatures exist (20 K and 100 000 K, respectively).

The star formation history in cooling flows can vary between short duration bursts or more extended episodes lasting between 0.1 and 1 Gyr (McNamara & O'Connell 1993). For some cluster galaxies, the short duration bursts can be explained by the triggering from a central radio source, however, neither the short nor long duration bursts are consistent with the steady cooling and accretion of mass directly dropping out of the ICM. Rather, the mass is likely deposited into molecular clouds which are than reheated by one of many possible processes - hot stars, shocks, or AGN (Wilman et al. 2002), for example. The ICM and radio sources seen in the *Chandra* images often appear to be interacting. These interactions form cavities, or bubbles, in the surface brightness of the X-ray gas which move buoyantly through the ICM (McNamara 2004). In some of these systems, the bubbles carry enough energy to be able to balance the radiative losses emerging from the center of the clusters in the X-ray band. This is one explanation for a lack of gas seen below 2 keV.

The question now is less if there is star formation, but more how it may or may not be linked to the cooling flow. To test the new, self-regulated cooling and reheating paradigm, McNamara (2004) is currently attempting to show that the cooling upper limits are systematically below the star formation levels. In particular, the cooling rates and star formation rates agree for several clusters (Abell 1795 and Abell 2597 amongst others).

1.6 Objective

Thus, it is not just the cluster environment that is boisterous with activity; several of the elliptical galaxies themselves are far from being "old, red, and dead." Many of the large ellipticals and cD galaxies have evidence of emission lines and new stars forming in their central regions. This, coupled with the possiblilty that the cooling X-ray gas may be adding to the mass of these galaxies has served as motiviation for the research I present in this thesis.

The role of the cooling X-ray gas on the present state of the stellar populations of the BCG will be elucidated by examining BCGs and non-BCGs, in both cooling flow systems and non-cooling flow systems. This will illuminate the effect of the cooling flow on the formation of the galaxy, and on its evolution as well. To accomplish this first goal, the fraction of line-emitting BCGs in two large galaxy cluster surveys is determined. In order to study the characteristics and morphology of the stellar populations of the

central galaxies, imaging spectroscopy data from the Gemini GMOS North and South Integral Field Units (hereafter, Gemini IFU) and from the William Herschel Telescope (WHT) OASIS instrument is collected for 9 BCGs. Detailed maps of the central activity (described mainly by the Hα emission line) are created. By observing the bright Hα emission lines in the spectra of spiral and irregular galaxies, it has become well known that they are currently forming stars, and in many cases undergoing starbursts. In such cases, the star formation rate reaches 10-1000 $M_{\odot}\,yr^{-1}$ as opposed to the $2\,M_{\odot}\,yr^{-1}$ produced on average in the disks of normal spirals (Inoue et al. 2000). Thus, the appearance of Hα emitting gas in BCGs is an exciting find, and that it is not seen in non-cooling flow clusters (Edwards et al. 2007) adds to the intrigue.

In Chapter 2, the paper entitled Line Emission in the Brightest Cluster Galaxies of the NOAO Fundamental Plane and Sloan Digital Sky Surveys is presented. In Chapter 3 I give more details and discuss tests that were performed in the study of Chapter 2. Chapter 4 presents the observations and analysis of the very central regions of 9 BCGs using integral field spectroscopy. I conclude by relating the two studies and discussing future work in Chapter 5.

Chapter 2

Line Emission in the Brightest Cluster Galaxies

This chapter presents the paper entitled "Line Emission in the Brightest Cluster Galaxies of the NOAO Fundamental Plane and Sloan Digital Sky Surveys" by L. O. V. Edwards, Michael J. Hudson, Michael L. Balogh, and Russell J. Smith. Under the supervision of Michael Hudson and Michael Balogh, I investigated the fraction of line emitting BCGs in two large samples of galaxy clusters. This paper (Edwards et al. 2007) was published in July, 2007 in volume 397 of the *MNRAS* journal. The chapter following this one discusses tests that were performed on the galaxy samples, but which were not included in the article. It consists of a more general discussion of the BCG sample, the cluster designations, and the way in which I match optical galaxies to radio and X-ray counterparts.

Abstract

We examine the optical emission line properties of Brightest Cluster Galaxies (BCGs) selected from two large, homogeneous datasets. The first is the X-ray selected National Optical Astronomy Observatory Fundamental Plane Survey (NFPS), and the second is the C4 catalogue of optically selected clusters built from the Sloan Digital Sky Survey Data Release 3 (SDSS DR3). Our goal is to better understand the optical line emission in BCGs with respect to properties of the galaxy and the host cluster. Throughout the analysis we compare the line emission of the BCGs to that of a control sample made of the other bright galaxies near the cluster center. Overall, both the NFPS and SDSS show a modest fraction of BCGs with emission lines (∼15%). No trend in the fraction of emitting BCGs as a function of galaxy mass or cluster velocity dispersion is found. However we find that, for those BCGs found in cooling flow clusters, 71^{+9}_{-14}% have optical emission. Furthermore, if we consider only BCGs within 50 kpc of the X-ray center of a cooling flow cluster, the emission-line fraction rises further to 100^{+0}_{-15}%. Excluding the

cooling flow clusters, only ~10% of BCGs are line emitting, comparable to the control sample of galaxies. We show that the physical origin of the emission line activity varies: in some cases it has LINER-like line ratios, whereas in others it is a composite of star formation and LINER-like activity. We conclude that the presence of emission lines in BCGs is directly related to the cooling of X-ray gas at the cluster center.

2.1 Introduction

The brightest cluster galaxy (BCG) is typically a giant, red elliptical or cD galaxy, located near the center of the gravitational potential. It is likely that a rich history of galaxy-galaxy interactions and mergers is responsible for the unique morphology of such galaxies. This is supported indirectly by several pieces of evidence, including: the luminosity of the BCG is correlated with the cluster mass (Scott 1957; Lin & Mohr 2004) and X-ray luminosity (Hudson & Ebeling 1997); BCGs in the most X-ray luminous clusters are larger and have surface brightness profiles which are less steep than their low X-ray luminosity counterparts (Brough et al. 2005); and the velocity dispersion of BCGs rises less steeply with luminosity than for other bright galaxies (von der Linden et al. 2007). All this indirect evidence for a rich merger history is supported by high resolution imaging of BCGs obtained with the *Hubble Space Telescope*, which has revealed that the cores of these galaxies can be complex, often showing multiple nuclei and prominent dust signatures (Laine et al. 2003).

However, the evolutionary history of these galaxies is still not completely understood, and work on cooling flow (CF) clusters has hinted at another possible mechanism for adding to the stellar mass of BCG. The original cooling flow hypothesis is that hot cluster X-ray gas cools and condenses out of the intracluster medium (ICM) into the cluster's potential well, forming molecular clouds and stars (Fabian 1994). This drop-out occurs at the center of the cooling flow, within the cooling radius, i.e. onto the BCG. Cooling flow clusters are common in the local universe (making up about 50% of the population in an X-ray flux limited sample Peres et al. 1998; Chen et al. 2007)), and cD galaxies are often found at the center of these systems. Because of this, a link between the cooling X-ray gas and recent star formation in the BCG has been discussed for many years (Fabian 1994). Convincing observations which support this idea have been presented: a blue and UV-colour excess (McNamara et al. 1996; McNamara 2004; Hicks & Mushotzky 2005), molecular gas (Edge et al. 2002; Jaffe et al. 2001; Salomé & Combes 2003) and Hα emission (Crawford et al. 1999; Donahue et al. 2000; Crawford et al. 2005a) have all been seen in the cooling flow cluster's BCG. However, although the morphology of the Hα emission is diffuse and filamentary, indicating star formation in some CF BCGs, in others it is very compact and more characteristic of AGN dominated emission (Donahue et al. 2000; Edwards & Robert 2007; Hatch et al. 2007). As well, von der Linden et al. (2007) recently showed that optical emission lines in BCGs

predominantly arise from LINER emission, rather than normal star formation.

More recent X-ray satellite measurements from *Chandra* and *XMM-Newton* have shown that the gas does not cool directly from the hot X-ray phase through to the cool molecular gas phase (Böhringer et al. 2002), but rather that a large amount of the cooling gas is being reheated before condensing out of the ICM. The current paradigm is that AGN activity in the BCG is reheating the cooling X-ray gas, which implies a more complicated feedback process between the cooling gas and the central galaxy (e.g Pizzolato & Soker 2005). This leads to revised, predicted mass deposition rates that are now in reasonable agreement with the observed values (Böhringer et al. 2002; Pizzolato & Soker 2005). The observed molecular and ionic gas may be attributed to a small amount that has cooled from the cooling flow; alternatively, the Hα may be excited by the AGN itself. Detailed studies of star formation indicators in galaxy groups and clusters in cooling flows and non-cooling flows, discriminating between those with and without AGN activity, are required in order to analyze the relative importance of the different processes.

A correlation between optical line emission in the BCG and cluster properties has been explored by several authors, most notably Crawford et al. (1999), who found that 27% of BCGs have optical line emission, and that the projected distance from the BCG to the X-ray center is less for line emitting galaxies than for non-emitting galaxies. Recently, von der Linden et al. (2007) and Best et al. (2007) have explored the properties of BCGs in the SDSS, using the C4 cluster catalogue (Miller et al. 2005). These authors find that radio-loud AGN activity is more frequent in BCGs than in other galaxies of the same mass, but that this frequency does not depend strongly on cluster velocity dispersion. On the other hand, in their study of radio-loud properties of an X-ray selected cluster sample, Lin & Mohr (2007) find the overall radio-loud fraction to be 30% in BCGs, and that the fraction is higher in more massive clusters. Importantly, von der Linden et al. (2007) find that many of these radio-loud galaxies would not necessarily be identified as AGN from their optical emission lines and, in fact, that optical AGN activity appears to be *less* frequent among BCGs than other cluster galaxies of similar mass. The interpretation is complicated by the fact that the radio-selected galaxy sample, though restricted to red galaxies, could be contaminated by galaxies in which the low luminosity radio emission arises from star formation, rather than AGN activity.

In this paper, we explore optical line emission in BCGs with respect to properties of the galaxy and the host cluster, using two large, homogeneous datasets. One sample is taken from the X-ray selected, National Optical Astronomy Observatory Fundamental Plane Survey (NFPS), for which the X-ray properties are known for all clusters. For many of these clusters, we are able to identify those with short cooling times (CF clusters) based on *ROSAT*, *Chandra*, or *XMM-Newton* observations. We complement this sample with optically-selected clusters drawn from the Sloan Digital Sky Survey

Data Release 3 (SDSS DR3), which is not biased toward X-ray luminous clusters, and is therefore more representative of the cluster population. In addition, the greater spectral coverage of the SDSS allows us to use emission line ratios to identify whether the emission arises predominantly from composite H II region and LINER activity, or from LINER activity alone (pure H II region, and Seyfert-like emission are both rare).

The paper is organized as follows. In section 2.2, we introduce our galaxy samples and selection criteria. In section 2.3, we report our results. For the X-ray selected NFPS we compare the frequency of Hβ emission in BCGs as a function of BCG magnitude and distance to the cluster center. Similar results are found for the SDSS sample, based on the Hα emission line. However, we find that there are differences between the BCGs in the two samples, which we can attribute to the nature of the X-ray emitting gas. In section 2.4, we consider the impact of our results on various galaxy and cluster formation hypotheses, and summarize our results. We conclude in section 2.5. Unless otherwise stated our analysis assumes the values $\Omega_m = 0.3$, for the matter density parameter, $\Omega_\Lambda = 0.7$ for the cosmological constant, and $H_0 = 100\,\mathrm{km\,s^{-1}\,Mpc^{-1}}$ for the Hubble parameter. L_X refers to the bolometric X-ray luminosity throughout.

2.2 Data and Sample Selection

For both NFPS and SDSS, our goal is to identify the BCG and a similar sample of luminous "control" galaxies that is located in the inner regions of the cluster. We first discuss the sample selection of the NFPS.

2.2.1 NOAO Fundamental Plane Survey

The NFPS is an all sky study of 93 X-ray selected rich clusters with redshifts between 0.010 and 0.067 (Smith et al. 2004). The goals of the project are to measure cosmic flows on the scales of $100\,h^{-1}$ Mpc and to build a large homogeneous sample with which to investigate physical effects and environmental influences on early-type galaxy evolution and formation (Smith et al. 2004). The spectroscopic observations are made though a fiber diameter of $2''$ and are limited to red sequence galaxies; galaxies more than 0.2 magnitudes bluer than the red sequence were not generally observed spectroscopically. There are spectra for 5388 galaxies with a wavelength coverage between 4000 and 6100 Å and a resolution of $\sim$3 Å (Smith et al. 2004).

Cluster, BCG, and Control Sample Definitions

In order to respect the completeness of the NFPS cluster sample, we exclude the 13 clusters that were observed serendipitously and that did not meet the original L_X limit of $10^{42.6}\,\mathrm{erg\,s^{-1}}$. For each cluster, the redshifts were used to calculate the cluster velocity dispersion and the radius at which the mean density interior to the cluster

is 200 times the critical density (σ_{cl} and r_{200}, respectively). We used the prescription $r_{200} = \sqrt{3}\,\sigma_{cl}/1000\,\mathrm{km\,s^{-1}\,Mpc^{-1}}$ as derived in Carlberg et al. (1997). Note that r_{200} is typically of order 1.5 $h^{-1}\,$Mpc, much larger than the cooling radius of a typical cooling-flow cluster (about 200 kpc). The center of the cluster is taken to be at the peak of the X-ray emission (Ebeling et al. 1996, 2000). The galaxies are then assigned to the clusters based on a radial and a velocity weighting as in Smith et al. (2004). For this analysis, we are interested in only the bright galaxies in the central regions of the cluster and so include a magnitude limit of $M_K < -24$, based on K-band total magnitudes obtained from 2MASS catalogues (Skrutskie et al. 2006). This is about half a magnitude brighter than the characteristic K-band magnitude of $M_{K^*} = -23.55$ (Lin et al. 2004, for $H_0 = 100\,\mathrm{km\,s^{-1}\,Mpc^{-1}}$). Since we are interested only in galaxies occupying a similar environment as the BCG, i.e. in the central regions of the cluster, we consider only galaxies within $0.5\,r_{200}$, and with velocity differences with respect to the cluster mean velocity less than twice the cluster velocity dispersion.

The BCG is then defined as the first rank cluster galaxy using the K-band magnitudes. In twenty cases, the BCG was not observed spectroscopically due to constraints in the fiber positioning, and these clusters have been excluded from our analysis. Our final sample consists of 60 clusters with BCGs, as summarized in Table 2.1 and listed in Table 2.2. Our control sample consists of the 159 other bright ($M_K < -24$) galaxies within the same radial and velocity cuts described above. The BCGs are, of course, excluded from the control sample.

For the NFPS, we use the stellar absorption-corrected Hβ emission as an indicator of star formation activity, since Hα is not generally available in these spectra. Although Hβ emission is relatively weak, the high signal-to-noise ratio of these spectra allow us to measure its strength reliably after correcting for underlying stellar absorption (see the errors quoted in Table 2.2). The observed galaxy spectra are divided by best fit absorption template stellar population synthesis models from Vazdekis (1999), which have been redshifted and broadened to match the velocity dispersion of the observed galaxy. Subsequently, the Hβ equivalent width is measured directly, without assuming a particular line profile, from the ratio of the observed spectrum to the best fit model (Nelan et al. 2005). A thorough discussion of the emission line measurements can be found in Nelan et al. (2005). For two of the NFPS BCGs, in Abell 780 and in Abell 1795, the nebular emission is strong enough that our standard methods for obtaining reliable velocity dispersions, and hence stellar absorption corrections, fail. For galaxies of similar magnitude, the typical stellar absorption at Hβ is $\sim$1.5 Å with an uncertainty of 0.3 Å. This error dominates our uncertainity in the total equivalent width of emission for these two special cases. For the BCGs in Abell 780 and Abell 1795, the Hβ equivalent widths are 7.8 Å and 7.2 Å, respectively. However, to achieve a plot that is more easily read, these points are set to respective lower limits of 3.3 Å and 3.7 Å in Fig. 2.5 and Fig. 2.6.

We will define emission-line galaxies to be those with an equivalent width > 0.5 Å. Since the Hα and [NII] lines are generally unavailable, we are unable to use Baldwin et al. (1981, hereafter BPT) diagrams to reliably distinguish emission due to star formation from that arising from AGN activity.

Cooling Flow definition

In general, we designate an NFPS cluster as "cooling flow" (CF) or "non-cooling flow using mass deposition rates and X-ray cooling times from published catalogues (Peres et al. 1998; White 2000; Allen et al. 2001; Bîrzan et al. 2004). This is a somewhat subjective classification complicated by the fact that not only are mass deposition rates calculated from *ROSAT* observations typically 2-10 times higher than those calculated from *Chandra* observations (Böhringer et al. 2002), but also higher resolution spectra from *XMM-Newton* are not well matched to an isobaric cooling model (Peterson et al. 2003); thus the mass deposition rate may not be an exact indicator of a cooling flow cluster. Therefore, whenever possible, we prefer to use recent cooling flow designations based on the presence of a central temperature gradient in *XMM-Newton* or *Chandra* observations. For the rest, we are left with using the mass deposition rate based on *ROSAT* data as an indicator. For the 11 cases where observations are from the *Chandra* or *XMM-Newton* satellites, we define a CF cluster to be one with a mass deposition rate $\dot{M} > 0$; otherwise, we require $\dot{M} > 100\,\mathrm{M}_{\odot}\,\mathrm{yr}^{-1}$. Within this framework we have 14 CF clusters and 19 non-CF clusters. The CF status of another 27 clusters is unknown. Clearly this is not an unassailable definition; however, it is likely that most, if not all, of the clusters we classify as CF clusters really do have short cooling times in the center. Some galaxies with low mass deposition rates will undoubtedly fall in our non-CF sample. With this in mind, our results are not sensitive to this definition. We further discuss this point in Section 2.3.1, as well as a continuous method of defining a CF cluster, based on an excess of observed X-ray luminosity to predicted values (McCarthy et al. 2004).

2.2.2 Data from the Sloan Digital Sky Survey

Our second sample of galaxy clusters is derived from the C4 catalogue (Miller et al. 2005), based on the third data release (DR3) of the SDSS. This release covers 5282 square degrees in imaging, and 4188 square degrees in spectroscopy (Abazajian et al. 2005). Imaging was taken in five optical bands, u′, g′, r′, i′ and z′ with a median spatial resolution of 1.4″ in r′. Spectra are observed with a aperture diameter of 3″, cover the wavelength range from 3800 to 9200 Å and have a spectral resolution of $\sim$3 Å in r′. Redshifts measured from these spectra are accurate to $\sim$30 km s^{-1} (Abazajian & et al. 2005). The Hα line strengths are measured by fitting Gaussian functions to the line profile in a standard pipeline (Stoughton et al. 2002). For $W_{\circ}(H\alpha) > 5$Å, the

equivalent width uncertainty is less than 20%. For weaker lines, $W_\circ(H\alpha) < 5\,\text{Å}$ the errors are known to be large (Gómez & et al. 2003). We have made no correction to the emission-line strengths for underlying stellar absorption. For our purposes this is safe to neglect because, whereas even a modest star formation rate generates considerable Hα emission, the stellar absorption doesn't vary by more than $\sim$1 Å for moderately old populations.

As described in Miller et al. (2005), clusters and groups are identified as over-densities in the multi-dimensional space spanned by position, redshift, and five-colour photometry. There are 1106 clusters identified in the SDSS DR3 using this algorithm. We further select objects with redshifts $z < 0.10$, to minimize the incompleteness of the sample. In order to reduce the number of clusters with uncertain velocity dispersions, we exclude clusters flagged as having significant substructure. Specifically we include only clusters flagged as SUB = 0, i.e. those for which the ratio of the standard deviation of the cluster velocity dispersion profile to the mean cluster velocity dispersion is less than 15 (Miller et al. 2005). This reduces the number of clusters in our sample to 825.

Cluster, BCG, and Control Definitions

For the SDSS we define the BCG and clusters in as close a manner as possible to the NFPS case. Again, the BCG is the brightest galaxy in the K-band (and with $M_K < -24$), within half of r_{200} of the geometric center of the cluster, and within two times the cluster velocity dispersion. However, the geometric centers we use are different than those in the C4 catalogue. We start with the C4 catalogue geometric centers measured using the luminosity weighted position average of all the galaxies within 1 Mpc and four times the velocity dispersion. As this definition encompasses such a large area, multiple substructures along the line of sight heavily influence the position of the center. For example, the geometric center will be placed in between two obvious subclumps. Thus, we iteratively recalculate a luminosity-weighted center using only galaxies within two times the cluster velocity dispersion, and with magnitude $M_K < -24$.

Due to the incomplete spectral coverage of the central galaxies, there are 154 cases in which the brightest cluster galaxy had not been observed spectroscopically. We exclude these clusters from the sample. To ensure this is not introducing an important bias, we verified that the subset of BCGs observed in the photometric catalogue but not in the spectroscopic catalogue have an equivalent ($u'-r'$) colour distribution to those in our final, spectroscopic sample. Finally, we also remove those clusters whose geometric centers are within $15'$ of a survey boundary, as well as those with measured velocity dispersions greater than $1200\,\text{km}\,\text{s}^{-1}$. The latter restriction is made because such high values are usually a result of significant contamination from line-of-sight substructure. These selections leave us with a final sample of 328 BCGs.

Our control sample is built from the other bright galaxies near the center of the

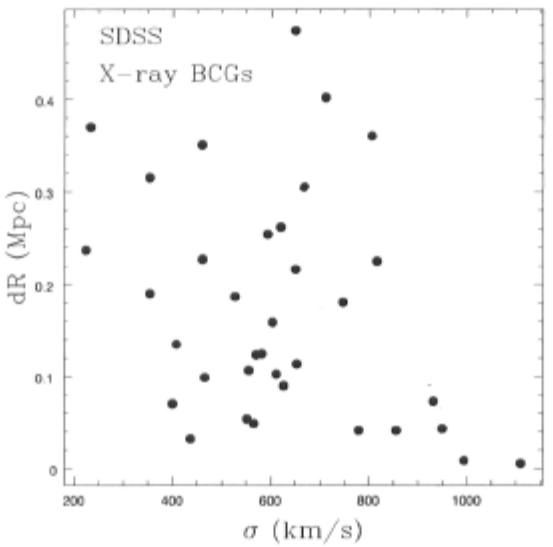

Figure 2.1: **Cluster velocity dispersion as a function of the difference in the X-ray and geometric centers for the 35 SDSS BCGs that have available X-ray positions.** *The clusters with large discrepancies between the two centers are generally found to have geometric centers highly influenced by in-falling groups.*

clusters, as in the NFPS case. In order to increase the size of our control sample, we include clusters where the brightest central galaxy was not measured spectroscopically. There are 526 control galaxies in 353 groups and clusters with a velocity dispersion less than 1200 km s^{-1}. We note that the number of control galaxies per cluster is significantly larger in the X-ray luminosity selected NFPS clusters, probably because they are richer than the optically-selected SDSS clusters.

Because the centers of the NFPS clusters are based on the X-ray centroid, whereas in the SDSS the geometric center is used, it is important to compare the two definitions. In order to find X-ray centers for the SDSS clusters, we have matched them to X-ray cluster catalogues including: NORAS (Böhringer & et al. 2000), REFLEX (Böhringer & et al. 2001), BAX (Sadat et al. 2004), XBACS (Ebeling et al. 1996), RASSCALS (Mahdavi et al. 2000), as well as Popesso et al. (2004); Mulchaey & Zabludoff (1998) and Horner et al. (2001). Most of the cluster catalogues are based on *ROSAT* observations, where the flux limit is high. This restricts our sample of SDSS clusters with X-ray detections to the small subset of massive clusters at $z < 0.03$. There are 35 X-ray cluster matches, i.e. cases where the X-ray center is within half of r_{200} of one of our 328 SDSS clusters. Fig. 2.1 shows that for most of the matched clusters, there is good agreement between the X-ray and geometric centers. However, also depicted in the figure is how some cases exhibit differences of up to 0.5 Mpc, especially for lower mass clusters. It is unlikely that this is caused by an uncertainty in the X-ray centers, as the centers of the NORAS, BCS, and XBACS samples were found by determining the two-dimensional center of mass

using the Voronoi Tessellation and Percolation method (Ebeling & Wiedenmann 1993), and are generally accurate to about $1'$ (Ebeling et al. 1998), corresponding to $\sim$90 kpc at $z \sim 0.08$. More likely, is that the geometric centers do not trace the gravitation potential of the cluster as well as the X-ray centers. We note that for many of the cases in which the centers are discrepant by > 200 kpc, the geometric center appears to be contaminated by in-falling groups; which is not surprising as it is measured using a typical line of sight projection of $\sim$3 Mpc (for $\sigma = 500\,\mathrm{km\,s^{-1}}$).

Emission Line diagnostics

Optical emission line galaxies in the SDSS are identified from the Hα line, which is the line in our wavelength range that is most sensitive to star formation activity. To ensure a fair comparison with the NFPS, we must choose a threshold in Hα equivalent width that is comparable to the Hβ limit used in that survey. Recall that the lines are measured using different techniques, from spectra of different resolution and signal-to-noise, and obtained with different fibres; furthermore, the NFPS Hβ measurements are corrected for underlying stellar absorption, while the SDSS Hα lines are not. Therefore we opt for an empirical "calibration" between the two, by plotting the NFPS Hβ equivalent widths against the SDSS Hα equivalent widths, for galaxies that appear in both surveys (Fig. 2.2). Although there is plenty of scatter, there is a strong correlation between the two lines, and we find the Hα index is about four times larger than the Hβ; encouragingly, this is comparable to the factor of 4.5 derived by comparing the Hα/Hβ ratio for the subset galaxies in the NFPS for which measurements of both emission lines are available (Nelan et al. 2005). Thus, an Hα equivalent width cut of 2 Å is comparable to an Hβ equivalent width of 0.5 Å, and the fraction of galaxies in our samples above either of these thresholds is similar. Note that the points at $W_\circ(\mathrm{H}\alpha) = 0$ are non-detections (plotted with the average uncertainty of 0.15 Å), and those with $W_\circ(\mathrm{H}\alpha < 0)$ are detected in absorption. We have experimented with SDSS Hα equivalent width cuts of 2 ± 1 Å and find that our final results do not change significantly. The good correlation also gives us additional confidence in the template correction used to correct the Hβ equivalent widths for stellar absorption, which is relatively much more important here than for Hα (the average stellar absorption strength is $\sim$1 Å, with variations at the $\sim$0.15 Å level).

Due to the proximity of the galaxies in our sample and the finite fiber size through which they are observed, the amount of extended line emission could be underestimated. However, as we do not know if the emission is extended we have not explicitly accounted for the finite fiber size, nor for the difference in fiber diameters between two surveys. Here again, we argue that the effect on the line strength measurements is calibrated by our use of an empirical relation.

Hα line emission may arise from either ionization by hot stars, or ionization from AGN activity. We use the AGN classification taken from the emission-line analysis

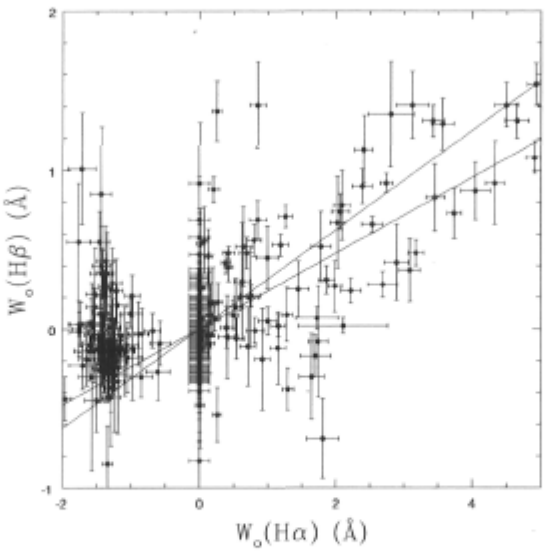

Figure 2.2: **The absorption-corrected NFPS Hβ equivalent width versus the SDSS Hα equivalent width (uncorrected for stellar absorption) for galaxies present in both surveys.** *The points with $W_o(H\alpha) = 0$ are non-detections (plotted with the average Hα error of 0.15 Å), and those with $W_o(H\alpha) < 0$ are detected in absorption. We identify line-emitting NFPS galaxies as those with W_o (Hβ) $\geq$ 0.5 Å. Correspondingly, we use a value of W_o (Hα) $\geq$ 2 Å for the SDSS galaxies. The best fit lines are constrained to go through (0,0) and are only fit to galaxies with W_o (Hα) $\geq$ 2 Å and ignore an outlier at W_o (Hα) $\approx$ 40. The two different lines are fitting for W_o (Hβ) as a function of W_o (Hα) or vice versa.*

discussed in Kauffmann et al. (2003), which is based on Hα/[NII] and [OIII]/Hβ diagnostic ratios, which separates AGN, star-forming, and composite (intermediate between star-forming and AGN) regions on BPT diagrams. Table 2.1 shows that, in our SDSS sample, ~65% of galaxies with emission have line ratios consistent with AGN or composite emission, and this fraction may be somewhat higher for the BCG population, relative to the control galaxies. Using Ho et al. (1997) to separate Seyferts from LINERs, along with the Kauffmann et al. (2003) definitions, we find that ~33% of emitting SDSS BCGs can be reliably measured as LINERs, ~27% as composite; Seyfert-like emission is negligible (~3%). If we assume the ionizing source for the H II regions is stellar, and that all of the Hα emission is within the fibre diameter, then typical Hα luminosities of our emitting BCGs correspond to star formation rates of ~0.5 to ~1.6 $M_\odot\, yr^{-1}$ (Kennicutt 1998).

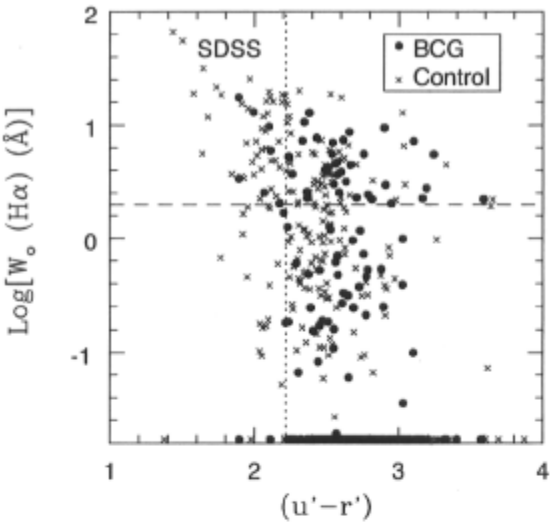

Figure 2.3: **The logarithm of $W_\circ(\mathrm{H}\alpha)$ as a function of (u′−r′) colour of the galaxies in the SDSS.** *The crosses are the control sample, and the filled circles are the BCGs. The colour break of 2.2 is shown as the vertical dotted line, and the horizontal dashed line separates the emitting galaxies from the quiescent. The galaxies at Log[$W_\circ(H\alpha)$]= −1.7 are those with Hα absorption.*

Galaxy Colour

Fig. 2.3 shows the distribution of Hα equivalent width as a function of (u′−r′) colour. Following Strateva et al. (2001), we use the value of 2.2 for the (u′−r′) colour separation of blue and red galaxies. As the NFPS galaxies are red selected, we include a corresponding colour cut of (u′−r′) > 2.2 for the SDSS galaxies when directly comparing to the NFPS results (as in Section 2.3). This colour cut excludes 10 of the 328 SDSS BCGs (only one with X-ray data) as well as 53 control galaxies.

As seen in Fig. 2.3, most BCGs are redder than this cut whether or not they show optical emission. Thus, if the line emission is due to star formation, it does not dominate the global colours of these BCGs, which are presumably quite old. Because of this, results based on BCGs in the NFPS are not likely to be affected by the colour cut in that sample. For the control sample, most of the emission-line galaxies are bluer than our cut. Therefore we expect the fraction of control galaxies with emission, as presented in Section 2.3, to be biased low relative to the BCGs. This is evident from Table 2.1: in the red-selected SDSS sample, the overall fraction of emission line galaxies is similar (∼11%) for both control galaxies and BCGs, while for the unrestricted sample the fraction of control galaxies with emission is ∼18%. This difference is not large enough to affect any of our conclusions in Section 2.3, however.

Table 2.1: Summary of Results

Survey	Sample	Total	Emitting	Emitting Fraction(%)	AGN or Comp. $W_o(H\alpha) > 2$ Å	Known CF	Emitting CF	Emitting Fraction(%)
NFPS	BCGs	60	12	20±6	N/A	14	10	71^{+9}_{-14}
	Controls	159	15	9±2	N/A	36	5	14±6
SDSS	BCGs	328	42	13±2	31	N/A	N/A	N/A
	Controls	526	94	18±2	57	N/A	N/A	N/A
SDSS (RED)	BCGs	318	35	11±2	25	N/A	N/A	N/A
	Controls	446	51	11±2	39	N/A	N/A	N/A
SDSS (X-ray)	BCGs	34	6	18^{+8}_{-5}	3	N/A	N/A	N/A

Note: The first column presents the survey studied, NFPS or SDSS. SDSS (RED) includes only the red-selected SDSS galaxies, and SDSS (X-ray) only those with X-ray counterparts. Column 2 indicates if the results are for the BCGs or Controls. Column 3 shows the total number of galaxies for each sample. The number of these which are emitting is shown in column 4, and column 5 shows the fraction of emitting galaxies. Column 6 lists the number of strongly emitting ($W_o(H\alpha) > 2$ Å) galaxies in each sample for which the emission line ratios are characteristic of AGN activity (usually LINER). We present the number of galaxies in our sample which are known to belong to a CF cluster in column 7. Column 8 shows the number of these galaxies in CF which are also emitting, and the final column shows the fraction of emitting galaxies in CF clusters.

2.3 Results

In this section we examine the line emission in the galaxies in our cluster samples as a function of X-ray luminosity, K-band magnitude, and distance from the center of the cluster. The numbers of emission-line galaxies in both surveys are given in column 4 of Table 2.1. There is a higher fraction of emitting galaxies among the NFPS BCGs; 20±6% are emitting, compared to only 9±2% of the controls. If we look only at those BCGs identified with a CF cluster we find an even higher fraction of them show emission, 71^{+9}_{-14}, while the control sample is unchanged (14±6%). On the other hand, only 11±2% of the red BCGs selected from the SDSS sample show emission, comparable to that of the control population (11±2%). In this section we will explore these trends, and differences between the two samples, in more detail. We use errors derived from the posterior probability distribution where sample sizes are small[1].

2.3.1 Dependence on the Presence of a Cooling Flow

The most prominent result from the NFPS clusters is that the presence of a cooling flow is highly correlated with the presence of emission lines in the BCG. Fig. 2.4 shows the bolometric X-ray luminosity against the cluster velocity dispersion (a proxy for

[1]These errors are presented as error bars on the histograms of Fig. 2.5 and Fig. 2.6

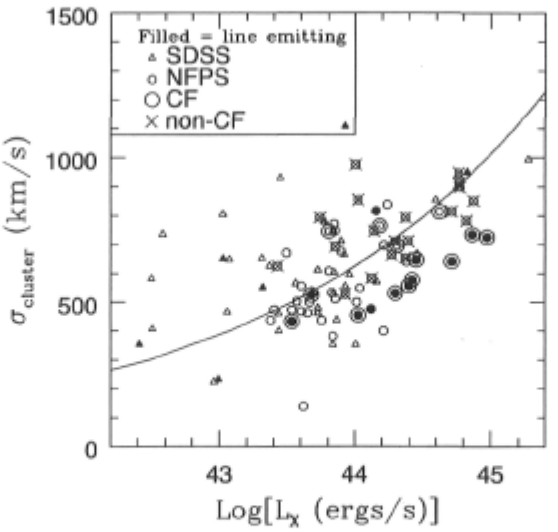

Figure 2.4: **The cluster velocity dispersion as a function of the bolometric X-ray luminosity.** *The solid line is the preheated model from Babul et al. (2002), which is known to provide a good match to non-CF clusters (McCarthy et al. 2004; Balogh et al. 2006). Known CF clusters in our sample do generally lie to the right of this model.*

dynamical mass). We can see that most of the cooling flow clusters have larger X-ray luminosities for their mass, and that it is these clusters that have a BCG with line emission. Therefore, in the rest of the NFPS analysis we separate our sample into CF and non-CF subsets. Notice that in Fig. 2.5 and Fig. 2.6 (which we discuss below), none of the emitting BCGs are non-CFs. As mentioned in Section 2.2.1, we use a rather strict cut for our definition of a CF, requiring *ROSAT* based $\dot{M} > 100\,\mathrm{M}_{\odot}\,\mathrm{yr}^{-1}$. However, changing our arbitrary definition of a CF cluster (e.g. to those with $\dot{M} > 10\,\mathrm{M}_{\odot}\,\mathrm{yr}^{-1}$) does not significantly change our results.

It would be useful to have a way to identify likely cooling-flow clusters without the need for high quality surface brightness and temperature maps. Recently, McCarthy et al. (2004) has shown that CF clusters show significantly higher total X-ray luminosities, relative to their total dynamical mass, consistent with predictions from steady-state cooling models. On the other hand, non-CF clusters can be well modelled with cosmological haloes in which the gas has been preheated to $\sim$300-500 keV cm^2 (see also Balogh et al. 2006). This suggests that one could use the excess X-ray luminosity relative to these preheated models as an indicator of CF status. The solid line in Fig. 2.4 represents models for clusters with preheating from Babul et al. (2002). Indeed, using this method arrives at results for the emission fraction which are very similar to those obtained when we use the mass deposition rate to define CF clusters. The separation is not as striking as in McCarthy et al. (2004), probably because the measured velocity

dispersion can be systematically affected by substructures.

2.3.2 Magnitude Dependence

We show in Fig. 2.5 the line emission strength as a function of K absolute magnitude for the NFPS and SDSS BCGs and control galaxies. The NFPS clusters are separated into CF and non-CF cases. In the non-CF clusters, there are no emitting BCGs, and the fraction of emission-line galaxies, shown in the bottom panels, is also very low for the control galaxies (∼5%). On the other hand, in CF clusters ∼70% of the BCGs show emission, as we noticed also in the previous section. Moreover, the BCGs with strong emission tend to be the brightest galaxies, $M_K < -25.5$, where by definition, there are few control galaxies. Hence, this trend is quite different from what is seen in the control sample, where almost all of the emission line galaxies are fainter than $M_K = -25$. For magnitudes near $M_K \approx -25$, where there is substantial overlap between the two populations, the emission line fraction of both populations are similar for non-CF clusters. The results from the SDSS, which include all clusters regardless of X-ray luminosity or CF status, are consistent with the results for the total NFPS. There are somewhat fewer emission-line BCGs at a given magnitude than the for NFPS, presumably because CF clusters make up a smaller proportion of the sample in the SDSS. We will say more about this in Section 2.4.

Also highlighted on Fig. 2.5 and Fig. 2.6 are the BCGs with LINER-like emission. Most of the emitting BCGs are more characteristic of LINER emission; this is especially true of the less luminous BCGs.

2.3.3 Dependence on Location in Cluster

In our samples, there are some BCGs that are found close to the X-ray center, while others can be found several hundred kpc away. In this section we will investigate whether or not the presence of emission lines in the BCG depends on its distance to the X-ray center.

This is illustrated in Fig. 2.6 where we show the line emission as a function of cluster radius for the NFPS galaxies. *All of the strongly emitting BCGs are within 50 kpc of the X-ray center.* As discussed in the previous section, these emitting galaxies are also usually found in a cooling flow cluster. In the rightmost panel we show the equivalent plot for the 34 BCGs in the SDSS sample for which we have X-ray centers. Although the sample is small, our results are consistent with those seen in the NFPS; only those BCGs that are close to the X-ray center have significant line emission.

A Kolmogorov-Smirnov test on the Hβ distributions of the non-CF BCGs and the controls shows no evidence for a difference in the two populations. Therefore, to summarize, we conclude that an increased frequency of optical line emission in BCGs is observed only for those galaxies that lie within 50 kpc of the X-ray center of a CF

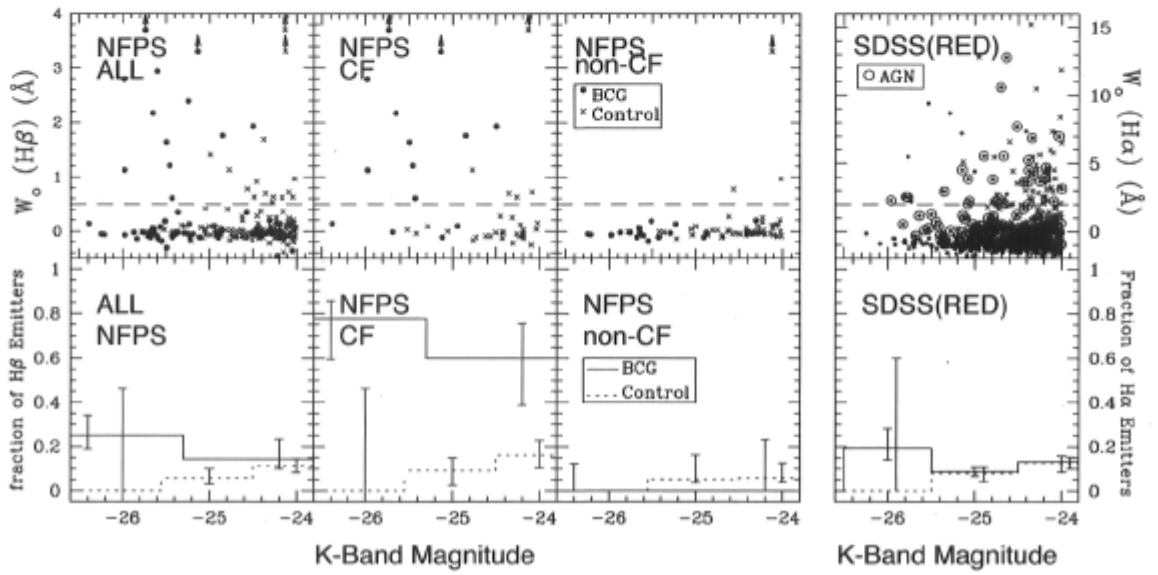

Figure 2.5: **Line emission as a function of K-Band Magnitude.** *Top Panel: The equivalent width of the line emission as a function of K-band magnitude for the NFPS galaxies on the left, and for the SDSS galaxies on the right. The NFPS galaxies are in subsets: a) All galaxies, including those in clusters where the CF status is unknown, b) those which are in known CF clusters, and c) those which are in known non-CF clusters. Filled circles represent BCGs, Xs for control galaxies, and open circles indicate LINER emission (for the SDSS sample only). The dashed line represents the cut between emitting and non-emitting galaxies. The BCGs for Abell 780 and Abell 1795 have unreliable Hβ equivalent widths, but nonetheless strong emission, and are represented by lower limits at $W_o > 3.3Å$ and $> 3.7Å$, respectively. Bottom Panel: Using the same subsamples as the top panel, we plot the fraction of line emitting galaxies as a function of K-band magnitude. The solid line represents the BCGs, and the dotted line the control galaxies.*

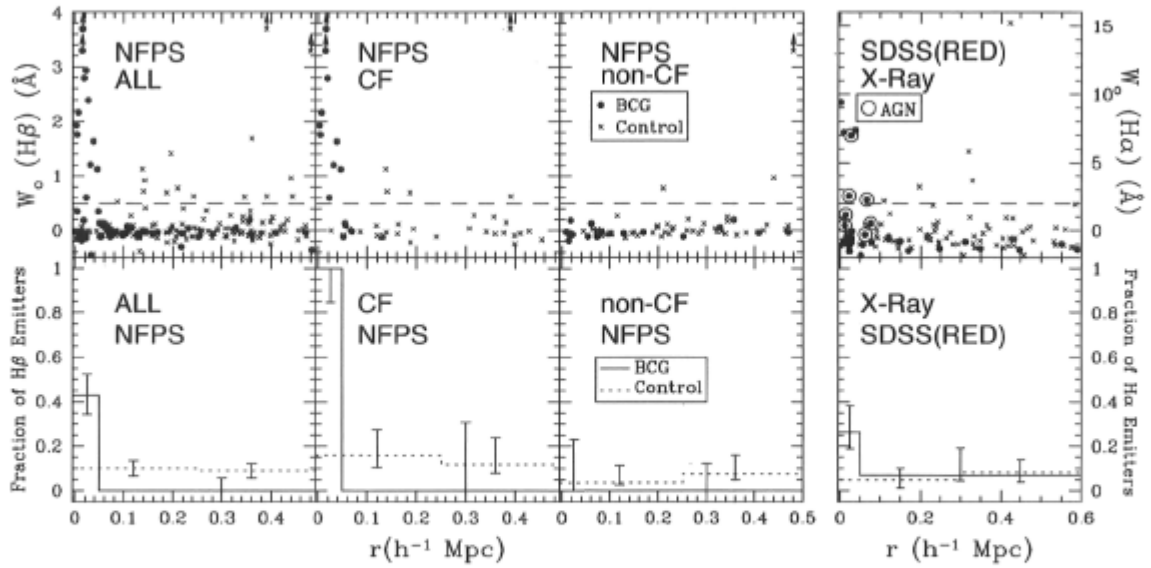

Figure 2.6: **Line emission as a function of distance from the cluster X-ray center.** *Subsample definitions and symbols are the same as in Figure 2.5.*

cluster. For the remainder, the frequency of emission in BCGs is consistent with that observed in the control population.

2.3.4 Dependence on Cluster Mass and Density

The SDSS provides us with an optically-selected sample, spanning a wide range in velocity dispersion, that should be representative of the cluster population independent of X-ray properties. In this section we use this full sample (including those galaxies with $(u'-r') < 2.2$ that were excluded when comparing directly with the NFPS) to explore the effect of environment on the presence of line emission in BCGs.

Since the cooling flow status of a cluster might be correlated with its total mass, or central mass density, we wish to explore whether the trends we have observed are merely reflecting a more fundamental correlation with either of these quantities. First, in Fig. 2.7, we plot the fraction of BCGs with Hα emission as a function of the cluster velocity dispersion. There is no strong trend. Rather, a fraction $\sim$10-15% of BCGs in each bin showing Hα emission is observed (the Spearman correlation coefficient is 0.17). We note that the frequency of radio-loud AGN is also found to be independent of velocity dispersion (Best et al. 2007). The control galaxy population in the SDSS sample also shows no strong correlation between emission line fraction and group velocity dispersion (the Spearman correlation coefficient is 0.38). For the control galaxies, the overall fraction of emitting galaxies is somewhat higher than for BCGs, closer to 15-20%.

Next, we examine in Fig. 2.7 the frequency of emission lines in BCGs as a function of

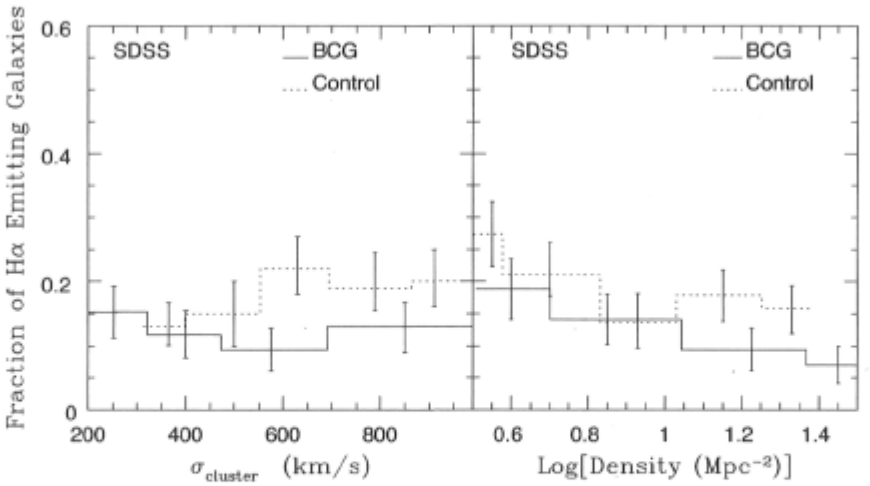

Figure 2.7: **The fraction of Hα emitting galaxies and function of group properties.** *Left Panel: The fraction of Hα emitting galaxies in the SDSS as a function of group velocity dispersion. The solid line refers to BCGs and the dotted line are the control galaxies. This adaptive histogram contains 85 galaxies per bin for the BCGs and 100 galaxies per bin for the controls. Right Panel: The fraction of Hα emitting galaxies in the SDSS as a function of the galaxy density. This adaptive histogram contains 85 galaxies per bin for the BCGs and 95 galaxies per bin for the controls.*

the galaxy density, as measured by the distance to the fifth-nearest spectroscopic neighbour. Even in the densest regions this corresponds to a smoothing scale of ~200 kpc, so the measurement here is of the total mass density on scales larger than the cooling radius. Generally, one would expect the central regions of CF clusters to be the densest environments, and if the presence of a cooling-flow was correlated with the mass or galaxy density on larger scales our previous results would lead us to expect the most star formation occurring in the most dense regions. On the contrary, we observe a clear correlation with the emission line fraction decreasing with increasing number density, and so BCGs are *less* likely to show emission lines if they are found in the densest regions of clusters (in both cases of the BCG and the controls, the Spearman test yields a correlation coefficient of ~0.9, and the correlation is significant at the ~95% confidence level). At all densities, the fraction of emission-line galaxies is higher in the control population than the BCG population. The fact that we observe enhanced emission for those galaxies within the smaller 50 kpc scale of the X-ray center of CF clusters (Section 2.3.3) is therefore very likely related directly to the presence of cooling, X-ray gas on small scales, rather than the overall gravitational potential.

2.4 Discussion

The overall fraction of BCGs with emission lines is ~13% in the SDSS, and ~20% in the NFPS. The latter is in good agreement with Crawford et al. (1999) who find a fraction of 27% emission-line BCGs in their sample of X-ray selected clusters. We do not know what the CF fraction is in an optically-selected sample, or as a function of mass. Nonetheless, since the fraction of massive clusters that host a cooling flow is likely no more than about 50% (Peres et al. 1998; McCarthy et al. 2004; Chen et al. 2007), and CF clusters are systematically overluminous, we attribute the factor of two difference in emission fraction between our two surveys to the fact that NFPS (and Crawford et al. 1999) is X-ray selected, and therefore biased toward CF clusters.

There is currently much observational and theoretical work exploring the possible feedback between a central galaxy's AGN, current star formation, and the cooling X-ray gas (e.g. Silk & Rees 1998; Best et al. 2007; Croton & et al. 2006; Bower et al. 2006; Sijacki & Springel 2006; De Lucia & Blaizot 2007). AGN in the BCGs are thought to play an important role in suppressing cooling, and lowering mass deposition rates (and hence star formation rates). Our main result is that the majority of line emitting BCGs are positioned close to the X-ray center of clusters classified as hosting a cooling flow directly from the mass deposition rates (as defined in Section 2.2.1). Furthermore, this result holds when we classify cooling flow clusters instead by their excess X-ray luminosity relative to other clusters with similar dynamical mass (a definition we explored at the end of Section 2.3.1). Similar conclusions, based on smaller samples, have been reached by others (e.g. Johnstone et al. 1987; McNamara & O'Connell 1989; Crawford et al. 1999; Rafferty et al. 2006). Importantly, we have shown that, in the absence of a cooling flow, emission lines are rare in BCGs, regardless of the mass density or velocity dispersion of the cluster. Moreover, a control population of similarly bright, centrally located cluster galaxies does not exhibit an increased frequency of emission lines in CF clusters. We therefore conclude that the observed emission (arising from star formation and/or an AGN) is directly related to the presence of cooling gas.

For the most part, we have not concerned ourselves with the origin of the observed emission, since starburst galaxies and optically-selected AGNs are probably closely linked (Kauffmann et al. 2003). However, it is worth investigating this further here. Crawford et al. (1999) find that the very strongest Hα emitters have star formation-like emission line ratios, while von der Linden et al. (2007) find that most BCGs, which display weaker Hα emission, are more characteristic of LINER activity. The six NFPS BCGs that have [NII]/Hα line ratios available from Crawford et al. (1999) lie in the regime straddling LINERs and Seyferts. Of the six emitting BCGs in the SDSS-X-Ray sample, the three stronger Hα emitters are non-AGN, which means that they are likely composite, whereas the somewhat weaker emitters are classified as AGN. Thus the emission-line BCGs found near the X-ray center of galaxy clusters appear to be a

heterogeneous class of objects.

In the unrestricted SDSS sample, we find only ∼13% of BCGs have line emission, compared to ∼18% for controls. This exhibits the same trend as in the von der Linden et al. (2007) study of SDSS C4 cluster galaxies, where detectable emission line luminosity measurements (with S/N > 3) are found in 30% of BCGs, as opposed to 40% for the other massive, central, galaxies (i.e. controls). Our numbers cannot be compared directly, as their cut includes more weakly emitting systems as emitters than does our more strict criterion of $W_o > 2$ Å. If we relax our definition of an emitting galaxy being one with $W_o > 0$ Å, we find the percentage of line emitters increases to 27% for BCGs, and 38% for controls.

Our Fig. 2.7 reiterates the above point, that in the SDSS sample, the BCGs have a lower fraction of line emitting galaxies than the controls. This is also consistent with what Best et al. (2007) find: that emission line AGN activity is suppressed in the galaxies near the center of the cluster with respect to the other massive cluster galaxies. They point out that emission line AGN and radio-loud AGN are partly independent populations, but that BCGs with emission-line AGN are more likely to host radio-loud AGN than other galaxies. Best et al. also find that radio-loud AGN are preferentially found in BCGs within $0.2\,r_{200}$ of the center of the cluster and that there is a strong dependence on galaxy stellar mass, with ∼40% of the most massive galaxies showing radio loud AGN emission. Therefore it is plausible that our emission-line BCGs in the NFPS (which are found at the center of CF clusters) and in the SDSS (many of which show LINER-like activity), host radio-loud AGN.

We therefore matched our NFPS BCGs to radio sources from the Faint Images of the Radio Sky at Twenty-Centimeters survey (White et al. 1997b; hereafter FIRST) and NRAO VLA Sky Survey (Condon et al. 1998, hereafter NVSS). We find that indeed, all 12 of our Hβ emitting BCGs are radio sources. Furthermore, for the 50 BCGs in the FOV of the surveys, 28 of our BCGs have radio counterparts (∼56±11%). Thus ∼42±11% of non-Hβ emitting BCGs have radio emission. Again, the cooling flow status of the cluster appears important: $\sim 71^{+9}_{-14}$% of CF BCGs are radio sources, and $\sim 80^{+7}_{-16}$% of central CF BCGs are radio sources. For non-CF BCGs only $\sim 32^{+12}_{-9}$% have radio emission. For the controls, 36 of 144 galaxies in the FOV of the surveys are radio sources (∼25±4%).

Recently, Lin & Mohr (2007) have studied the radio-loud properties of a large X-ray selected cluster sample, and find the overall radio-loud fraction to be ∼35% for K-band selected BCGs within r_{200} of the cluster center (compared with ∼20% for bright cluster galaxies, excluding the BCGs). This is in reasonable agreement with our results, although the radio-loud BCG fraction we measure is somewhat higher. Lin & Mohr (2007) also find a strong trend with cluster mass (inferred from the X-ray luminosity), though the strength of the trend is sensitive to the radio power limit and K-band luminosity of the galaxy. Our NFPS sample is too small to robustly identify such

trends, but we note that the fraction of BCGs with radio sources that are in clusters with a velocity dispersion $< 600\,\mathrm{km\,s^{-1}}$ is 54±15%, quite similar to that for BCGs in clusters with a velocity dispersion $> 600\,\mathrm{km\,s^{-1}}$, 58±15%. In the optically-selected SDSS, we find no significant trend with velocity dispersion, but an overall fraction of ∼40% of the BCGs with radio emission, and ∼25% of the controls. Because of the difference in sample selection, and the cluster mass estimators, we do not consider this a serious discrepancy with the results of Lin & Mohr (2007).

2.5 Conclusions

We have used two large, homogeneous galaxy cluster surveys to investigate the incidence of optical emission lines amongst BCGs. The NFPS consists of 60 BCGs in X-ray selected clusters, while the SDSS sample is a larger, optically-selected sample of 328 BCGs. From these data, we are able to draw the following conclusions:

- Of the 10 BCGs that lie within 50 kpc of the peak of X-ray emission in a cluster with evidence for a significant cooling flow, all show optical emission lines. Moreover, of the 12 BCGs that show emission, all are located within 50 kpc of the X-ray emission peak, all are radio sources, and none are in clusters of known non-CF status (10 are in CF clusters, and 2 are in clusters with unknown CF status).

- Excluding the special circumstances noted above, the fraction of BCGs that exhibit optical emission lines is ∼10-20%, and is always comparable to or lower than the fraction for control galaxies with a similar luminosity and environment.

- For optically selected cluster samples, which are dominated by non-CF clusters, the fraction of BCGs with emission does not correlate strongly with cluster mass or galaxy density.

We have therefore demonstrated a direct connection between the presence of cooling gas, and enhanced optical emission in a centrally located galaxy. It would be very useful to obtain pointed X-ray observations of those SDSS clusters in which we have found a BCG with Hα emission, to determine if this correlation holds in optically-selected samples. These clusters would also be potentially interesting for observation with *Chandra* to observe the X-ray emission morphology, as other massive clusters with Hα emitting BCGs, such as Abell 426 and Abell 1795 show remarkable X-ray morphology, such as X-ray holes, and cooling tails.

Table 2.2: Properties of NOAO Fundamental Plane Survey Brightest Cluster Galaxies

Name (Clus)	RA_x (deg)	DEC_x (deg)	z	σ_{cl} ($km\,s^{-1}$)	r_{200} (Mpc)	MDR ($M_\odot\,yr^{-1}$)	CF	ref	L_X	Name (BCG)	M_K (BCG)	dr (Mpc)	$W_oH\beta$ (Å)	$H\beta_{err}$ (Å)
A0085	10.5	−9.3	0.0557	736	1.3	108	✓	p/s	4.920	MCG–02-02-086	−26.0	0.046	1.13	0.21
A0119	14.1	−1.2	0.0436	653	1.1	0	X	p	1.580	UGC-00579	−25.7	0.054	−0.11	0.06
A0133	15.7	−21.9	0.0561	794	1.4	25	X	b/m	1.590	ESO-541–G-013	−25.6	0.017	−0.08	0.09
A0262	28.2	36.2	0.0155	432	0.7	2	✓	b/s	0.230	NGC-0708	−24.8	0.005	1.76	0.06
A0376	41.5	36.9	0.0482	975	1.7	42	X	w	0.680	GIN-138	−24.4	0.408	−0.04	0.06
A0407	45.5	35.8	0.0465	670	1.2	N/A	?	?	0.210	UGC-02489-NED02	−25.6	0.022	−0.14	0.10
A3128	52.6	−52.5	0.0595	838	1.5	N/A	?	?	1.160	2MASX-J03295060-5234471	−25.5	0.217	−0.30	0.13
RXJ0341	55.3	15.4	0.0288	502	0.9	N/A	?	?	0.250	2MASX-J03412829+1515326	−24.5	0.231	0.04	0.11
A3158	55.7	−53.6	0.0586	814	1.4	292	✓	w	2.820	ESO-156–G-008-NED01	−25.7	0.069	−0.01	0.09
A3266	67.9	−61.4	0.0588	946	1.6	145	X	w/m	3.900	ESO-118-IG-030-NED02	−26.2	0.128	−0.05	0.15
A0496	68.4	−13.2	0.0321	577	1.0	70	✓	o/m	1.770	MCG–02-12-039	−25.5	0.031	1.21	0.18
A3341	81.4	−31.6	0.0376	500	0.9	N/A	?	?	0.310	MCG–05-13-019	−24.9	0.009	−0.01	0.07
A0548A	87.2	−25.4	0.0386	794	1.4	10	X	w	0.370	ESO-488-IG-031	−24.3	0.356	0.20	0.13
A3376	90.4	−40.0	0.0464	710	1.2	0	X	w	1.320	ESO-307–G-013	−25.3	0.470	−0.03	0.06
A3389	95.5	−65.0	0.0270	626	1.1	25	X	w	0.180	NGC-2235	−25.2	0.061	0.13	0.07
A3391	96.6	−53.7	0.0556	696	1.2	131	✓	w	1.370	ESO-161-IG-007-NED02	−26.4	0.055	0.14	0.10
A3395	96.8	−54.5	0.0491	640	1.1	N/A	?	?	1.610	ESO-161–G-008	−25.4	0.158	−0.05	0.12
A0576	110.4	55.8	0.0383	854	1.5	3	X	p/k	0.710	CGCG-261-056-NED01	−25.9	0.008	−0.02	0.05
UGC03957	115.2	55.4	0.0339	511	0.9	N/A	?	?	0.480	UGC-03957	−25.3	0.017	−0.04	0.05
A0602	118.4	29.4	0.0605	675	1.2	N/A	?	?	0.530	2MASX-J07532661+2921341	−24.2	0.032	−0.45	0.12
Z1665	125.8	4.4	0.0296	437	0.8	N/A	?	?	0.160	IC-0505	−24.9	0.072	0.02	0.05
A0754	137.3	−9.7	0.0546	784	1.4	218	X	w/h	4.460	2MASX-J09083238-0937470	−25.7	0.328	0.06	0.10
A0757	138.4	47.7	0.0514	381	0.7	N/A	?	?	0.460	2MASX-J09134460+4742169	−24.5	0.142	−0.01	0.10
A0780	139.5	−12.1	0.0551	641	1.1	492	✓	w/m	3.470	Hydra-A	−25.1	0.015	7.8	0.30
Z2844	150.7	32.7	0.0504	462	0.8	N/A	?	?	0.300	NGC-3099	−25.4	0.048	0.35	0.07
A1367	176.2	19.8	0.0219	747	1.3	0	X	o/m	0.930	NGC-3842	−24.9	0.252	−0.11	0.05
Z4803	181.1	1.9	0.0206	474	0.8	N/A	?	?	0.170	NGC-4073	−25.4	0.000	−0.01	0.05
A1631A	193.2	−15.4	0.0461	531	0.9	N/A	?	?	0.330	2MASX-J12523166-1512150	−24.4	0.358	−0.06	0.07
A3528B	193.6	−29.0	0.0547	500	0.9	N/A	?	?	0.690	ESO-443–G-004	−25.8	0.005	−0.14	0.07
A3528A	193.7	−29.3	0.0535	698	1.2	N/A	?	?	1.100	2MASX-J12543999-2927327	−24.0	0.482	−0.36	0.25
A3530	193.9	−30.4	0.0544	436	0.8	N/A	?	?	0.380	AM-1252-300-NED02	−25.0	0.018	N/A	N/A
A1656	194.9	27.9	0.0230	898	1.6	85	X	w	3.980	NGC-4889	−25.6	0.169	−0.03	0.03
A1668	195.9	19.3	0.0641	476	0.8	N/A	?	?	0.880	IC-4130	−25.2	0.027	2.39	0.09
A3558	202.0	−31.5	0.0476	814	1.4	235	X	w/s	3.450	ESO-444–G-046	−26.2	0.019	−0.06	0.12

Table 2.2: Continued

Name (Clus)	RA_x (deg)	DEC_x (deg)	z	σ_{cl} ($km\,s^{-1}$)	r_{200} (Mpc)	MDR ($M_\odot$/yr)	CF	ref	L_X	Name (BCG)	M_K (BCG)	dr (Mpc)	$W_o H\beta$ (Å)	$H\beta_{err}$ (Å)
A1736A	201.7	−27.1	0.0465	664	1.2	79	X	w	1.250	IC-4252	−25.8	0.512	−0.02	0.04
A3560	203.1	−33.1	0.0487	548	0.9	N/A	?	?	0.730	2MASX-J13322574-3308100	−25.2	0.097	−0.05	0.06
A3571	206.9	−32.9	0.0392	913	1.6	130	X	w/s	3.910	ESO-383–G-076	−26.0	0.022	−0.07	0.14
A1795	207.2	26.6	0.0627	725	1.3	18	✓	b/m	6.330	CGCG-162-010	−25.7	0.016	7.2	0.30
A3581	211.9	−27.0	0.0225	525	0.9	18	✓	w/j	0.320	IC-4374	−24.5	0.003	1.93	0.09
A1983A	223.2	16.7	0.0448	472	0.8	N/A	?	?	0.230	ABELL-1983-1:[CBW93]-C	−24.2	0.050	0.14	0.09
A1991	223.6	18.6	0.0589	454	0.8	37	✓	w/r	0.710	NGC-5778	−25.4	0.023	0.61	0.10
A2052	229.2	7.0	0.0352	531	0.9	81	✓	b/m	1.330	UGC-09799	−25.5	0.038	1.64	0.09
A2063	230.8	8.6	0.0344	764	1.3	99	✓	w/v	1.020	CGCG-077-097	−24.9	0.056	0.10	0.08
A2107	234.9	21.8	0.0415	527	0.9	57	X	w/f	0.570	UGC-09958	−25.5	0.014	−0.18	0.06
A2147	240.6	16.0	0.0370	711	1.2	119	X	w/s	1.660	UGC-10143	−24.9	0.082	−0.02	0.07
A2151A	241.2	17.7	0.0352	746	1.3	173	✓	w	0.430	NGC-6041A	−25.1	0.051	−0.11	0.07
A2199	247.2	39.5	0.0293	647	1.1	2	✓	b/m	1.900	NGC-6166-NED01	−25.7	0.007	2.17	0.11
RXJ1733	263.3	43.8	0.0319	468	0.8	N/A	?	?	0.270	IC-1262	−24.6	0.005	0.35	0.08
RXJ1740	265.1	35.7	0.0434	556	1.0	N/A	?	?	0.270	CGCG-199-007-NED01	−24.9	0.013	−0.12	0.08
Z8338	272.7	49.9	0.0494	532	0.9	N/A	?	?	0.450	NGC-6582-NED02	−25.7	0.098	−0.09	0.04
A3667	303.1	−56.8	0.0549	852	1.5	196	X	w/m	5.020	IC-4965	−25.8	0.700	N/A	N/A
A3716	312.9	−52.7	0.0447	748	1.3	N/A	?	?	0.480	ESO-187–G-020	−25.2	0.098	−0.07	0.08
IIZW108	318.5	2.6	0.0482	399	0.7	N/A	?	?	1.090	IC-1365-NED02	−25.6	0.115	0.04	0.06
A2399	329.3	−7.8	0.0577	608	1.1	N/A	?	?	0.430	2MASX-J21572939-0747443	−24.5	0.218	−0.05	0.06
A3880	337.0	−30.6	0.0583	817	1.4	N/A	?	?	0.960	PKS-2225-308	−25.6	0.022	2.94	0.15
Z8852	347.6	7.6	0.0402	771	1.3	N/A	?	?	0.470	NGC-7503	−25.6	0.108	0.08	0.07
A2572B	349.3	18.7	0.0386	138	0.2	N/A	?	?	0.280	NGC-7602	−24.5	0.105	−0.04	0.05
A2589	351.0	16.8	0.0411	583	1.0	0	X	o/m	0.890	NGC-7647	−25.4	0.073	−0.11	0.07
A2634	354.6	27.0	0.0309	692	1.2	0	X	w	0.480	NGC-7720-NED01	−25.5	0.018	0.19	0.08
A4059	359.2	−34.8	0.0496	556	1.0	7	✓	b	1.680	ESO-349–G-010	−26.0	0.019	2.80	0.12

Note: The cluster name is shown in column 1. Columns 2 and 3 give the position of the cluster X-ray center. The cluster redshift is given in column 4, the cluster velocity dispersion and r_{200} are given in columns 5 and 6. Column 7 gives the cooling flow mass deposition rate (MDR) in ($M_\odot\,yr^{-1}$). Column 8 gives the cooling flow status of the cluster. Column 9 gives the reference for the MDR/CF status: b stands for Bîrzan et al. (2004), f for Fujita et al. (2006), j for Johnstone et al. (2005), h for Henry et al. (2004), k for Kempner & David (2004), m for McCarthy et al. (2004), p for Peres et al. (1998), r for Sharma et al. (2004), s for Sanderson et al. (2006), v for Kanov et al. (2006), w for White (2000), and o for other. Column 10 is the X-ray luminosity in units of $10^{44}\,erg\,s^{-1}$, column 11 gives the name of the BCG, column 12 is the BCG K-band magnitude, column 13 gives the distance between the BCG and the cluster X-ray center. Columns 14 gives the Hβ equivalent width, and column 15 gives the error, which is the noise in the line-free regions of the absorption-corrected spectrum.

Acknowledgments

We are very grateful to C. Miller and R. Nichol for their help with the SDSS database, and the C4 cluster catalogue. We also thank R. Finn for useful discussions about the C4 clusters. LOVE wishes to thank C. Robert for helpful comments and support during her stay at the University of Waterloo. MJH and MLB acknowledge support from their respective NSERC Discovery grants. We also thank the anonymous referee for a careful reading of the manuscript and useful suggestions.

Chapter 3

Further Results in the NOAO Fundamental Plane and Sloan Digital Sky Surveys

There were several tests which I performed that were not published in the paper of the previous chapter. In the first part of this chapter these tests are described. It includes details on how the clusters are classified as either cooling flow (CF) or non-CF, on when and how stellar absorption corrections are performed, and on which equivalent width cut is used for the classification of an "emitting" galaxy. Following this, there is a discussion as to how the optically selected clusters were paired to X-ray clusters and radio sources. Some of the main results are split into AGN and non-AGN sets. The chapter closes with an exploration of the Hβ emission as a function of velocity dispersion in the X-ray selected sample, of the Hα emission as a function of the number of galaxies in the host cluster, and a with presentation of the L_X-T_X relation.

3.1 Cooling Flow Designation in the NFPS

Choosing the appropriate indicator to define the cooling flow status of the cluster is not a trivial task, and there are several methods that can be employed for separating out the CFs from non-CFs. Section 2.2.1 defined a CF cluster to be one with either a direct observation of a central temperature drop in *Chandra* and *XMM-Newton* data or, for clusters only observed with *ROSAT*, a large mass deposition rate (MDR). Here, I offer a more complete argument for the CF definition used in the previous chapter. First, I test the effect of relaxing the minimum allowed mass deposition rate. Second, I explore an independent method for determining cooling flow status which is not used, but alluded to in Section 2.3.1, and which is based on the L_X residual (the difference in observed to modeled cluster X-ray luminosity).

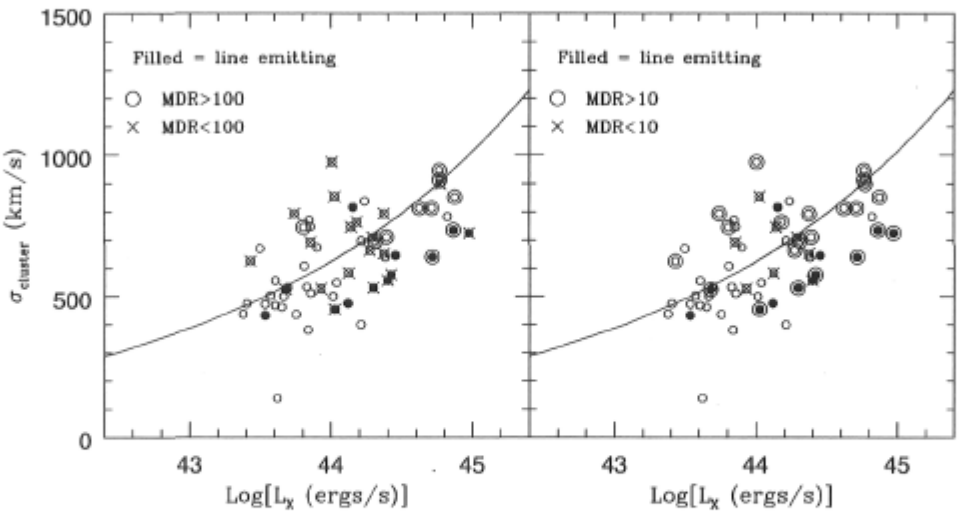

Figure 3.1: **Cluster velocity dispersion as a function X-Ray luminosity for galaxies in the NFPS sample.** *Left Panel: The cluster velocity dispersion as a function of the cluster bolometric X-ray luminosity for ROSAT MDR* $> 100\,M_{\odot}\,yr^{-1}$. *Right Panel: The same for MDR* $> 10\,M_{\odot}\,yr^{-1}$ *on the right. The solid lines are pre-heated models from Babul et al. (2002), which are known to provide a good match to non-CF clusters (McCarthy et al. 2004; Balogh et al. 2006). Known CF clusters in our sample do generally lie to the right of this model.*

3.1.1 Choosing a Minimum Mass Deposition Rate

At the time of writing this thesis, the sample of clusters with *Chandra* and *XMM-Newton* observations is substantially lower than those listed in catalogues giving mass deposition rates based on *ROSAT* data, which covers the entire sky. Therefore, in order to boost the sample of clusters with known cooling flow status, clusters observed only with *ROSAT* must be included.

The mass deposition rate is determined by fitting the observed X-ray spectral data to isobaric cooling flow models. In these models, the mass flow rate fixes the temperature phase, and hence the luminosity. The issue in using MDRs is that the surface brightnesses measured (by *Chandra* and *XMM-Newton*) do not recover rates that correspond to low enough temperatures at the center of the cooling flow. The predicted MDRs are too high. And so, using the MDR as an indicator of cooling flow status is done with the assumption that it is a gross overestimate. Böhringer et al. (2002) suggest that the rates are 1-2 orders of magnitude too high, thus I test cuts of MDR $> 10\,M_{\odot}\,yr^{-1}$ and MDR $> 100\,M_{\odot}\,yr^{-1}$ to be used for discriminating between the CFs, and non-CFs.

In Figures 3.1 and 3.2 I show the main results of Chapter 2, but use instead a definition of a cooling flow cluster based solely a cut in mass deposition rate. Figure 3.1

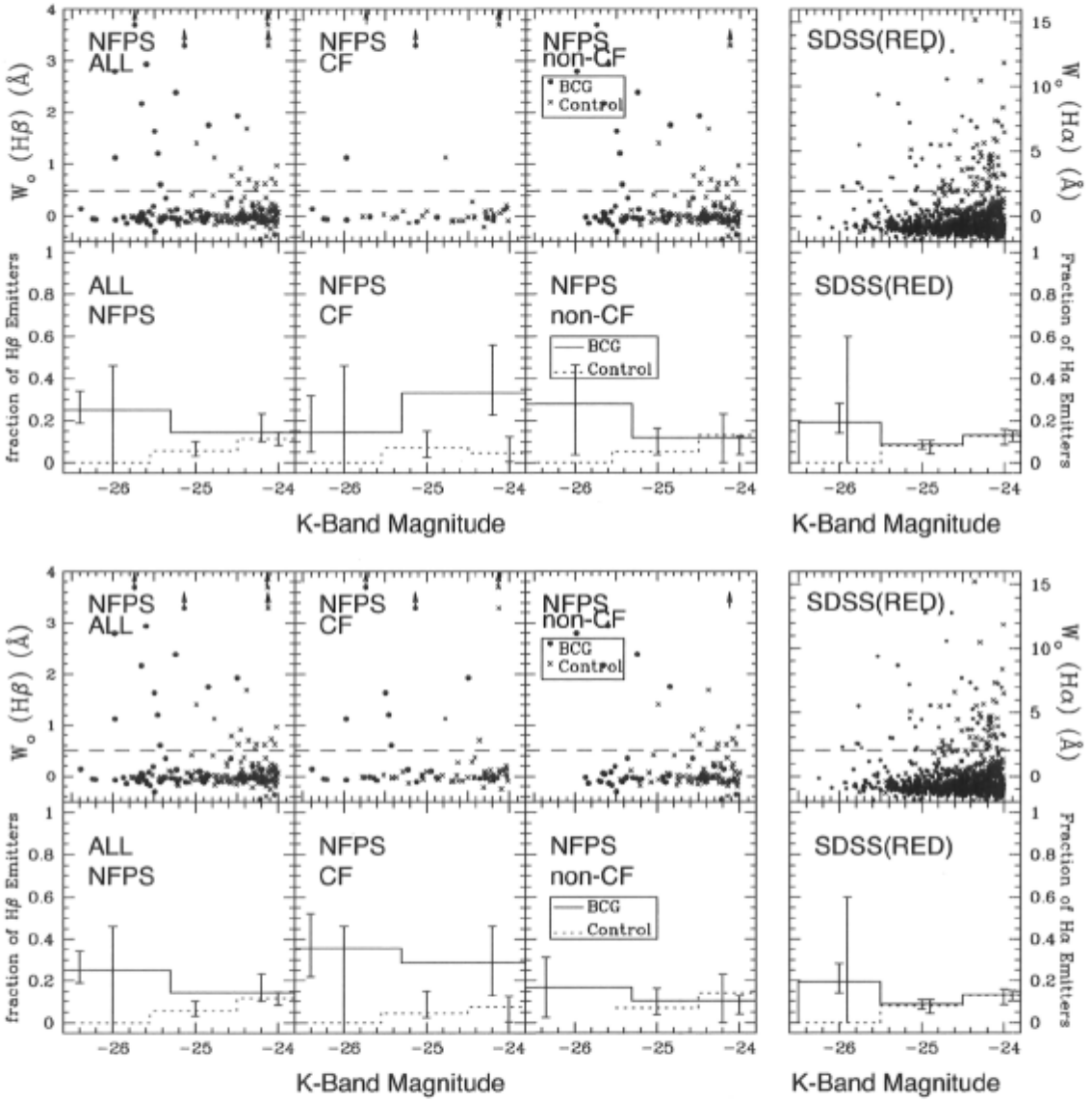

Figure 3.2: **The emission line strength as a function of K-band magnitude for different MDRs.** *Top Panels: The results for MDR* $> 100\,M_\odot\,yr^{-1}$. *Bottom Panels: The same for MDR* $> 10\,M_\odot\,yr^{-1}$. *The error bars on the histograms are as described in Chapter 2.*

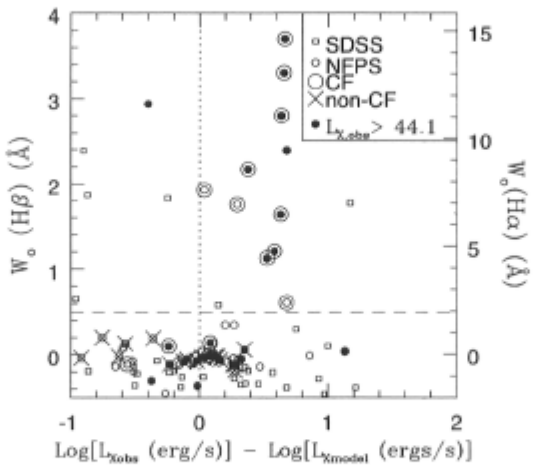

Figure 3.3: **The Hβ emission as a function of L_X residuals.** *The residual is the observed L_X − the model L_X from figure 2.4. Known cooling flow clusters (as defined in the article), are indicated by the large circles; all have positive residuals. Few clusters with positive residuals are classified as non-CF, and at least some of these nevertheless have non-zero mass deposition rates measured with ROSAT. The fraction of BCGs with optical emission lines is much larger for those clusters with larger residuals.*

is equivalent to Figure 2.4, and shows the cluster velocity dispersion as a function of X-ray luminosity. The left panel considers a CF cluster to have a MDR $> 100\,M_\odot\,yr^{-1}$, and the right panel allows for a MDR $> 10\,M_\odot\,yr^{-1}$. Figure 3.2 is equivalent to Figure 2.5, showing the emission line strength and the fraction of line emitting BCGs as a function of K-band magnitude. Cooling flow clusters, as defined by a MDR $> 100\,M_\odot\,yr^{-1}$ are displayed in the top panel, and those defined by MDR $> 10\,M_\odot\,yr^{-1}$ are in the bottom panel. No matter the MDR cut used, and the number of CF or non-CF clusters in each bin, the overall results remain unchanged - it is the CF clusters with a higher fraction of line emitting galaxies. There is no doubt that I am including some non-CF clusters in the CF set, but this bias is minimized by the strict cut in the MDR, and so the cut of MDR $> 100\,M_\odot\,yr^{-1}$ was preferred in Chapter 2.

3.1.2 The L_X Residual Method

McCarthy et al. (2004) simulate the hydrodynamic evolution of flowing X-ray emitting gas. These models are readily available and are explored in an attempt to obtain the status of a cluster, without relying on CF model outputs like MDR and cooling time. Clusters which suffered a large amount of entropy injection (pre-heating) develop into non-CF clusters, and those which only experience a mild amount of entropy injection

were found to become CF clusters. CF clusters can then be distinguished from non-CF clusters by finding the difference in the observed L_X to that from the preheated models (the residual). Figure 3.3 shows the emission line strength plotted against the L_X residuals for this sample. A positive residual in the difference between the observed and pre-heating models would imply a CF, and the figure shows that this is in fact where most of the high MDR clusters fall. Although in Chapter 2 the results of these models were not used, there are a couple of advantages, which are detailed below.

First of all, when the MDRs are used to discriminate between the CFs and non-CFs, they are generally derived from fits to the cooling models from White (2000) or Peres et al. (1998). Despite the extensive number of sources listed in these catalogues, they do not encompass all of our NFPS data, so several clusters are left with an "unknown" status. Using residual cuts therefore assigns a binary CF definition applicable to all clusters. Figure 3.4, equivalent to Figure 2.5, shows the emission line strength, and the fraction of line emitting BCGs as a function of K-band magnitude. Results using a cooling flow cluster definition based on a residual cut ($\mathrm{Log}[L_{X\,obs}]-\mathrm{Log}[L_{X\,model}]$) of 0 are showed in top panel, and those using a residual cut of 0.5 are shown in the bottom panel. Even when using this alternate method for defining the CF status of a cluster, the main conclusions from Chapter 2 persist: the BCGs in the cooling flow clusters are more frequently emitters.

The second potential advantage of the L_X residuals method is that the CF status can now be determined in the optically selected SDSS clusters, which do not have MDRs. Thus, the SDSS clusters with X-ray data have been included in the previous figures. With this method, one would now be able to show our SDSS results in the same fashion as in Figures 2.5 and 2.6 for the NFPS, i.e. split into CF and non-CF. Figure 3.5 shows the emission line strength as a function of K-band magnitude for the BCGs in the SDSS. There is a hint that the same trends are observed in this subset, that is, fewer emitting galaxies are in the non-CF case than in the CF case. Unfortunately there are only ~35 SDSS clusters for which I can find X-ray data. It is dangerous to make any strong conclusions from this very small dataset, and more X-ray observations are required before statements can be made about the feasibility of using this method with optically selected clusters.

3.1.3 The Final Verdict on Cooling Flow Status Indicators

Despite the potential advantages of using the L_X residual method for determining the CF status of the clusters, the binary segregation is less satisfying for the CF clusters. In the real universe, there are several processes occurring which could influence the CF status of the cluster, thus it is unlikely that there is a definite split between CF and non-CF clusters. A prime example is the merging of clusters, which have been shown to both encourage (Poole et al. 2006) and hinder the CF process in clusters. It is plausible then that several systems could be in an intermediary state. In fact, Abell 3558 has

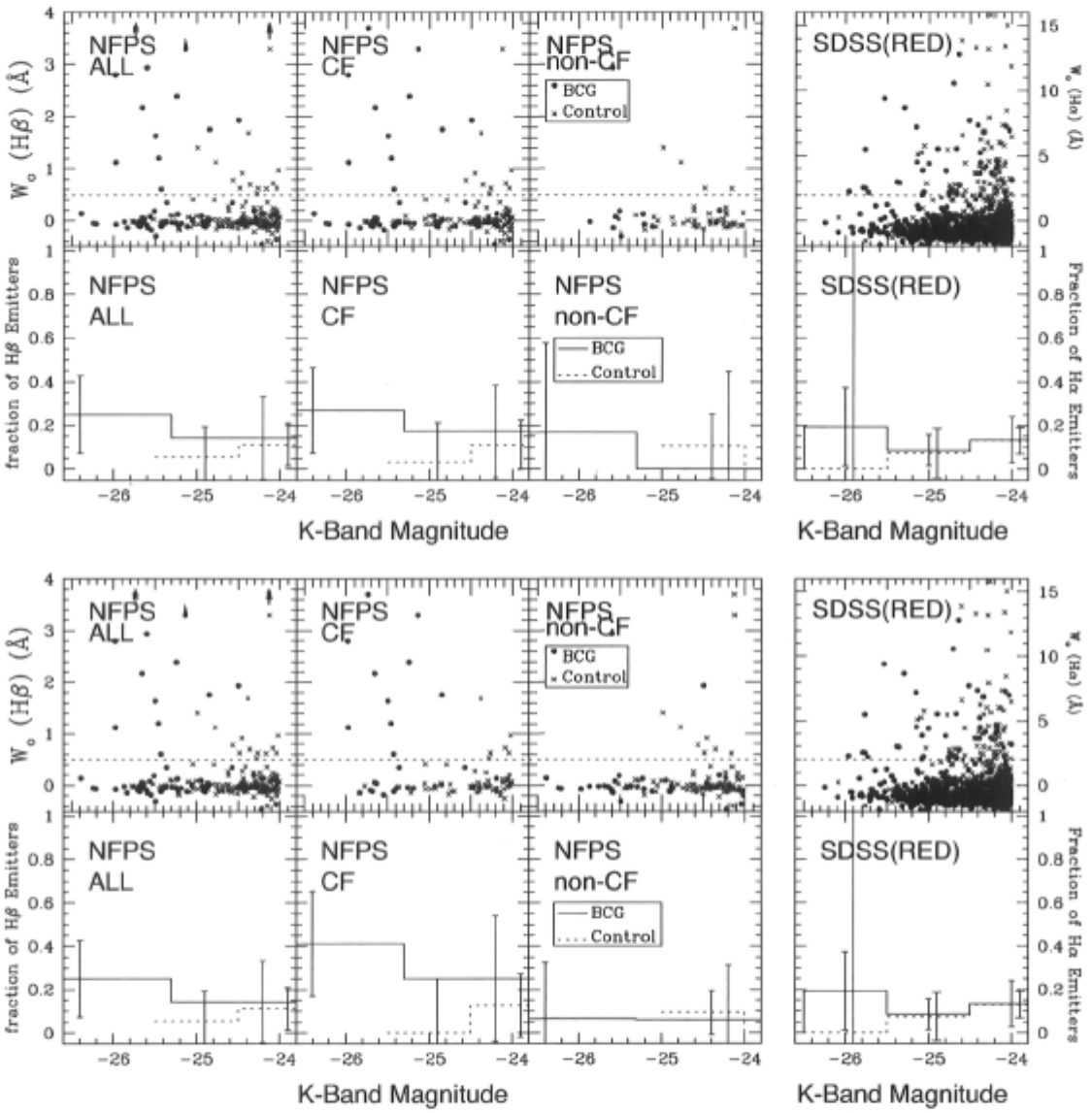

Figure 3.4: **The Hβ equivalent width of the NFPS galaxies as a function of galaxy K-band magnitude for different residuals.** *Top Panels: The results for $Log(L_{Xobs}) - Log(L_{Xmodel}) > 0$. Bottom Panels: The same for $Log(L_{Xobs}) - Log(L_{Xmodel}) > 0.5$.*

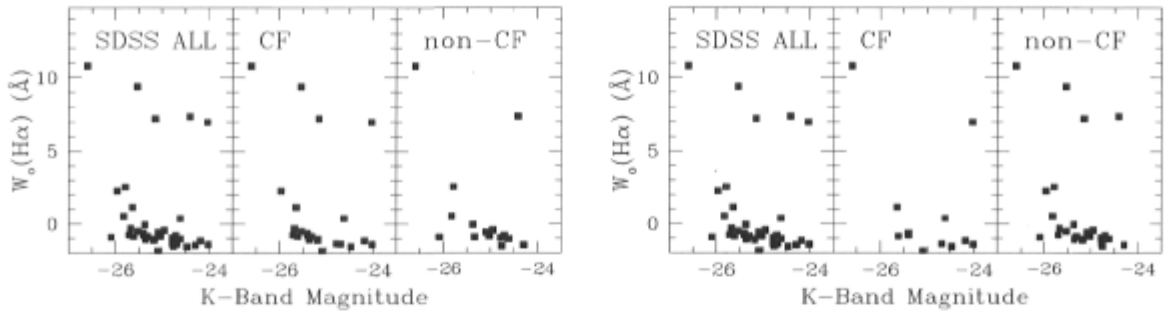

Figure 3.5: **The Hα equivalent width of the SDSS galaxies as a function of galaxy K-band magnitude for different residuals.** *Left Panels: The results with CF defined as Log($L_{X obs}$)−Log($L_{X model}$) > 0. Right Panels: The same for Log($L_{X obs}$)−Log($L_{X model}$) > 0.5.*

recently been shown to possess properties of both a recent merger, and a CF (Rossetti et al. 2007). The previous chapter was particularly concerned with separating out the strong CFs, which the MDR allows for. No further exploration on the use of the L_X residual method for analyzing the properties of the line emitting SDSS BCGs as a function of the CF status was included, as there was not a large enough sample to test this method with this observational dataset.

In the end, a conjunction of the methods described above was used in Chapter 2 in order to exploit the most recent data available, while allowing for some continuity. The definitions from McCarthy et al. (2004) are the most robust, since they are based on direct observational evidence and are not associated with assuming any fits isobaric cooling flow models. Therefore, their definitions were used when available, with the exception of Abell 85, which was kept as a CF because Sanderson et al. (2006) show that it is in fact a CF. McCarthy et al. (2004) refer to Kempner & David (2004), who were looking at an infalling group of Abell 85, not Abell 85 itself. Next, observed temperature drops and central density peaks seen in *Chandra* and *XMM-Newton* data were taken as indicators (the references for CF status are included in the notes to Table 2.2). Finally, if the cluster cannot be found in any new publications, the MDR from older *ROSAT* based catalogues of White (2000) and Peres et al. (1998) were used. Realizing that the MDR might not be the perfect indicator of the cooling flow status of the cluster, I reiterate in saying that they were nonetheless included in the interest of increasing the numbers (from 11 to 33 clusters with known CF status). The MDR method was favoured over that of L_X residual method for the reasons discussed above. Using the MDR as a guide in determining the CF status for the *ROSAT* clusters is acceptable, as the exact definitions of the individual clusters make no significant difference to the overall results, which was proved by testing MDR cuts of 10 and 100 $M_\odot\,yr^{-1}$.

3.2 Stellar Absorption Corrections and Line Emission Cuts

It is not straightforward to account for stellar absorption, as the features are not necessarily dependant on the strength of the emission line.

In the NFPS case, the Hβ stellar absorption line in the individual spectra has been accounted for, as the spectra are of very high quality and separating the different components is possible by removing a best fit emission-free galaxy model (Vazdekis 1999; Nelan et al. 2005) to recover the absorption. However, in Figure 2.2, the Hβ values seem to cluster around -0.1 or -0.2, instead of 0. It is therefore likely that the stellar absorption has been slightly underestimated by about this much, so that there is still some residual stellar absorption; hence the clustering around small negative values. Nonetheless, this does not affect the article's conclusions as emitting galaxies are always very strong emitters, i.e. typical values of emission are $W_o(H\beta) \simeq 1$ to 4 Å. So whether an equivalent width cut of 0.5 or 0.6 Å is used makes little difference to the strongly emitting fraction.

In the case of the SDSS, no correction for the Hα stellar absorption is made, as the S/N of the spectra is not high enough to be able to decompose the absorption and emission features for the individual galaxies. Another important consideration is the different ratio of stellar absorption versus emission in each line. At Hα, even a modest star formation rate (SFR) generates a lot of emission, but the stellar absorption does not vary by a huge amount for moderately old populations (e.g. $\Delta\ W_o(H\alpha) \simeq 1$ Å between 1 and 10 Gyr). At Hβ, the change in absorption between 1 and 10 Gyr is still not much more than 1 Å, but nebular emission from the same SFR is lower by a factor $\sim$4. So the Hα equivalent width measurements (without stellar absorption corrections) are probably sensitive at the 0.3 Å level, whereas the threshold used in Chapter 2 is 2 Å, so variations in the stellar absorption are probably small enough to ignore. Additionally, the average stellar absorption (of $\sim$1 Å) is effectively accounted for by correlating Hα with Hβ and making an empirical cut based on this correlation.

It would have been possible to make an absorption correction for Hα, using the average (and dispersion) of those points with measured Hα absorption, i.e. $W_o(H\alpha) < 0$. From Figure 2.2, this is 1.3 ± 0.25 Å. After making this correction, and measuring the Hα/Hβ correlation only for $W_o(H\alpha) > 5$ Å, a factor of about 4.1 ± 0.2 is found. In fact, at face value this would say that $W_o(H\beta) = 0.5$ Å corresponds to $W_o(H\alpha) = 2$ Å corrected, or 0.75 Å uncorrected. Rather than applying this scaling for $W_o(H\alpha) < 5$ Å, where systematics dominate over statistical errors, the original empirical approach is preferred. Based on the scatter near zero, it seems $W_o(H\beta) = 0.5$ Å is a sensible cut. There are 60/468 galaxies with $W_o(H\beta) > 0.5$ Å, and a cut of $W_o(H\alpha) = 2$ Å (uncorrected) or 3.4 Å (corrected) yields the same fraction. This inspires some confidence that the cut chosen is useful in finding a broad consistency between the surveys, and that any trends

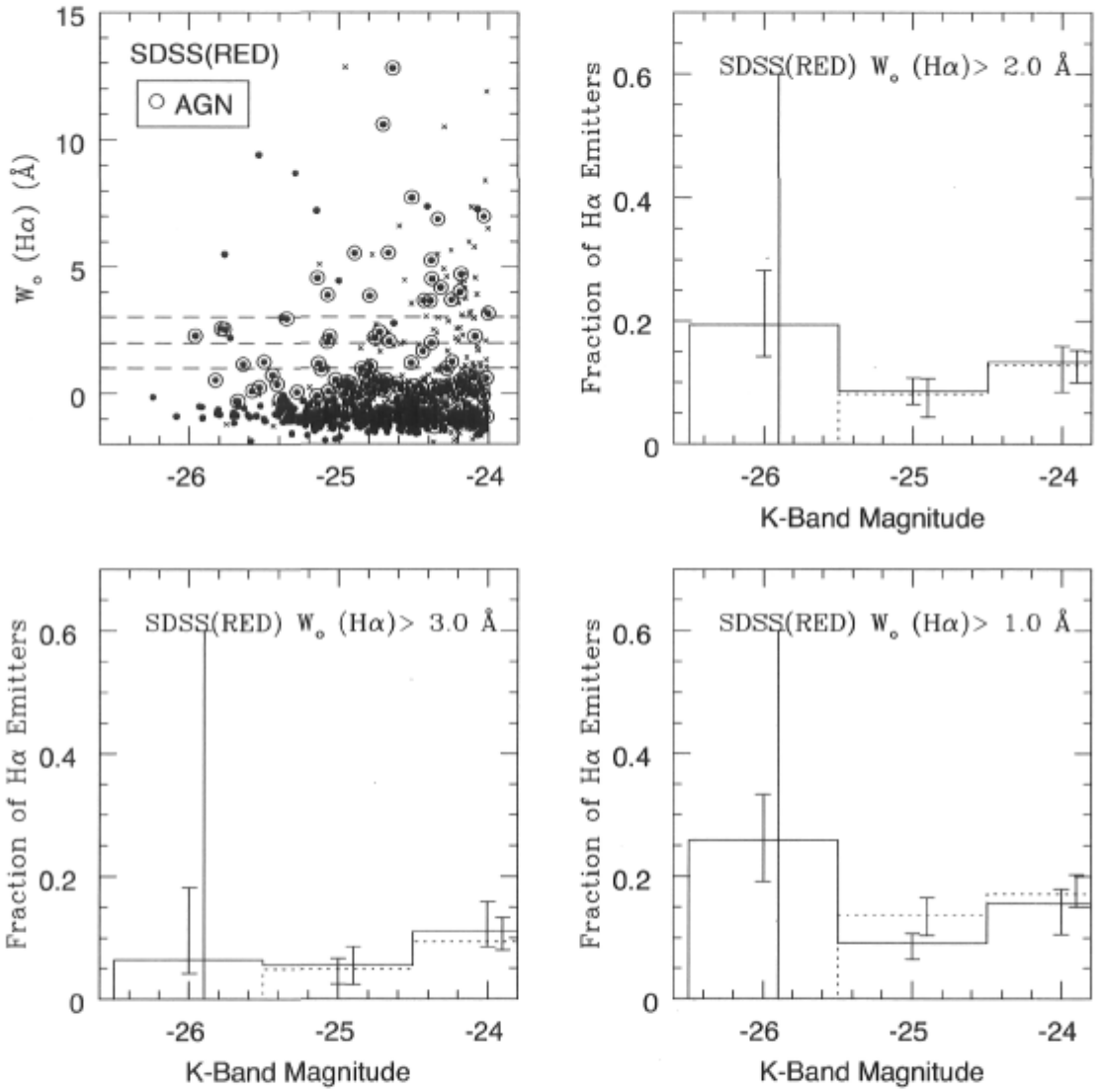

Figure 3.6: **SDSS emitting galaxy cuts.** *Top Left Panel: The Hα equivalent width as a function of galaxy magnitude with cuts of $W_o(H\alpha) = 1$, 2, and 3 Å. Top Right Panel: The fraction of Hα emitting galaxies as a function of K-band magnitude for a cut of $W_o(H\alpha) = 2$ Å. Bottom Left Panel: As before, but $W_o(H\alpha) = 3$ Å. Bottom Right Panel: As before, but $W_o(H\alpha) = 1$ Å. The error bars on the histograms are as described in Chapter 2.*

in emission line fraction should compare well.

Figure 3.6 shows this by displaying how the results do not change significantly if the SDSS cuts are adjusted by ±1 Å. Recall that originally, with a cut of $W_o(H\alpha) > 2.0$ Å, the global fraction of Hα emitters is ∼11%. With a cut of $W_o(H\alpha) > 1.0$ Å the average fraction of Hα emitters is 12.6%, for $W_o(H\alpha) > 3.0$ Å the fraction is 7.2%. Thus, even if a global average of 1 Å of absorption had been taken into account explicitly, i.e. a cut of $W_o(H\alpha) > 1.0$ Å, the global fraction of emitting red BCGs would be ∼13%, not significantly different than the original fraction, but still quite below the fraction of NFPS emitters (20%).

3.3 Finding X-ray Matches to SDSS C4 Clusters

In Chapter 2, corresponding X-ray clusters for the optically selected SDSS cluster sample were found. The details of how the SDSS clusters were matched to the available X-ray source catalogues are discussed here.

With the high resolution of *Chandra*, point sources can be distinguished from extended sources such as those of the intracluster medium (Blanton et al. 2004). Recently, Branchesi et al. (2007) have used the *Chandra* data to deduce that the X-ray temperatures measured for clusters, especially those above $z > 0.7$, are raised by several percent if point sources are not removed. However, in the case of low resolution instruments such as *ROSAT*, a conglomeration of point sources can be confused with the extended emission of cluster gas. Therefore, catalogs based on low spatial resolution data include optical follow-up for cluster identifications (Horner et al. 2001). The X-ray cluster catalogues that I use to match the SDSS clusters have all been created meticulously, with a subtraction of the X-ray background and a removal of likely point sources (Böhringer & et al. 2000, 2001).

The following publicly available catalogues were searched: The Northern *ROSAT* All-Sky Galaxy Cluster Survey (NORAS), the Horner sample of clusters observed with ASCA, the Mulchaey *ROSAT* groups catalogue, the *ROSAT*-ESO Flux Limited X-ray Galaxy Cluster Survay (REFLUX), the X-ray Galaxy Clusters Database (BAX), the X-ray Brightest Abell-type Clusters Sample (XBACS), the *ROSAT* All-Sky Survey Center for Astrophysics Loose Systems (RASSCALS), the Highest X-ray Flux Galaxy Cluster Sample (HIFLUGCS), the Serendipitous High Redshift Cluster (SHARC) sample, the *ROSAT* based Vilkhlinin sample, and finally, the Popesso catalogue, where galaxy clusters in the *ROSAT* All Sky Survey to the Early Data Release (EDR) are matched to clusters in the SDSS and in which the non-public data of NORAS2 are included. The X-ray clusters gathered were subsequently sent through a matching algorithm in order to choose the X-ray cluster center that was closest in RA and DEC to the geometric centers of the C4 clusters of the SDSS-DR3. Table 3.1 shows the final list of the number of matches found in each catalogue.

Table 3.1: X-Ray Catalogues Explored

Catalogue	In DR3	Unique	Reference
NORAS	17	12	Böhringer & et al. (2000)
Horner	13	12	Horner et al. (2001)
Mulchaey	4	2	Mulchaey et al. (2003)
REFLUX	7	4	Böhringer & et al. (2001)
BAX	25	9	Sadat et al. (2004)
XBACS	23	3	Ebeling et al. (1998, 2000)
RASSCALS	15	3	Mahdavi et al. (2000)
HIFLUGCS	10	0	Reiprich & Böhringer (2002)
SHARC	0	0	Romer & et al. (2000)
Vilkhlinin	2	0	Vikhlinin et al. (1998)
Popesso	31	7	Popesso et al. (2004)

Note: The first column is the Catalogue Name, the second is the number of clusters from the X-ray catalogue that are in the SDSS-DR3 strips, within the appropriate redshift range, and who's C4 match has a spectrum for the BCG. The third column gives the number of X-ray catalogue clusters that do not appear in other catalogues. The final column is the X-ray catalogue reference.

Out of a total of 328 C4 clusters, there are 52 with X-ray matches, 35 of which have velocity dispersions $< 1200\,\mathrm{km\,s^{-1}}$.

Although each cluster catalogue starts with several hundred clusters, very few of the C4 clusters will match these sources. At first this small number might seem surprising, but there are several reasons for this which inlcude a) the fact that each C4 cluster is constrained to within the redshift slice of z = 0.01 - 0.1 and a velocity dispersion of only $< 1200\,\mathrm{km\,s^{-1}}$, b) the C4 clusters with a large amount of substructure are not included, c) the SDSS-DR3 covers less than a quarter of the sky, and d) a large fraction of C4 BCGs are unobserved spectroscopically (∼30 - 50%) and therefore, are removed from the sample. Using a more complete release of the SDSS, for example DR6, will greatly increase the number of candidates for future studies. The following two examples illustrate how only 35 X-ray cluster matches are found for the 328 SDSS clusters, while testing the integrity of the matching program.

First, the NORAS catalogue lists 378 clusters. Only 155 are in the redshift range of 0.01 - 0.1. Furthermore, only 33 are within the DR3 imaging strips, with 21 having spectroscopy for the BCG. The algorithm matches 17. There are 4 clusters that the program does not match. The C4 cluster 1349 has a match to a cluster without a name, which is not in the BCG list because there is a substructure flag for the cluster. The C4 cluster 3230 is similarly matched to a cluster without a name. In this case it is because there is no BCG with a $M_K < -24$ magnitudes and within the radial and velocity dispersion cuts. However, the cluster velocity dispersion is small, $\sim 500\,\mathrm{km\,s^{-1}}$. There

is also a cluster without a name that has no match in the C4 cluster list. However, if one looks at the optical image, this cluster is dubious. There is one small galaxy a few arc seconds away from a slightly larger galaxy, suggesting the C4 algorithm may not have counted this as a valid cluster. Finally, NGC 4325 has no C4 match. This is a small group that the C4 algorithm appears not to have picked up either.

A second example is in the Popesso catalogue, in which there are 144 clusters. Forty-eight are in the redshift range of 0.01 - 0.1, with 34 having spectroscopy for the BCG, and 31 that match a single C4 galaxy to a single X-ray cluster. This algorithm picks up and matches all of these clusters.

It is important to keep in mind that there are many factors which lower the detection rate of the C4 clusters in the X-ray catalogues. Most obviously, there are some X-ray cluster catalogues, including NORAS2, which are not public, and thus not included. Also, if there are several clusters of high mass that are very hot, but not very dense, they would not be easily detectable in X-rays. Finally, the velocity dispersion is perhaps not the best way to assume the real mass of the clusters, as not all the clusters must be virialized, and it is also well known that the larger C4 velocity dispersions are somewhat inaccurate (von der Linden et al. 2007). The subset of massive C4 clusters with more reliable velocity dispersions between 800 and 1000 $\mathrm{km\,s^{-1}}$ includes 41 clusters, 35 of which have no corresponding X-ray detections. Even taking into account the above considerations, this is a hugely unexpected number of massive galaxy clusters without X-ray emission. Figure 3.7 shows the images of these 41 C4 clusters. The six with X-ray detections from catalogues of bright X-ray sources are labeled with an x beside their name. Strikingly, many of the clusters with X-ray detections look like rich clusters, with lots of galaxies in the center. Almost all the others, despite having high velocity dispersions, look less rich.

Figure 3.8 gives the number and fraction of C4 clusters with X-ray matches. This figure shows that the detection rate of C4 clusters in X-rays is far from 100%, despite the fact several X-ray catalogues have been searched, including those based on *ROSAT* data. Reflecting on the questions of how many of the SDSS clusters are expected to be massive clusters with corresponding bright X-ray emission, how many are expected to be detected, and how many are detected, the detection rate of $\sim$10% is reasonable.

It is possible to test how easy it is to match the optical clusters to the X-ray source catalogues using the NFPS clusters. Since all the NFPS clusters are X-ray selected from the *ROSAT* observations, they should all be matched to X-ray clusters. What this exercise shows is that there are not very many X-ray bright clusters in the SDSS strips. Of the 60 BCGs in the (all-sky) NFPS sample, there are only 9 that are in the DR3 strips: Abell 0085, Abell 0119, Abell 0602, Z1665, Abell 0757, Z4803, Abell 2052, Abell 2063, Abell 2199. Furthermore, only 5 have spectroscopy for the BCG, all of which are in the Horner or XBACS catalogues, and part of our C4 sample: Abell 0085 (SDSS 2132), Z1665 (SDSS 356/1283), Abell 0757 (SDSS 3165), Z4803 (SDSS 1118),

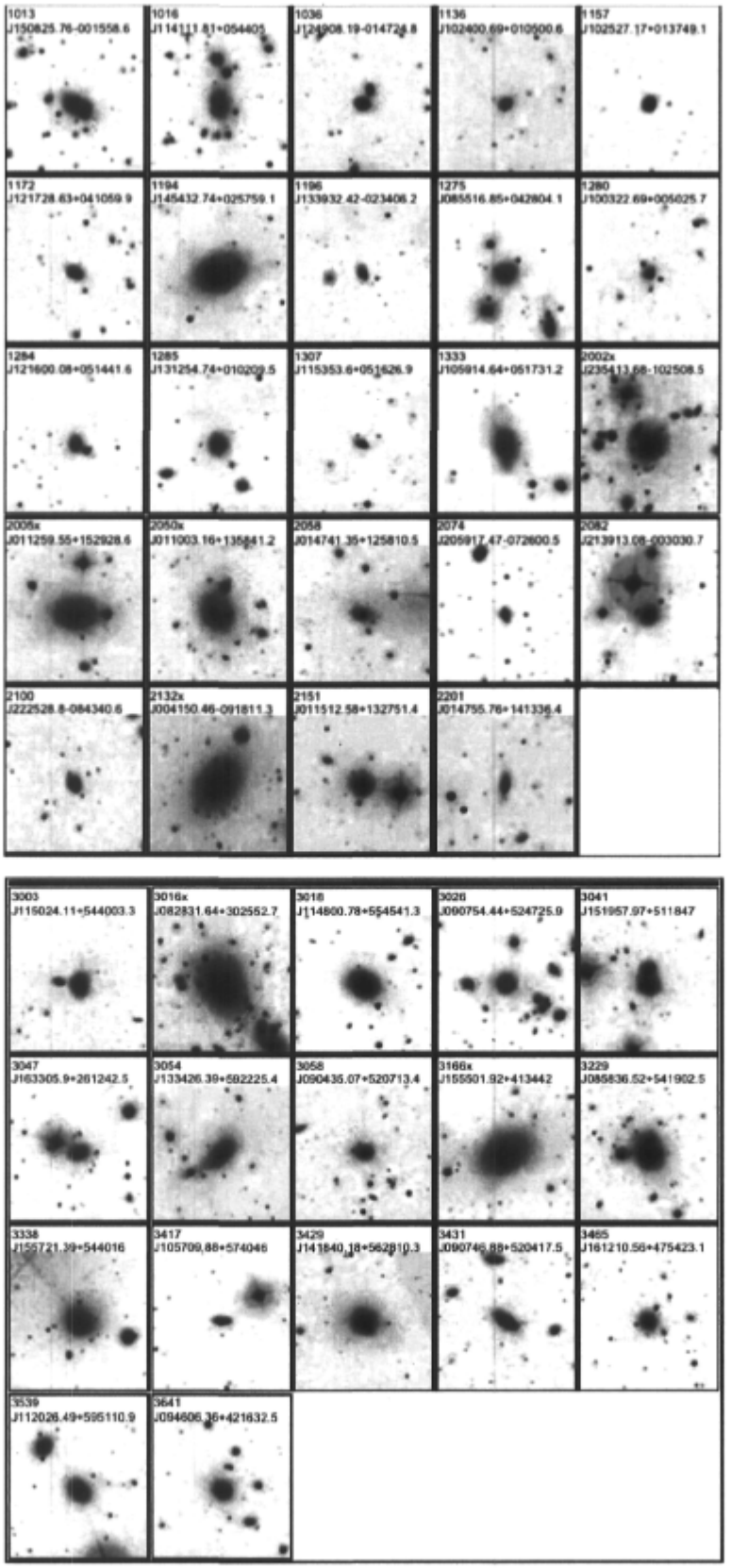

Figure 3.7: **C4 clusters with velocity dispersions between 800 and 1000 km s^{-1}.** *Those with X-ray detections are labeled with an x beside their name.*

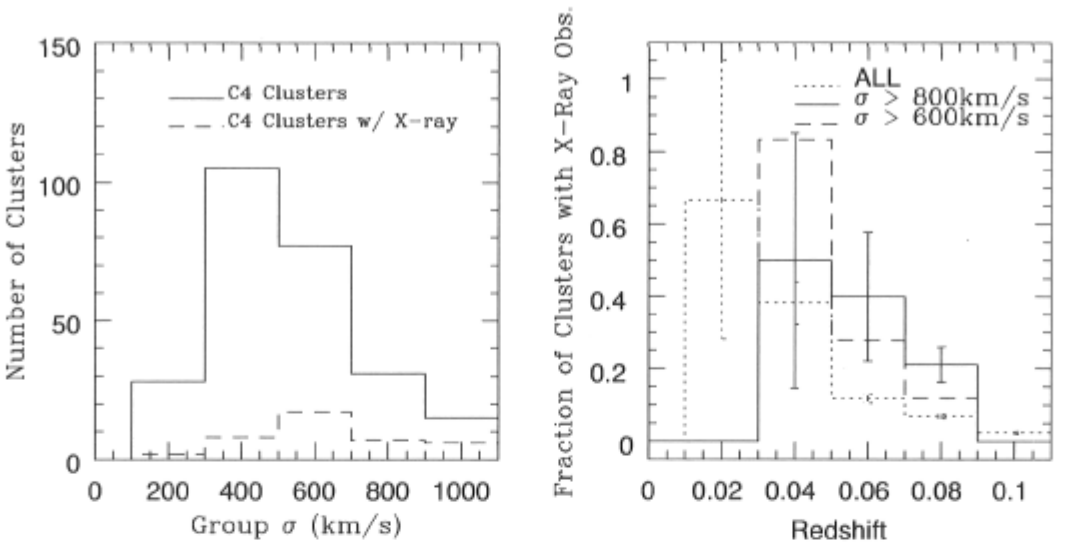

Figure 3.8: **Distribution of C4 galaxies as a function of velocity dispersion and redshift.** *Left Panel: Histogram of the number of C4 galaxies. Clearly there are globally only ∼12% of C4 clusters with X-ray data from the samples of Table 3.1. Right Panel: Histogram of the fraction of SDSS clusters with X-ray matches as a function of redshift. The error bars are as described in Chapter 2.*

Abell 2199 (SDSS 3471).

So, despite the fact that not all massive C4 clusters with high velocity dispersion have X-ray counterparts, in fact, the vast majority of the X-ray bright clusters expected in DR3 are matched to C4 clusters. Thus the small number of matches is most likely due to the fact that the *ROSAT* flux limit is so high, and only clusters with $z < 0.03$ are expected to be detected (for example, REFLUX has a flux limit of $3 \times 10^{12}\,\mathrm{erg\,s^{-1}\,cm^{-2}}$). In fact, Popesso et al. (2004) find a similar result. Only 34% of their clusters are Abell clusters. Miller et al. (2005) allude to this by comparing the C4 cluster catalogue from DR2 with the X-ray sources of Popesso et al. (2004). The recovery rate of the *ROSAT*-SDSS is found to be 98% when a larger matching radius is used for very low redshifts, when edge effects and cluster deblending issues are accounted for and, most importantly, when the volume constraints of the Popesso et al. (2004) catalogue are constrained to those of the optically selected clusters.

3.4 Matching Radio Sources

Radio emission in galaxies at 1.4 GHz is generally associated with the non-thermal synchrotron radiating processes of radio-loud AGN, or star forming galaxies (i.e. syn-

Table 3.2: Brightest Cluster Galaxy Radio Source Hosts

Status	Total	With Radio	%	Central	With Radio	%
CF	14	10	71^{+9}_{-14}	10	8	70^{+7}_{-16}
non-CF	19	6	32^{+12}_{-9}	6	4	67^{+12}_{-21}

Note: The first column shows the CF status of the cluster, the second column the total number of BCGs, and the third column the number of BCGs with radio counterparts. The fourth column gives the percentage of BCGs with radio counterparts. The fifth column lists the number of BCGs within 50 kpc of the X-ray centroid, the sixth column the number of central BCGs with radio detections, and the final column the percentage of central BCGs with radio counterparts.

chrotron from supernova remnants). It is not possible to discriminate between the two processes with only monochromatic radio observations, as the flux density covers a range of ~5 - 100 mJy (Best et al. 2006b) for emission originating from both sources. However, Best et al. (2006b) created a table of radio-loud galaxies within the SDSS, using detections from the Images of the Radio Sky at Twenty-Centimeters survey (FIRST; White et al. 1997b) and NRAO VLA Sky Survey (NVSS; Condon et al. 1998). They then go on to distinguish between radio sources originating from radio-loud AGN, versus those from star forming galaxies by investigating the D4000 break (which describes the mean stellar age of the galaxy) as a function of the radio luminosity per stellar mass of the galaxy. They find that 82% of their 2712 radio sources are in fact signatures of radio-loud AGN, and the radio emission from the rest of the galaxies comes from star formation.

In Section 2.4 the NFPS BCGs are matched to radio sources taken from the FIRST and NVSS radio surveys to show that the Hβ emitting galaxies are all also radio sources, and to show that the cooling flow status of the galaxy was correlated with the presence of a strong radio source. Table 3.2 shows the number of BCGs that have radio sources, and their properties. Clearly, the CFs form a subset of clusters with a much higher fraction of radio sources (~70%) than do the non-CFs (~30%). All but 2 of the CF cluster BCGs with radio emission are Hβ emitters, and these two have positions displaced by more than 50 kpc from the X-ray peak (i.e. are non-central). Conversely, none of the 4 non-CF clusters with radio emission is an Hβ emitter.

This experiment was somewhat more crude, as I did not distinguish between radio sources dominated by emission from an AGN, and that from star forming galaxies, although both cases are interesting (see Section 3.5). Therefore, some of the radio-loud sources that I match could be radio-quiet AGN, whose radio emission comes from recent star formating activity within the galaxy. Nevertheless, considering the work of Best et al. (2006b) (and the fact that most of our galaxies are ellipticals), a detection of radio emission is likely signaling the existence of a radio-loud AGN in most cases.

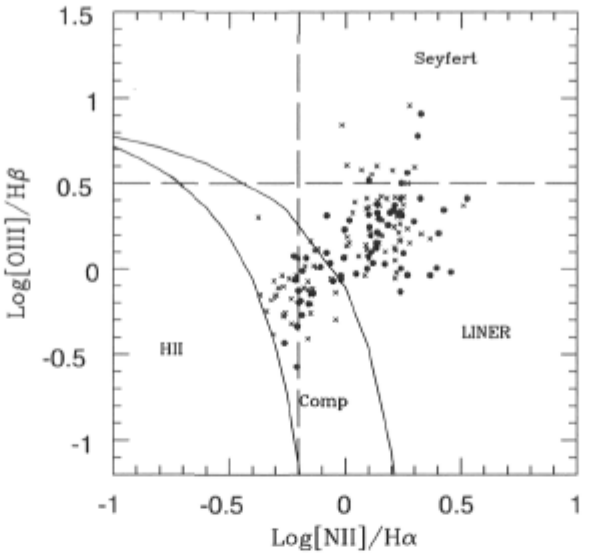

Figure 3.9: **The BPT diagram for SDSS galaxies.** *This figure using the definitions of H II region, Composite and AGN ionizing sources from Kauffmann et al. (2003).*

3.5 AGN versus Star Formation

A detection of Hα emission in the BCGs is a signature of interesting activity. However, several line ratios are required in order to discriminate the ionizing source of the Hα emission. Although the two prime candidates for this may actually be linked together by feedback processes, it is nevertheless true that the line emission can be characterized as originating either from an AGN or a population of young stars. For the SDSS cluster galaxies, it is straightforward to create a BPT diagram that may discriminate between the two ionizing sources. One simply plots the flux ratio of [N II]/Hα versus the flux ratio of [O III]/Hβ, all four components of which have measured line strengths. In Figure 3.9 the emitting SDSS BCGs are plotted as filled circles and the emitting SDSS controls as X's on the same plot as the AGN and starburst definitions from Kauffmann et al. (2003). Here, the vast majority of emitting sources are LINERs, or composite types (LINER + contamination by star formation), with very few Seyferts, and no cases that are clearly dominated by starbursts.

Because the composite types may involve some feedback between the AGN and current or recent star formation (as discussed in Section 1.3; Kauffmann et al. 2003), the results in Chapter 2 were not separated into categories which include and reject the AGN. In Figure 3.10, the fraction of galaxies with a significant amount of Hα emission as a function of cluster velocity dispersion is $\sim$10 - 20% in the case of both the sample including the LINERs and that for just the galaxies with composite emission. Additionally, the controls show a higher fraction than the BCGs in both cases. Thus,

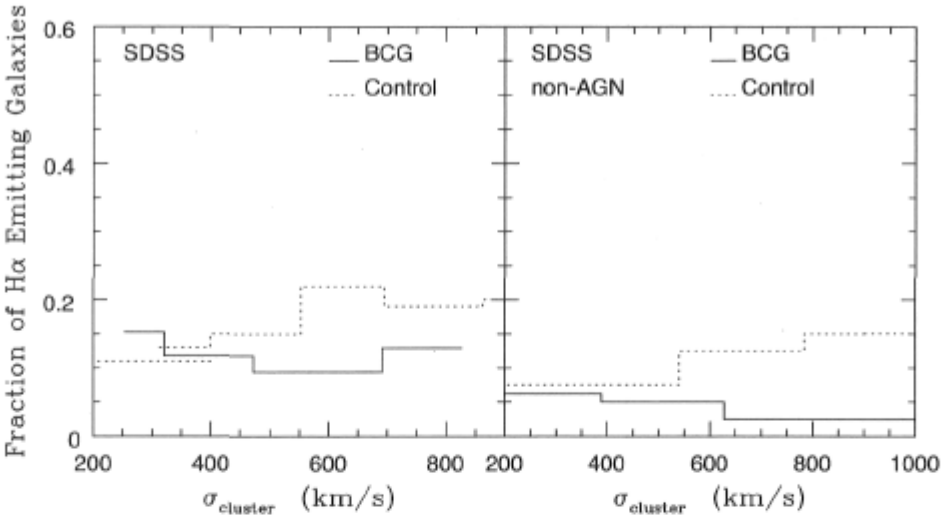

Figure 3.10: **The fraction of line emitting galaxies as a function of velocity dispersion taking into account AGN-like line ratios.** *Left Panel: The fraction of line emitting galaxies as a function of velocity dispersion in the SDSS, including AGN. Right Panel: The fraction of line emitting galaxies as a function of velocity dispersion in the SDSS, excluding the AGN. Note that these are adaptive histograms, and therefore no error bars are included.*

it is clear that the overall results do not vary significantly whether line emission caused by AGN ionization is included or excluded.

For the NFPS data, it is not possible to create a BPT diagram and distinguish between gas ionized by HII regions or AGN since observations in the Hα-[N II] region of the spectrum have not been made.

3.6 More Properties of Cluster BCGs Explored

In this section some results which are related to, but were omitted from Chapter 2 are discussed. First, there is a discussion of the line emitting fraction of NFPS galaxies as a function of velocity dispersion, and why it is excluded from Chapter 2. Then, the role of galaxy group density in the SDSS sample is explored. Finally, it is shown how the clusters follow the L_X-T_X and σ-L_X relations.

3.6.1 Optical Properties of the NFPS Galaxies

In Chapter 2, one of the main results presented for the SDSS sample is the fraction of line emitting galaxies as a function of velocity dispersion, which is used as a proxy for

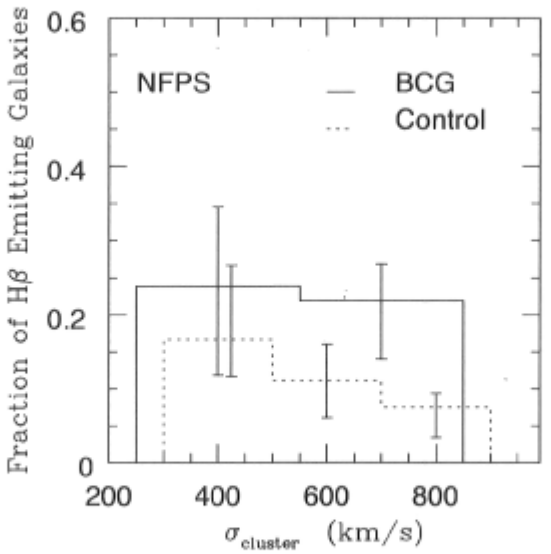

Figure 3.11: **The fraction of line emitting galaxies as a function of velocity dispersion in the NFPS.**

the cluster mass. Although this property can be effectively extracted from Figure 2.4, which highlighted the line emitting BCGs in a plot of the cluster velocity dispersion as a function of bolometric luminosity, in this section I present explicitly this data for the NFPS X-ray selected sample. In fact, the steadiness in the fraction of line emitting galaxies as a function of velocity dispersion which was seen for the SDSS (Figure 2.7, left panel) is not so clear the case of the NFPS galaxies. Figure 3.11 shows this. A decline in the fraction of line emitting control galaxies (recall the Hβ line is used in the NFPS sample) with cluster velocity dispersion is instead observed, although the error bars are large. However, the main difference, which is difficult to explain, is that the fraction of emitting BCGs is slightly more than for the SDSS. As well, the fraction of controls in the case of the NFPS, is noticeably less than that for the BCGs, the opposite of what the SDSS results show. The big difference between the two datasets is that the NFPS is X-ray selected, thus, there is naturally a huge number of CF clusters in the sample. Therefore, the special nature of the BCG, which was linked in Chapter 2 to the presence of a CF in the host cluster, increases the fraction of line emitting BCGs to controls.

Although the SDSS clearly includes galaxies in groups as well as more massive NFPS-like clusters, it would have been expected that, at least at the high mass end of the SDSS, one would recover the same results as for the NFPS. This mirrors what was found in Section 3.3, where it was shown that most of the SDSS clusters are not nearby massive X-ray clusters. In general, the X-ray mass is a much more reliable measurement

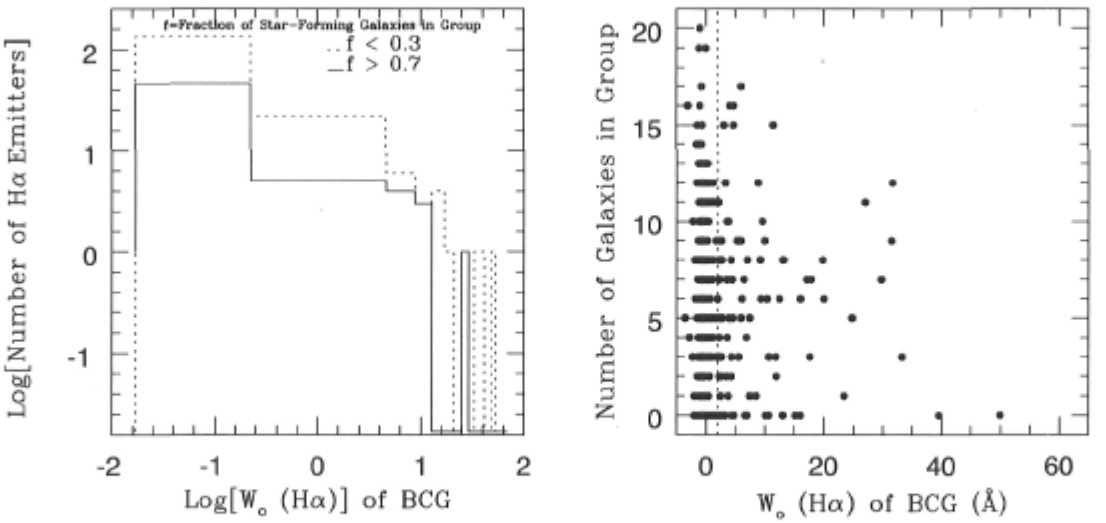

Figure 3.12: **SDSS Hα emission and group properties.** *Left Panel: The log of the number of Hα emitting galaxies as a function of the log of the Hα equivalent width is plotted for groups with small and large fractions of emitting galaxies. Right Panel: The number of bright galaxies in each group or cluster as a function of the Hα equivalent width.*

of the overall cluster mass, than is the velocity dispersion, as the former does not depend on the virialized nature of the individual galaxies. For the same reasons, the velocity dispersion may not be the most perfect mass proxy for the SDSS clusters. However, as there are not X-ray measurements for the vast majority of SDSS clusters, the velocity dispersion is an acceptable compromise. As there are many more galaxies in the SDSS sample than in the NFPS sample in Figure 2.7, a respectable number of galaxies in each velocity dispersion bin is possible for the SDSS case.

3.6.2 Emitting Fraction as a Function of the Cluster Population

Does the line emission seen in BCGs show a dependence on the mass of the BCG or on that of the host group or cluster size? Figure 3.12 addresses this question by examining different properties as a function of the number of large galaxies in the central regions of the group or cluster. The left panel shows the number of Hα emitting galaxies as a function of Hα emission strength for 2 classes; where the fraction, of line emitting galaxies in the group is low, $f < 0.3$, and where it is high, $f > 0.7$. Most of the BCGs have moderate Hα equivalent widths, regardless of the fraction of line emitting galaxies in their host group, but there are more emitting BCGs in the groups with a smaller

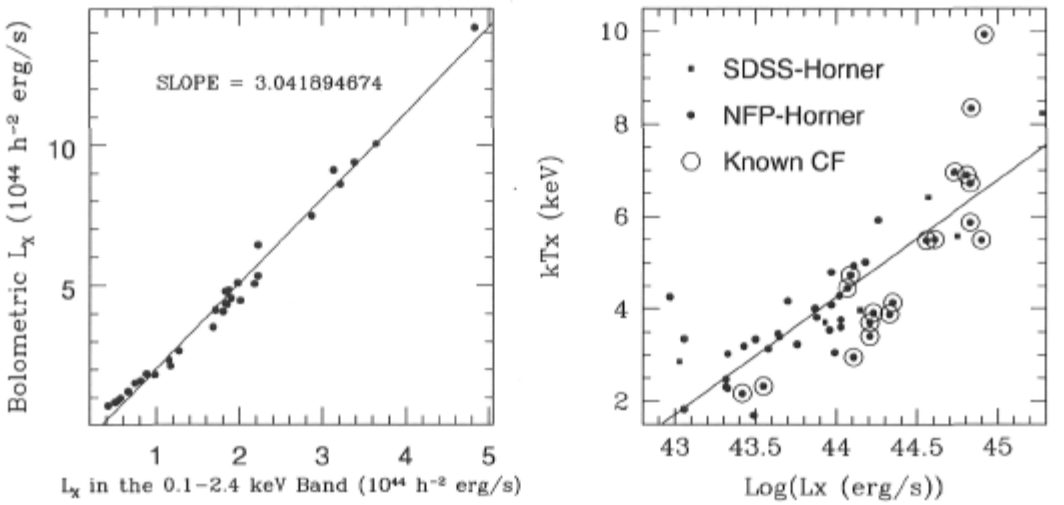

Figure 3.13: **Bolometric correction and L_X-T_X relation for clusters in the NFPS and SDSS.** *Left Panel: Bolometric correction for the X-ray data. Right Panel: The L_X-T_X relation for the NFPS and SDSS datasets. Here, the temperature is multiplied by k, the Boltzmann's constant. Both figures include linear fits to the data.*

fraction of emitting galaxies. The right pannel of Figure 3.12 shows the largest Hα equivalent widths occur in BCGs that are among poorer groups. If the line emission traces the star formation, then this is consistent with the popular notion that overall there is less star formation in the most dense regions.

3.6.3 X-ray Properties of the SDSS Clusters

The temperature of the hot X-ray emitting gas (T_X) depends not only on the profile of the gravitating mass (M), but also on the gravitational and non-gravitational heating processes that have occurred over the history of the gas. The cosmological models of Evrard et al. (1996), which include gravity, pressure gradients, hydrodynamic shocks, and feedback from galaxy winds predict $M \propto {T_X}^{1.5}$ and $L_X \propto {T_X}^2$, where L_X is the X-ray luminosity. The *Chandra* observations, however show a slightly higher slope, $M \propto {T_X}^{1.5-1.6}$ and $L_X \propto {T_X}^{2.6-2.8}$ (McNamara & Nulsen 2007), which implies the existence of excess heat. This is the motivation for exploring pre-heated models, where extra entropy is injected into the system before virialization (see Section 2.3.1).

The observed L_X - T_X relation is plotted in Figure 3.13. The fact that most points follow the linear regression shows that the data is much more tightly correlated than the observed L_X - σ relation of Figure 2.4. In order to plot the bolometric luminosity for all the SDSS clusters from all of the X-ray catalogues, it is necessary to find the

slope for the relationship between the X-ray bolometric and band luminosities using the Markevitch (1998) data (see Figure 3.13). This is applied to the different X-ray cluster catalogues after correcting for the value of H_0 in order to plot Figures 2.4 and 3.13. The cooling flow cluster with $kT_X = 10$ would be one with a large amount of pre-heating according to the models, as it lies very above the line, though most cooling flow clusters are seen to lie below the line and have less pre-heating. The L_X - T_X relation is interesting itself, as it shows that the temperature is a better indicator of the cluster mass than the velocity dispersion. However, this data has already been published separately for all datasets in their relative X-ray catalogues. As this exercise then does not present any new results, it was not included in the article of Chapter 2.

Chapter 4

Integral Field Spectroscopy on a Sample of Brightest Cluster Galaxies

This chapter begins the second part of this thesis, where the emission line morphology, stellar populations, and velocity structure of the gas within the central few arcseconds of 9 Brightest Cluster Galaxies (BCGs) are characterized in detail using integral field spectroscopy. I begin by describing the sample of clusters chosen for the study, then give an overview of the observations and data reduction procedure. I present maps of several prominent emission lines, and determine properties such as the age and metallicity for various stellar populations. Maps of relative velocity within the line emitting gas are also produced. The galaxies observed with OASIS are detailed after the presentation of the Gemini IFU targets. A full discussion of these results is reserved for Chapter 5.

4.1 The Sample

In order to make non-biased conclusions, it is important to study not only the high-luminosity systems, but also those in lower X-ray luminous clusters, those in non-cooling flows, and those with and without radio observations (which, as we saw in Chapter 3, seems important for the presence of emission lines). Therefore, this sample of 9 BCGs, listed in Table 4.1, is chosen from nearby clusters which span the range properties listed above. Both cooling flow (Abell 1204, MKW3s, Abell 1651, Abell 2052, Abell 2199, and Cygnus-A), and non-cooling flow (Abell 1060, Abell 1668, and Ophiuchus) clusters are included. The clusters possess different levels of X-ray luminosity, and central galaxies with and without radio sources are observed. The first column of Table 4.1 lists the name of the observatory at which the data were taken, the second lists the name of the cluster, the third the name of the BCG, and the fourth column lists the redshift

Table 4.1: Cluster Properties

Obs	Cluster Name	BCG Name	z	D Mpc	kpc/″	CF Status	MDR $M_\odot\,yr^{-1}$	L_X 10^{37}W	Radio
GS	Abell 1060	NGC 3311	0.0126	53	0.25	No[1]	0	0.47	Yes
GN	Abell 1204		0.1706	640	2.65	Yes[2]	675	6.77	No
GN	Abell 1668	IC 4130	0.0634	256	1.17	No[3]	0	1.61	Yes
GS	Ophiuchus		0.0280	116	0.55	No[2]	0	> 4	Yes
GN	MKW3s	NGC 5920	0.0450	184	0.85	Yes[4]	< 10	2.68	Yes
GS	Abell 1651		0.0849	337	1.51	Yes[2]	231	8.25	some
WHT	Abell 2052	UGC 9799	0.0345	146	0.68	Yes[5]	30	2.52	Yes
WHT	Abell 2199	NGC 6166	0.0310	125	0.59	Yes[6]	12	3.70	Yes
WHT	Cygnus-A		0.0561	227	1.04	Yes[7]	564	2.00	Yes

References for cooling flow status: [1]*Exosat data from Hayakawa et al. (2006);* [2]*ASCA data from White (2000);* [3]*Salomé & Combes (2003);* [4]*RGS XMM-Newton data from Peterson et al. (2003);* [5]*Chandra data from Blanton et al. (2003);* [6]*Chandra data from Johnstone et al. (2002); and* [7]*ROSAT data from Reynolds & Fabian (1996).*

(taken from NED[1]). The distance and angular scale, assuming $H_0 = 70\,km\,s^{-1}\,Mpc^{-1}$, $\Omega_m = 0.3$ and $\Omega_\Lambda = 0.7$, are listed in the fifth and sixth columns, respectively. Column seven gives the cooling flow status, and column eight gives the mass deposition rate (MDR). The X-ray luminosity is given in column nine, and whether or not there is an associated NRAO VLA Sky Survey (NVSS) image showing radio emission is listed in column ten.

4.2 Gemini IFU Observations and Data Reduction

Twin telescopes, Gemini North (GN) on Mauna Kea in Hawaii and Gemini South (GS) on Cerro Pachon in Chile, are among the largest and most powerful telescopes to which Canadian astronomers have access. Their 8 m diameter mirrors allow for detailed observations of extremely faint and distant objects. The GMOS integral field unit (IFU) is available to do imaging spectroscopy on a small field of view. The IFU harbors a lenslet array with 1000 elements and covers an area of $5'' \times 7''$. This instrument captures a spectrum for each element, allowing for the construction of an image at each wavelength within the object field of view. For each target, Table 4.2 lists the configuration (grating + filter), grating central wavelength, and useable wavelength coverage (converted to the rest frame of each galaxy). For both of the IFU configurations, R400+r and R400+i, the linear dispersion is 0.67 Å/pix. The Gemini website lists a spectral resolution of

[1]NASA Extragalactic Database

Table 4.2: Observational Data

Obs	Cluster Name	Config	Grating Central λ Å	Rest λ Coverage Å	Integration Time sec	Galactic E(B−V)[1] mag	Internal E(B−V) mag
GS	Abell 1060	R400+r	6300	5540-6830	1640	0.079	0.18 [2,3]
GN	Abell 1204	R400+i	7800	5940-6980	3720	0.017	- [4]
GN	Abell 1668	R400+r	6300	5560-6615	3600	0.032	0.3 [4]
GS	Ophiuchus	R400+r	6300/6350	5450-6850	6000	0.591	0.3 [4]
GN	MKW3s	R400+r	6300/6350	5450-6700	5400	0.035	0.3 [4]
GS	Abell 1651	R400+i	7800/7850	6460-7700	6000	0.027	0.3 [4]
WHT	Abell 2052	MR661	6610	6130-6740	3600	0.037	0.22 [4]
WHT	Abell 2052	MR516	5160	4700-5345	1800	0.037	0.22 [4]
WHT	Abell 2199	MR661	6610	6430-6770	2400	0.012	0.10 [4]
WHT	Abell 2199	MR516	5160	4700-5345	4800	0.012	0.10 [4]
WHT	Cygnus-A	MR661	6610	5915-6605	3600	0.381	0.6 [5]
WHT	Cygnus-A	MR516	5160	4695-5225	3000	0.381	0.6 [5]

Note: Observations that were obtained in two configurations show two values for the central wavelength and the integration time given is the total integration time.
[1] *Taken from NED. References for extinction:* [2] *Vasterberg et al. (1991);* [3] *Sadler & Gerhard (1985).* [4] *The value 0.3 is the average extinction for the BCGs in the sample of Crawford et al. (1999) - there is no correction for internal extinction in the case of Abell 1204 since the Balmer decrement could not be calculated in Crawford et al. (1999).*
[5] *Average extinction value from this data.*

R = 1900 for these configurations, which is in line with the value of ∼3.3 Å, the average measured FWHM of observed sky lines at ∼6300 Å. A signal-to-noise (S/N) ratio greater than 5 in each pixel was required and achieved for each galaxy. The integration times are also listed in Table 4.2.

The spectral analysis software IRAF was used to reduce and analyze the spectra. Several Gemini specific programs from the package *gemtools* have also been used for the data reduction. The tasks in this package perform the normal processing steps on IFU data (bias subtraction, cosmic ray rejection, flat fielding, wavelength calibration, sky subtraction, and atmospheric extinction-correction). Generally these programs worked well, however bright ripples at both sides of the final datacubes were seen in the BCGs of Abell 1651, and most notably in Abell 1060. These artifacts, known to the Gemini science team, are caused by imperfect sky subtraction of the flat field frames during the standard reduction procedures. Therefore, to make a cleaner continuum image for Abell 1060, the reduction process was slightly modified. Instead of working on the individual spectra, I constructed an image of the flat using the same wavelength range as for the construction of the continuum image, then I manually scaled and divided this flat image from the continuum image. In this case, the continuum and flat field regions

are a median average of three regions between 6300 and 6500 Å. Although this does not give a perfectly clean result, it does make for a noticeable improvement. For example, the bright and dark fringes on the right side of the continuum image in Abell 1060 have a flux difference which is 10% of the average continuum level, whereas this goes down to a 2% difference in the reworked image. The variation in the bright and dark regions in the continuum level stays constant at ∼35% in each case. The flux level of these artifacts is low compared to the emission line levels. Additionally, the fact that they disappear in the continuum-subtracted line images, as both the continuum, and line + continuum images contain the fringes.

Each lenslet is about 0.2″, and there are about 2 pixels per lenslet, therefore, as the typical seeing was ∼0.8 - 1″, each spectrum was median averaged with the value of its 8 closest neighbouring pixels to match the seeing and increase the S/N.

Table 4.2 includes a value for the reddening expected from dust column density maps in the Milky Way constructed by Schlegel et al. (1998). The galactic extinction is then removed using these values of $E(B-V)_{Gal}$ and the IRAF task *deredden*. Using *dopcor* and the well known cluster redshifts, the spectra are then de-redshifted. Unless otherwise specified, the continuum level is determined by using *splot* to find the median of a 100 Å-wide region around 6880 Å if observed using the R400+i configuration, and around 6450 Å if observed in the R400+r configuration. The intensities of the emission and absorption lines are subsequently measured by fitting Gaussian profiles using *deblend*. The S/N level for each pixel was calculated in the same spectral windows used to make the continuum image.

In order to calculate properties such as age and metallicity, and in order to compare the emission between galaxies, a knowledge of the internal reddening in each galaxy is important. Some elliptical galaxies are known to be dusty (Sadler & Gerhard 1985) and this dust can be uniform, filamentary, or patchy (Laine et al. 2003). So ideally, one would map the internal extinction to the same scale as the spatial resolution. The Balmer decrement is normally taken into consideration when obtaining a measurement of the internal extinction. This method involves measuring the difference between the Hα and Hβ intensity, and associating the difference between the measured and theoretical values to the extinction, which affects the blue light more than the red (see Equation 4.3 of Section 4.12 for an example). The bandwidth of the IFU observations does not allow for a measurement of Hβ. Rather than observe far fewer objects in an alternate configuration in order to catch these lines, I chose to observe a larger sample with only Hα data. Often an integrated value for the Hβ strength exists from previous studies and can be taken from the literature. The integrated value (given in Table 4.2) is then associated to all the pixels in the field of view. If there are no known values of the internal extinction for a particular galaxy, a value of $E(B-V)_{int} = 0.3$ is adopted. This value is quoted by Crawford et al. (1999) as their average value for X-ray selected BCGs with strong Hα emission lines. The values used for internal extinction are listed

in Table 4.2.

In the following sections, optical emission line ratios for the extinction corrected images are used as a diagnostic to characterize the ionization source, derive SFRs if the source is likely to be stellar, constrain the metallicity of any star-forming regions, and derive the kinematics of the line emitting gas. The presence, or lack, of a hard ionizing source such as an AGN is inferred from standard optical diagnostic line ratios (Osterbrock & Ferland 2006). To discriminate between the signatures of a young stellar population from those of an AGN, the emission line ratios of [N II] λ 6584/Hα, [O I] λ 6300/Hα, and [S II] $\lambda\lambda$ 6716,6731/Hα are usually plotted against [O III] λ 5007/Hβ and placed on Baldwin et al. (1981, BPT) diagrams (Kewley et al. 2001a). Unfortunately, [O III] and Hβ are not included in the Gemini IFU observations, as they are too far towards blue wavelengths. Also, the [O I] measurements are generally too noisy to obtain reliable values. Therefore, throughout most of the analysis I rely on the [N II] λ 6584/Hα and [S II] λ 6716+λ 6731/Hα to give constraints on the ionization mechanism.

If the line ratios indicate star formation, then I calculate the Hα equivalent width (W_o) corrected for absorption as well as internal and galactic extinction and use the W_o to derive the age of the young stellar population with the population synthesis code Starburst99. The metallicity is constrained using measured [N II] λ 6584, Hα, and [S II] $\lambda\lambda$ 6716,6731 emission lines, and the ratio of [S II] λ 6716/[S II] λ 6731 can constrain the electron density. The star formation rate is calculated using the following equation from Kennicutt (1998):

$$\mathrm{SFR}[\mathrm{M}_\odot\,\mathrm{yr}^{-1}] = 7.9 \times 10^{-42} \times \mathrm{L}(\mathrm{H}\alpha)\,\mathrm{erg\,s}^{-1}. \tag{4.1}$$

The Hα flux, F(Hα), of each region is converted to the luminosity, L(Hα), with the following equation:

$$\mathrm{L}(\mathrm{H}\alpha) = 4\pi\,\mathrm{D}^2\,\mathrm{F}(\mathrm{H}\alpha), \tag{4.2}$$

where D is the distance calculated using the redshift of the galaxy (Table 4.1). The Kennicutt (1998) equation has been calibrated using population synthesis models based on Case B recombination, a Salpeter initial mass function, a solar metallicity and a temperature of 10 000 K. The equation assumes the Hα luminosity has been corrected for extinction, and that there is a low escape fraction of ionizing photons. Finally, the kinematics of the line emitting gas are shown as maps of relative velocity which is derived from the difference between the measured line centroid corrected for the galaxy redshift, and the rest frame value of the emission line. When the FWHM of the lines is quoted, it refers to the measurement made using *deblend*. The FWHM is not corrected for the instrumental line profile, which is nevertheless similar throughout all of the observational configurations.

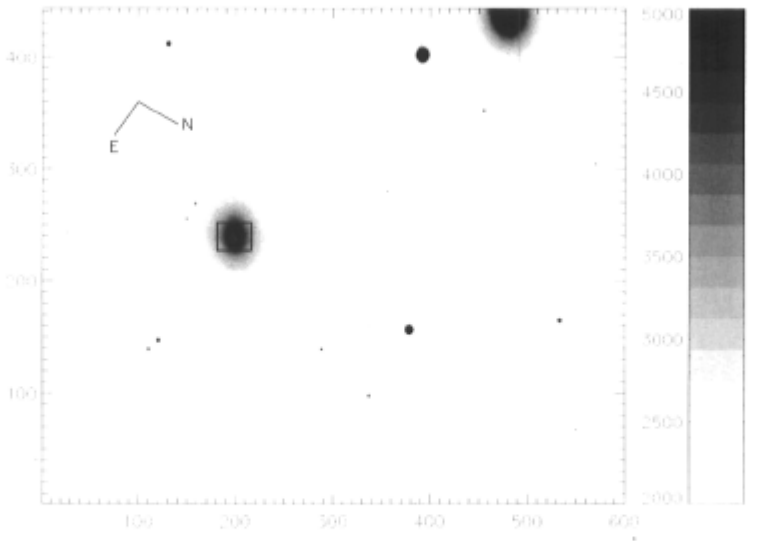

Figure 4.1: **The center of Abell 1060 taken in the r-filter.** *The IFU field is marked as a box with dimensions of 5 × 7″ (1.3 × 1.8 kpc) around the BCG NGC 3311. The central dust patch is already noticeable in this image. The scale is in arbitrary flux units.*

4.3 NGC 3311 in Abell 1060

In this section, the data and results for NGC 3311, the BCG of Abell 1060 (Figure 4.1) are presented. Abell 1060 is a nearby (z = 0.0126) relaxed cluster (McCarthy et al. 2004) with little brightness difference between the 1st and 2nd rank galaxies (i.e. of Bultz-Morgan type BM III) and a velocity dispersion of 597 km s^{-1} (Laine et al. 2003). This cluster is at a distance of ∼50 Mpc, such that the angular scale 1″ ≃ 250 pc. The X-ray luminosity in the 0.1 - 2.4 keV band is 0.46 × 10^{44} ergs s^{-1} (Jones & Forman 1999) and this emission is centered ∼30 kpc NE of NGC 3311. While this cluster was originally classified as a cooling flow cluster with a MDR of 6 $M_\odot$ yr^{-1} (White 2000), new X-ray measurements based on *Chandra* data find no central temperature drop, and this cluster is no longer considered a cooling flow (Hayakawa et al. 2006). Laine et al. (2003) studied this BCG as part of their HST snapshot survey. They found that 38% of the BCGs in their sample had central dust features, including this one, for which the dust was described as filamentary and patchy. In fact, this dust feature is also visible in the r-band image of Figure 4.1.

Hα emission has already been detected in NGC 3311 by Vasterberg et al. (1991), who, using longslit spectroscopy, reported that the ionization mechanism was likely to be due to a young stellar population. Here, with IFU observations, we are able to investigate the line emission to a much higher degree in terms of spatial resolution. Because of the relative proximity of this cluster, the 5 × 7″ field of view of the IFU

allows for a detailed analysis of the inner 1.3×1.8 kpc of the BCG. Therefore, each pixel represents a width of only $\sim$26 pc on a side.

4.3.1 Line Images and Region Spectra

Figure 4.2 shows an image of the continuum in a line-free region around Hα λ 6563. It has been created by averaging the flux between 6300 and 6500 Å. Figure 4.2 also shows the Hα flux image (displayed on other panels as contours); each pixel value has been determined using the *splot* task *deblend* to fit the emission line. The line is deblended from the surrounding [N II] emission, and the continuum level is subtracted. Similarly, Figure 4.2 presents the continuum-subtracted and deblended [N II] λ 6584 and [S II] λ 6716 + λ 6731 images.

Vasterberg et al. (1991) and Laine et al. (2003) both note a large dust patch that corresponds in position to the obscuring feature going North-South seen in the continuum image. In fact, in comparing the HST I-band image of the center of the BCG from Laine et al. (2003), one notices the striking similarity both in extent and morphology between the dust patch they identify, to the regions strongly emitting Hα. The Hα contours on the continuum image of Figure 4.2 clearly show that much of the Hα emission is confined to within the same projected spatial extent of the dust. As the Hα emission is visible, much of what we observe is necessarily in front of the dust lane, however, some additional Hα emission could be obscured. Overall, the bright regions in [N II] follow those seen in the Hα emission image. The [S II] λ 6716 + λ 6731 emission is weak, and in several pixels too close to the noise to allow for line fits.

In general, the pixel to pixel variation of the spectra for all BCGs, is smooth and gradual. Therefore, selecting regions which are representative has two significant advantages. First, in doing so the S/N value of low-level emission lines and weak absorption features is boosted. Typical S/N values of the individual pixels in the continuum are $\sim$10 - 20, as shown in Figure 4.3, which is fairly low for the reliable measurement of the weaker features. Second, the spectra of the representative regions allow for the perusal of the full wavelength coverage. Each pixel of the reconstructed images presented here corresponds to one spectrum, making for a very large number of spectra in total. Thus, it is not practical to present such a large number of individual spectra, several of which are quite similar. The images created from fitting the strong well measured lines (e.g. Hα, in Figure 4.2) and diagnostics (e.g. the [N II] λ 6584/Hα ratio and the Hα relative velocity, to be discussed below) are complemented by choosing several regions within which to add the spectra. In this way, the weaker lines (e.g. [S II] λ 6716 + λ 6731)/Hα and the absorption features) can be measured and a manageable number of spectra can be displayed. I maintain this technique throughout the chapter.

The continuum and Hα images of Figure 4.2 are used in order to select 11 regions within which similar spectra are co-added, increasing the S/N to > 20. These areas, which include 5 regions of very strong emission, 2 regions of weaker emission, 2 regions in

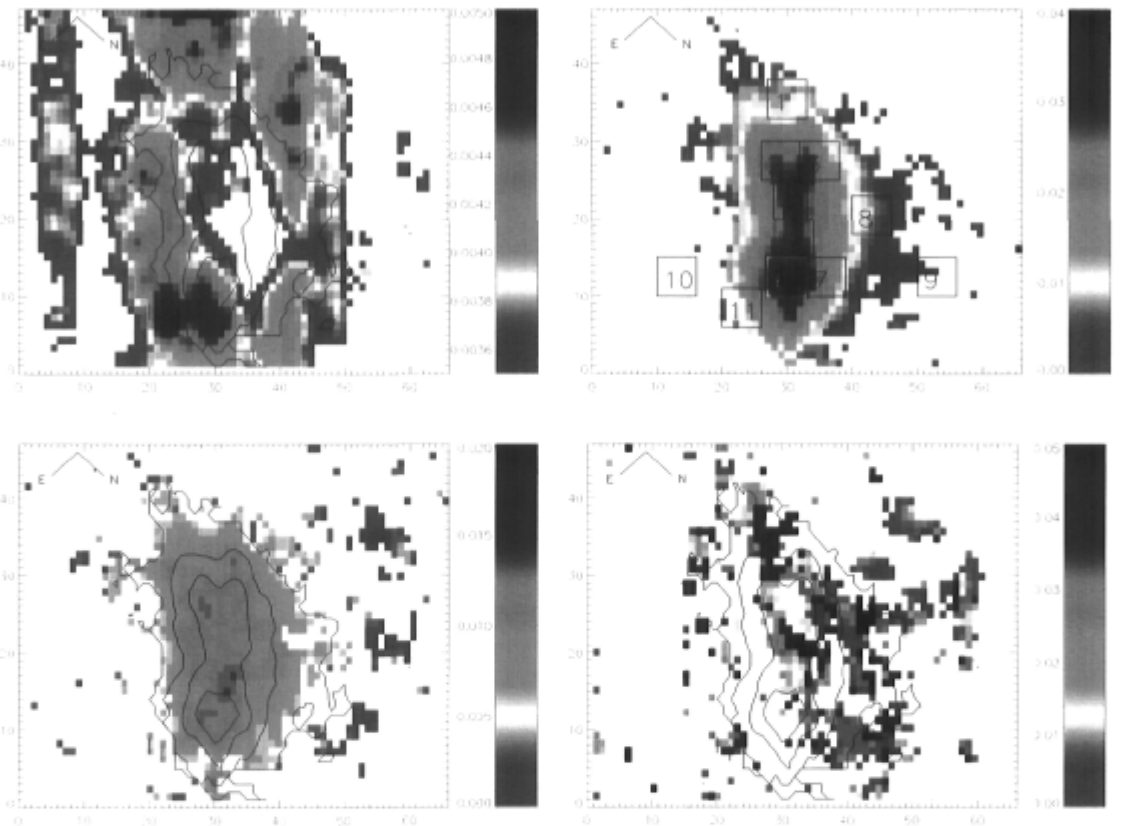

Figure 4.2: **Reconstructed images for NGC 3311 in Abell 1060.** *Top Left Panel: The continuum surrounding the Hα emission line. A dust patch in the N-S direction is clearly visible. The vertical bands seen on the left and right sides of the figure are associated to fringes (see Section 4.2). Top Right Panel: The continuum-subtracted Hα emission flux. The regions used in the subsequent analysis are represented as boxes. Bottom Left Panel: The continuum-subtracted [N II] λ 6584 flux. Bottom Right Panel: The continuum-subtracted [S II] λ 6716 + λ 6731 emission. The Hα emission is overlain as contours. All panels are in reverse colour scale and in units of* 10^{-15} *erg s*$^{-1}$ *cm*$^{-2}$ *Å*$^{-1}$. *One pixel is ∼26 pc across, for all panels.*

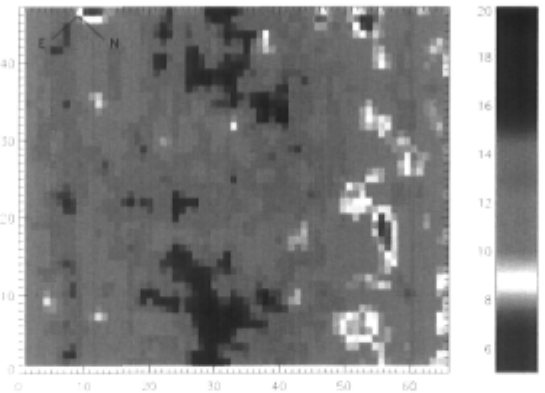

Figure 4.3: **S/N ratio of the continuum for NGC 3311 in Abell 1060.** *One pixel is ∼26 pc across.*

Hα emission-free zones, and one region centered on the peak of the continuum emission, are marked on one of the images of Figure 4.2. Further along, these high S/N regions are used to derive the emission line ratios.

Each of the 11 sections is made of 6 × 7 pixels. This translates to 0.59 × 0.72″, and a physical area, per sectin, of ∼175 pc across. The integrated spectra for these regions are presented in Figure 4.4. Emission lines from [O I] $\lambda\lambda$ 6300,6364, Hα, as well as, [N II] $\lambda\lambda$ 6548,6584, and [S II] $\lambda\lambda$ 6716,6731 are marked on the figure. Strong absorption lines from the old stellar populations are also apparent: the broad sodium line, NaD at 5890 Å is labeled. Because the IFU spectra are observed over 3 chips, there are two chip gaps, one around ∼5775 Å (not shown), and the other near 6640 Å. The chip gap and a region of poor subtraction of sky lines near 6220 Å have been hashed out on the figure. There was some question as to whether the Fe I and Mg II at 6778 Å were observed. However, these lines are redshifted into a region full of OH lines near 6863 Å (Osterbrock et al. 1996), which dominate their signal. There is a prominent emission feature in panels where Hα is strong - this feature is at ∼5686 Å (not shown); although [N II] does emit at this wavelength, it is not usually this strong and it would be surprising if the feature were physically associated to the BCG. It is unlikely that any significant population of Wolf-Rayet stars are present in the IFU spectra. The most prominent feature of these objects is a line in the blue, outside the wavelength coverage of this instrument. However Wolf-Rayets do contain weaker broad lines (up to ∼2000 km s^{-1}) at ∼6560 Å and ∼6678 Å. No additional broad features are seen at these wavelengths for NGC 3311, though a low level component which is hidden in the continuum noise can not be ruled out (the same is true for all the BCGs in this chapter). Sky lines are abundant near [S II] λ 6731 and make the measurement of this emission line difficult.

It is convenient that the regions have been chosen to cover an equal area, as the

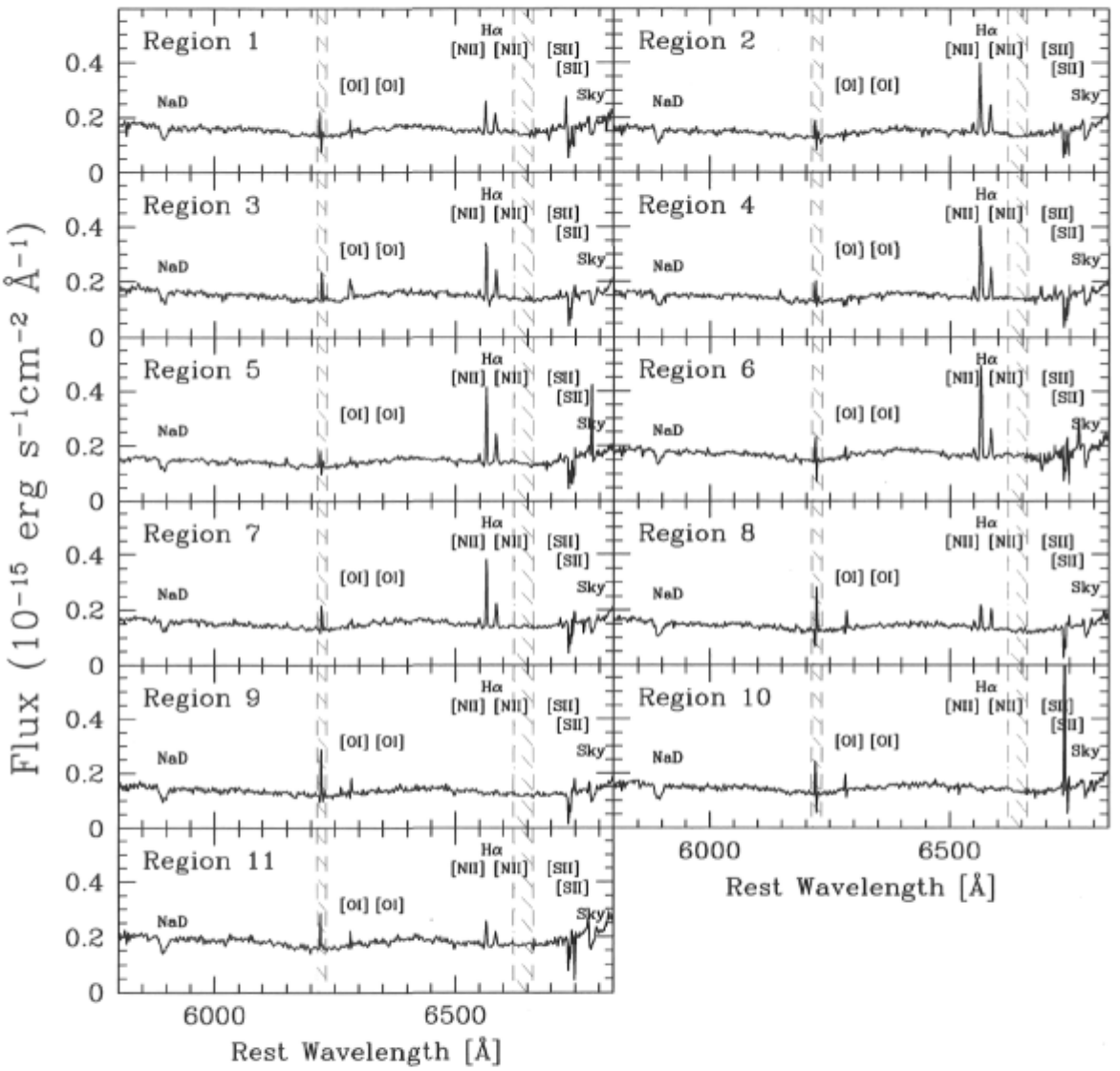

Figure 4.4: **Summed spectra of the 11 selected regions in the Hα image of NGC 3311 in Abell 1060.** *The regions are labeled as in Figure 4.2. Prominent emission and absorption features are identified. The chip gap, and the poorly subtracted oxygen sky lines are hashed out in regions near 6640 and 6220 Å, respectively.*

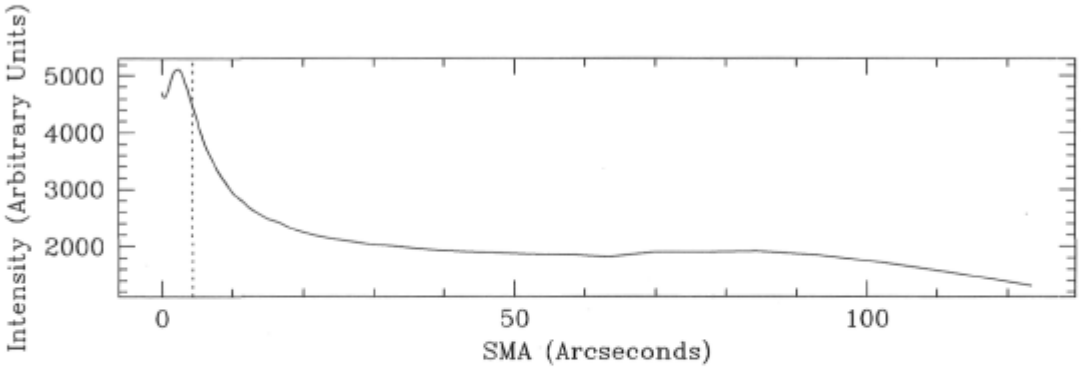

Figure 4.5: **Luminosity Profile for NGC 3311 in Abell 1060.** *Measured from the r-band acquisition image. The vertical dotted line marks the maximum extent of the IFU field of view. The x-axis displays the Semi-Major Axis as calculated using the IRAF task, ellipse.*

spectra can be directly compared to each other. If one compares, for example, the spectrum of Region 5 (which is in a very high Hα emitting zone) to that of Region 10 (which is out of the Hα emitting area and away from the dust patch), one sees the same absorption features from the underlying old population, but none of the emitting features that would be caused by ionization from a younger population are present in the spectrum of Region 10. Region 11, the area chosen to cover the peak continuum emission, has the same spectral features as Region 1, also on the border of the Hα emitting area, plus the increased continuum level. With the possible exception of Region 8, none of the integrated spectra show line ratios that immediately suggest the requirement of a hard ionizing source.

4.3.2 The Underlying Stellar Population

The effect of any underlying old stellar population should be determined in order to derive the absorption corrected Hα emission, and characterize the young stellar population. Because the Hα emission seems to be constrained to the very central region of the image, an integrated spectrum from the surrounding regions, presumably the underlying older population, can be used to find an average contribution from Hα absorption once it is scaled to the level of the central luminosity. It is well known that elliptical galaxies follow a deVaucouleurs law for their radial luminosity profile however, the IFU sees only the very central regions of the center of the galaxy and this region is plagued with patchy dust features. The luminosity profile is calculated by fitting elliptical isophotes on the r-band image using the IRAF task *ellipse*. It is in Figure 4.5 for NGC 3311. Up to the maximum extent of the IFU field of view, the extinction

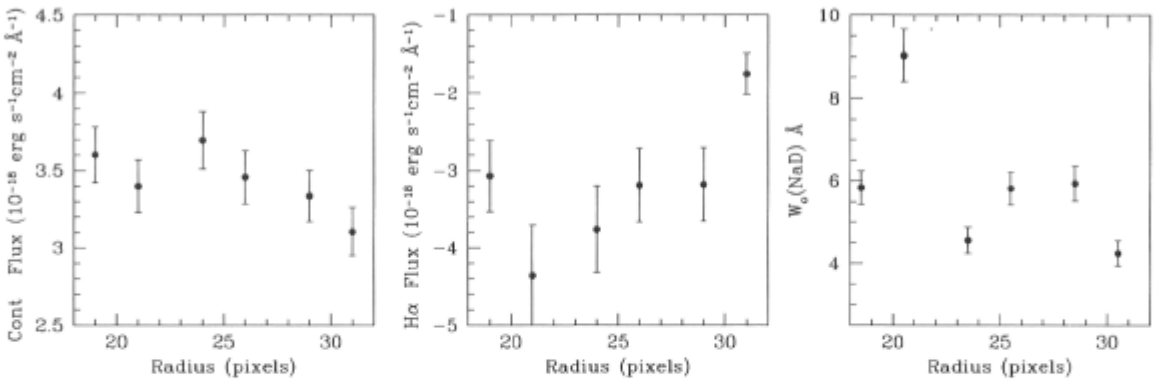

Figure 4.6: **Radial cuts of the underlying population for NGC 3311 in Abell 1060.** *The x-axis shows the distance, at pixel (a,b), from the center of the IFU frame. Left Panel: The continuum flux near Hα. Central Panel: The Hα absorption line flux. Right Panel: The NaD absorption line equivalent width. There is no evidence for a trend with radius in any panel and most of the points are equal to each other, to within the error (as discussed in the text).*

significantly distorts a regular deVaucouleurs profile. Therefore, I assume that the level of the intensity from the underlying stellar distribution is flat throughout the IFU field.

Figure 4.6 shows a radial cut in y across the middle of the image for the continuum flux near Hα, for the Hα absorption line continuum-subtracted flux, and for the NaD equivalent width. Only the area away from the Hα emission regions are plotted. That is, the values are measured from a median of all the y-axis spectra using bins that are 5 pixels wide and located to the left and right of the BCG center (avoiding the central region of intense Hα emission). The errorbars are determined by taking the difference between measured values calculated using the left hand continuum (which has a higher value) and those using the right hand continuum. Generally, this is $\sim\pm7\%$ for the NaD equivalent widths, and $\sim\pm15\%$ for the Hα flux. The figure shows that there is no evidence of a trend with radius and that most of the points are equal to each other, to within the error. Although, note that the spectra responsible for the NaD outlier are contaminated by Hα emitting pixels. Therefore, it is the final integrated spectrum shown in Figure 4.7, which is created from an average of the absorption spectra (located away from the central Hα emitting region) that will be used to subtract the contribution of the old population from the central region. This central region contains 173 Hα emitting pixels whose average Hα emission spectrum is also shown in Figure 4.7. The average Hα absorption is $3.2\pm0.4 \times 10^{-18}$ erg s^{-1} cm^{-2}, increasing the average Hα emission by $\sim$9%. To get an estimate of the error in the line intensity measurements, I measure the flux of the line using different continuum levels. The errors are $\sim$4% for the strongly emitting spectra like Region 6, and $\sim$10% for low line luminosities of Region 1. Thus, the absorption correction is significant and will be taken into account

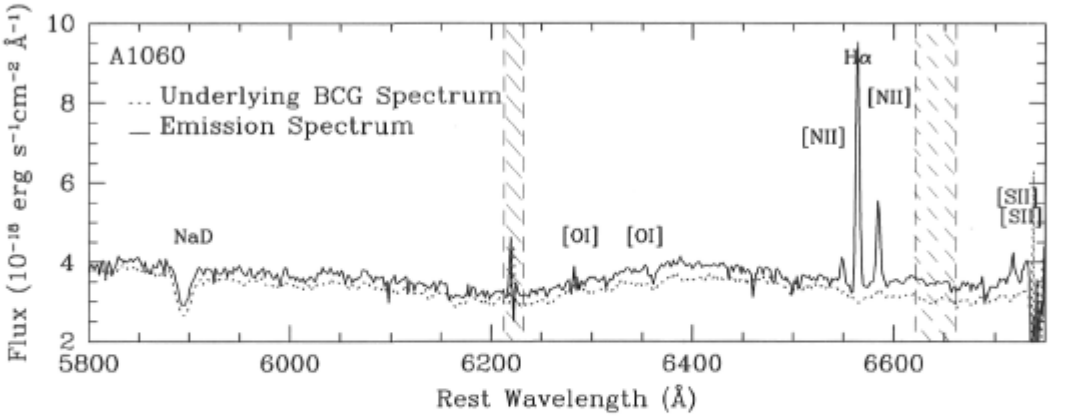

Figure 4.7: **Average spectra of the emitting and underlying population of NGC 3311 in Abell 1060.** *A median average of Hα emitting spectra are shown alongside the average spectrum for the underlying population in the regions surrounding the intense emission.*

in the following subsection.

Since the underlying spectrum gives an integrated value for the NaD equivalent width, the population synthesis code of Mollá & García-Vargas (2000) is used to determine an age for the underlying population. The value is 4.5±0.4 Å, allowing for an age of $1.00\pm0.01 \times 10^{10}$ yr and only a supersolar metallicity ($2\,Z_\odot$, is used). Ideally, the Hβ line strength, along with Fe I, CaT, and Mgb would be used as well, however in this case the spectral bandwidth does not contain all the aforementioned lines. An estimate of the mass is made by scaling the continuum level (per solar mass) at 6400 Å of the model to the observed continuum level of the old population (Figure 4.7) where the galactic and internal extinction have been considered. Using the model with a metallicity of $2\,Z_\odot$ and an age of 10^{10} yr, $2 \times 10^8\,M_\odot\,\mathrm{kpc}^{-2}$ are required in order to match the observations. Typical stellar masses for BCGs can be deduced from cosmological merger simulations, and are $\sim 10^{12}\,M_\odot$ (De Lucia & Blaizot 2007). Gonzalez et al. (2003) have found effective radii (the radius at which half of the luminosity is captured) of 20 - 300 kpc by studying the surface brightness profiles of BCGs. Thus, the stellar mass found here, extrapolated to the effective radius, is consistent with typical BCG masses. The ages and masses for the galaxies studied here are compiled at the end of this chapter in Table 4.12.

4.3.3 Line Measurements and the Ionization Mechanism

For 9 of the 11 regions, those with emission lines, the spectrum of the underlying population has been scaled to match the number of pixels in the region, and subtracted

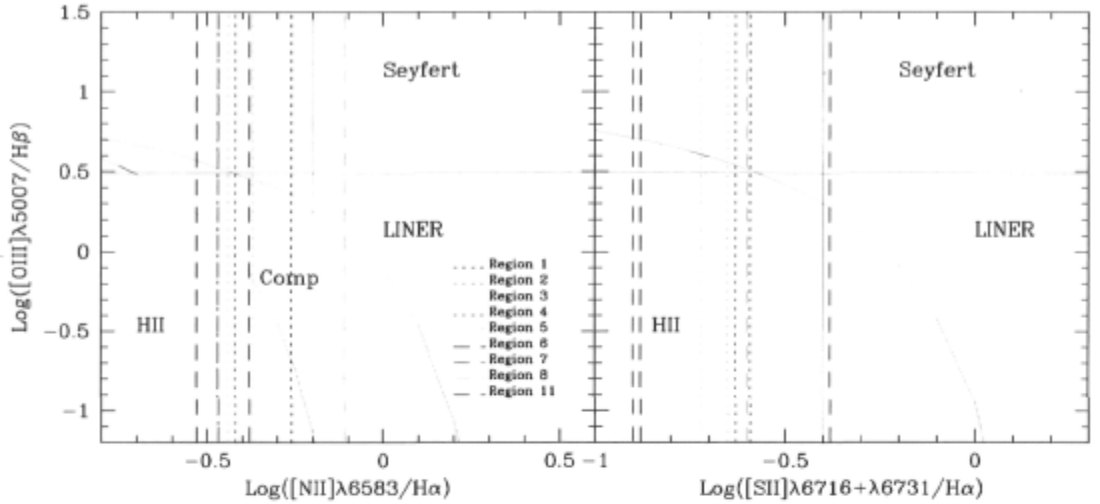

Figure 4.8: **Ionizing source diagnostics for NGC 3311 in Abell 1060.** *On the left, the BPT diagram is shown with the [N II] λ 6584/Hα and the [S II] λ 6716 + λ 6731/Hα ratios of the regions is on the right. The curve which represents the upper limit to ratios effected by H II regions is from Kewley et al. (2001a, shown in both panels), and that which represents the limit of significant contribution from an AGN is from Kauffmann et al. (2003, in left panel only). The solid vertical and horizontal lines illustrate the convential definitions of LINER and Seyfert (Osterbrock & Ferland 2006). It is clear that all regions are reasonably constrained to the H II and composite areas of the diagrams if we assume a low value of the ratio for [O III] λ 5007/Hβ.*

from the region spectrum. The central position, flux, equivalent width (W_o), and line width (FWHM, uncorrected for the instrumental profile) are determined by fitting Gaussian functions to the emission line profiles using *deblend*. Table 4.3 shows these values for Hα, [N II] λλ 6548,6584, and [S II] λλ 6716,6731. Recall that the measurement of the [S II] λ 6731 line is less certain, due to the proximity of the sky lines. Additionally, the noise level in Region 1 does not allow for the measurement of the weak [S II] lines, and they are excluded from Table 4.3.

This data does not yield the [O III] λ 5007/Hβ ratio and so it is not possible to completely rule out the possibility of Seyfert emission from Figure 4.8, which places the [N II] λ 6584/Hα and ([S II] λ 6716 + λ 6731)/Hα ratios for the regions on a BPT diagram. But, assuming the [O III] λ 5007/Hβ ratio is reasonably low, than the low [N II] λ 6584/Hα ratios in almost all of the regions show emission more typical of star formation, or composite, rather than LINER. Region 8 stands apart with a high [N II] λ 6584/Hα ratio, and if the ionization is caused by a population young stars, it could include some contamination from a LINER as well. But it is unlikely that

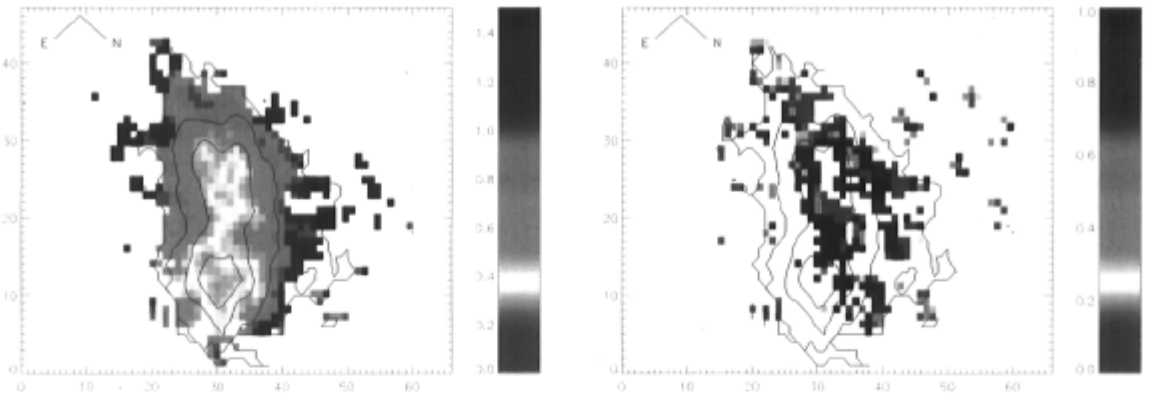

Figure 4.9: **Line flux ratios for NGC 3311 in Abell 1060.** *Left Panel: A reverse scale image of the [N II] λ6584/Hα ratio in NGC 3311 of Abell 1060. Right Panel: A reverse scale image of the [N II] λ 6584/([S II] λ 6716 + λ 6731) ratio. Only pixels where S/N > 1.5 are displayed. The contours represent the Hα emission. One pixel is ∼26 pc across.*

Region 8 is dominated by an AGN. An image of the [N II] λ 6584/Hα across the center of the galaxy is shown in Figure 4.9; notice how the central regions have the lowest [N II] λ 6584/Hα ratios which increase steadily towards the edge of Hα emission. The edges, which include Region 8, are the only areas in which the [N II] λ 6584 is more intense than the Hα emission, but this is where the Hα intensity starts to fall to the level of the noise (note the Hα contours overlaid on the figure). Thus, the ionization is probably not a result of a hard radiation field supplied by an AGN. This is consistent with the work of Laine et al. (2003) and Tran et al. (2001) who have classified the dust in NGC 3311 as filamentary and patchy (i.e. not disky). Tran et al. (2001) have studied dust in 67 early type galaxies and find that dust which is disky is aligned to the major axis of the galaxy whereas dust which is filamentary may take on any position angle. They conclude that filamentary dust originates from outside of the elliptical galaxy (or has not yet settled into a disk). Therefore, based on these conclusions, one would then not assume that the dust in NGC 3311 is intimately linked to an active nucleus. The ionization source, which, from the Hα image, appears to be in front of the dust patch would then be even further (or at least as far) from a central black hole. In this context, line ratios typical of a young stellar population are easier to understand. The patchy dust and young stellar population could have been captured from another galaxy during a tidal encounter.

Table 4.3: Spectral Line Values for Regions of NGC 3311 in Abell 1060

Measurement	Region 1	Region 2	Region 3	Region 4	Region 5	Region 6	Region 7	Region8	Region 11
[N II] λ 6548									
Center (Å)	6548.6	6548.1	6548.7	6548.6	6549.2	6549.1	6549.2	6550.2	6549.0
Flux × 10^{-15} erg s^{-1} cm^{-2}	0.07	0.15	0.12	0.17	0.14	0.12	0.13	0.11	0.04
W_o (Å)	−5.5	−15.5	−17.1	−50.7	−53.5	−4.5	−20.3	−18.9	−1.0
FWHM (Å)	3.3	3.6	3.8	3.1	3.6	3.2	4.5	3.7	2.2
Hα									
Center (Å)	6563.0	6563.1	6563.7	6563.7	6564.1	6564.3	6564.6	6564.8	6564.3
Flux × 10^{-15} erg s^{-1} cm^{-2}	0.47	1.11	0.91	1.25	1.22	1.43	1.04	0.40	0.43
W_o (Å)	−34.0	−102.1	−103.5	−211.1	−286.5	−51.5	−164.2	−83.2	−11.4
FWHM (Å)	3.6	3.9	3.7	4.0	3.9	3.8	3.8	3.8	4.2
[N II] λ 6584									
Center (Å)	6583.6	6583.8	6584.6	6584.3	6584.7	6584.8	6585.1	6585.8	6584.4
Flux × 10^{-15} erg s^{-1} cm^{-2}	0.26	0.42	0.39	0.42	0.44	0.42	0.35	0.31	0.18
W_o (Å)	−16.7	−33.5	−35.6	−44.1	−68.0	−14.3	−53.7	−49.1	−4.7
FWHM (Å)	3.8	3.7	3.7	3.6	4.1	4.1	3.8	4.1	3.7
[S II] λ 6716									
Center (Å)	-	6717.2	6717.4	6717.4	6717.3	6718.2	6718.2	6719.3	6718.9
Flux × 10^{-15} erg s^{-1} cm^{-2}	-	0.12	0.11	0.20	0.14	0.08	0.09	0.07	0.12
W_o (Å)	-	−10.3	−11.2	−20.4	−12.8	−2.7	−8.2	−13.5	−2.4
FWHM (Å)	-	2.6	3.1	4.2	4.4	1.8	3.6	3.1	5.1
[S II] λ 6731									
Center (Å)	-	6730.5	6731.5	6730.5	6731.3	6733.7	6732.0	6732.7	6732.5
Flux × 10^{-15} erg s^{-1} cm^{-2}	-	0.14	0.06	0.12	0.13	0.11	0.04	0.03	0.06
W_o (Å)	-	−11.8	−6.9	−11.5	−12.2	−3.5	−5.2	−3.8	−1.2
FWHM (Å)	-	4.6	3.0	4.8	7.1	2.4	3.1	2.5	3.7

Note: The central positions are given in terms of the rest wavelength. The error for the fit to the line center is of the order ±0.2 Å. The error for the flux measurements of the strong lines are of order 5-10%, as discussed in the text. The weak lines of [S II] have large errors of 20-30%. Emission lines are not seen in Regions 9 and 10, therefore they are omitted from the table.

4.3.4 Metallicity, Age, and Mass for the Young Population

A good way to determine metallicity from abundance ratios is described in Kewley & Dopita (2002). In this method, theoretical models of stellar populations in star forming galaxies are used to constrain line ratio pairs that are dependent on the ionization parameter (q) and metallicity (Log(O/H) + 12) in a mutually exclusive way. Optimally, one would use the [O III] λ 5007/([O II] λ 3726 + λ 3729) ratio as a diagnostic for the ionization parameter, and subsequently [N II] λ 6584/([S II] λ 6716 + λ 6731), which is a function of metallicity at high metallicities, with [N II] λ 6584/Hα to determine the abundance (Kewley & Dopita 2002).

The observed wavelength range of this dataset does not allow for the complete repertoire of diagnostic ratios, since the required oxygen lines are found in the blue portion of the spectrum. Nevertheless, it is possible to make a rough estimate of the metallicity by assuming an average ionization parameter, and comparing the ratios of [N II] λ 6584/([S II] λ 6716 + λ 6731) and [N II] λ 6584/Hα. A map of the [N II] λ 6584/([S II] λ 6716 + λ 6731) ratio is shown in Figure 4.9, indicating a fair number of pixels with trustworthy fluxes. Although, as Kewley & Dopita (2002) strongly caution and because both ratios depend strongly on the ionization parameter, this method is not precise. They note the metallicities derived using [N II] λ 6584/([S II] λ 6716 + λ 6731) diagnostics are underestimated systematically by 0.2 dex in their models with respect to the metallicity derived from other work (Charlot & Longhetti 2001, for example). They attribute this to different sulfur to oxygen abundance ratios used in their models. Therefore, in Figure 4.10 which presents the measured constraints on the abundances as a function of metallicity, I add a shift of 0.2 dex to their model metallicities based on the [N II] λ 6584/([S II] λ 6716 + λ 6731) ratio.

Figure 4.10 shows the two line ratios available as a function of metallicity. Assuming the ionization parameter is between average values of $q = 5 \times 10^6\,cm\,s^{-1}$ and $2 \times 10^7\,cm\,s^{-1}$, the metallicities from the [N II] λ 6584/([S II] λ 6716 + λ 6731) ratio are compared against those from the [N II] λ 6584/Hα ratio. The latter generally has two possible points on the curve, therefore constraints from the former, although large uncertainties exist for the [S II] λ 6731 line measurement, enable the correct point to be chosen. The final estimation of the metallicity is given by the average of values given by the two ionization parameters of the [N II] λ 6584/Hα diagnostic. The derived metallicites are listed in Table 4.4. The error is from the difference between the two ionization parameters and in general is 0.1 dex. In Regions 4, 8, and 11 the allowed range in the metallicities match up better if more freedom is given to the ionization parameter.

Globally, the values are ~9.3, which is quite high, at about twice solar (note that in this scale 8.9 is solar). But, according to the mass-metallicity relation of Tremonti et al. (2004), the more massive galaxies have higher metallicities. And, the highest mass

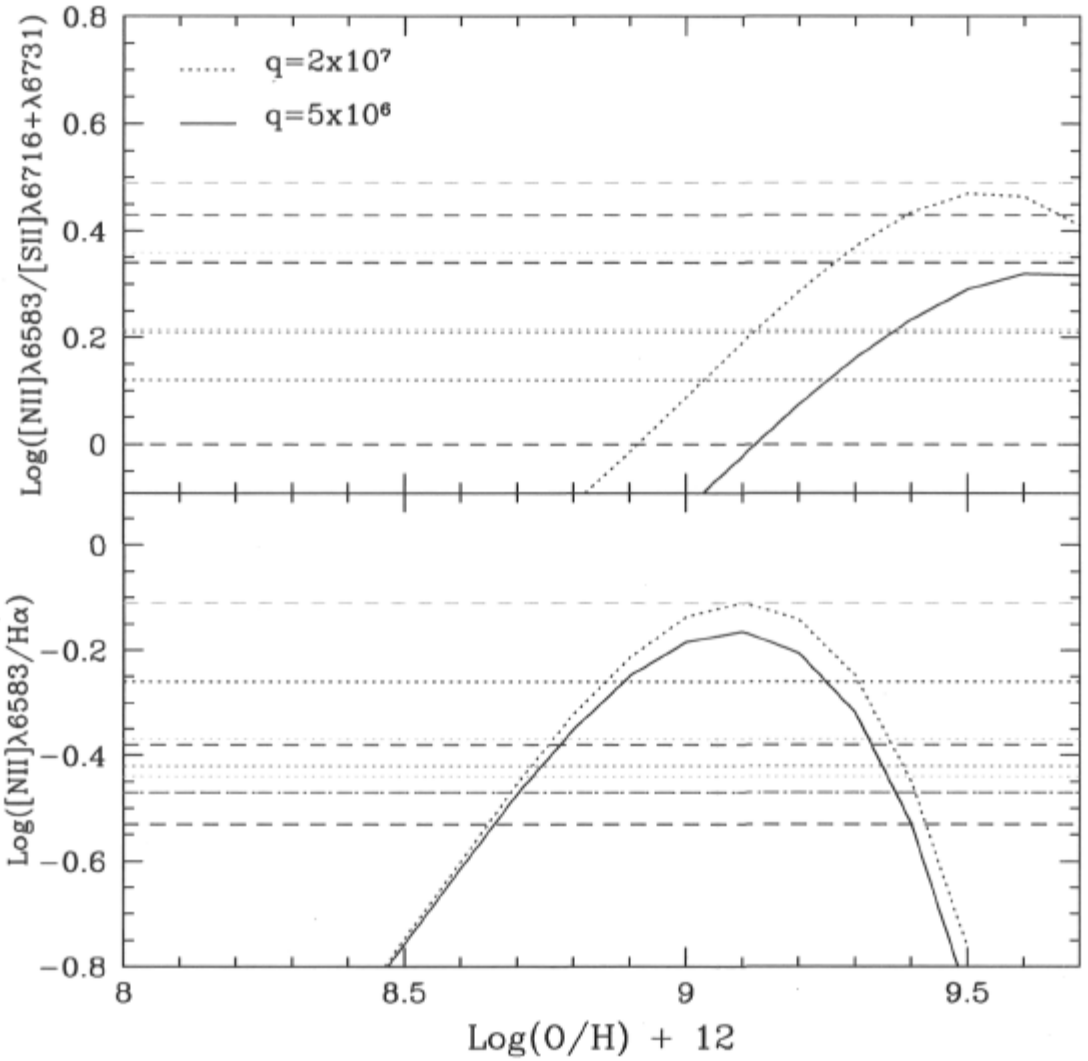

Figure 4.10: **Abundance ratio - metallicity diagrams for NGC 3311 in Abell 1060.** *The curves from Kewley & Dopita (2002) are shown with the ratios from the regions as labeled in Figure 4.8. The curves in the top panel have been shifted by 0.2 dex in Log(O/H) +12 as explained in the text.*

Table 4.4: Derived Parameters for Regions of NGC 3311 in Abell 1060

Region	Log(O/H) + 12	Ages 10^6 yr	Mass $10^4 M_\odot$	SFR 10^{-3} $M_\odot$ yr^{-1}
1	8.9 or 9.3	6.9	4.7	1.29
2	9.4	6.5	3.6	3.06
3	9.3	6.5	2.9	2.51
4	9.3	5.2	2.2	3.34
5	9.4	4.9	1.6	3.36
6	9.4	6.8	9.3	3.94
7	9.4	5.4	2.4	2.86
8	9.3	6.7	< 0.1	1.10
11	8.9	11	35	1.18

Note: The errors in metallicity are from matching the two available diagnostics. They are large, typically 0.1dex. The errors in SFR due to the error in Hα equivalent width measurement are about 5%. The errors age and mass are more a function of matching to available model parameters, and are of order 5 and 15%, respectively.

galaxies, such as those in our survey, are expected to have metallicities at or above solar, even for the older underlying population. A high metallicity is correlated with the most intense Hα emission. There are 3 regions on the edge of the Hα emission: 1, 8, and 11. Region 11 shows much lower metallicity ($\simeq$ 8.9, recall Region 11 is at the continuum peak). Region 1 could also have a low metallicity or a metallicity similar to that of the central area while Region 8 has a high metallicity as in the center.

The age of the young stellar population is estimated using the evolutionary synthesis code Starburst99. The Hα equivalent width is calculated and matched to results from a run based on an instantaneous burst of star formation using a Salpeter IMF with $M_{up} = 100\,M_\odot$. I chose a model based on supersolar metallicities ($Z=2\,Z_\odot$) to best match the metallicities of the regions from Table 4.4, except in Region 11 where a solar metallicity is used. Note however that using solar metallicities rather than supersolar metallicities makes little difference to the age estimates, which in either case agree to within the 5% errors (for example, using a solar metallicity the age of Region 1 is 6.6 Myrs). The ages are listed in Table 4.4. The error on the age is derived from the uncertainty in the equivalent width measurement of the Hα emission line and translates to an error of roughly 5% in the age. The youngest ages, 4.9±0.2 to 5.4±0.3 Myr are found in the center of the Hα emission, Regions 4, 5, and 7. On the edges of Hα emission, Regions 1, 8, and 11, all show older ages of 6.7±0.3 - 11±0.6 Myr. This suggests the youngest stars are forming closest to the center. This is the location of the heart of the dust patch. Region 6, which is the brightest feature in the Hα image of Figure 4.2, but with an age of 6.8±0.3 Myr does not represent the youngest region.

The mass of the young stellar population can be estimated by comparing the theoret-

ical continuum luminosity from Starburst99 produced by a $1\,M_\odot$ burst to the observed background subtracted continuum luminosity. The factor required to scale the luminosities is then equal to the mass, in solar masses, of the young population. I use the continuum level around 6500 Å and Equation 4.2 to determine the luminosity. The continuum luminosity from the same wavelength of the model with the closest age is then divided out. Allowing for a generous error in age of ± 1 Myr, the typical errors in the mass are 15%. The mass of the young population determined in this way is given in Table 4.4. Region 11, the oldest region corresponding to the maximal flux, is the most massive. Otherwise, the highest masses are in Regions 1 and 6 where the continuum level is also high, as shown by Figure 4.2. These regions are on the edge of the dust patch seen by Laine et al. (2003). This underscores how the mass estimates are lower limits and may be obscured by the dust patch in most regions. The difference between the masses of Regions 6 and 3 (which have similar ages) suggests the masses may be underestimated by at least ~30% in the presence of dust.

4.3.5 Star Formation Rate

A lower limit on the SFR for each region has been calculated using Equation 4.1. Table 4.4 shows that the highest SFRs are in the central and high Hα emitting areas of Regions 4, 5, and 6. Excluding the error inherent to Equation 4.1, the dependance of the cosmology chosen, and the uncertainties due to dust, the errors in SFR are most sensitive to the error in Hα equivalent width measurement, about 5%.

In terms of deriving a total SFR for the Hα emitting region, we use the absorption corrected integrated spectrum from all of the Hα emitting pixels, which was shown in Figure 4.7, and for which there is a total Hα flux of $4.98\pm0.24 \times 10^{-15}$ erg s^{-1} cm^{-2}, or an $W_o(H\alpha) = -106$ Å, throughout the emitting region. This results in a total SFR of $1.37\pm0.07 \times 10^{-2}\,M_\odot\,yr^{-1}$. The SFR density is $1.17\pm0.06 \times 10^{-7}\,M_\odot\,yr^{-1}\,pc^{-2}$. As the SFR derived is possibly a lower limit as the dust patch suggests, and a global measure of the dust absorption in the galaxy has already been accounted for, it is reasonable to assume that the effects of the dust are more important in the dust patch, if a significant amount of the ionizing population is being obscured by the dust. A reasonable estimate on an upper limit to the SFR would be to suppose that all of the obscured emission has the same intensity as in Regioin 6 which is not behind the dust patch. Therefore, there should be no more than $1.64\pm0.08 \times 10^{-2}\,M_\odot\,yr^{-1}$ in total, or, $1.39\pm0.07 \times 10^{-7}\,M_\odot\,yr^{-1}\,pc^{-2}$.

This small amount of star formation found is less than the amount of star formation attributed to star formation rates derived for cooling flow cluster BCGs. For example, Hicks & Mushotzky (2005) found rates of 0.2-219 $M_\odot\,yr^{-1}$ derived from UV excess for cooling flow BCGs, and Edwards et al. (2007) found typical SFRs of 0.3 - 1.6 $M_\odot\,yr^{-1}$ for emitting BCGs. The original MDR of $6\,M_\odot\,yr^{-1}$ found for Abell 1060 would be between 0.06 and 0.6 (1 - 2 orders of magnitude below the *ROSAT* value). However, the *Chandra*

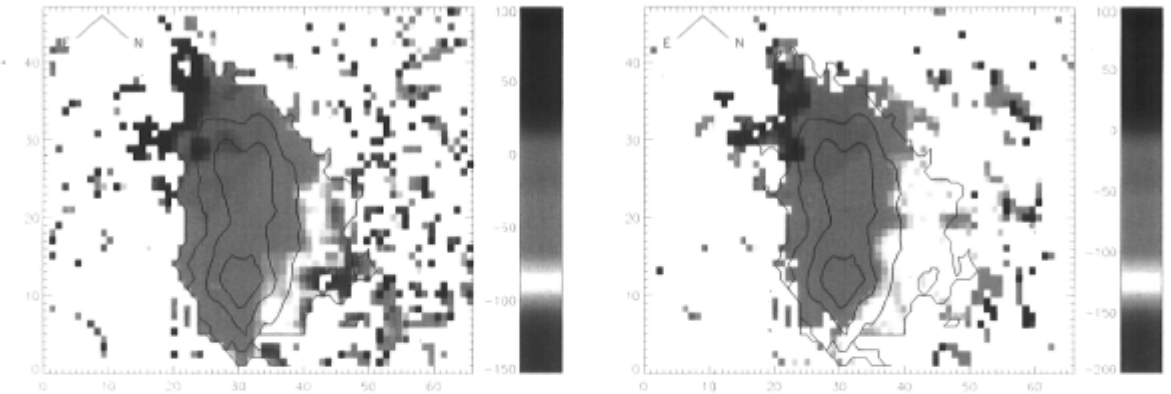

Figure 4.11: **Relative velocities for NGC 3311 in Abell 1060.** *Left Panel: Map of the Hα relative velocity for NGC 3311 in Abell 1060. Right Panel: Map of the [N II] λ6584 relative velocity for NGC 3311 in Abell 1060. The Hα emission is overlain as contours and the scale is in units of km s^{-1}. One pixel is ∼26 pc across, for all panels.*

observations (Yamasaki et al. 2002) show no evidence for any central temperature drop, and so no cooling flow is present in this system. Thus, the fact that we have measured only a very small amount of star formation activity is consistent with this picture.

4.3.6 Kinematics

Figure 4.11 shows maps of the relative velocity for the Hα and [N II] λ 6584 emitting gas. The relative velocity is determined by taking the difference between the rest frame wavelength and the centroid of the line (deredshifted to the known galaxy redshift, fit to a gaussian using *splot*, and deblended from surrounding lines). The maps show shear in both lines. The appearance is more smooth in Hα, which shows velocities of about ±100 km s^{-1}. The [N II] λ 6584 emitting gas shows a very similar field with velocities from around −150 km s^{-1} to ∼50 km s^{-1}. The FWHM of the Hα line measured from the same *splot* fit and is shown in Figures 4.12. The values presented are not corrected for the instrumental profile, and are thus not velocity dispersions. The emission lines have widths from ∼130 km s^{-1} to ∼200 km s^{-1} and a clumpy distribution. The spectral resolution is ∼150 km s^{-1} (see Section 4.2), the difference in values (∼50 km s^{-1}) within the image is close to the noise level (∼25 km s^{-1}), and no global structure is immediately present. The results are similar for the distribution of widths in the case of the [N II] λ 6584 line (not shown), and so I make no conclusion on the structure in the line widths based on this data. However, the smooth relative velocity distribution, along with the low velocity values, are an indication of rotation, rather than an indication of any outflow.

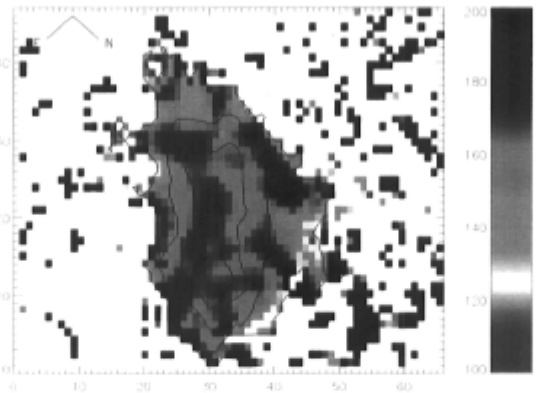

Figure 4.12: **Hα FWHM image of NGC 3311 in Abell 1060.** *The Hα emission is overlain as contours and the scale is in units of km s^{-1}. One pixel is ∼26 pc across.*

4.4 Abell 1204

Abell 1204 is the most distant cluster in our sample, having a redshift z = 0.1706, such that 1″ corresponds to ∼2.7 kpc. Figure 4.13 shows the BCG and the surrounding galaxies at the center of this rich, BM II-III cluster. The X-ray luminosity in the 0.1 - 2.4 keV band, is 6.77×10^{44} ergs s^{-1} (Allen et al. 1992), and cooling flow models based on this data calculated a mass deposition rate of 675 $M_\odot$ yr^{-1} (White 2000). This is large enough so that the cluster retains its cooling flow status even after taking into account general results from newer X-ray observations. In fact, the *Chandra* observations of Bauer et al. (2005) do confirm a small central temperature drop for this cluster, as well as a short cooling time (2.1 Gyr) with the BCG roughly 20 kpc East of the X-ray center. Just noticeable on Figure 4.13 is some emission which appears to connect the BCG and a chain of 4 other galaxies in the Northeast direction.

The IFU field of view is 13.5 × 18.9 kpc, and each pixel covers a distance of ∼270 pc on either side. This area catches most of the core luminosity of the BCG as well as part of another cluster galaxy to the West of the BCG. This BCG is a cD galaxy, but much of the cD halo is excluded from the IFU region.

4.4.1 Line Images and Region Spectra

Figure 4.14 shows the images of the continuum (between rest frame wavelengths of 6780 and 6980 Å), the continuum-subtracted Hα, [N II] λ 6584 emission, and [S II] λ 6716 line emission maps. The continuum and Hα images look similar in that the peak of the line emission is cospatial with the peak in the continuum emission. However, there are two prominent differences in these images. The first is the existence of a plume of bright Hα emission which extends from the central peak to the north, and then towards the East out to the edge of the image. This feature is not evident in the continuum image. The

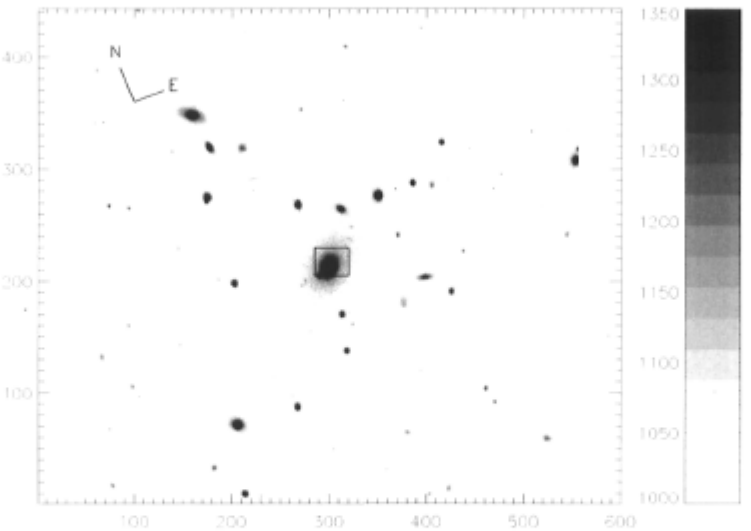

Figure 4.13: **The center of Abell 1204 taken in the i-filter.** *The IFU field is marked as a box with 5 × 7″ (13.5 × 18.9 kpc) centered around the BCG. There are several small galaxies near to the BCG, which could be nearby neighbours. A trail of light exists in the direction from the BCG to the small galaxies in the NE. The scale is in arbitrary flux units.*

second is the presence of a smaller galaxy in the western corner of the continuum image which has no counter part in the Hα emission line image. This is true for the other line emission images of the Figure 4.14 - the images of [N II] λ 6584 and [S II] λ 6716 show no evidence for the small galaxy to the West, but do show extended emission in the North and East directions. However, for [S II] λ 6716 the plume which extends North is not at as high a relative intensity with respect to the emission that extends East. There is a difference in throughput between the fibers that make up the left and right halves of the IFU image. This is noticed in the continuum and S/N images which show a slightly higher brightness level on the left half of the image, the error implied by this is less than 10%.

Within each of twelve regions, similar spectra are co-added, increasing the S/N. These are labeled on the Hα panel of Figure 4.14. This is an especially important step for Abell 1204 since Figure 4.15 shows the low continuum S/N values of the pixels on the edges of the image. All of the regions examined are in areas where the S/N > 5.

The 12 regions chosen include several areas within the intense Hα emission of the core. Using Figure 4.16, which presents the [N II] λ 6584/Hα ratio, sections where both the Hα emission is stronger than the [N II] emission (Regions 3 and 4), and vice versa (Region 5) are selected. There is a region of intense emission to the North-West of Regions 3 and 4, but it is not included in the analysis as the integrated spectrum is very similar to that of Region 3, with slightly lower flux values. Also, areas within the

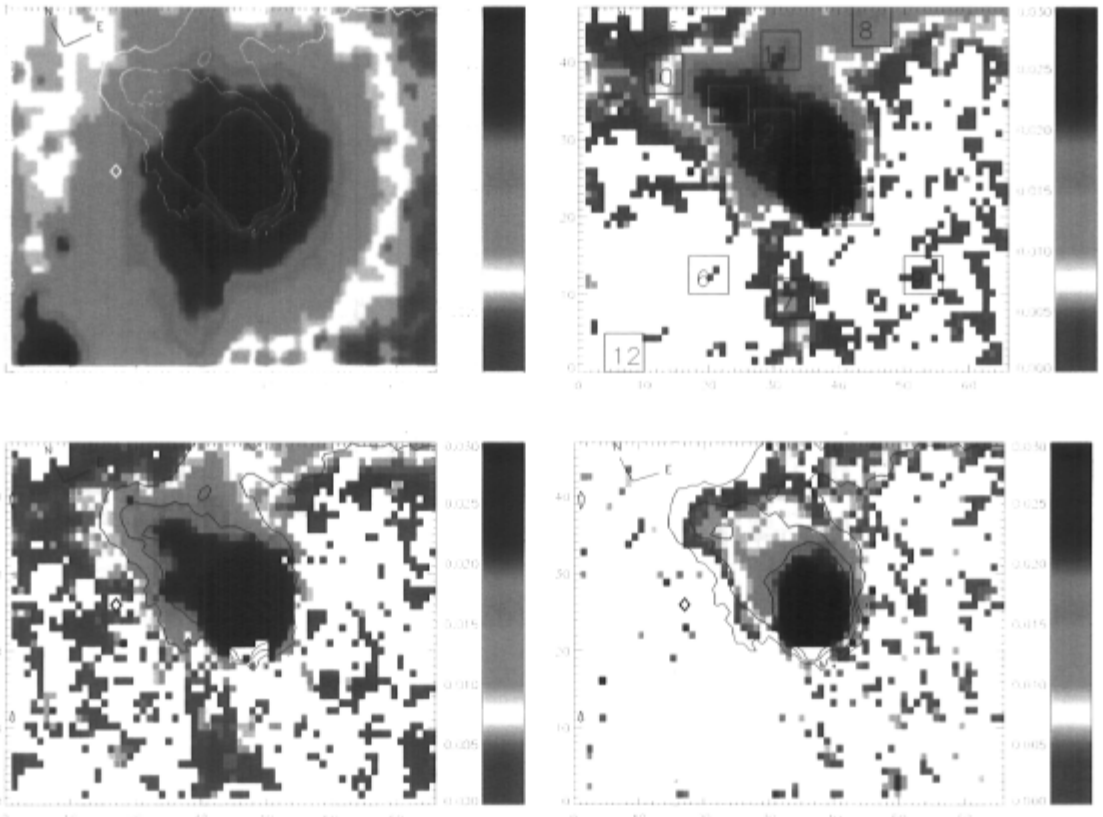

Figure 4.14: **Reconstructed images for the BCG in Abell 1204.** *Top Left Panel: The continuum surrounding the Hα emission. The BCG as well as part of a smaller, non-Hα emitting galaxy to the West is also captured. Top Right Panel: The continuum-subtracted Hα emission line flux. The regions used in the subsequent analysis are represented as boxes. Bottom Left Panel: The continuum-subtracted [N II] λ 6584 emission. Bottom RightPanel: The continuum-subtracted [S II] λ 6716 emission. The contours of Hα emission are overlain. Emission line maps are reverse colour scale and in units of* $10^{-15}\,erg\,s^{-1}\,cm^{-2}\,\AA^{-1}$. *One pixel is ∼270 pc across for all panels.*

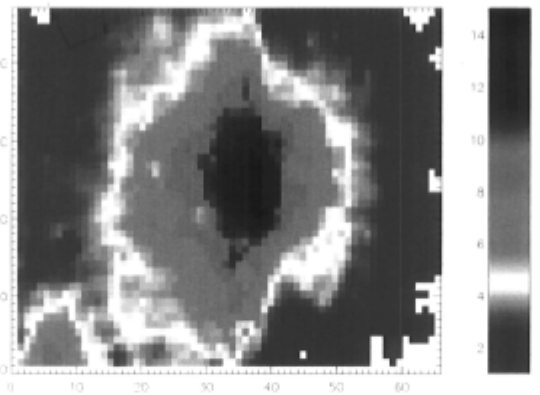

Figure 4.15: **S/N ratio of the continuum for the BCG in Abell 1204.** *One pixel is ∼270 pc across.*

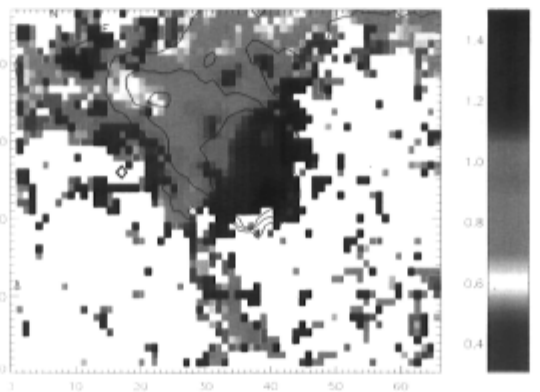

Figure 4.16: **A reverse scale image of the [N II] λ 6584 to Hα ratio in the BCG of Abell 1204.** *The Hα emission is overlain as contours. One pixel is ∼270 pc across.*

northern and eastern emission plumes are chosen, including those with strong emission (Regions 1 and 2) and weak emission (Regions 8 and 11). Region 12 covers the non-Hα emitting galaxy to the West of the BCG. Finally, diffuse emission (Regions 7 and 10), and two regions free of Hα emission (Regions 6 and 9) are included. The regions have been selected such that the velocity distribution is well sampled (for example, compare Regions 2, 4, and 5 with Figure 4.23, the map of the relative velocity in the Hα lines).

All of the regions cover ∼1.71 kpc on either side. The integrated spectra of these regions are presented in Figure 4.17, and are as previously labeled. The area around ∼6280 Å is affected by a chip gap, and unfortunately this limits the use of the [O I] λ 6300 emission line. Nevertheless, it is obvious that this line is apparent in the spectra. Other strong emission lines in this spectral region are [O I] λ 6364, Hα, [N II] λλ 6548,6584, and [S II] λλ 6716,6731. The bright emission lines in Regions 4 and 5, closest to the most intense emission, show lines which are much more broad than those of Regions 1,

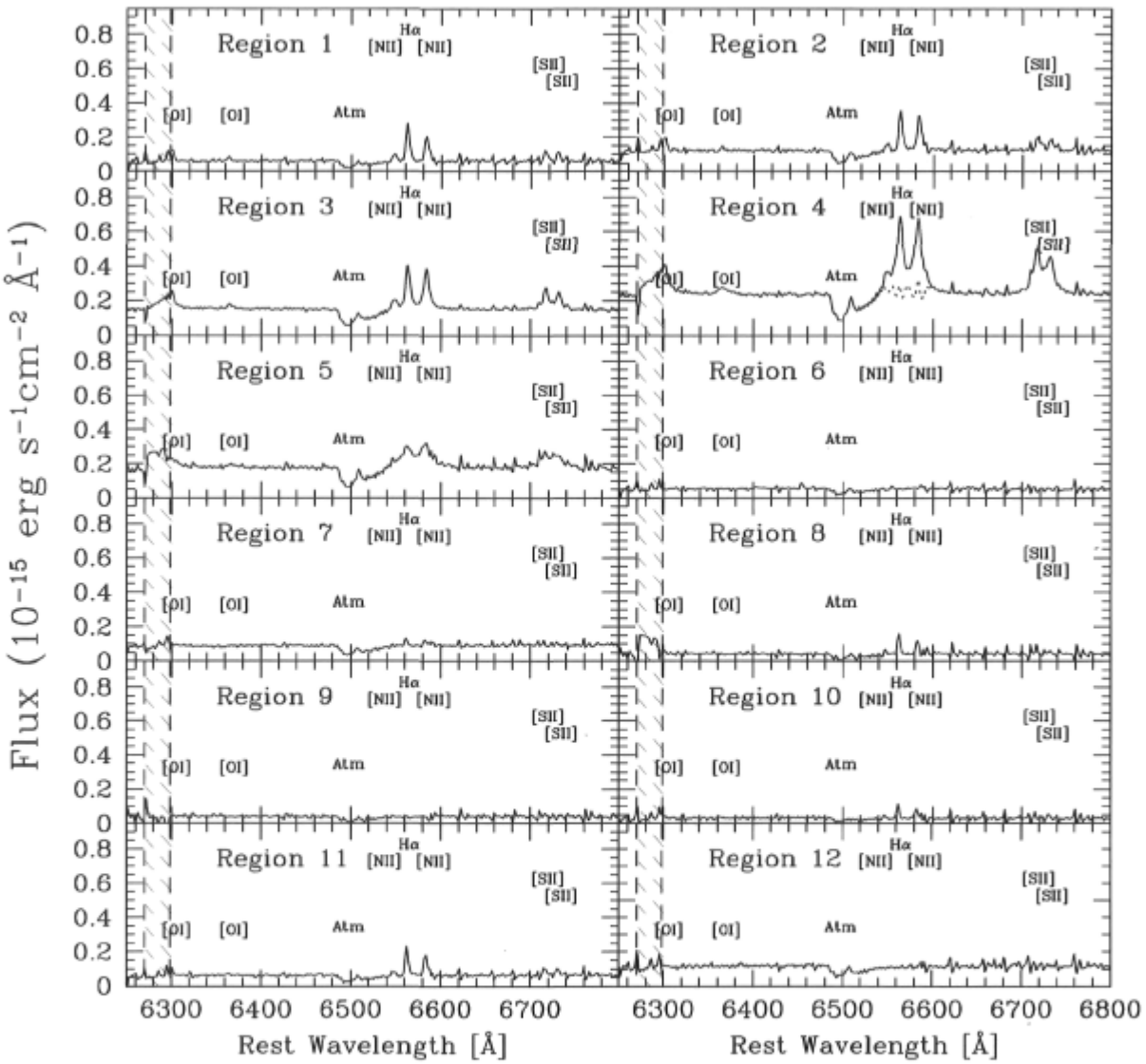

Figure 4.17: **Summed spectra of the 12 selected regions in the Hα image of the BCG in Abell 1204.** *Prominent emission features are labeled. The chip gap is shown hashed out near 6300 Å. The dotted line on Region 4 is the original spectrum with the gaussian fit subtracted.*

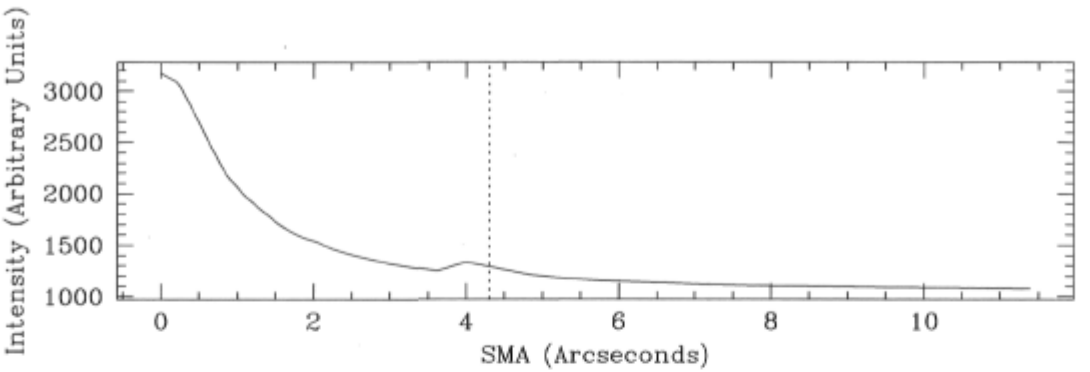

Figure 4.18: **Luminosity profile for the BCG in Abell 1204.** *Measured from the i-band acquisition image. The vertical dotted line marks the maximum extent of the IFU field of view. The x-axis displays the Semi-Major Axis as calculated using the IRAF task, ellipse. The other small galaxy caught in the IFU image can be discriminated as the bump ~4″ from the center.*

2 and 3. These broader lines are necessarily more difficult to fit with the *splot* deblend task, but with a careful selection of the continuum region (away from the atmospheric feature) a satisfactory fit can be achieved. This is shown for the Hα-[N II] line complex in Region 4. Atop the original spectra, the gaussian fit-subtracted spectrum is overplotted as a dotted line. Clearly, all three lines are removed.

4.4.2 The Underlying Stellar Population

As Abell 1204 is at quite a far distance, a substantial amount of the light from the BCG fits into the IFU field of view, and the characteristic $r^{1/4}$ profile is observable. This is shown in Figure 4.18, which displays the luminosity profile of the BCG measured from the i-band acquisition image using IRAF's *ellipse* task. Therefore, when constructing an integrated spectrum for the underlying galaxy, a scale factor must be found to account for the varying luminosity profile. Unfortunately, the S/N of the continuum does not allow for a measurement of the Hα absorption line, nor is the NaD line caught in the band width for this galaxy. Thus to obtain an accurate scale factor, an average of the continuum at each column outside of the Hα emitting area is constructed. Specifically, this includes the average of rows 15 - 35 for columns 50 - 67 in the IFU image. Figure 4.19 shows a radial cut in y across the center of the continuum image, assumed to be from the old population as the Hα emitting regions have been excluded. It shows significant variation with radius. The luminosity profile from the i-band acquisition image for the area within the IFU field of view is used in order to characterize the shape of the underlying continuum in the inner (Hα emitting) pixels. As the luminos-

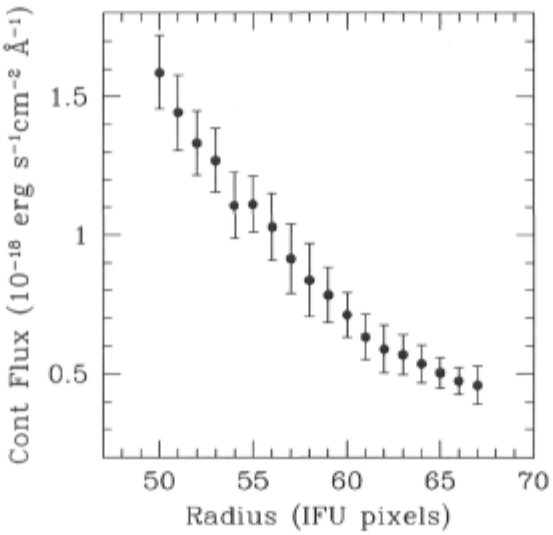

Figure 4.19: **Radial cut in the continuum for the BCG in Abell 1204.** *The outer portion of the continuum flux, unaffected by the Hα emission (i.e. between columns 50 - 67, see text) is shown.*

ity profile is from the very wide i-band image, the dominant older population should be determining the profile. Notice that the radial cut of the continuum image can be approximated by two linear functions. One for the inner regions (pixels $50 < 61$ pixels) and one with a more shallow slope for the outer regions. I assume a spherical symmetry for the radial cut of the continuum image. The scale factors obtained from these slopes are then subtracted from the region spectra to account for the underlying population. The integrated background spectrum, scaled to the mean of the outer regions is shown in Figure 4.20. There is no Hα absorption that can be measured in this image. There are two likely reasons for the lack of observation of any absorption. First, it could be that there is diffuse low level Hα emission at just the right level to fill in the absorption. Also possible is that the absorption level is too low to be distinguished from the continuum level at this S/N level as the spectrum is made from a composite of pixels at rather low S/N (see Figure 4.15).

This cluster's BCG has already been observed with longslit spectroscopy, and several integrated line strength measurements can be found in Crawford et al. (1999). In comparing the spectra from this work to theirs, it is important to keep in mind that their values are based on lower spectral and spatial resolution (10 Å/pix and an integrated spectrum from a $6''$ long slit). Crawford et al. (1999) also note that for Abell 1204, their spectrum is noisy.

The bandwidth for these observations does not include the strong absorption line of NaD that can be used to characterize the underlying stellar population, so no estimate

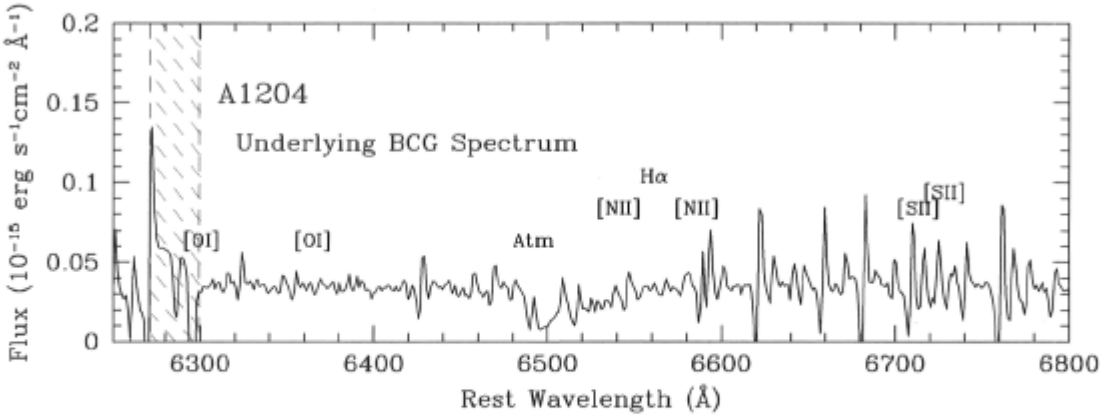

Figure 4.20: **Underlying spectrum for the BCG in Abell 1204.** *A median combined spectrum of the non-Hα emitting spectra excluding contribution from the smaller galaxy South-West of the BCG is shown. It is scaled to the mean outer continuum level (see discussion in text). The red side of the spectrum is plagued by a region where sky lines are ill-subtracted and increases the noise level redward of [N II] λ 6584. A strong atmospheric absorption feature near 6500 Å is present.*

of the age for the underlying population is made.

4.4.3 Line Measurements and the Ionization Mechanism

After being scaled to the proper radius, the spectrum of the underlying stellar population is subtracted from each region. The resulting central position, line flux, W_o, and FWHM are shown in Table 4.5 for [O I] λ 6364, Hα, [N II] λ 6548,6584, and [S II] λλ 6716,6731. For Regions 2 and 11, the underlying galaxy produces nearly all the continuum flux, and after it is subtracted, the continuum value is too close to zero to be able to measure an accurate W_o, thus these values do not appear on the table. Regions 6, 9, and 12 have no emission lines and are omitted from the table. In Regions 5, 7, 8, and 10 the emission line fluxes are lower, and those of [O I] λ 6364 and [S II] λλ 6716,6731 are too close to the noise level to be measured accurately, likewise, they are excluded. Except the [S II] λλ 6716,6731 measurements are included for Region 5. However, their broader nature increases the effect of the high noise level in this portion of the spectrum, and the lines are surely contaminated.

The IFU measurements will be used to distinguish different ionization zones, those by hot stars or a harder ionization source. When searching for constraints in the BPT diagram, Hβ and [O III] λ 5007 are required but cannot be measured from the data. Integrated along their slit, Crawford et al. (1999) measured a ratio of Log([O III] λ 5007/Hβ) > 0 and Log([N II] λ 6584/Hα) = 0.14. This ratio will not

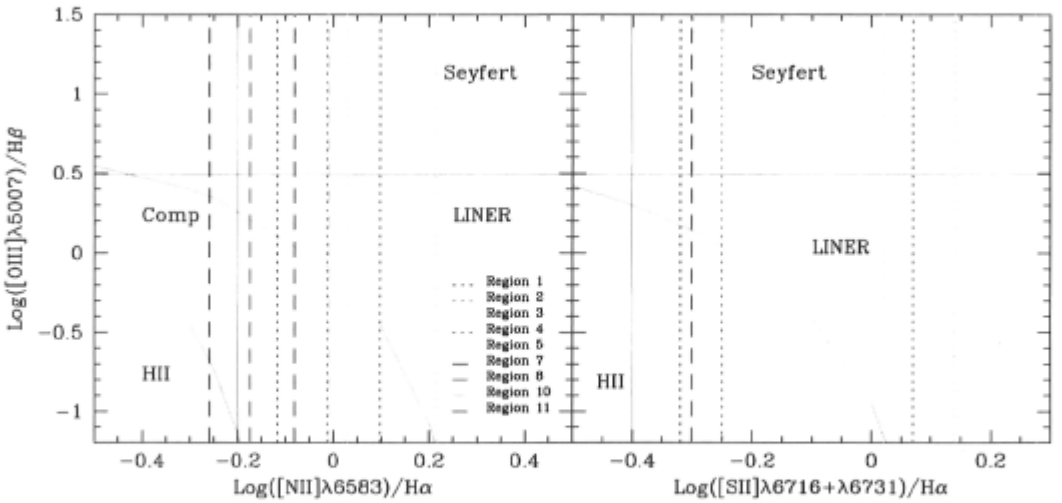

Figure 4.21: **Ionizing source diagnostics for the BCG in Abell 1204.** *On the left, the BPT diagram is shown with the [N II] λ 6584/Hα and the ([S II] λ 6716 + λ 6731/Hα) ratios of the regions is on the right. The line fits are from Kewley et al. (2001a, shown in both panels) and Kauffmann et al. (2003, in left panel only). The solid lines illustrate the convential definitions of LINER and Seyfert (Osterbrock & Ferland 2006). Certain regions are left off of the plot as no [S II] lines are measured for Regions 7, 8, or 10, and no emission lines are seen in Regions 6, 9, and 12. Most regions are reasonably constrained to the composite area, except Regions 3, 4, and 5 which are close to the AGN area.*

be uniform throughout the central regions of the BCG. Nevertheless, their integrated value for [N II] λ 6584/Hα is between those of our regions. It is therefore useful to keep in mind their result of Log([O III] λ 5007/Hβ) > 0 as an average value. Figure 4.21 suggests that most regions are likely composite, while Regions 3, 4, and 5 are closest to the AGN section of the BPT diagram. Surrounding this, in Regions 1, 2, 7, 8, 10, and 11 where emission lines have been observed, the line ratios of Figure 4.21 classify the regions as being a composite of H II and LINER signatures, with excitation by H II regions playing a significant role. The possibility of Seyfert objects, as opposed to LINERs, cannot be ruled out since the Log([O III] λ 5007/Hβ) assumed is a lower limit. The diagnostic for Region 2, which is physically in between the central and bright surrounding emission shows composite ratios; higher than those of the surrounding emission, but lower than those at the center. Regions 6, 9, and 12 are left off the plots as no emission lines are observed in those areas.

Table 4.5: Spectral Line Values for Regions of the BCG in Abell 1204

Measurement	Region 1	Region 2	Region 3	Region 4	Region 5	Region 7	Region 8	Region 10	Region 11
[O I] λ 6364									
Center (Å)	6363.4	6364.2	6364.8	6365.9	-	-	-	-	6363.8
Flux	0.09	0.12	0.14	0.50	-	-	-	-	0.05
W_o (Å)	−6.7	-	−164.9	−9.5	-	-	-	-	-
FWHM (Å)	3.5	3.6	5.1	13.0	-	-	-	-	3.4
[N II] λ 6548									
Center (Å)	6548.2	6548.7	6548.9	6549.5	6549.8	6549.7	6547.2	6546.2	6547.9
Flux	0.19	0.18	0.26	1.17	0.40	0.09	0.08	0.07	0.14
W_o (Å)	−15.3	-	−26.1	−18.1	−11.5	−4.2	−11.0	−14.0	-
FWHM (Å)	4.7	4.6	5.4	9.1	10.1	10.1	2.3	3.1	4.7
Hα									
Center (Å)	6562.6	6563.3	6563.3	6563.1	6562.5	6561.6	6562.3	6561.4	6562.6
Flux	1.06	1.22	1.48	4.13	1.30	0.16	0.48	0.30	0.74
W_o (Å)	−85.7	-	−139.3	−62.5	−35.1	−6.7	−67.1	−61.3	-
FWHM (Å)	4.7	5.0	5.8	9.6	10.9	3.2	3.7	3.3	4.1
[N II] λ 6584									
Center (Å)	6583.7	6584.5	6583.9	6583.2	6582.4	6582.3	6583.1	6582.3	6583.5
Flux	0.81	1.18	1.58	5.17	2.14	0.09	0.32	0.29	0.61
W_o (Å)	−65.3	-	−136.0	−76.7	−53.7	−2.9	−44.0	−57.4	-
FWHM (Å)	5.7	6.0	7.5	13.6	17.7	2.9	3.7	6.0	5.1
[S II] λ 6716									
Center (Å)	6716.3	6717.4	6717.1	6716.3	6713.5	-	-	-	6716.2
Flux	0.30	0.42	0.88	2.74	0.67	-	-	-	0.21
W_o (Å)	−19.8	-	−140.5	−41.9	−16.2	-	-	-	-
FWHM (Å)	4.8	6.4	7.7	11.4	10.4	-	-	-	4.3
[S II] λ 6731									
Center (Å)	6730.5	6731.5	6731.4	6730.9	6727.9	-	-	-	6730.8
Flux	0.21	0.26	0.67	2.15	1.13	-	-	-	0.17
W_o (Å)	−13.3	-	−115.7	−32.5	−27.4	-	-	-	-
FWHM (Å)	3.5	4.6	7.7	10.7	16.5	-	-	-	4.0

Note: The central positions are given in terms of the rest wavelength. The flux is in units of 10^{-15} erg s^{-1} cm^{-2}. Regions 6, 9, and 12 are not listed as they have no lines above the noise level. As discussed in the text, fits for several lines were not possible, and they are marked here with a dash. Errors in the flux measurements for the strong lines are of order 5-10%, as discussed in the text. Errors for determining the central wavelength are of order ∼2 Å. The weak lines of [S II] have large errors of 20-30%.

Table 4.6: Derived Parameters for Regions of the BCG in Abell 1204

Region	Log(O/H) + 12	Ages 10^6 yr	Mass $10^6 M_\odot$	n_e cm^{-3}	SFR $M_\odot\,yr^{-1}$
1	9.1	6.7	21	> 40	0.56
7	8.9 or 9.3	9.9	75	1000	0.09
8	9.0 - 9.2	6.7	12	200	0.26
11	9.1	-	-	200	-

Note: The errors in metallicity are from matching the two available diagnostics. They are large, typically 0.1 dex. For Regions 7 and 8 only one diagnostic is available. The errors age and mass are more a function of matching to available model parameters, and are of order 5 and 15%, respectively.

4.4.4 Metallicity, Age, Mass, and Electron Density for the Young Population

Figure 4.22 shows the abundance ratios as a function of metallicity for regions with emission that is not dominated by AGN signatures (Regions 1, 2, 7, 8, 10 and 11). The metallicities are derived in the same way as for NGC 3311 of Abell 1060 and are listed in Table 4.6. Regions 2 and 10, with high [N II] λ 6584/Hα ratios, do not fit to the diagnostic curves. This may be because the AGN contamination is too great, and they are left of the table. Metallicities North and East of the central peak (Regions 1, 8, and 11) are supersolar, with most regions having Log(O/H) $\simeq$ 9.1. Region 7 to the South could have a different metallicity, although the availability of only one diagnostic limits the constraints that can be made here.

The ages of the young stellar populations are again found using Starburst99 and the model with a metallicity of $2\,Z_\odot$. The regions North and East of the center show the youngest ages (see Table 4.6), while Region 7 to the South is the oldest with an age of 9.9 ± 0.5 Myr. Using solar metallicities increases the age by $\sim$20%. Region 11 has no significant level of continuum emission once the background galaxy has been subtracted, which precludes a measurement of the equivalent width. The fact that some emission lines are seen suggest there is a small population that exists, and the real continuum level is hidden in the noise.

Table 4.6 shows the mass of the young population, calculated using the same method as for NGC 3311 of Abell 1060. Region 7, to the South, is the most massive ($75\pm11 \times 10^6 M_\odot$), may have a different metallicity, but as the oldest would have formed the bulk of its ionizing stars already, which are all contributing to the ionization of the molecular gas. Regions 1 and 8 to the North and East, respectively, are smaller in mass, but have higher star formation rates typical for starburst regions (see following section).

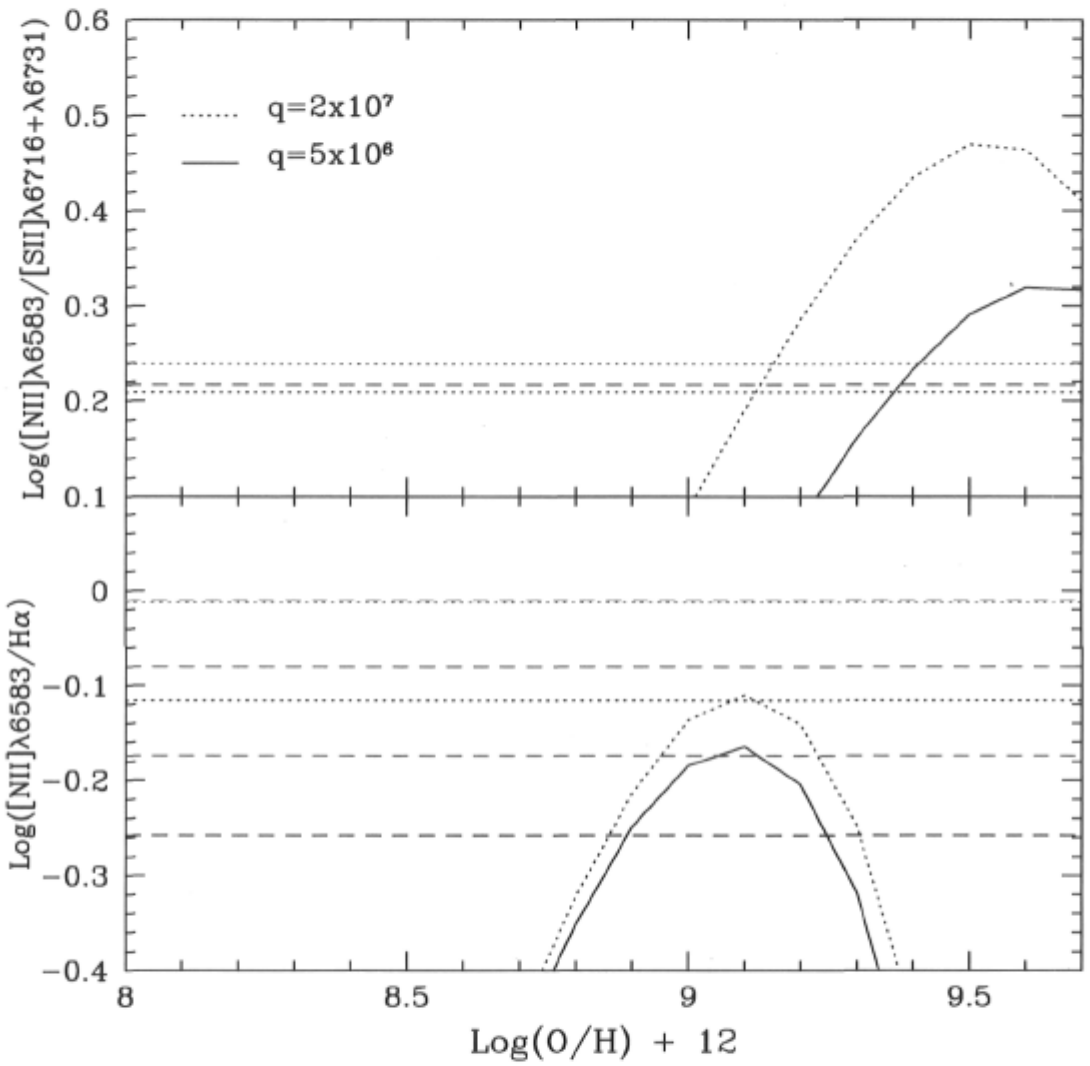

Figure 4.22: **Abundance ratio - metallicity diagrams for the BCG in Abell 1204.** *Curves from Kewley & Dopita (2002) are shown with the ratios from the regions as labeled in Figure 4.21. The curves in the top panel have been shifted by 0.2 dex in Log(O/H) + 12 as explained in the text.*

As [S II] $\lambda\lambda$ 6716, 6731 are lines which are emitted with nearly the same excitation level, their intensity difference reflects mainly collisional deexcitation processes, and hence is a good measure of n_e, the electron density (Osterbrock & Ferland 2006). Figure 5.8 of Osterbrock & Ferland (2006) shows the calculated variation of the intensity ratio as a function of n_e for a temperature of 10^4 K. The function varies quickly for ratios below 1.4, however for ratios which describe this data (all regions with measured [S II] lines show ratios above 1.6) the function is fairly flat and the method is less accurate. The modest electron densities found in the best case composite/H II regions of Regions 1, 7, 8, and 11, are between 100 and 1000 cm^{-3} as listed in Table 4.6. These values are typical for H II regions, Seyfert 2 and narrow-line radio galaxies. Hatch et al. (2007) also used this method finding similar electron densities in their sample of emitting BCGs.

4.4.5 Star Formation Rate

It is not possible to calculate a SFR for Regions 3, 4, and 5 for example, as they are clearly dominated by AGN signatures. It is also possible that the SFR calculated in the other regions are affected by the AGN, so in this way the rates presented in Table 4.6, should be interpreted as upper limits, contaminated by AGN ionization. A total SFR is derived from the combined spectrum of the brightest 255 Hα emitting pixels and yields a flux value of 13.9×10^{-15} erg $\mathrm{s}^{-1}\,\mathrm{cm}^{-2}$. This yields a SFR of 7.0 $\mathrm{M}_\odot\,\mathrm{yr}^{-1}$, or a SFR density of $2.3 \times 10^{-8}\,\mathrm{M}_\odot\,\mathrm{yr}^{-1}\,\mathrm{pc}^{-2}$. This rate is an upper limit, since some of the Hα emission is from the AGN, however, it is not inconsistent with the old MDR of 675 $\mathrm{M}_\odot\,\mathrm{yr}^{-1}$ found by *ASCA* (White 2000), as not all the molecular gas will convert to stars, and as the current estimates of MDRs are an order of magnitude *below* the previously derived rates.

4.4.6 Kinematics

The left panel of Figure 4.23 shows a map of the relative velocity for the Hα emitting gas for the BCG in Abell 1204. The map shows regions of slight blueshifting, as well as redshifting. The physical scale goes from $-100\,\mathrm{km\,s}^{-1}$ to $+150\,\mathrm{km\,s}^{-1}$, with the most negative values echoing the structure of the Hα emission. There is no obvious ordered motion such as the rotation seen seen in NGC 3311 of Abell 1060. There is however some structure in the relative velocity map at the North side of the central emission, is clearly blueshifted with respect to the rest of the emission.

The emission lines become more broad in Regions 4 and 5. The velocity differences are not as high as those seen in typical outflows, but these two regions are amongst the highest [N II] λ 6584/Hα ratios and the emission lines are certainly ionized by the AGN. The line widths are consistent with Regions 4 and 5 being closer to the broad line region of the AGN than Regions 2 and 10. This is demonstrated in the right panel of

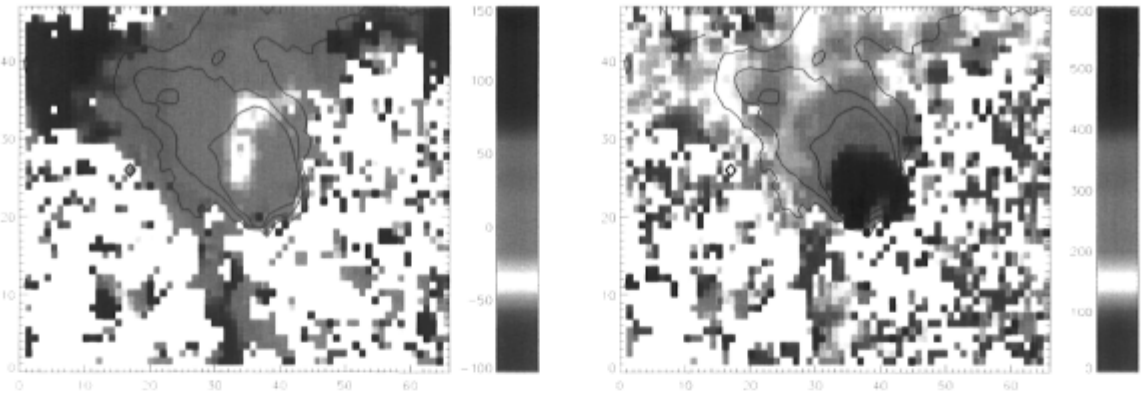

Figure 4.23: **Maps of the kinematics for the BCG in Abell 1204.** *Left Panel: Map of the Hα relative velocity Right Panel: Map of the Hα FWHM. The Hα emission is overlain as contours and the scale is in units of km s^{-1}. One pixel is ∼270 pc across.*

Figure 4.23 which shows a map of the FWMH (uncorrected for the instrumental profile, and so not the actual velocity dispersion). The most broad lines are found at the center of the BCG and on the image this refers to pixels at $31 < x < 39$ and $19 < y < 28$. Here, there is an area where the broad lines are co-spatial with the most extreme negative relative velocities. The morphology and kinematics can be explained if the AGN is located in this area, enshrouded by the broadest lines and influencing most extreme velocities. The values of the highest FWHM in this image are $< 600\,\mathrm{km\,s^{-1}}$, which is on the boarder side of typical values for the Narrow Line Region ($\lesssim 500\,\mathrm{km\,s^{-1}}$). Typical values for the Broad Line Region however, are 1 - 25 $\times$ $10^3\,\mathrm{km\,s^{-1}}$ (Peterson 2006). Nonetheless, the broader values represent gas which is physically closer to the central engine.

4.5 IC 4130 in Abell 1668

Figure 4.24 presents the r-band image of Abell 1668, a rich cluster of galaxies, of BM type II, with a velocity dispersion of $\sim$475 km s^{-1}. This cluster, located at a distance of $\sim$256 Mpc, such that $1''$ corresponds to $\sim$1.2 kpc, has an X-ray luminosity of $1.61 \times 10^{44}\,\mathrm{erg\,s^{-1}}$ in the 0.1 - 2.4 keV band, which is centered only $\sim$30 kpc SE of IC 4130, the BCG. Previous long slit spectroscopy on the BCG by Crawford et al. (1999) has revealed an Hα luminosity of $1.2 \times 10^{41}\,\mathrm{erg\,s^{-1}}$. This cluster is included in the NFPS sample as well, and Hβ emission has been observed. No CO emission was detected when Salomé & Combes (2003) observed this non-cooling flow cluster galaxy, and they quote an upper limit for the mass of $H_2 = 1.5 \times 10^9\,M_\odot$.

The $5 \times 7''$ field of view of the IFU covers 5.9×8.2 kpc, and each pixel covers a

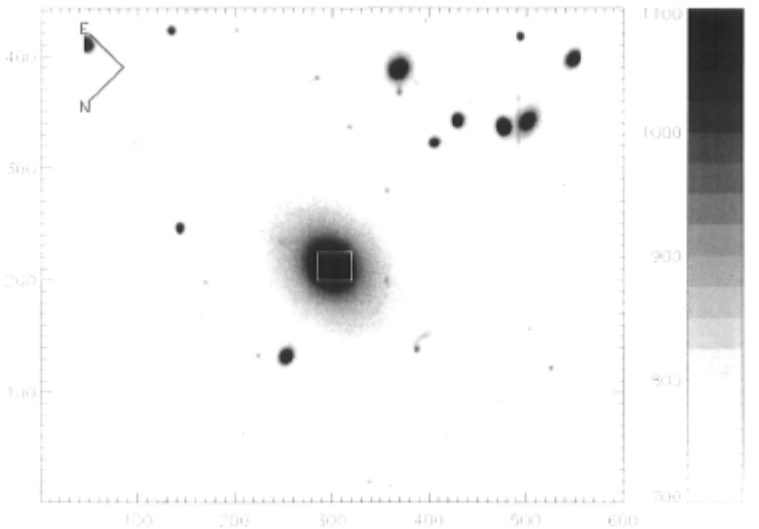

Figure 4.24: **The center of IC 4130 in Abell 1668 taken in the r-filter.** *The IFU field is marked as a box with dimensions of 5 × 7″ (5.9 × 8.2 kpc) centered around IC 4130, the BCG. The scale is in arbitrary flux units.*

distance of ∼120 pc on either side. This area is within the core luminosity of the IC 4130.

4.5.1 Line Images and Region Spectra

The image of the continuum between 6315 and 6440 Å for IC 4130 is shown in Figure 4.25. Also in the figure are panels displaying the continuum-subtracted Hα flux image, the continuum-subtracted [N II] λ 6584 flux image, and the image of the S/N ratio. Several of the emission lines in the individual pixels are not well fit by single Gaussian functions. There are several reasons for this, the integration time for this galaxy is low, the galaxy itself is fairly distant, and the Hα luminosity is lower by a factor of 10 from that of the BCG in Abell 1204 (Crawford et al. 1999). Therefore, a cleaner line image, that is easier to interpret is constructed by simply added the flux within a certain window, instead of using *deblend* to model the emission lines as Gaussians as was done for the previous clusters. The flux is added in between 6554 and 6572 Å for Hα and between 6575 and 6593 Å for [N II] λ 6584. Unlike the smooth elliptical distribution of the continuum image, both the Hα and [N II] λ 6584 flux images show much more patchy and filamentary emission structure throughout. The bright regions on the [N II] λ 6584 image correspond to bright regions on the Hα image, and the two emission lines share the same overall structure. However, the peak emission is displaced in the images. The S/N of the continuum between 6000 and 6200 Å is also shown on Figure 4.25. The S/N level remains above 15 throughout much of the central

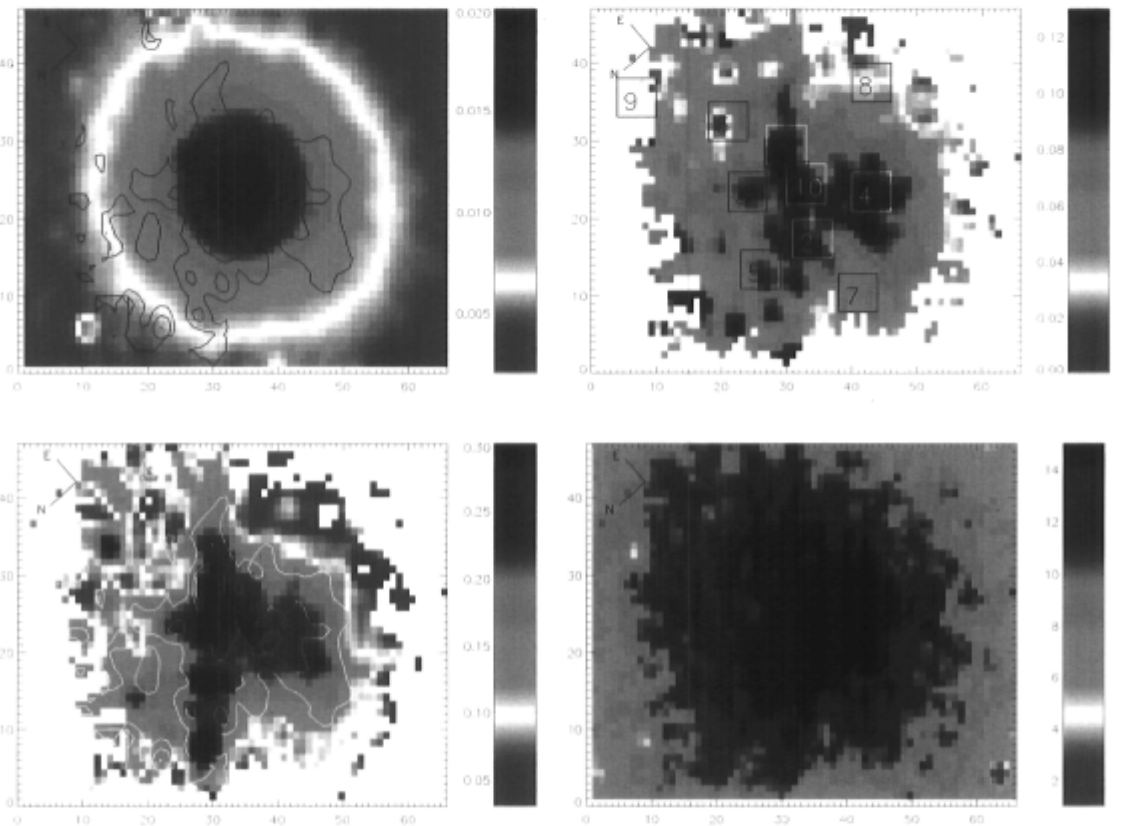

Figure 4.25: **Reconstructed images for IC 4130 in Abell 1668.** *Top Left Panel: The continuum surrounding the Hα emission line. Top Right Panel: The continuum-subtracted Hα emission flux. The regions used in the subsequent analysis are represented as boxes. Bottom Left Panel: The continuum-subtracted [N II] λ 6584 flux. Bottom Right Panel: The S/N ratio in the continuum. The contours are of the Hα emission. Image maps are in reverse colour scale and in units of* 10^{-15} *erg s*$^{-1}$ *cm*$^{-2}$ *Å*$^{-1}$. *One pixel is ∼120 pc across, for all panels.*

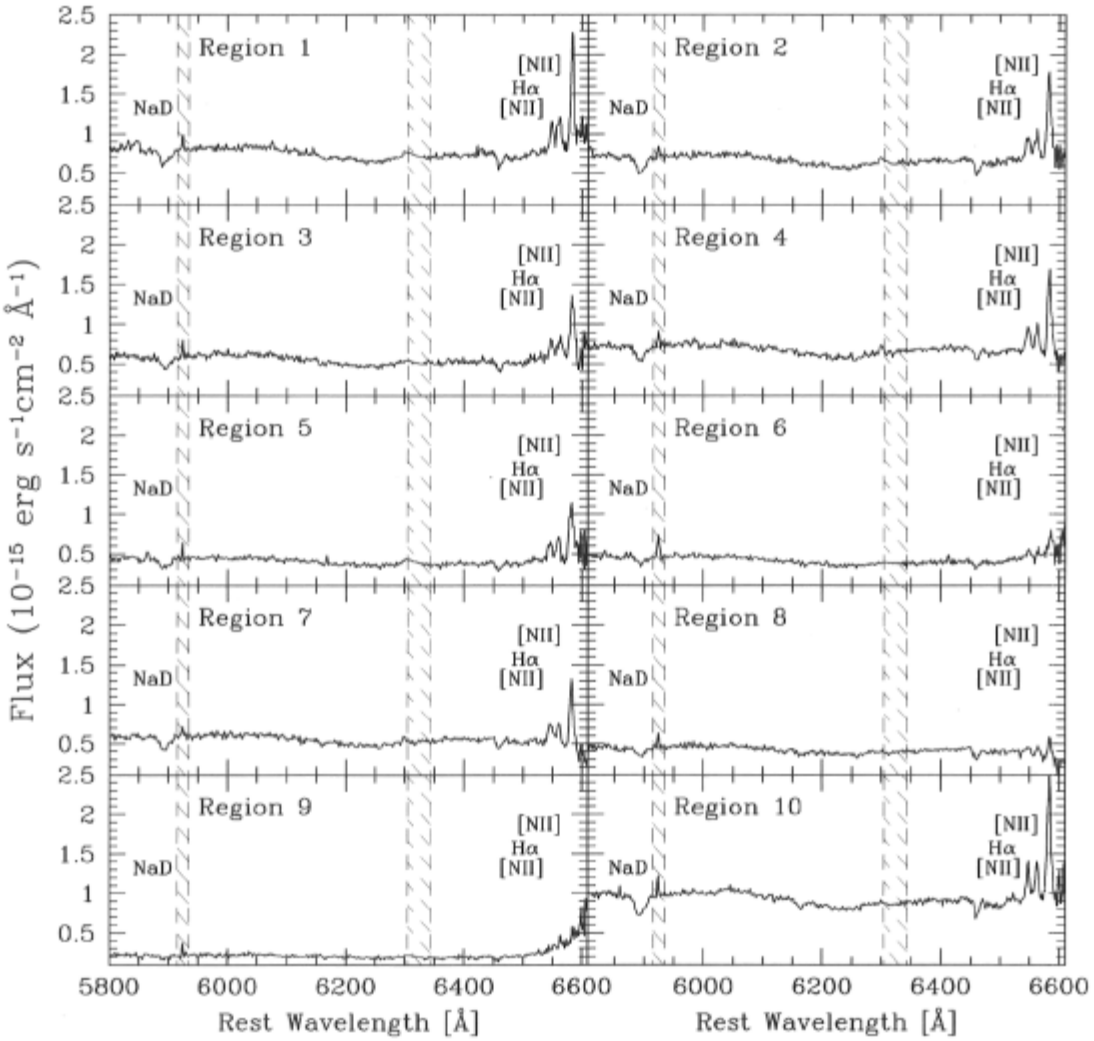

Figure 4.26: **Summed spectra of the 10 selected regions in the Hα image of IC 4130 in Abell 1668.** *Prominent emission features are labeled. Poor sky subtraction and the area affected by a chip gap, are hashed out in regions near 5925 Å and 6300 Å, respectively.*

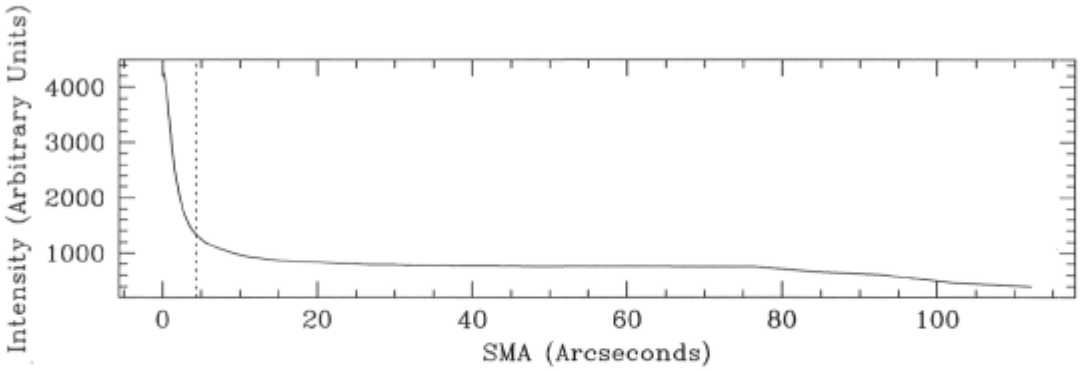

Figure 4.27: **The luminosity profile for IC 4130 in Abell 1668.** *Measured from the r-band acquisition image. The vertical dotted line marks the maximum extent of the IFU field of view. The x-axis displays the Semi-Major Axis as calculated using the IRAF task, ellipse.*

regions of the image, however drops to below 5 near the edges. Consequently, only those pixels with a S/N > 10 are plotted in the emission line images.

Within each of ten regions, similar spectra are co-added in order to increase the S/N. They are labeled on one of the panels of Figure 4.25 and are chosen for an investigation of several areas within the Hα emitting area, including: Region 1 with the highest Hα flux, Regions 2, 3, 4, and 5 which have lower Hα flux, Regions 7 and 8 which have even lower flux, and Region 6 which has very low flux. Region 10 is placed on the peak of the continuum emission. Region 9, outside of the high S/N area, is included to show the large error in these pixels near Hα.

All of the regions cover ~710 pc on either side. The integrated spectra of these regions are presented in Figure 4.26, and are as previously labeled. The areas around ~5925 and ~6300 Å are affected by the poor sky subtraction and a chip gap, and unfortunately this limits accurate measurements of the [O I] λ 6300 emission line, although the line is obviously apparent in many spectra. Other strong emission lines in this spectral region are Hα and [N II] $\lambda\lambda$ 6548,6584. The [S II] $\lambda\lambda$ 6716,6731 lines are outside of the observable window. [N II] λ 6584 is often very strong compared to Hα, indicating the presence of a hard ionizing source. The absorption line of NaD, which reveals the presence of an older stellar population, is strong.

4.5.2 The Underlying Stellar Population

Figures 4.27 and 4.28 show the luminosity profile measured from the r-band acquisition image and the radial variation of the continuum emission across the center of the galaxy, respectively. Both curves share the same shape, despite the fact that the r-band image

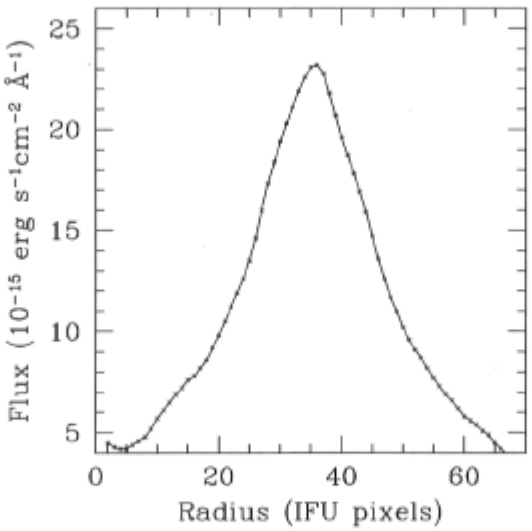

Figure 4.28: **Radial cut in the continuum for IC 4130 in Abell 1668.** *This presents a horizontal cut across the central row of pixels in the continuum image.*

covers a much wider bandwidth and the emission lines (if they are localized to the center of the BCG) are not dominant. Therefore, the flux levels of the continuum profile are used to scale the underlying and emitting spectra to a common distance from the galaxy center. The integrated spectrum for the underlying population, created from an average of 350 spectra on left and right hand edges of the IFU image is shown in Figure 4.29. This is the region where the line emission is lowest but S/N in the individual pixels is low. The average Hα emitting spectrum, which is created from 1258 central pixels with high flux levels measured within the highest S/N regions is also shown in Figure 4.29. Both of these spectra are scaled to values corresponding to the center of the continuum emission.

The underlying spectrum has a lower continuum than that of the integrated spectrum made from the central pixels, however it is not free of emission lines and remains contaminated. The ratio of the [N II] λ 6584 and Hα emission lines show the emission is due to ionization from an AGN, in which case its effect on the continuum level could be negligible (this is discussed further in the section below). It is possible to obtain an age and mass of the underlying population using the NaD absorption line and continuum level. Keeping in mind that the strong AGN ionized lines could be masking the presence of an intermediate or young population which could potentially influence the NaD strength, the integrated spectrum of the underlying galaxy presented therefore corresponds to a lower limit on the age, and the difference in scaled continuum levels represents the upper limit to its mass.

Comparing with the results from the Mollá & García-Vargas (2000) code, the NaD

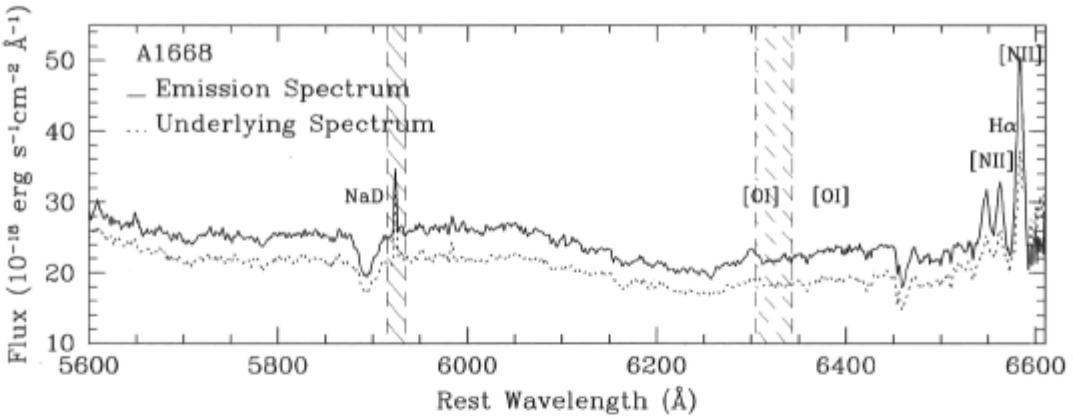

Figure 4.29: **Underlying spectrum of IC 4130 in Abell 1668.** *A median combined spectrum of the low-level emission line spectra (Underlying Spectrum) is shown along with the average spectrum of the strongly Hα emitting spectra (Emission Spectrum).*

equivalent width of 4.0 Å supports only a supersolar metallicity and an age of 5×10^9 yr for the older stellar population of the underlying cD galaxy. The continuum level between 6300 and 6400 Å of a $1\,M_\odot$ burst after 5 Gyr using the same code with a metallicity of twice solar is $1 \times 10^{30}\,\mathrm{erg\,s^{-1}}$. Therefore the scaled integrated spectrum of the underlying population, corresponds to $8 \times 10^7\,M_\odot$ per pixel, or $6 \times 10^3\,M_\odot\,\mathrm{pc}^{-2}$. Most of the bright emission stellar mass of the galaxy is captured in the IFU image, and averaging this mass density over the entire image yields $3 \times 10^{11}\,M_\odot$, a reasonable result for this cD galaxy.

4.5.3 Line Measurements and the Ionization Mechanism

As for the previous two clusters, the background spectrum has been scaled and subtracted from each region spectrum in order to remove the underlying galaxy. However, for Abell 1668 it should be kept in mind that the resulting values in Table 4.7 are affected by the fact that there still exists line emission in the so-called background spectrum. Note also that no Hα absorption is observable, so it is not possible to correct the Hα line strengths for this. Nonetheless, the relative intensities of the [N II] λ 6584 and Hα throughout are well described by hard, AGN-like ionizing source in all of the regions, and in the underlying galaxy. It is true that subtracting this would be removing real flux from the lines to be measured. Table 4.7 shows the centroid, flux, equivalent width and FWHM for [N II] λλ6548,6584 and Hα.

Table 4.7: Spectral Line Values for Regions of IC 4130 in Abell 1668

Measurement	Region 1	Region 2	Region 3	Region 4	Region 5	Region 6	Region 7	Region 8	Region 10
[N II] λ 6548									
Center (Å)	6548.4	6546.7	6547.7	6547.2	6545.9	6548.2	6546.9	6546.2	6547.6
Flux	1.74	2.15	1.46	2.57	1.16	0.52	2.32	0.72	2.12
W_o (Å)	−2.6	−4.1	−3.3	−4.7	−3.2	−1.4	−5.1	−2.3	−2.8
FWHM (Å)	5.2	8.1	6.4	8.5	6.3	5.9	9.5	9.9	4.8
Hα									
Center (Å)	6561.0	6561.0	6563.2	6562.2	6560.0	6564.6	6560.9	6564.0	6562.3
Flux	2.66	2.52	2.30	2.29	1.54	0.50	1.86	0.49	2.63
W_o (Å)	−3.8	−4.7	−5.2	−4.1	−4.1	−1.3	−4.2	−1.6	−3.5
FWHM (Å)	8.1	8.5	11.2	6.9	6.0	5.8	7.0	5.4	6.1
[N II] λ 6584									
Center (Å)	6583.7	6582.1	6583.8	6582.9	6581.7	6585.7	6582.2	6583.7	6583.0
Flux	6.97	7.11	5.74	6.61	4.90	1.72	5.28	0.84	9.72
W_o (Å)	−9.4	−12.8	−12.5	−11.9	−12.5	−4.2	−12.2	−2.8	−13.1
FWHM (Å)	5.0	7.1	8.8	6.6	7.8	7.4	6.4	3.9	6.8

Note: The central positions are given in terms of the rest wavelength. The flux is in units of 10^{-15} erg s^{-1} cm^{-2}. Region 9 is not listed as there are no lines that can be measured. Errors in the flux measurements for the strong lines are of order 5-10%, as discussed in the text. Errors for determining the central wavelength are of order ∼2 Å.

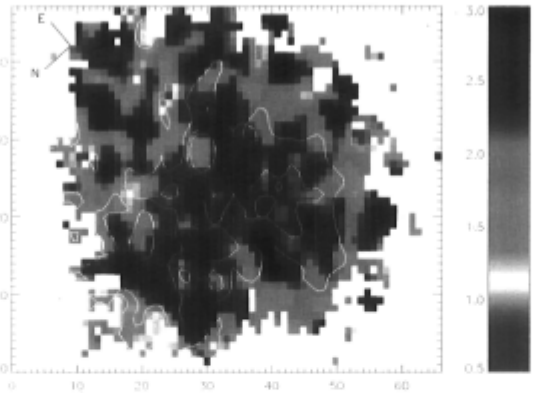

Figure 4.30: **[N II] λ6584/Hα ratio for IC 4130 in Abell 1668.** *One pixel is ∼120 pc across.*

All regions show stronger [N II] λ6584 line fluxes than those for Hα. The lowest ratio that can ascribed to ionization by an AGN, without contamination from ionization from hot stars is 1.6. Region 8 has the smallest ratio of all the regions, but the value is 1.7, still well described by AGN emission. It is not possible to differentiate between Seyfert, or LINER emission as the [O III] λ5007/Hβ values are not known. Figure 4.30 shows the [N II] λ6584/Hα ratios on a pixel to pixel basis. Note that these values are derived from the integrated flux within the bandpasses described in the section above. On the other hand, the region spectra are a combination of several pixels and thus have an increased S/N. The ratios quoted for the regions are therefore determined by fitting each line with a Gaussian using *splot* and thus more reliable than those of Figure 4.30.

The facts that the [N II] λ6584/Hα ratio does vary across the image, and that the scaled underlying spectrum has a lower continuum than the emitting spectrum (although some amount of continuum is surely from the AGN) suggest a young population may still exist. Its lines however are completely masked by the presence of the AGN, and therefore, it is not possible to use the Hα emission line to characterize a SFR or an age for the younger stellar populations.

4.5.4 Kinematics

The map of the relative Hα line velocities is shown on the left side of Figure 4.31. The low S/N values at the edge of the figure are especially noticeable in those pixels of negative relative velocity on the East side of the image. There are a few central patches where the emission lines could not be fit as single Gaussians and they are plotted as having zero relative velocity, as are the pixels with no Hα emission. Figure 4.31 shows a gradient from positive values North of the center ($> 100\,\mathrm{km\,s^{-1}}$), to negative values ($< -100\,\mathrm{km\,s^{-1}}$) at the South with the zeropoint near the center of the continuum. The velocity gradients could be rotation or evidence of the gas flowing into and out of the

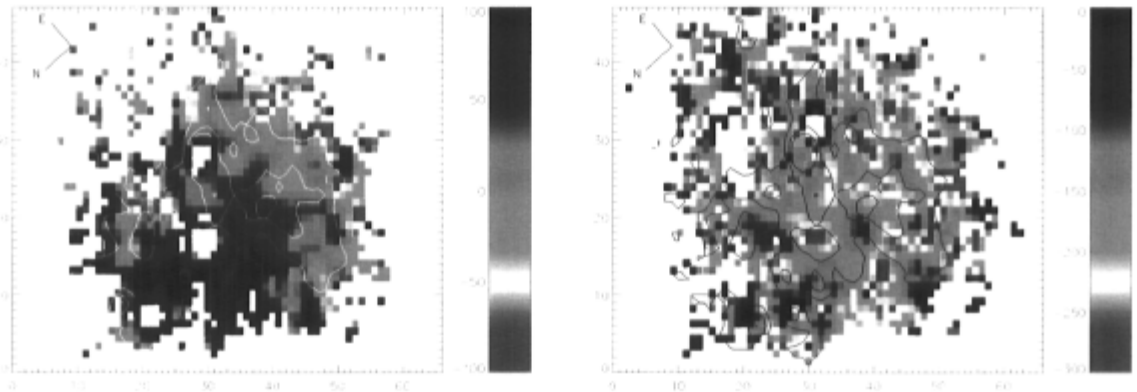

Figure 4.31: **Relative velocities for IC 4130 in Abell 1668.** *Left Panel: Map of the Hα relative velocity. Right Panel: Map of the NaD relative velocity. The scale is in units of km s^{-1} and is normalized to the redshift of IC 4130. Contours of the Hα emission line are overlain and one pixel is ∼120 pc across.*

central source. The [N II] λ 6584 map shows similar structure, and is not shown. On the right side of Figure 4.31, the relative velocities of the NaD lines are presented. This map traces the motion of the older underlying population, as opposed to the line emitting gas. The velocites of the NaD absorption lines show a smaller variation in magnitude ($\sim \pm 70\,\mathrm{km\,s^{-1}}$), no smooth gradient, and all of the velocities are negative. This implies the line emitting gas is not at rest with respect to the underlying population traced by the NaD line.

4.6 Ophiuchus

Figure 4.32 shows the Ophiuchus cluster as observed with Gemini. It is a nearby (z = 0.028) rich cluster of galaxies with a velocity dispersion of $880\,\mathrm{km\,s^{-1}}$ (Peres et al. 1998) and is at a distance of ∼115 Mpc, such that 1″ corresponds to ∼0.6 kpc. Watanabe et al. (2001) analyze the *ASCA* X-ray emission from this cluster and conclude that it is not relaxed and has recently experienced a merger. These authors find the X-ray surface brightness profile to be centrally concentrated, as in cooling flow clusters, however the central temperature is quite high (10 keV). Edge et al. (1992) derived a mass deposition rate of $\sim 17\,\mathrm{M_\odot\,yr^{-1}}$ using EXOSAT data, but newer observations from *ASCA* (White 2000) show no evidence for a cooling flow. The bolometric X-ray luminosity of the cluster, using $\mathrm{H}_o = 50\,\mathrm{km\,s^{-1}\,Mpc^{-1}}$, is $31.4 \times 10^{44}\,\mathrm{erg\,s^{-1}}$ according to White et al. (1997a). Peres et al. (1998) list this cluster as having optical lines in an optical counterpart 6″ from the X-ray center as well as radio emission in the 1.4 GHz band. My observations of this system show that indeed the BCG (with J2000 coordinates of 17:12:27.8 -23 22 11.5) is offset a few arcseconds south of the X-ray

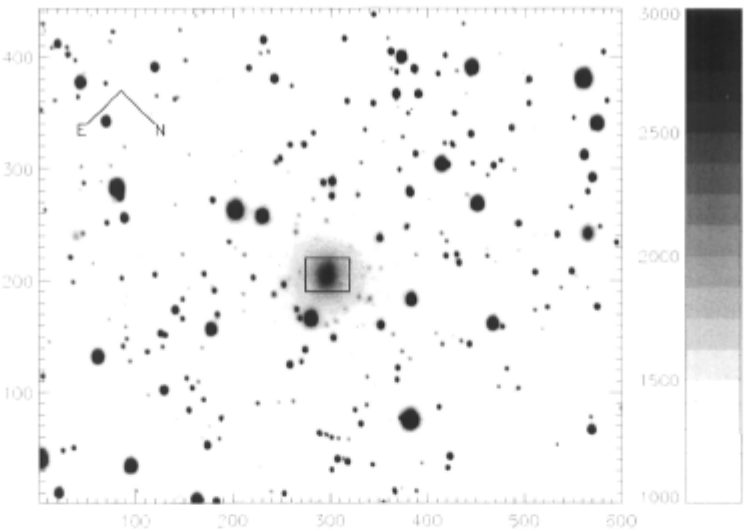

Figure 4.32: **The center of the Ophiuchus cluster taken in the r-filter.** *The IFU field is marked as a box with dimensions of 5 × 7″ (2.7 × 3.8 kpc) around the BCG. A hint of extinction is seen in the northern corner of the IFU FOV. The scale is in arbitrary flux units.*

emission centroid (J2000 coordinates of 17:12:27.8 -23 22 09).

The $5 \times 7''$ field of view of the IFU covers 2.7×3.8 kpc, and encapsulates the central region of the BCG, as well as another small emitting structure to the North, hereafter known as Object B, and the apparent extinction that surrounds it. Each pixel covers a distance of $\sim$60 pc on either side.

4.6.1 Line Images and Region Spectra

Before the line flux measurements are made, the two integrations obtained for this cluster are shifted and added, which accounts for the chip gaps. An image of the continuum between 6300 and 6500 Å is displayed in the top left corner of Figure 4.33. The BCG is clearly in the center of the IFU frame, and is the brightest galaxy in this continuum image. A patch of extinction is seen in the Northern direction.

Also displayed in Figure 4.33 is the continuum-subtracted Hα flux image and the continuum-subtracted [N II] λ 6584 flux image. These observations show that the optical emission lines previously reported are not in the center of the BCG. There is no line emission at the center of the BCG. However, there is another region which is strong in line emission. It is clearly co-spatial with the extinction patch seen in Figure 4.32 and the continuum image of Figure 4.33, I will refer to this region as Object B. The S/N of the continuum at each pixel is shown on the same Figure 4.33. It shows a S/N > 5 throughout most of the frame.

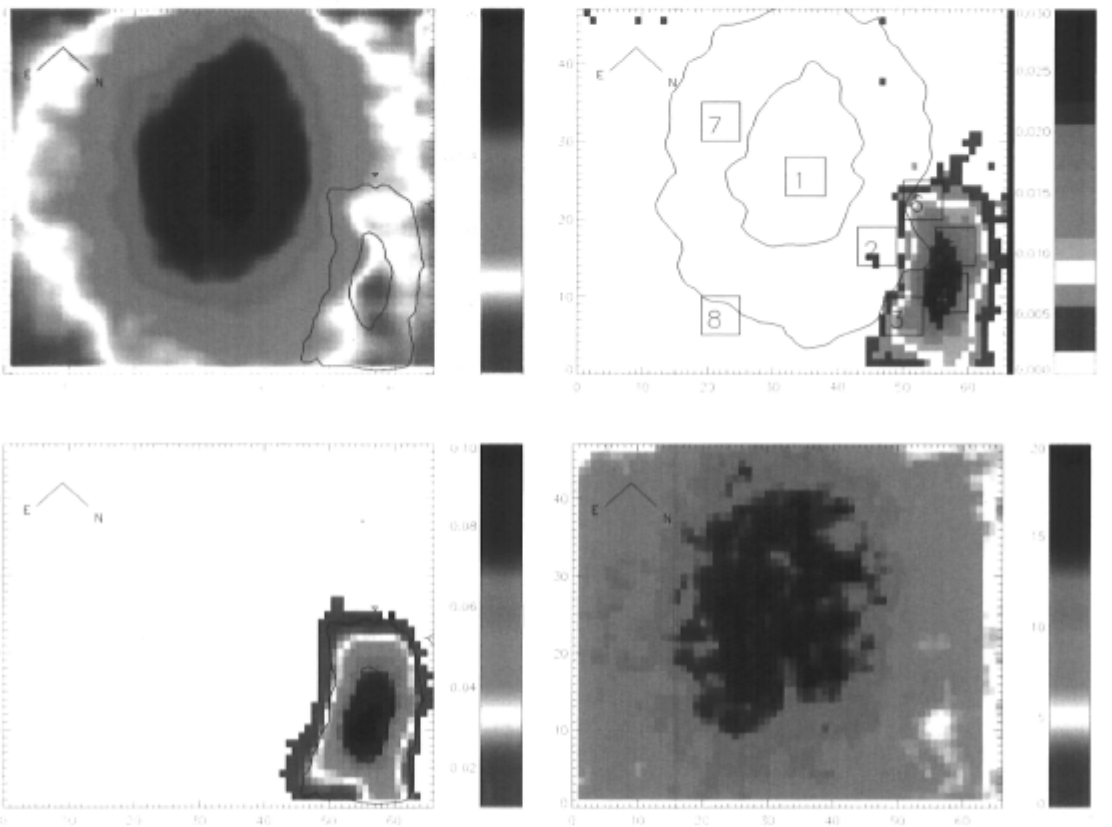

Figure 4.33: **Reconstructed images for the BCG in Ophiuchus.** *Top Left Panel: The continuum surrounding the Hα emission line, with the Hα flux overlain as contours. Extinction is seen in the Northern corner, co-spatial with the Hα contours. Top Right Panel: Map of the continuum-subtracted Hα emission flux. The continuum image is shown in contours, and the regions used in the subsequent analysis are represented as boxes. Bottom Left Panel: Map of the [N II] λ6584 emission, with the Hα flux overlain as contours. Bottom RightPanel: S/N ratio of the continuum. Emission line maps are in reverse colour scale and in units of 10^{-15} erg s^{-1} cm^{-2} Å^{-1}. One pixel is ∼60 pc across, for all panels.*

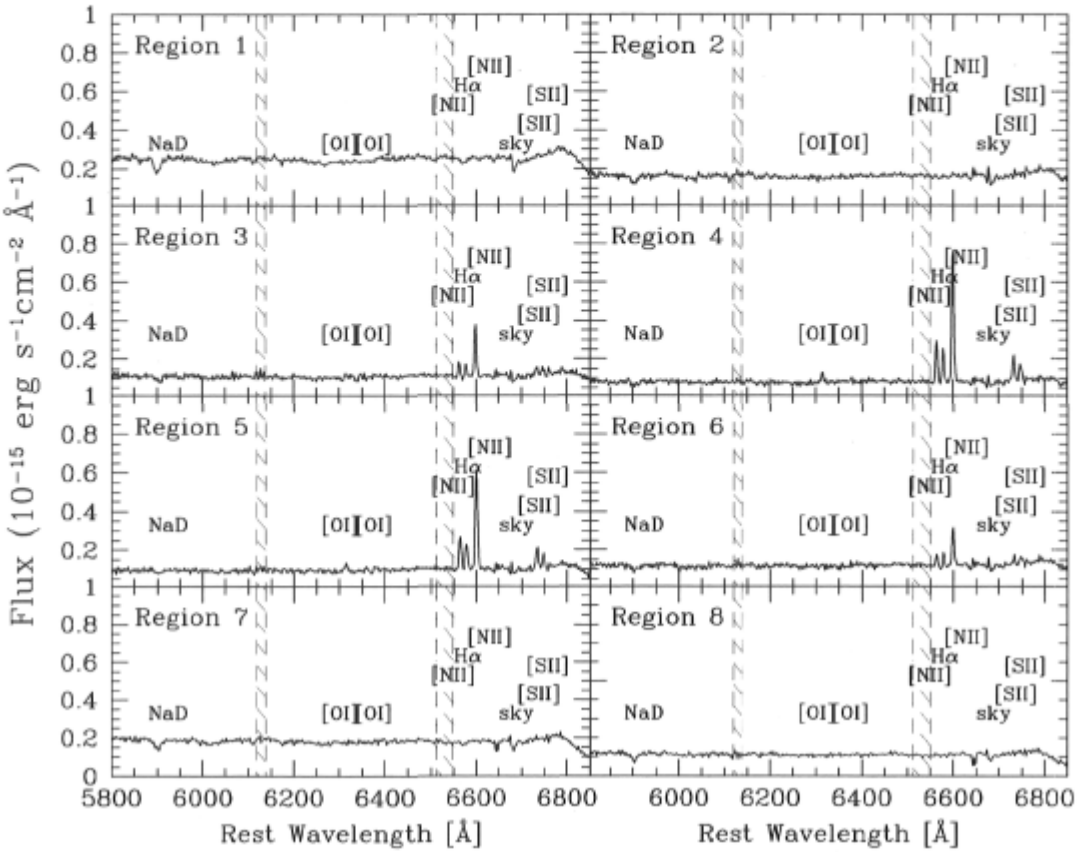

Figure 4.34: **Summed spectra of the 8 selected regions near the BCG in Ophiuchus.** *Prominent emission features are labeled. Bad sky subtraction and a chip gap are hashed out in regions near 6125 Å and 6500 Å, respectively. The spectra are displayed at the rest wavelength of the BCG.*

Eight regions, as labeled on the top right panel of Figure 4.33, are chosen in order to investigate the emission further. Regions 1, 2, 7, and 8 are within the BCG continuum emission but outside of the line emitting area. Regions 3 and 6 appear to have lower [N II] λ 6584/Hα line ratio than the bright Hα emitting area of Regions 4 and 5 (the [N II] λ 6584/Hα ratio is also presented in Figure 4.40). The small relative velocities (see Figure 4.38) in Object B are also sampled. Adding the signal within the regions increases the S/N of the continuum to at least 10 in all regions.

All of the regions cover ~330 pc on either side. The integrated spectra of these regions are presented in Figure 4.34, and are as previously labeled. Strong emission lines present include [O I] λ 6300 (in Regions 4 and 5), Hα, [N II] $\lambda\lambda$ 6548,6584, and [S II] $\lambda\lambda$ 6716,6731 (in Regions 3 - 6). These, however are only seen in Object B, and are well described by ionization by a hard source, such as an AGN. There is no evidence

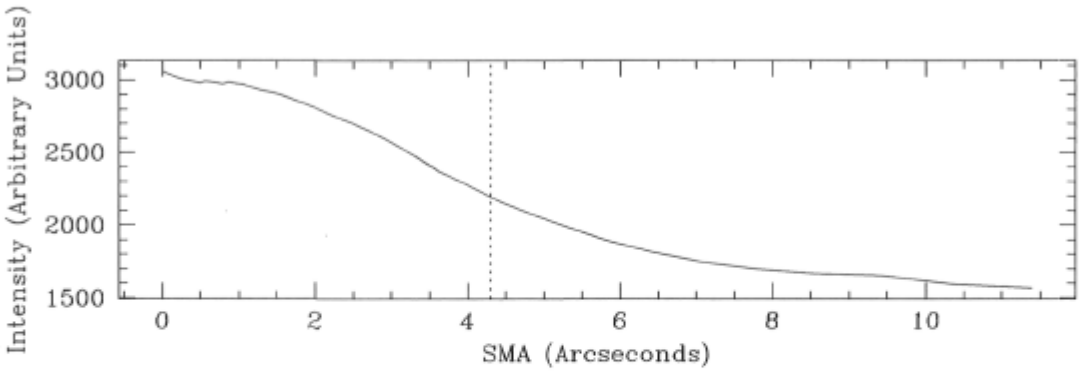

Figure 4.35: **Luminosity profile for the BCG in Ophiuchus.** *Measured from the r-band acquisition image. The vertical dotted line marks the maximum extent of the IFU field of view. The x-axis displays the Semi-Major Axis as calculated using the IRAF task, ellipse.*

for a dominating young star forming population. NaD is seen throughout. Regions 1 and 7 sample the BCG, and Hα in absorption is seen in these spectra.

4.6.2 The Underlying Population of the BCG

For completeness, the luminosity profile of the BCG in Ophiuchus is shown in Figure 4.35, though it will not be used in any further analysis. It shows that much of the intense emission from the BCG is constrained to the IFU field of view, as also obvious in Figure 4.36 which presents a radial cut in y of the BCG across the center of the image. A median averaged spectrum from ~2660 non-Hα emitting pixels of the BCG is shown in Figure 4.37. These pixels are throughout the image, excluding those where $x > 45$ and $y < 35$ on the images of Figure 4.33 (the coverage of Object B). Figure 4.37 very clearly shows Hα and NaD absorption the cD galaxy.

The observed NaD absorption corresponds to an equivalent width of 4.4 Å and an age of $\sim 1 \times 10^{10}$ yr using the code of Mollá & García-Vargas (2000), and allowing only for supersolar metallicities. A mass of $6 \times 10^4\,M_\odot\,pc^{-2}$ is calculated in the same way as for IC 4130 in Abell 1668.

4.6.3 The Nature of Object B

The integrated Object B spectrum gives the wavelengths of the [N II]-Hα emission line complex of Object B at 6564, 6576, and 6597 Å after the cluster redshift has been accounted for. This corresponds to a velocity difference of $+750\,km\,s^{-1}$ between Object B and the recessional velocity of the cluster, but is within the cluster velocity dispersion. Indeed, the absorption line of NaD, derived from the underlying BCG is found at rest

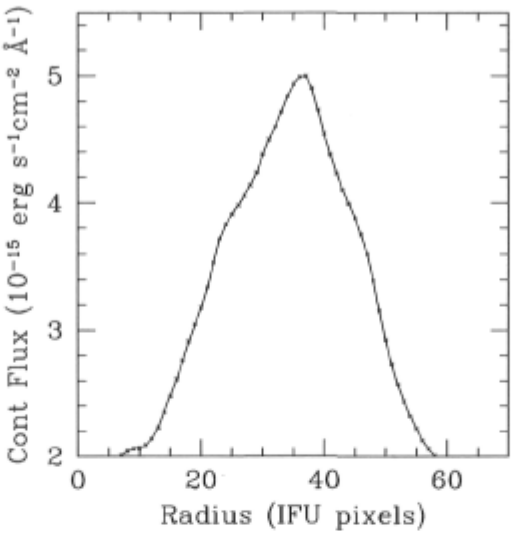

Figure 4.36: **Radial cut in the continuum for the BCG in Ophiuchus.** *This presents a horizontal cut across the central row of pixels in the continuum image.*

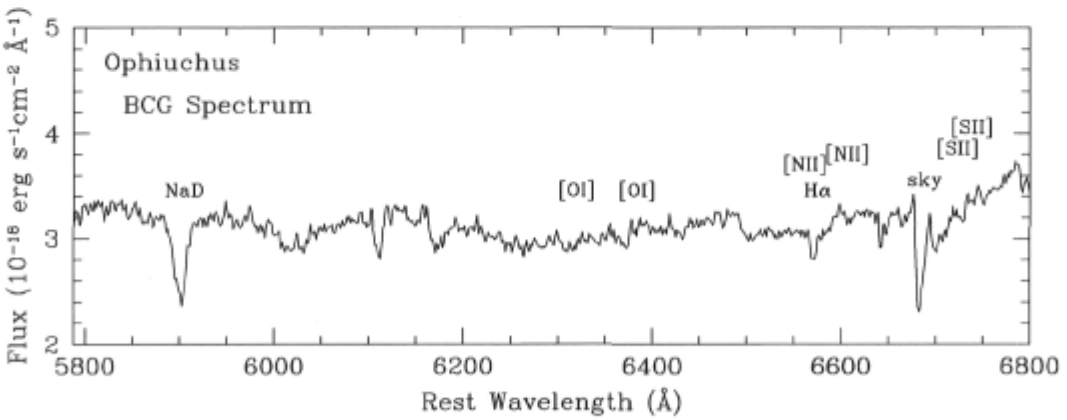

Figure 4.37: **Ophiuchus BCG spectrum.** *The median averaged spectrum of the BCG.*

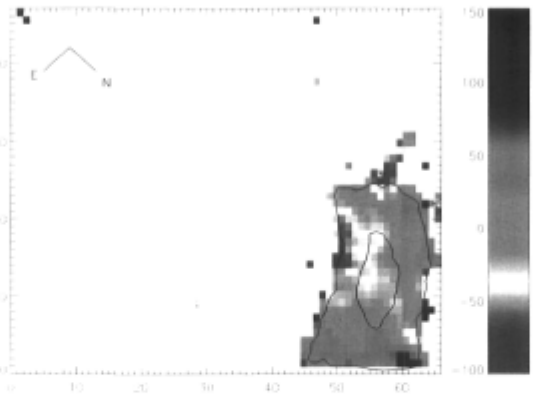

Figure 4.38: **Map of the Hα relative velocity for Object B in Ophiuchus.** *The Hα flux is overlain as contours. The scale is in units of* $km\,s^{-1}$ *relative to the average Object B velocity. One pixel is ∼60 pc across.*

with respect to the cluster and only the position of the emission lines from Object B are offset.

As mentioned above, there is an extinction patch near Object B clearly seen in absorption on Figure 4.32 and the continuum image of Figure 4.33. This feature is at the same projected position as Object B, and shares the same morphology as it.

The velocity difference of $+750\,\mathrm{km\,s^{-1}}$ between Object B and the BCG is quite a high velocity and could imply either an outflow from the BCG, or simply that Object B is well behind the centroid of the BCG.

The relative velocities can most simply be explained if Object B were a galaxy external to the BCG at a redshift of z = 0.031 which is beyond the BCG. Although this is within the velocity dispersion of the cluster, if Object B was a galaxy at rest with respect to the Hubble flow, this velocity difference corresponds to a physical distance of 10 Mpc. This is a very large difference and Object B would therefore not be related to processes going on in the cD, or to the cooling X-ray gas (recall, a typical cooling radius is ∼200 kpc).

Thus, if the emission lines in Object B are related to the cooling flow, or the BCG, the difference in velocity would be due to a bulk flow. The relative velocity map of Hα is shown in Figure 4.38 with respect to the average Object B velocity. It is clear that the velocity gradients in Object B are small, also indicative of a bulk flow. Since the velocity difference with respect to the BCG is positive, there are two possible scenarios. The hypothesis is that Object B is in front of the center of the BCG and moving towards it, in which case the extinction patch would be real association with Object B. In the second, Object B would be an outflow emanating from the BCG heading away from us, here extinction patch is in front of the BCG, but the gas is behind the BCG, and the alignment of the extinction patch with Object B would be a coincidence.

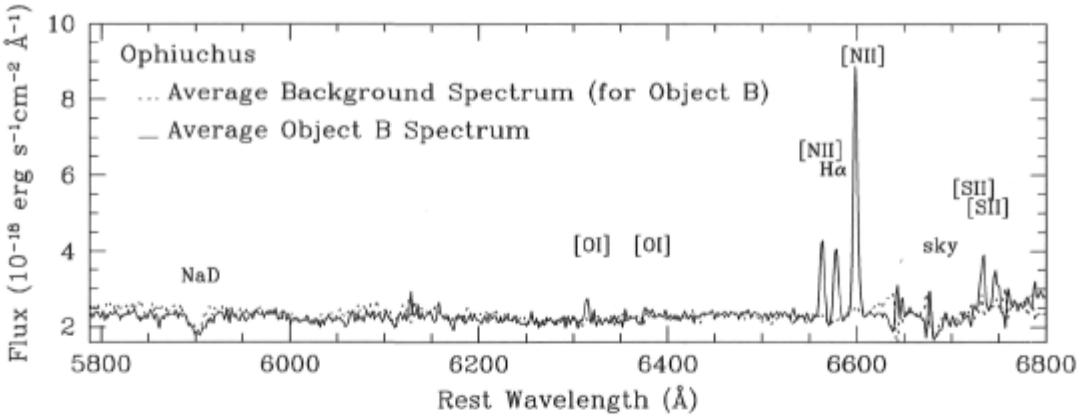

Figure 4.39: **Ophiuchus Object B and Object B background spectra.** *The median averaged spectrum of Object B is shown alongside the median averaged spectrum of the corresponding BCG region (see text). Both spectra are shown in terms of the rest wavelength scale assuming the redshift of the BCG.*

4.6.4 Object B - Line Measurements and the Ionization Mechanism

If Object B is in front of the center of the BCG, the BCG would then be polluting the spectrum of Object B. Therefore, before studying the lines of Object B, I propose to build an average background spectrum of the BCG and subtract it from the Object B spectrum. Defining the worst case scenario, a corresponding BCG spectrum is built from an average of 286 pixels on the bottom left side of the IFU images; those pixels with the same coverage in y-values as Object B, but with x-values on the other side of the continuum peak. These two spectra are shown in Figure 4.39, both deredshifted with respect to the cluster. The internal extinction correction utilized to the BCG in Ophiuchus, applies mostly to the central region of the BCG, this correction is then removed for the two spectra of Figure 4.39, as the pixels are far from the center of the BCG. Nonetheless, the extinction correction makes little difference to the continuum-subtracted line ratios since the lines analyzed are close in wavelength.

Once a background BCG spectrum is subtracted from Object B, no NaD absorption, or continuum emission remains, suggesting there is no massive stellar population belonging to Object B. Table 4.8 shows the centroid, flux, and FWHM for the background subtracted emission lines of Regions 3, 4, 5, and 6 in Object B. The integrated spectrum of Object B has Log([N II] λ6584/Hα) = 0.50, values which are similar to those in the individual regions of Object B, and which indicate an AGN ionizing source according to the BPT diagram. Figure 4.40 shows that even the individual pixels have high ratios of [N II] λ6584/Hα, above 3, and that this ratio varies slowly across Ob-

Table 4.8: Spectral Line Values for Regions of Object B in Ophiuchus

Measurement	Region 3	Region 4	Region 5	Region 6
[O III] λ 6300				
Center (Å)	6314.0	6314.4	6313.5	6312.5
Flux	0.13	0.29	0.35	0.10
FWHM (Å)	5.7	5.6	8.8	6.8
[N II] λ 6548				
Center (Å)	6562.6	6563.9	6564.2	6563.4
Flux	0.37	1.12	1.01	0.28
FWHM (Å)	4.5	4.9	5.5	4.5
Hα				
Center (Å)	6577.7	6578.4	6578.5	6578.4
Flux	0.39	1.02	0.88	0.37
FWHM (Å)	5.3	5.5	6.0	4.5
[N II] λ 6584				
Center (Å)	6598.1	6599.2	6599.5	6599.2
Flux	1.44	3.70	3.10	1.01
FWHM (Å)	5.1	5.0	5.8	5.0
[S II] λ 6716				
Center (Å)	6734.0	6733.0	6733.6	6734.0
Flux	0.15	0.73	0.66	0.16
FWHM (Å)	3.1	5.4	5.8	2.4
[S II] λ 6731				
Center (Å)	6745.1	6747.3	6747.5	6748.5
Flux	0.13	0.50	0.45	0.20
FWHM (Å)	3.2	6.0	6.1	6.3

Note: The central positions are given in terms of the rest wavelength. The flux is in units of 10^{-15} erg s^{-1} cm^{-2}. The values of FWHM have not been corrected for the insrumental profile. Regions 6, 9, and 12 are not listed as they have no lines above the noise level. As discussed in the text, fits for several lines were not possible, and they are marked here with a dash. Errors in the flux measurements for the strong lines are of order 5-10%, as discussed in the text. Errors for determining the central wavelength are of order ∼2 Å. The weak lines of [S II] have large errors of 20-30%. W_o is not measured since the continuum level is too close to zero.

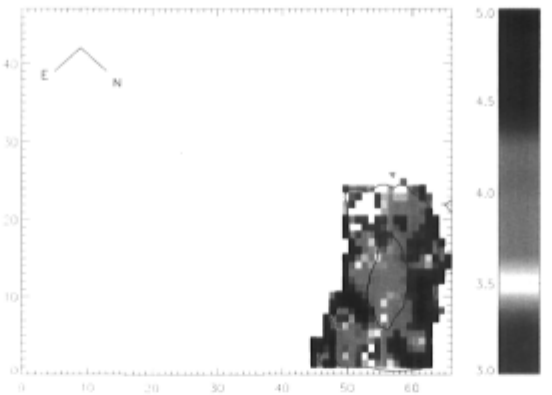

Figure 4.40: **The [N II] λ6584/Hα ratio near the BCG in Ophiuchus.** *Contours trace the Hα emission. One pixel is ∼60 pc across.*

ject B. Log([O I] λ6300/Hα) = −0.48, and Log([S II] λ6716 + λ6731/Hα) = −0.04, again, similar to the values in the individual regions of Object B, and consistent with the AGN region of the BPT diagrams, though less clear. The ([S II] λ6716 + λ6731)/Hα for instance, varies in the different regions, from 0.72 to 1.26, which is nearer to but on the border of the AGN side of the BPT diagram. Thus, using only the ([S II] λ6716 + λ6731)/Hα ratio as a diagnostic, it is not possible to distinguish between LINER, Seyfert, or ionization from H II regions without knowing the [O III] λ5007/Hβ ratio.

The full integrated spectrum of Object B shows [S II] λ6716 / [S II] λ6731 ratio of 1.08 reveals an n_e of ∼350 cm^{-3}. However the individual regions show variations from 0.8 - 1.5 corresponding to n_e between 100 and 1000 cm^{-3}. Such moderate densities are typical for both H II regions and Seyfert 2 and narrow-line radio galaxies (Osterbrock & Ferland 2006).

Since no lines are seen in the center of the BCG, and since the dust feature appears to be so well associated with Object B (and is not absorbing emission from the center of the BCG) and absorbing continuum emission, it seems reasonable to conclude that Object B is in front of the center of the BCG (although, it could still be within the extended halo of the cD), and hence flowing towards it. Object B could be a molecular cloud flowing towards the BCG, ionized by the AGN at the center of the BCG (not seen, hidden perhaps by its disk). The fact that no continuum is observed in the corrected line spectra are consistent with the conclusion that Object B is a cloud of gas. The coordinates of Object B are those of the X-ray emission centroid, however, modern observations show no evidence for significant cooling in Ophiuchus.

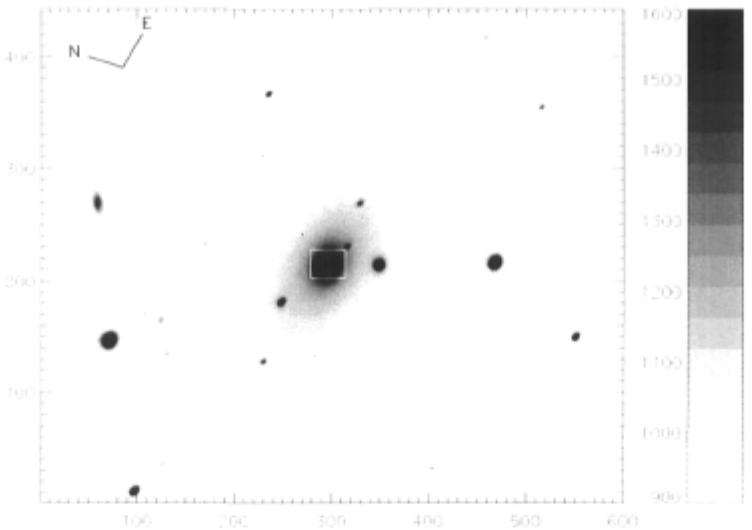

Figure 4.41: **NGC 5920 in the center of MKW3s taken in the r-filter.** *The IFU field is marked as a box with dimensions of 5 × 7″ (4.3 × 6.0 kpc) around NGC 5920, the BCG. The scale is in arbitrary flux units.*

4.7 NGC 5920 in MKW3s

MKW3s, shown in Figure 4.41, is a poor cluster of galaxies (Morgan et al. 1975), yet it is amongst the sample of brightest X-ray clusters (Ebeling et al. 1998), having an X-ray luminosity of $2.68 \times 10^{44}\,\mathrm{erg\,s^{-1}}$ in the 0.1 - 2.4 keV band. This cluster is located at a distance of ∼184 Mpc, such that 1″ corresponds to ∼0.9 kpc, and there is no sign of any major cluster merger in this relaxed system (Mazzotta et al. 2002). The central X-ray temperature drop of ∼3.5 keV (Kaastra et al. 2004), relative to the temperature outside the cooling radius validates the cooling flow status of this cluster, and the X-ray surface brightness peak is coincident with the position of NGC 5920, the BCG. MKW3s is host to an extended radio source which appears to be interacting with the X-ray gas. Mazzotta et al. (2004) argue that in fact a radio lobe arising from short-lived nuclear outbursts from the central AGN is heating the central regions and has created an easily observable X-ray cavity. Hicks & Mushotzky (2005) find evidence for a small UV excess in NGC 5920, calculating a star formation rate of $0.1 \pm 0.1\,\mathrm{M_\odot\,yr^{-1}}$, although McNamara & O'Connell (1989) find no evidence for UV excess in their spectrum. Crawford et al. (1999) find no obvious line emission, but their observations are unable to rule out small levels which might be apparent. No CO emission was detected by Salomé & Combes (2003) who quote an upper limit for the mass of $\mathrm{H_2} = 5.2 \times 10^8\,\mathrm{M_\odot}$.

The $5 \times 7''$ field of view of the IFU covers the central region of NGC 5920, which is 4.3×6.0 kpc. Each pixel covers a distance of ∼90 pc on either side.

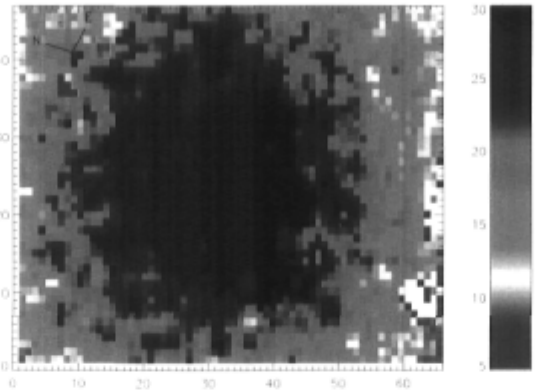

Figure 4.42: **S/N ratio of the continuum for NGC 5920 in MKW3s.** *One pixel is ∼90 pc across.*

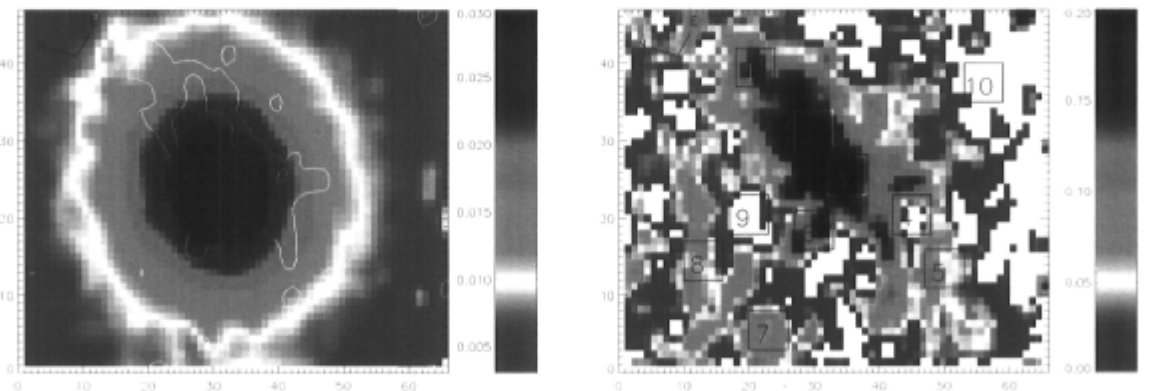

Figure 4.43: **Reconstructed images for NGC 5920 in MKW3s.** *Left Panel: Map of the continuum near Hα. Right Panel: Map of the continuum-subtracted Hα + [N II] λλ 6548,6584 with the regions used in the subsequent analysis represented as boxes. The images are in reverse colour scale and in units of* 10^{-15} *erg s*$^{-1}$ *cm*$^{-2}$ *Å*$^{-1}$. *One pixel is ∼90 pc across, for all panels.*

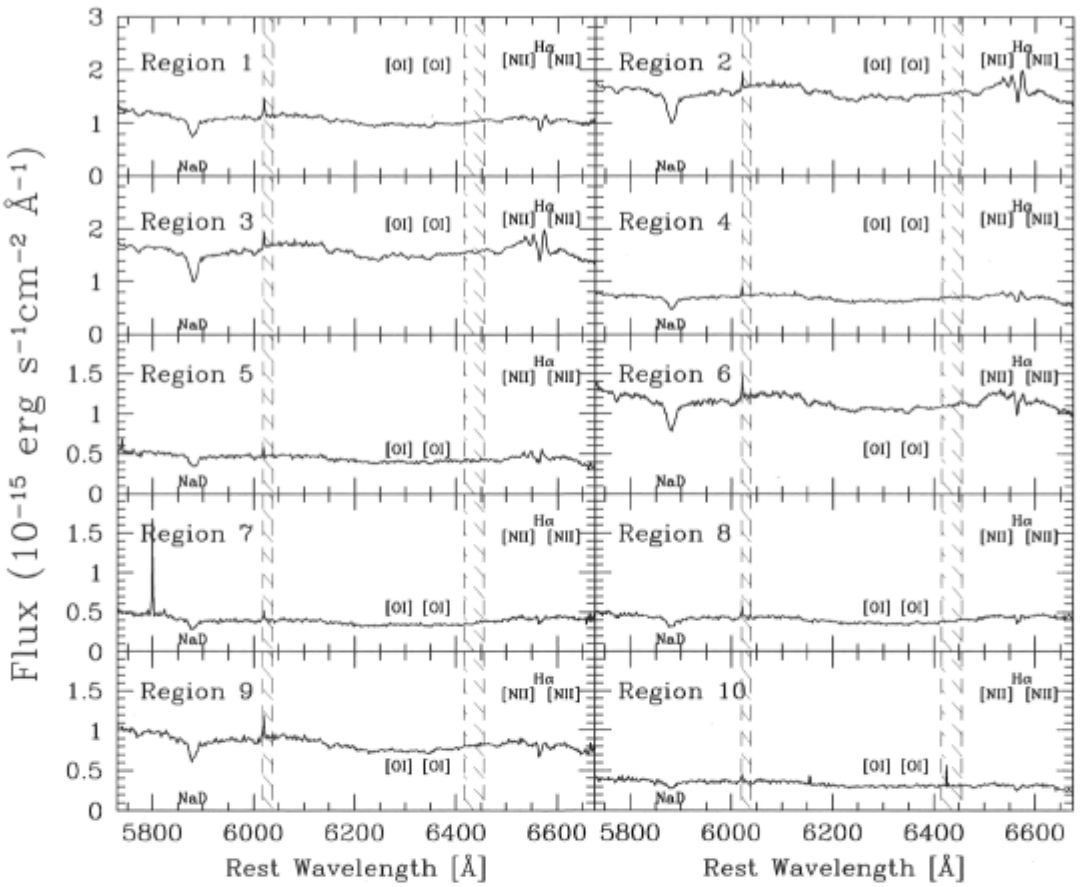

Figure 4.44: **Summed spectra of the 10 selected regions of NGC 5920 in MKW3s.** *Prominent emission features are labeled. Bad sky subtraction and a chip gap are hashed out in regions near 6000 and 6400 Å, respectively.*

4.7.1 Line Images and Region Spectra

A map of the S/N of the continuum surrounding Hα is shown in Figure 4.42 with the corresponding image of the continuum between 6400 and 6500Å in Figure 4.43. Most pixels have a high S/N, greater than 30 near the center. The continuum image shows no immediate extinction caused by dust features, but has a flux which increases towards the center. Each pixel of the image corresponds to a spectrum for which if Hα appears in emission, there is also an adjacent absorption line which cuts into the emission rendering a fit using *deblend* impossible (this can be seen in the region spectra of Figure 4.44 which are discussed below). Thus, for this case an image of Hα + [N II] $\lambda\lambda$ 6548,6584 is shown (Figure 4.43) which has been created by obtaining the integrated flux between 6530 and 6590 Å. There is a strong elongated emission feature which crosses the center of the cD galaxy from the North-East to the South-West. Several regions are chosen for further

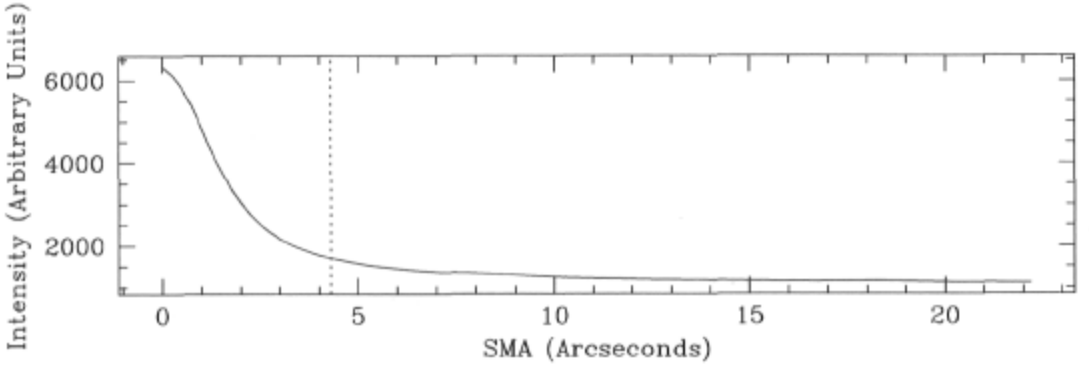

Figure 4.45: **Luminosity profile for NGC 5920 in MKW3s.** *Measured from the r-band acquisition image. The vertical dotted line marks the maximum extent of the IFU field of view. The x-axis displays the Semi-Major Axis as calculated using the IRAF task, ellipse.*

exploration and they are labeled in Figure 4.43. Regions 1, 2, and 3 of intense line emission, Regions 4, 5, 6, 7, and 8 of lower line emission, and Regions 9 and 10 without emission lines.

Each region covers 580 pc on either side. Figure 4.44 presents the integrated spectra for the regions as labeled above. Notice how the Hα + [N II] $\lambda\lambda$ 6548,6584 emission line is complex, present in Regions 1 - 6 is effected by underlying absorption. The emission lines are blueshifted by $\sim$10 Å with respect to the Hα absorption line. The deep Hα absorption is at the expected wavelength for the redshift of the BCG and is present in all region spectra. It will be removed before commenting on the ionization mechanism and the emission line ratio [N II] λ 6584/Hα. NaD absorption is seen in all region spectra.

4.7.2 The Underlying Population

The luminosity profile for NGC 5920 in the r-band image is plotted in Figure 4.45. Figure 4.46, shows a radial cut in y across the central pixels of the continuum emission image (note, this horizontal cut includes an external galaxy on the edge of the IFU image that is away from the fitted elliptical isophots). The integrated spectrum of the underlying cD galaxy is presented in Figure 4.47. It was created from a median average of 650 non-Hα emitting pixels; those generally found between pixels x > 50 and y > 10 on Figure 4.43.

An equivalent width for NaD of 5.1 Å is measured, corresponding only to the supersolar metallicity of 2 $Z_\odot$ (the only supersolar value available) and an age of $\sim 2 \times 10^{10}$ yr using the Mollá & García-Vargas (2000) code. Using the same method as for the pre-

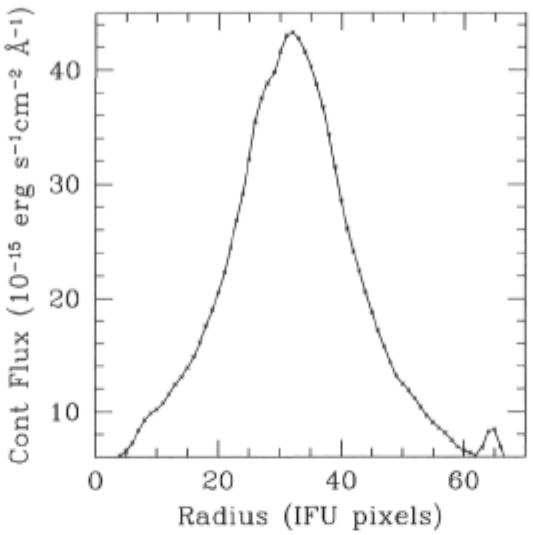

Figure 4.46: cut in the continuum for NGC 5920 in MKW3s. *This presents a horizontal cut across the central row of pixels in the continuum image.*

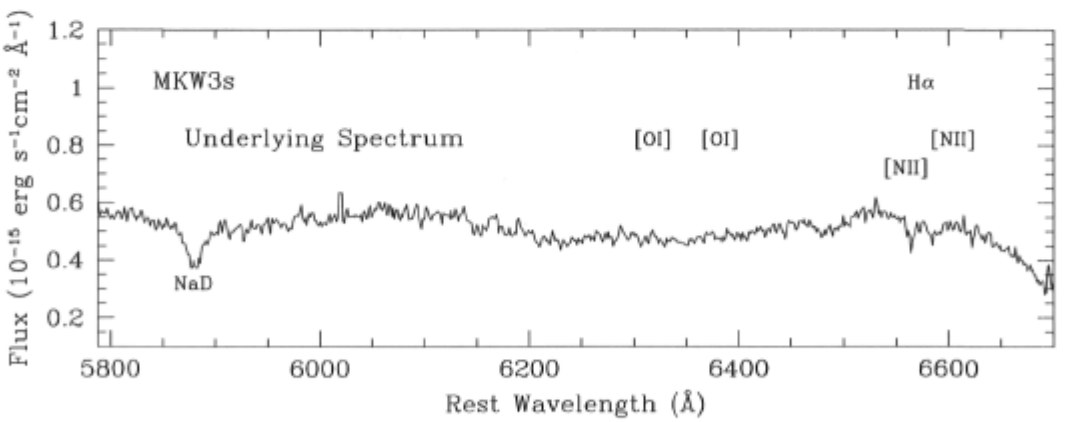

Figure 4.47: **Underlying spectra for the regions of NGC 5920 in MKW3s.** *The median averaged underlying spectrum scaled to match the same number of pixels of each of the 10 regions.*

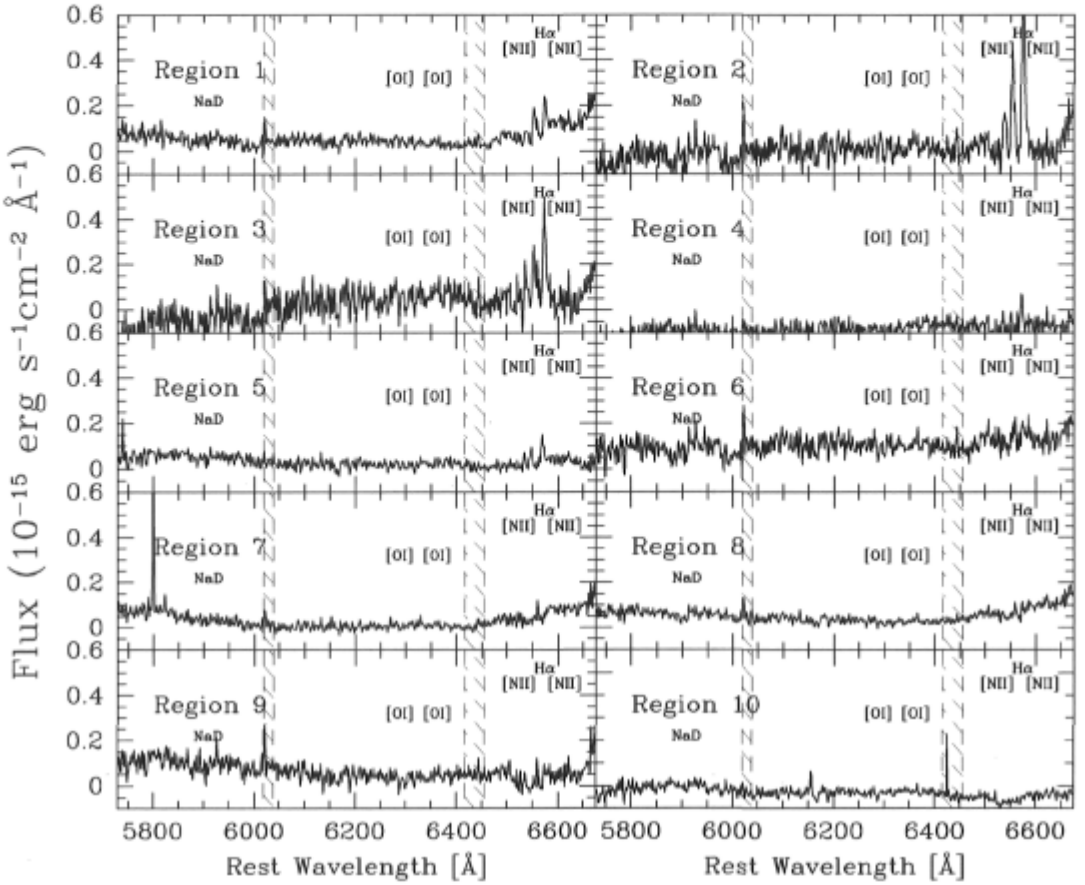

Figure 4.48: **Background subtracted spectra of the 10 selected regions of NGC 5920 in MKW3s.** *Prominent emission features are labeled. Bad sky subtraction and a chip gap are hashed out in regions near 6000 and 6400 Å, respectively.*

vious clusters, a mass of the underlying population in a pixel at a distance of 15 pixels from the peak of emission is $1.65 \times 10^9\,M_\odot$. The continuum luminosity profile is then used to scale this to a corresponding mass at the continuum peak. The result is a mass of $2 \times 10^5\,M_\odot\,pc^{-2}$.

4.7.3 Line Measurements and the Ionization Mechanism

Each region spectrum is subtracted by the underlying spectrum scaled by the r-band luminosity profile to get the shape and the radial cut in y of the continuum image and then the value of the scale factor at the radial distance of the region from the luminosity peak. These background subtracted spectra are plotted in Figure 4.48, they are markedly different from the non-background subtracted spectra of Figure 4.44 as the emission lines have been corrected for the underlying Hα absorption. The values

Table 4.9: Spectral Line Values for Regions of NGC 5920 in MKW3s

Measurement	Region 1	Region 2	Region 3	Region 4	Region 5
[N II] λ **6548**					
Center (Å)	6537.4	6538.9	6536.4	6535.6	6534.1
Flux	0.14	1.36	0.63	0.16	0.18
FWHM (Å)	5.2	6.5	4.2	1.8	2.7
Hα					
Center (Å)	6554.3	6554.3	6553.9	6550.7	6547.7
Flux	0.74	3.42	2.04	0.28	0.41
FWHM (Å)	6.5	7.5	10.1	3.7	5.0
[N II] λ **6584**					
Center (Å)	6575.0	6574.8	6573.5	6572.0	6569.7
Flux	0.95	4.91	2.70	0.73	0.69
FWHM (Å)	5.8	6.6	6.1	4.7	6.0

Note: The central positions are given in terms of the rest wavelength. The flux is in units of 10^{-15} erg s^{-1} cm^{-2}. Regions 6 - 10 are not listed as they have no lines above the noise level. Errors in the flux measurements for the strong lines are of order 5-10%. Errors for determining the central wavelength are of order ~2 Å. W_o is not measured since the continuum level is too close to zero.

of the line centroid, flux, and FWHM (uncorrected for the instrumental line width) of the measured background subtracted emission lines are in Table 4.9. Often, the entire continuum has been subtracted, and so the equivalent widths in these cases are not shown.

Region 4 has been slightly over-subtracted as the continuum emission falls below zero, and an examination of the integrated background spectrum of Figure 4.47 shows some of the [N II] λ 6584 emission remains, filling in some Hα absorption. Hence, certainly some of the [N II] λ 6584 emission has been subtracted and the [N II] λ 6584/Hα ratios are lower limits. The lower limits of Log([N II] λ 6584/Hα) for Regions 1 - 5 are 0.11, 0.16, 0.12, 0.42, and 0.22, respectively. Therefore all emitting regions are likely ionized by a hard source, like AGN emission. The emission lines are blueshifted from the underlying population by $-560\,\mathrm{km\,s^{-1}}$. This is a known radio galaxy and the velocities are probably suggesting an outflow in our direction.

4.8 Abell 1651

The central region of the rich, BM type I-II (where the 1st rank galaxy is much brighter than the 2nd rank cluster galaxy), cooling flow cluster (White 2000) Abell 1651, is shown in Figure 4.49. This cluster is at a distance of ~340 Mpc, such that 1″ corresponds to

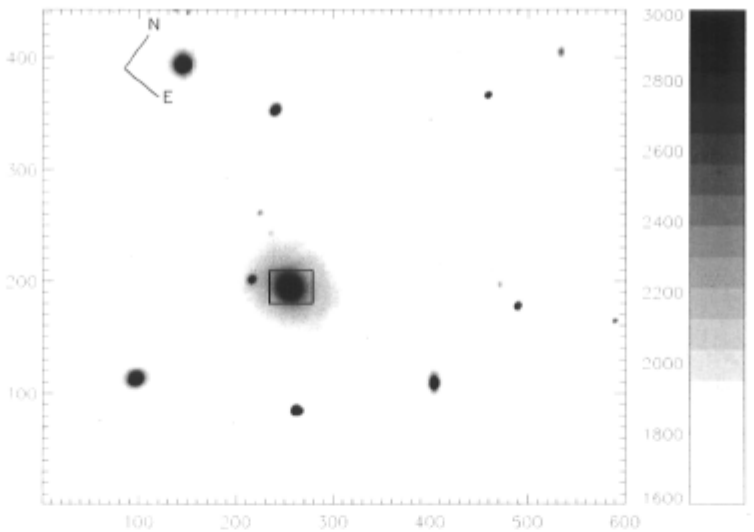

Figure 4.49: **The center of Abell 1651 taken in the i-filter.** *The IFU field is marked as a box with dimensions of 5 × 7″ (7.6 × 10.6 kpc) around the BCG. The scale is in arbitrary flux units.*

~1.5 kpc. The $5 \times 7''$ field of view of the IFU covers the central region of NGC 5920, 7.6×10.6 kpc. Each pixel covers a distance of ~150 pc on either side.

An image of the S/N in the continuum between 6850 and 6950 Å along with the image of the continuum emission itself are shown in Figure 4.50. Although it is not the highest S/N galaxy in the sample, it is comparable to that of the other galaxies. The continuum emission follows the same overall shape as the other BCGs, but flat field fringes on the left and right hand sides of the images are just visible.

Figure 4.51 displays the integrated spectra of the central and outskirt regions of the BCG in Abell 1651. The central spectrum is constructed by averaging 650 pixels at the center of the image, and the spectrum of the outskirts from 400 pixels on the left hand edge of the IFU (where the S/N is slightly higher). There are no emission lines detected in the BCG. Hα exists only in absorption. NaD is not covered in this configuration, so I make no estimate of the age or mass. I present in Figure 4.52, the luminosity profile of the i-band image for completeness. It shows that most of the intense emission from the BCG is constrained to within the IFU image. Although this cluster is a cooling flow, there are no signs of gas ionized by AGN emission, or from a population of hot young stars.

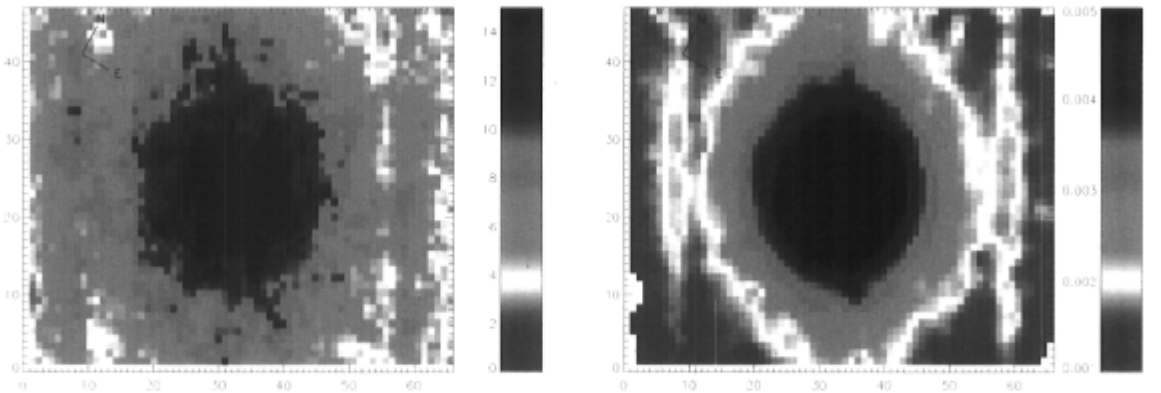

Figure 4.50: **Reconstructed images for the BCG in Abell 1651.** *Left Panel: S/N ratio of the continuum. Right Panel: Map of the continuum near Hα. The images are in reverse colour scale and in units of 10^{-15} erg s^{-1} cm^{-2} Å^{-1}. One pixel is ∼150 pc across, for all panels.*

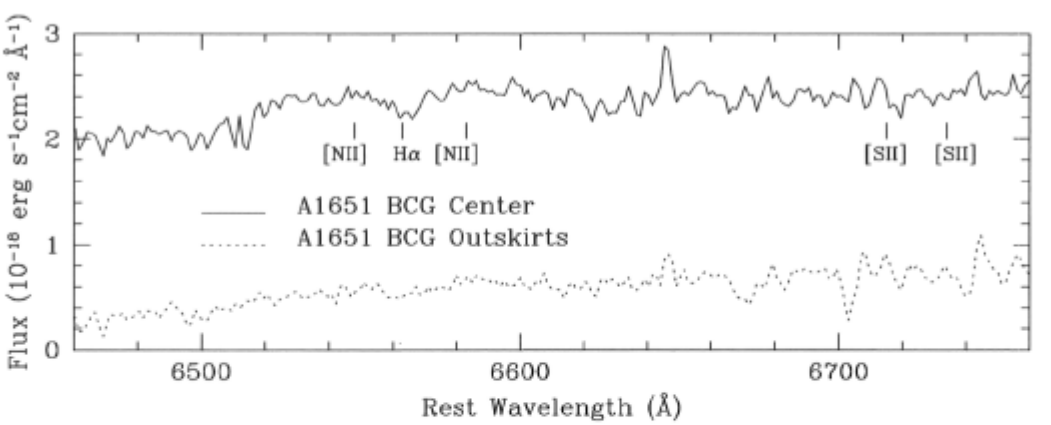

Figure 4.51: **Spectra of the center and outskirts of the BCG in Abell 1651.** *The combined, normalized spectrum of the center of the BCG in Abell 1651 are shown alongside the combined, normalized spectrum of regions on the outskirt.*

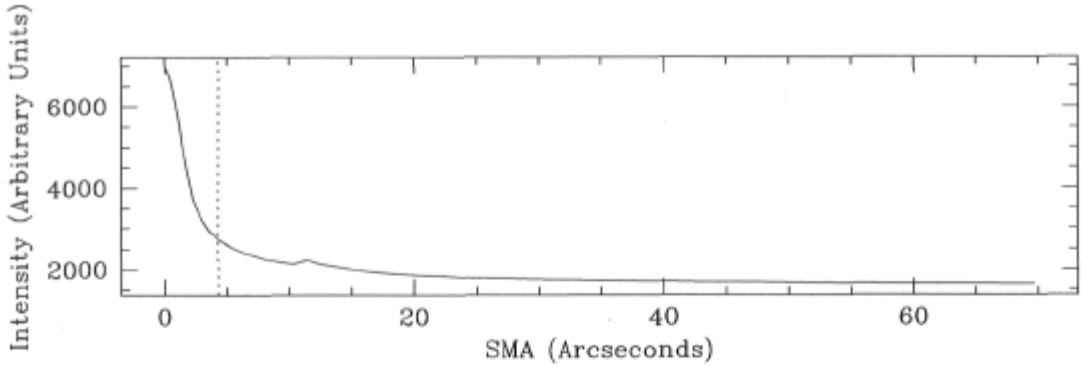

Figure 4.52: **Luminosity profile for the BCG in Abell 1651.** *Measured from the i-band acquisition image. The vertical dotted line marks the maximum extent of the IFU field of view. The x-axis displays the Semi-Major Axis as calculated using the IRAF task, ellipse.*

4.9 OASIS Observations and Data Reduction

Three additional BCGs in the cooling core clusters Abell 2052, Abell 2199, and Cygnus-A (see Table 4.1) were observed with the OASIS instrument at the William Herschel Telescope (WHT) on the nights of the 28th and 30th of June, 2005. Additional time on Cygnus-A was completed by Samantha Rix, the support astronomer, on the night of July 2, 2005. The imaging spectrometer is used with an enlarger such that the IFU covers $7.4 \times 10.3''$ and the 1100 lenslets capture the central region of the dominant galaxy in each cluster. The grating configurations only allow for a few hundred angstroms to be covered simultaneously. However I chose to observe the important regions surrounding the Hβ and Hα lines. Depending on the cluster redshift, the first region includes absorption features from old stellar populations (Hβ at 4861 Å, Mg_2 at 5177 Å, and Fe I $\lambda\lambda\lambda$ 5270, 5335, 5406) as well as emission lines from gas ionized by the young populations (Hβ and [O III] $\lambda\lambda$ 4959, 5007). The second region captures the [O I] $\lambda\lambda$ 6300, 6364, [N II] $\lambda\lambda$ 6548, 6583, Hα at 6563 Å, and [S II] $\lambda\lambda$ 6716, 6731 lines (see Table 4.2). These configurations both result in a spatial sampling of $0.26''$ and a dispersion of $2.2\,\text{Å}\,\text{pixel}^{-1}$. The spectral resolution of the MR1 and MR2 configurations is comparable, though a bit lower than for the GMOS IFU data being R $\simeq$ 1500 (according to the OASIS instrument webpages), or $\simeq 200\,\text{km}\,\text{s}^{-1}$. Integration times are listed in Table 4.2. Using the NAOMI adaptive optics corrector, the seeing throughout the observations was typically $0.7''$.

In order to reduce the OASIS data, a combination of three packages was used. The Euro3D (Sánchez 2004) package was utilized for visualization of the data cubes and IRAF for the manipulation of the processed data. The XOasis package, developed

by the TIGER (Bacon & et al. 2000) instrument team at the Centre de Recherche Astrophysique de Lyon (CRAL), was used for the bias subtraction, spectral extraction, flat fielding, and wavelength calibration as well as a first cosmic ray subtraction and absolute flux calibration. The cosmic rays were removed by median averaging, except in the sky frames where less than three exposures were taken. In this instance I used IRAF's *imreplace* to create a bad pixel mask and the *crfix* routine to interpolate across the cosmic ray ruined pixels. The sky subtraction itself was performed using IRAF after the flux calibration was completed in XOasis. I chose this method as opposed to the routines included in XOasis as there was a small LED accidentally left on in the instrument housing chamber during the observations. Consequently, the entire sky frame was subtracted from the entire object frame, as the signature of the LED is apparent in both frames (each with the same integration time). Abell 2199 had data taken in the MR516 configuration that was spread over two days. After sky subtraction, flux calibration and cosmic ray removal, the data from two days were averaged together.

The seeing of $0.7''$ is a few times larger than the spatial resolution, $0.26''$ of the configurations. Therefore, to account for this and to increase the signal-to-noise ratio, each pixel was combined with its closest 8 neighbours. The IRAF task *calib* was used to perform corrections for the atmospheric extinction. In order to achieve this for the dates of these observations, I applied the theoretical extinction curve for the WHT site, and the difference in the average r' extinction on the days of observation to the typical extinction at the WHT, given on their website. The tasks *deredden* and *dopcor* were used to perform corrections for the galactic extinction and the de-redshifting, respectively. Tables 4.1 and 4.2 show the values (obtained from NED) used for these last two corrections.

The final correction performed was to account for the internal extinction of the galaxies, and the *deredden* task was used for this. In the case of Cygnus-A, this data is of adequate quality to be able to create an extinction map of the galaxy based on the relative strengths of the Hα and Hβ emission lines. However, for the other two objects, the S/N and the strength of the Hβ emission line is too low, therefore an integrated value based on longslit data published by Crawford et al. (1999) is used. These are given in Table 4.2 under the column $E(B-V)_{int}$.

4.10 UGC 9799 in Abell 2052

Abell 2052 is a rich galaxy cluster of type BM I-II, at a distance of $\sim$145 Mpc, such that $1''$ corresponds to $\sim$0.7 kpc, and having a velocity dispersion of $\sim$530 km s^{-1}. This is an X-ray luminous cooling flow cluster with an X-ray luminosity of $L_X = 2.52 \times 10^{44}$ erg s^{-1} in the 0.1 - 2.4 keV band and a MDR $\simeq 30\,M_\odot\,yr^{-1}$ derived from *Chandra* observations (Blanton et al. 2003). A strong temperature drop from 3 keV to 1 keV in the central few arcseconds is indeed observed (Kaastra et al. 2004).

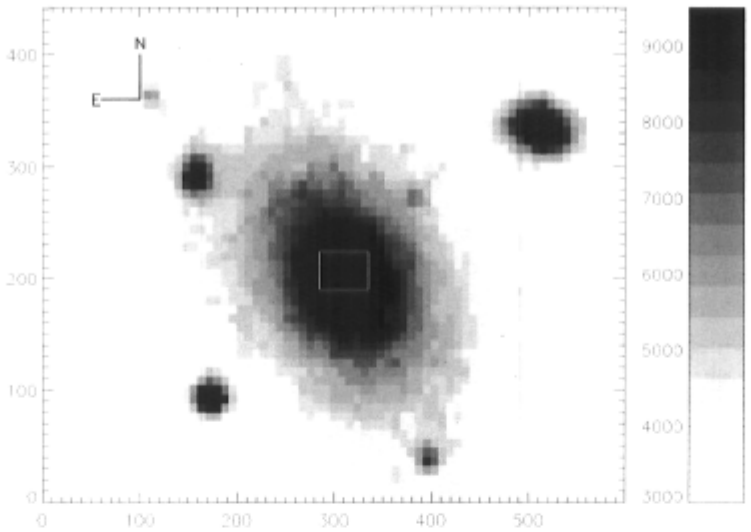

Figure 4.53: **UGC 9799 in the center of Abell 2052 taken in the DSS red filter.** *The IFU field is marked as a box with dimensions of 10.3 × 7.4″ (4.4 × 6.0 kpc) around UGC 9799, the BCG. The scale is in arbitrary flux units.*

The BCG, UGC 9799, is co-spatial with the highest X-ray temperatures of the cluster, as well as an X-ray point source. It is included as part of the NFPS dataset, which lists an Hβ emission. In the Crawford et al. (1999) sample it is listed as having low line luminosity, with a luminosity in Hα of $4.8 \times 10^{40}\,\mathrm{erg\,s^{-1}}$. From the emission line fluxes published in Crawford et al. (1999), the integrated line values can place the dominant emitting population on a BPT diagram. The values of Log([N II] λ 6584/Hα) = 0.35 and Log([O III] λ 5007/Hβ) = 0.98 place the ionizing source in the Seyfert part of the diagram. Edge et al. (2002) observed this BCG as part of their survey of molecular hydrogen in cooling flow clusters; they placed an upper limit on the H_2 luminosity of $2.2 \times 10^{39}\,\mathrm{erg\,s^{-1}}$. There is patchy dust found by Laine et al. (2003) around a point-like central source, associated with the optical AGN.

Based on a UV-IR ratio in excess of that for passively evolving non-cooling flow cluster elliptical and cDs, Hicks & Mushotzky (2005) derive a star formation rate of $0.19 \pm 0.08\,\mathrm{M_\odot\,yr^{-1}}$ within a radius of 7″ of the center of UGC 9799. These authors disregard any contribution from AGN as their images show no significant *central* UV excess. Blanton et al. (2003) analyze U-band observations, which have been decomposed by HST into two components: an unresolved core, and a second area surrounding this core. To calculate a SFR as well, they model the U-band emission from the galaxy as an $r^{1/4}$ profile, and the observed excess is attributed to a star forming population. They arrive at a value of $0.6\,\mathrm{M_\odot\,yr^{-1}}$ within a radius of 3″ from the center, and note that it is an upper limit as the central source likely contributes a small amount. Martel et al. (2002) have discovered a UV filament outside the central few kiloparsecs of the

nucleus, however it is not associated with optical line emission and they conclude it is not related to the cooling flow.

An image of the Hα + [N II] line emission by Baum et al. (1988) reveals emission extended over ~30 - 40″. This line emission is coincident with the bright X-ray rims that surround large radio bubbles emanating from the bright radio source 3C 317 (Blanton et al. 2001) which is at the center of UGC 9799. The regions where obvious interaction exists between the X-ray, radio, and line emitting species are outside of the OASIS field of view. Although Blanton et al. (2003) state the AGN contribution to their star formation rate is small, Tadhunter et al. (2002) have found that the UV-excess in radio galaxies can have significant contributions from star formation as well as from AGN.

Figure 4.53 draws the location of the $7.4 \times 10.3''$ window, which covers the central 5.1×7.1 kpc of UGC 9799, in Abell 2052. There are no broad filter acquisition images taken for the OASIS data, so the image of the cluster center shown is derived from publicly available data. In this case, a red filter image from the DSS is used.

Since the AGN seems to be confined to the inner 2.5″ (Blanton et al. 2003), the OASIS field of view should be able to discriminate the effect of the central AGN from that of a young stellar population, if the latter is significant. An analysis of the emission line dynamics of the central line flux in this area is also presented here.

4.10.1 Line Images and Region Spectra

The image of the continuum of UGC 9799 in Abell 2052 between 6380 and 6430 Å is shown in Figure 4.54. Also shown are the images of the continuum-subtracted Hα flux, the continuum-subtracted [N II] λ 6584 emission, and the continuum-subtracted [S II] λ 6716 + λ 6731 flux. Overall, the morphology of the emission lines is similar, with strong line emission following the same distribution, and sharing the same peak location as the continuum light. Although, in Hα the structure is less smooth, and the bright core extends a few pixels South. Faint halos surround the intense emission in all three lines.

The S/N in the red configuration is ~10, but falls to between 3 and 5 in the blue configuration, as seen in Figure 4.55. The blue continuum is measured between 5025 and 5100 Å and shown in Figure 4.54. It is of lower flux, but shares the same condensed, regular elliptical morphology as the continuum near Hα. Also on the Figure 4.54 is the low intensity [O III] λ 5007 emission, again with the condensed, regular morphology as in the continuum images. There are no strong Hβ emission lines, so no image of this is presented.

Within each of eight regions, similar spectra are co-added in order to increase the S/N, and explore the spectral variation. The chosen regions are labeled on the Hα panel of Figure 4.54 and allow investigation of several areas within the Hα emission, including: Regions 1, 3, 6, and 7 on the edge of the bright central emission, Region 2, with the highest Hα flux, and Region 4 with lower Hα flux. Regions 5 and 8 have little

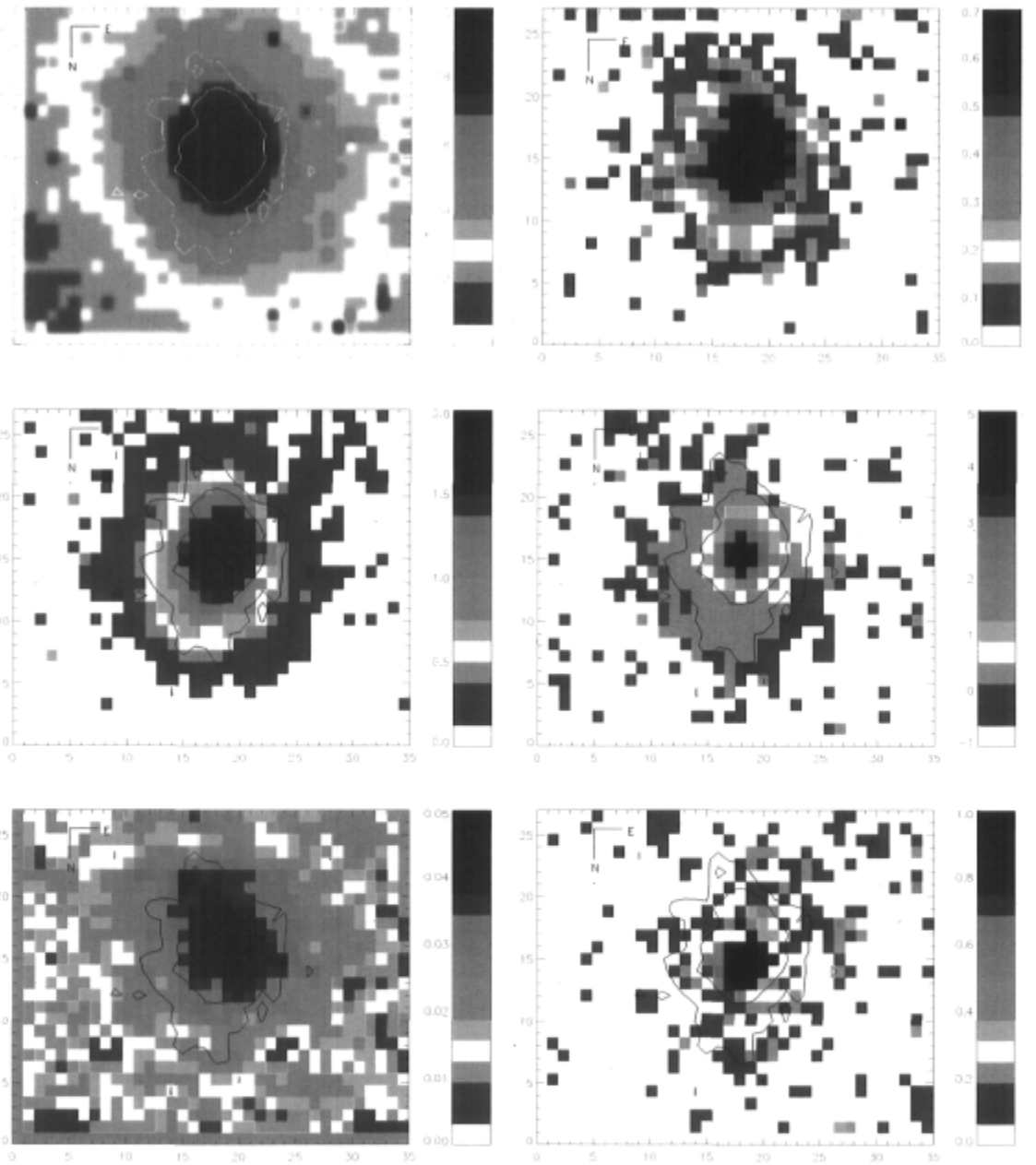

Figure 4.54: **Reconstructed images for UGC 9799 in Abell 2052.** *Top Left Panel: The continuum surrounding the Hα emission line. Top Right Panel: The continuum-subtracted Hα emission flux. The regions used in the subsequent analysis are represented as boxes. Middle Left Panel: The continuum-subtracted [N II] λ 6584 flux. Middle Right Panel: The continuum-subtracted [S II] λ 6716 + λ 6731 flux. Bottom Left Panel: The continuum surrounding the Hβ emission line for UGC 9799 in the center of Abell 2052. Bottom Right Panel: The continuum-subtracted [O III] λ 5007 flux. All images are reverse colour scale and in units of 10^{-16} erg s^{-1} cm^{-2} Å^{-1}. The contours represent the Hα flux. One pixel is ∼150 pc across, for all panels.*

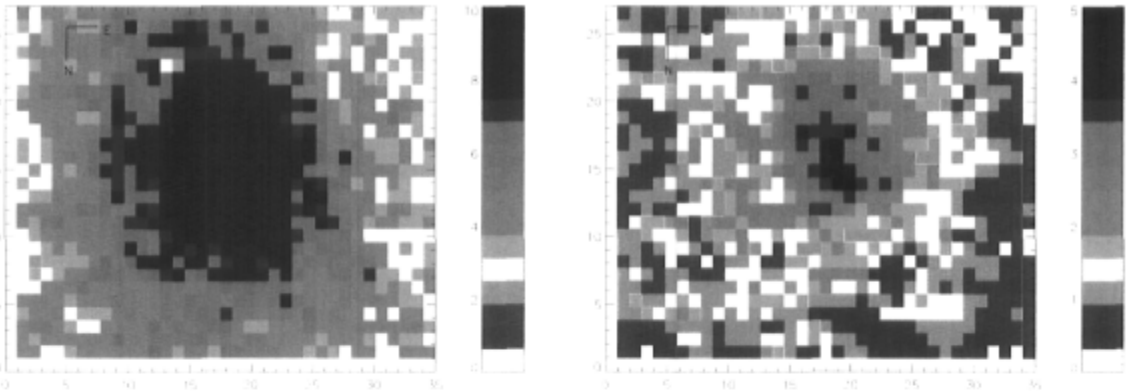

Figure 4.55: **S/N ratio of the continuum for UGC 9799 in Abell 2052.** *The S/N of the continuum around Hα is shown on the left, and the S/N of the continuum around Hβ is shown on the right. One pixel is ~150 pc across.*

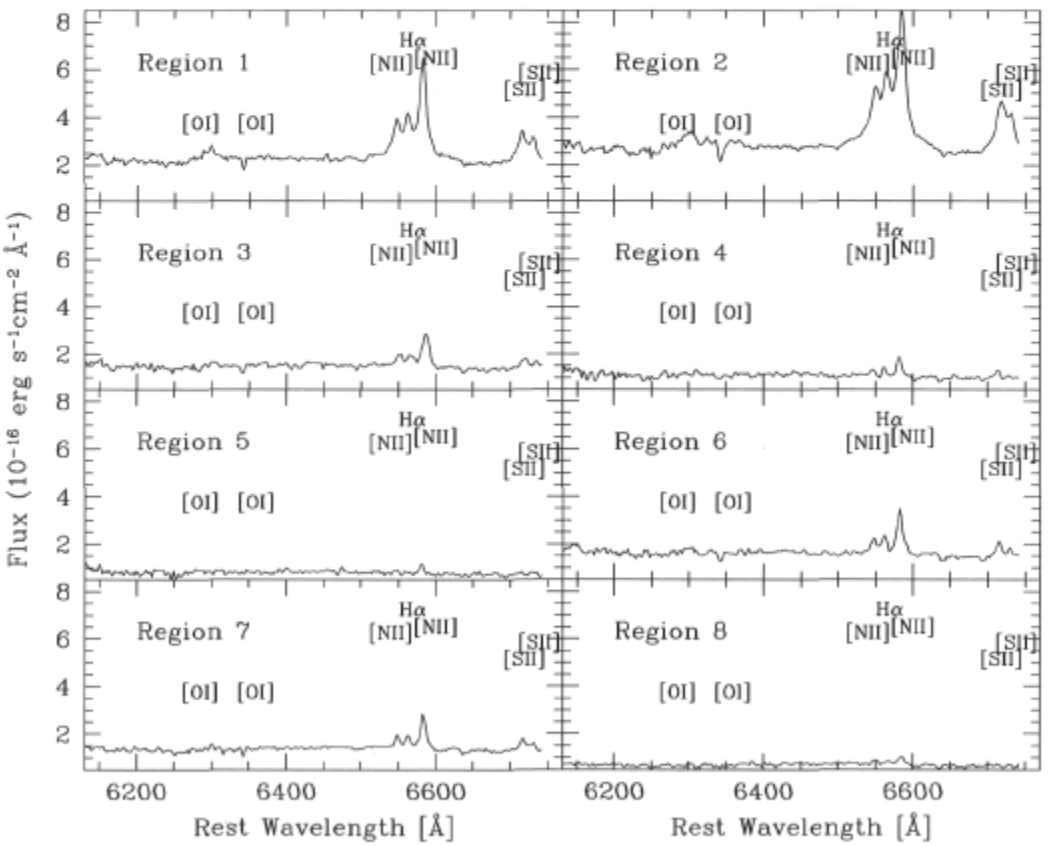

Figure 4.56: **Summed spectra of the 8 selected regions of the Hα image of UGC 9799 in Abell 2052.** *Prominent emission features are labeled.*

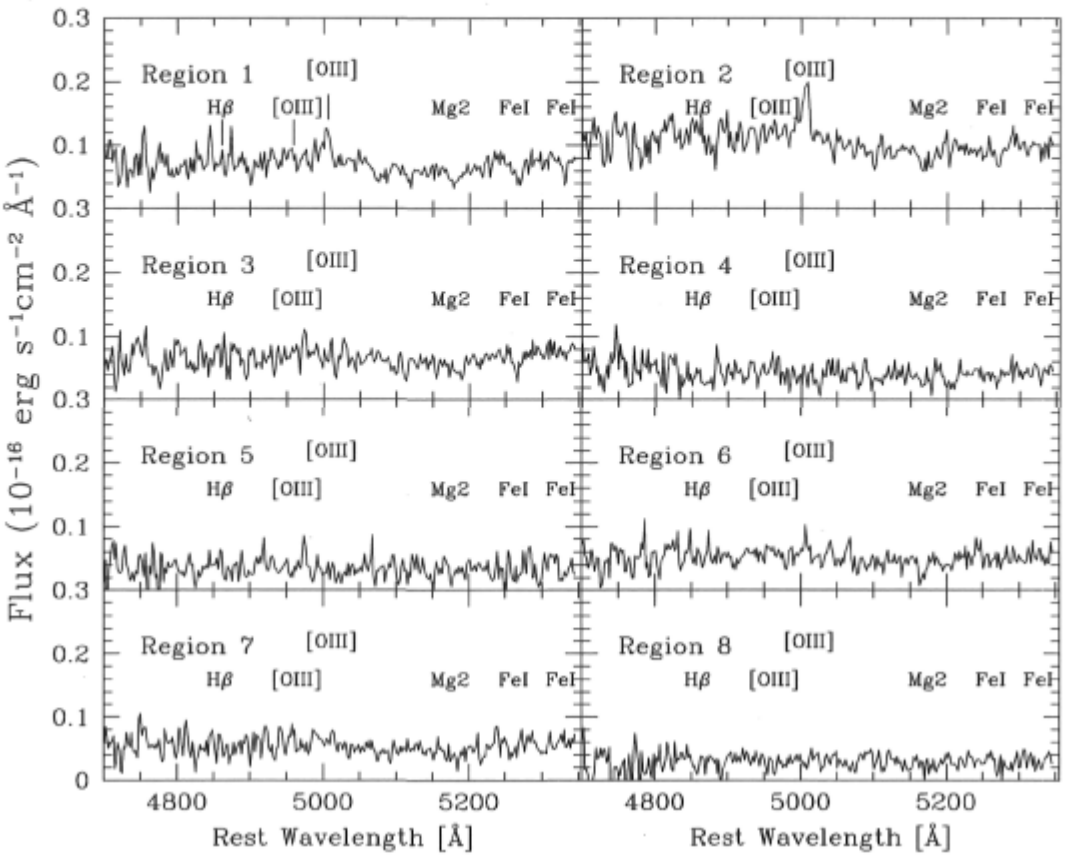

Figure 4.57: **Median combined spectra of the 8 selected regions of the Hβ image of UGC 9799 in Abell 2052.** *Prominent emission features are labeled.*

or no emission.

All of the regions cover 4×4 pixels, $\sim$710 pc on either side. The integrated spectra of these regions are presented in Figure 4.56, and are as previously labeled. Strong emission lines in this spectral region are [O I] λ 6300, Hα, [N II] $\lambda\lambda$ 6548,6584, and [S II] $\lambda\lambda$ 6716,6731. The relative intensities of these lines are a characteristic AGN signature (note that the spectral resolution is only 2.2 Å here, so the lines appear more broad than in the Gemini observations). The blue spectra in Figure 4.57 are very noisy, however they show [O III] λ 5007 emission is stronger in Regions 1 and 2. These spectra are of very poor S/N, and it is not possible to detect Hβ in absorption or emission above or below the level of the noise. The strong absorption lines of Mg_2 and Fe I from the underlying galaxy are clearly seen in all Regions 1, 2, and 3. These absorption lines are all clear in the total spectrum which is an average of all spectra (not shown here, but see Figure 4.58).

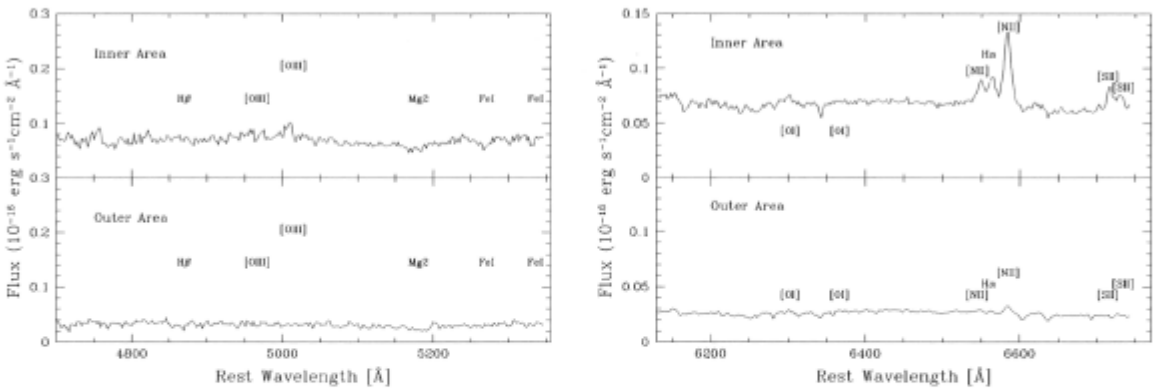

Figure 4.58: **Spectra for the center and outskirts of UGC 9799 in Abell 2052.** *The median averaged spectrum of the center alongside that of the outskirts. Left Panel: The blue portion of the spectrum. Right Panel: The red portion of the spectrum.*

4.10.2 The Underlying Population

The age of the underlying population is determined by comparing observed Fe I λ 5270 and Mg_2 λ 5177 absorption line equivalent widths to the theoretical values given by Mollá & García-Vargas (2000). The same technique which was followed for the NaD line in the Gemini IFU data is used here. The equivalent width from Fe I λ 5335 is not used as the fits produce a shifted centroid, likely due to the low signal-to-noise ratio, and the shallowness of the absorption. Because the integrated spectrum of the 350 pixels in the outer area of the image (where the Hα emission is lowest) produce a spectrum in which the absorption lines are too low to be measured accurately, I use measurements based on the integrated spectrum of the 350 inner pixels, since the inner spectra have a much higher S/N (see Figure 4.55). The continuum in this area may contain emission from the ionizing source, however, the metal absorption line equivalent widths which are produced by the older population, should not be significantly affected. The measured equivalent width of Fe I λ 5270 is 3.5 Å, and that of Mg_2 λ 5177 is 4.7 Å. This large equivalent widths for both these lines agree only with a supersolar metallicity ($2\,Z_\odot$), and best match an age of $\sim 8 \times 10^9$ yr for this type of population. An Hβ equivalent width of 1.4 Å is predicted. Unfortunately, attributing the Hβ values in our spectra to a particular population is not a clean process. That is, despite the low S/N around the Hβ region, there appears to be no Hβ in absorption or emission. It could be that strong emission from whatever is causing the strong Hα emission is conspiring with deep Hβ absorption from a young or moderately aged stellar population to produce a flat Hβ level. This problem should be minimized away from the intensely emitting regions. Unfortunately the low S/N is a likely cause of the lack of an Hβ line, as shown in the left panel of Figure 4.58 which displays the integrated spectrum from 350 pixels near

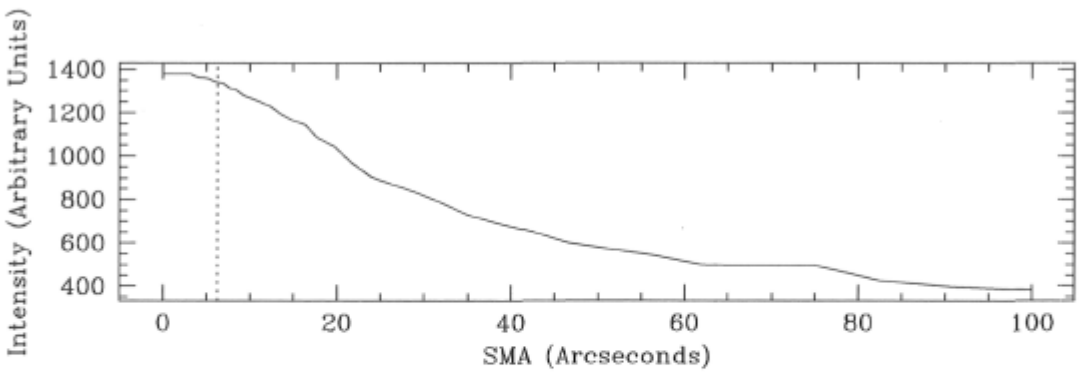

Figure 4.59: **Luminosity profile for UGC 9799 in Abell 2052.** *Measured from the DSS red filter image. The vertical dotted line marks the maximum extent of the OASIS field of view. The x-axis displays the Semi-Major Axis as calculated using the IRAF task, ellipse.*

the outer edge of the image, away from the emitting zone.

Even away from the bright line emitting center of the image some emission lines remain, which suggests the outer regions are not completely free from pollution of the source which is producing the emission lines. As seen in the right panel of Figure 4.58 which shows some [N II] λ 6584 emission in the red spectra for the outer area, there is still some contamination from the emission away from the center. Though the effect of the ionizing source is much less on the outskirts, it is not completely removed. Therefore, the mass determined from the continuum level of the integrated outer area spectrum likely includes some continuum emission from the source that is causing the emission lines, and therefore the value of $1.3 \times 10^7\ M_\odot\ kpc^{-2}$ is an upper limit.

4.10.3 Line Measurements and the Ionization Mechanism

Before measuring the emission line strengths in each region, a scaled spectrum from the outer 350 pixels, shown in Figure 4.58, is subtracted from the region spectra. Figure 4.59 displays the luminosity profile of UGC 9799 from the DSS red filter data. It shows that much of the BCG emission is not captured by the IFU image. But, the overall shape is the same as that for the radial cut in the continuum emission (near Hα) across the center of the galaxy in the IFU image (created assuming spherical symmetry), which is shown in Figure 4.60. The scale factor is determined using this data of Figure 4.60. The measured values of the background subtracted line center, flux, equivalent width and FWHM (uncorrected for the instrumental profile) of the emission lines are shown in Table 4.10.

Figure 4.61 shows an image of the [N II] λ 6584/Hα ratio from the unsubtracted

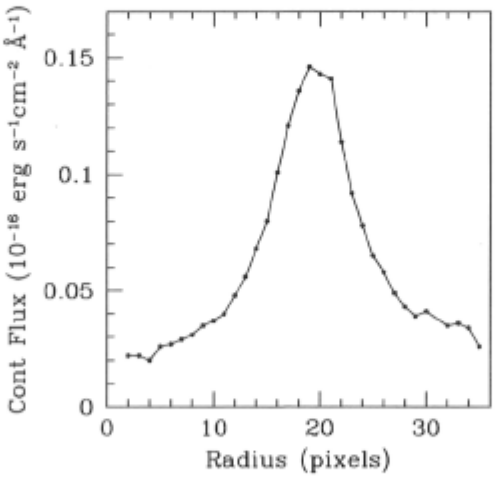

Figure 4.60: **Radial cut in the continuum for UGC 9799 in Abell 2052.** *This presents a horizontal cut across the central row of pixels in the continuum image.*

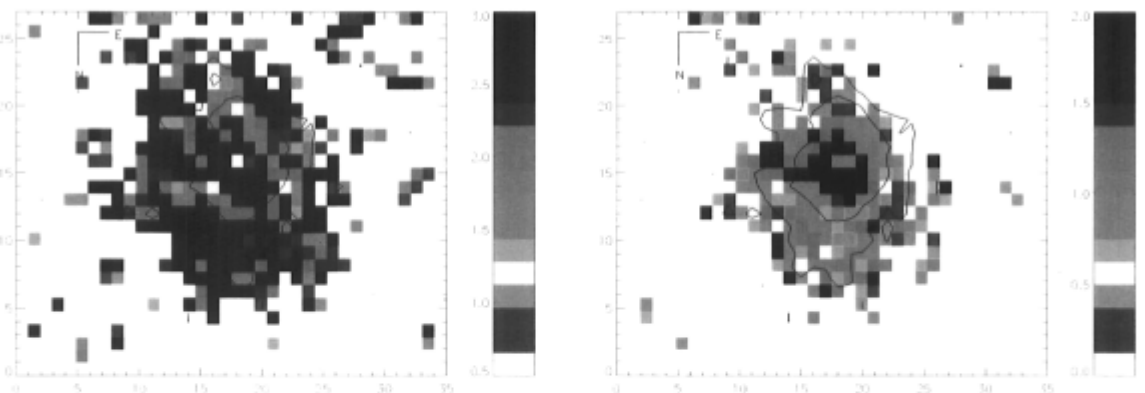

Figure 4.61: **Line ratio maps for UGC 9799 in Abell 2052.** *Left Panel: Map of the [N II] λ 6584/Hα ratio. Right Panel: Map of the ([S II] λ 6716 + [S II] λ 6731)/Hα ratio. The Hα flux is overlain as contours. One pixel is ∼180 pc across.*

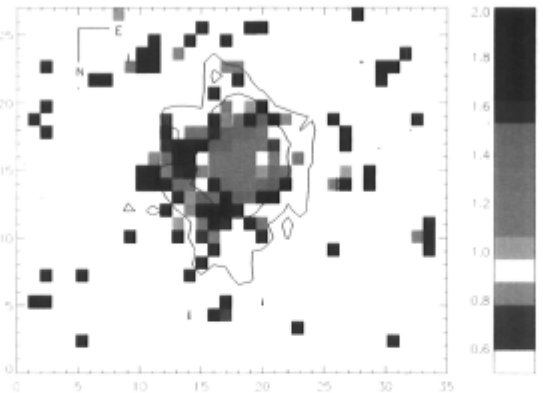

Figure 4.62: **Map of the [S II] λ 6716/ [S II] λ 6731 ratio for UGC 9799 in Abell 2052.** *The Hα flux is overlain as contours. One pixel is ∼180 pc across.*

spectra. No Hα absorption is resolved in the background spectra, so the ratios are similar to those of the background subtracted region spectra, however, the continuum level of the latter become more representative of the ionizing population. Some [N II] λ 6584 emission is still apparent on the spectrum of the outer pixels, therefore some excess of [N II] λ 6584 emission is being subtracted, likely more than Hα, so the [N II] λ 6584/Hα ratios from Table 4.10 are lower limits.

The map of the [N II] λ 6584/Hα shows ratios characteristic of ionization due to AGN activity, as opposed to hot stars. Even all of the background corrected ratios of the region spectra have Log([N II] λ 6584/Hα) > 0.30, firmly placing them on the AGN side of the BPT diagram. The [O III] λ 5007 emission from Regions 1, 2, and 6 is measureable above the noise, but the Hβ emission is not detectable. This means that in these regions the [O III] λ 5007 emission is stronger than the Hβ emission and so the [O III] λ 5007/Hβ ratio is $\gtrsim 1$. This does little to help further constrain the AGN emission as either Seyfert or LINER, but recalling the integrated ratio from Crawford et al. (1999) of 9.5 cited in the introduction to this section, the emission is likely to be due to a Seyfert nucleus. The ([S II] λ 6716 + [S II] λ 6731)/Hα line ratio is also shown in Figure 4.61. The same conclusions are reached from the ([S II] λ 6716 + [S II] λ 6731)/Hα BPT diagram (not shown) as all region spectra have ratios > 1.10, well within the AGN side of the diagram. Therefore, it is not possible to use the Hα emission line to search for any young stellar population.

The ratio of [S II] λ 6716/ [S II] λ 6731, is shown in Figure 4.62 and ranges from ∼0.8 to ∼1.8. Figure 5.8 of Osterbrock & Ferland (2006) shows the calculated variation of the intensity ratio as a function of n_e for a temperature of 10^4 K. This implies electron densities $\leq 2000\,\mathrm{cm}^{-3}$. This is not atypical for condensations found in H II regions, which have $n_e \simeq 3 \times 10^3\,\mathrm{cm}^{-3}$ (Osterbrock & Ferland 2006). Densities on the order of $10^3\,\mathrm{cm}^{-3}$ are also typical of Seyfert 2 galaxies (Osterbrock & Ferland 2006).

Table 4.10: Spectral Line Values for Regions of UGC 9799 in Abell 2052

Measurement	Region 1	Region 2	Region 3	Region 4	Region 5	Region 6	Region 7	Region 8
[O III] λ 5007								
Center (Å)	5004.64	5007.6	-	-	-	5006.9	-	-
Flux	0.85	0.82	-	-	-	0.24	-	-
W_o (Å)	−6.0	−9.7	-	-	-	−3.7	-	-
FWHM (Å)	10.1	10.7	-	-	-	4.4	-	-
[O I] λ 6300								
Center (Å)	6297.4	6304.6	6304.7	-	-	-	6300.6	-
Flux	0.69	2.98	0.46	-	-	-	0.16	-
W_o (Å)	−4.0	−33.7	−9.8	-	-	-	−2.1	-
FWHM (Å)	18.0	51.7	26.7	-	-	-	12.9	-
[N II] λ 6548								
Center (Å)	6547.5	6553.7	6551.5	6545.7	6546.1	6547.5	6548.8	6550.0
Flux	1.98	6.00	0.38	0.15	0.06	0.49	0.36	0.13
W_o (Å)	−10.9	−55.2	−6.8	−2.4	−1.6	−6.2	−4.2	−4.0
FWHM (Å)	14.0	27.0	8.6	6.4	5.0	8.6	6.6	7.0
Hα								
Center (Å)	6563.4	6566.6	6567.2	6561.1	6558.5	6561.3	6563.2	6567.7
Flux	2.29	1.72	0.59	0.21	0.03	0.71	0.50	0.14
W_o (Å)	−12.6	−15.7	−10.7	−3.5	−0.8	−8.9	−5.8	−4.3
FWHM (Å)	13.1	9.7	13.7	5.2	2.0	9.6	10.4	9.7
[N II] λ 6584								
Center (Å)	6582.7	6584.6	6586.7	6581.4	6580.4	6582.1	6583.4	6584.7
Flux	4.82	8.32	1.29	0.61	0.23	1.67	1.16	0.27
W_o (Å)	−26.5	−74.8	−23.4	−10.5	−6.5	−20.7	−13.4	−8.6
FWHM (Å)	12.0	16.0	10.3	7.3	5.4	10.1	8.8	10.5
[S II] λ 6716								
Center (Å)	6716.2	6718.7	6718.9	6713.3	-	6715.5	6717.4	-
Flux	1.58	2.99	0.44	0.26	-	0.65	0.45	-
W_o (Å)	−9.1	−24.4	−8.1	−4.7	-	−8.8	−5.4	-
FWHM (Å)	13.8	15.0	8.7	8.1	-	10.2	8.8	-
[S II] λ 6731								
Center (Å)	6731.1	6732.5	6735.3	6728.5	-	6729.5	6730.5	-
Flux	0.80	0.76	0.18	0.05	-	0.16	0.20	-
W_o (Å)	−4.5	−5.7	−3.2	−0.8	-	−2.1	−2.4	-
FWHM (Å)	8.5	7.1	6.5	4.6	-	4.6	6.9	-

Note: The central positions are given in terms of the rest wavelength. The flux is in units of 10^{-15} erg s^{-1} cm^{-2}. Errors in the flux measurements for the strong lines are of order 5-10%.The weak lines of [S II] have large errors of 20-30%.

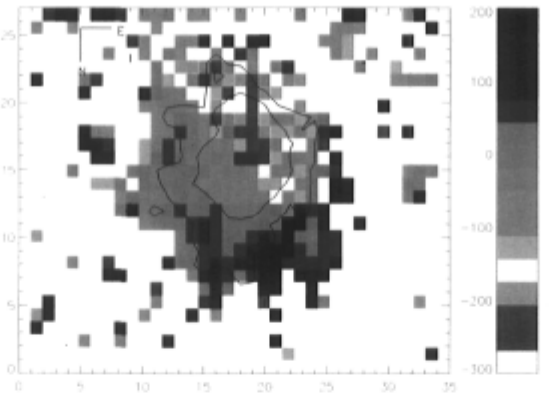

Figure 4.63: **Map of the Hα relative velocity for UGC 9799 in Abell 2052.** *The Hα flux is overlain as contours. The scale is in units of km s^{-1}, and values for pixels with bad Hα line fits are plotted as having zero relative velocity. One pixel is ∼180 pc across.*

4.10.4 Kinematics

The relative velocity map of Hα is shown in Figure 4.63. The relative velocity in the Hα emitting regions goes from $-300\,\mathrm{km\,s^{-1}}$ to $+200\,\mathrm{km\,s^{-1}}$. The figure shows negative velocities to South of the center of the emission, and more positive velocities North, and North-East of the center of the line emitting region. However, compared to cases with clear signs of rotation where the velocity gradient develops smoothly from positive to negative along an axis, in this case, it is less clear as to whether there is rotation or an outflow.

4.11 NGC 6166 in Abell 2199

Abell 2199 is a rich cluster of type BM I, located at a distance of ∼125 Mpc (see Table 4.1), such that $1''$ corresponds to ∼0.6 kpc, and has a velocity dispersion of $\sim 650\,\mathrm{km\,s^{-1}}$. This X-ray luminous cooling flow cluster has an estimated MDR of $12\,\mathrm{M_\odot\,yr^{-1}}$ (Johnstone et al. 2002) and an X-ray luminosity of $\mathrm{L_X} = 3.70 \times 10^{44}\,\mathrm{erg\,s^{-1}}$ in the 0.1 - 2.4 keV band. Johnstone et al. (2002) show the X-ray temperature dropping from 4.5 keV to 1.6 keV in the central few arcseconds.

The BCG, NCG 6166, is coincident with the peak in X-ray surface brightest, and is also included in the NFPS dataset showing Hβ emission. A low level Hα line luminosity of $3.5 \times 10^{40}\,\mathrm{erg\,s^{-1}}$ has been observed by Crawford et al. (1999). McNamara & O'Connell (1989) find evidence for a small spatially extended UV continuum excess which they attribute to a population of hot young stars with a star formation rate of $0.19 \pm 0.05\,\mathrm{M_\odot\,yr^{-1}}$. NGC 6166 is part of the Edge et al. (2002) sample, having an upper limit on $\mathrm{L_{H_2}}$ of $2.4 \times 10^{39}\,\mathrm{erg\,s^{-1}}$. Salomé & Combes (2003) were also unable to

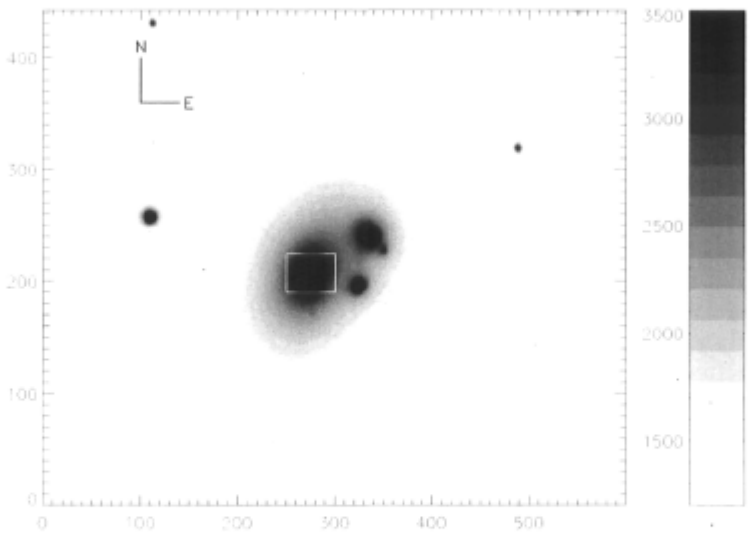

Figure 4.64: **NGC 6166 in the center of Abell 2199 taken in the Gemini i-filter.** *The IFU field is marked as a box with dimensions of 10.3 × 7.4″ (4.4 × 6.0 kpc) around NGC 6166, the BCG. The scale is in arbitrary flux units.*

detect any CO gas; they calculate an upper limit for the mass of H_2 of $2.6 \times 10^8\,M_\odot$. NGC 6166 is associated with the radio source 3C 338, whose core is coincident with the X-ray peak, and the center of NGC 6166. The radio lobes extend to ∼25 kpc and appear to be interacting with the hot gas (Owen & Eilek 1998) and are coincident with the X-ray surface brightness depressions seen by Johnstone et al. (2002).

The scale of the X-ray/radio interactions (∼30 kpc) is much larger than the OASIS field of view. In this thesis I present an analysis of the central $7.4 \times 10.3''$ region of NGC 6166, which covers a physical area of 4.4×6.0 kpc, as shown on Figure 4.64. The images of cluster center is the i-band image from the Gemini GMOS acquisition camera (N20030326S0115, from the Gemini Science Archive).

4.11.1 Line Images and Region Spectra

The continuum image of NGC 6166 in Abell 2199 between 6650 and 6700 Å is shown in Figure 4.65 with the continuum-subtracted Hα flux image, the continuum-subtracted [N II] λ 6584 emission, and the continuum-subtracted [S II] λ 6716 + λ 6731 emission. The continuum image shows a smooth increase in brightness towards the center, without any prominent dust features. The peak of the Hα emission does coincide with the peak of the continuum flux, however, a second Hα bright peak, not noticeable in any of the other line images is seen to the South. The Hα flux continues to extend towards the East, a morphology that is mirrored in the [S II] λ 6716 + λ 6731 emission line image, although the [N II] λ 6584 line image is much more condensed. The elliptical

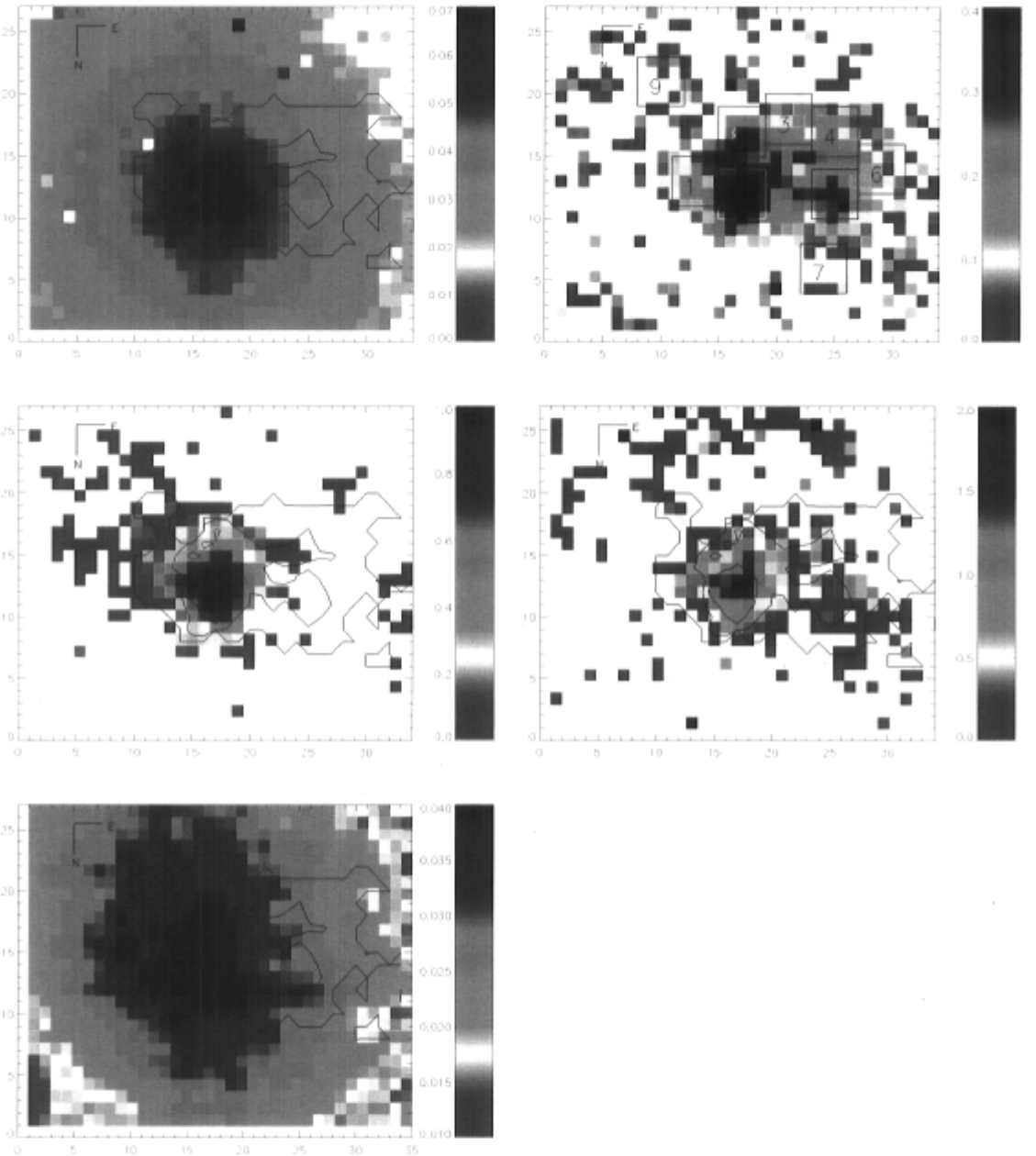

Figure 4.65: **Reconstructed images for NGC 6166 in Abell 2199.** *Top Left Panel: The continuum surrounding the Hα emission line. Top Right Panel: The continuum-subtracted Hα emission flux. The regions used in the subsequent analysis are represented as boxes. Middle Left Panel: The continuum-subtracted [N II] λ 6584 flux. Middle Right Panel: The continuum-subtracted [S II] λ 6716 + λ 6731 flux. Bottom Left Panel: The blue continuum. All images are reverse colour scale and in units of* $10^{-16}\,erg\,s^{-1}\,cm^{-2}\,Å^{-1}$. *The contours represent the Hα flux. One pixel is ∼150 pc across for all panels.*

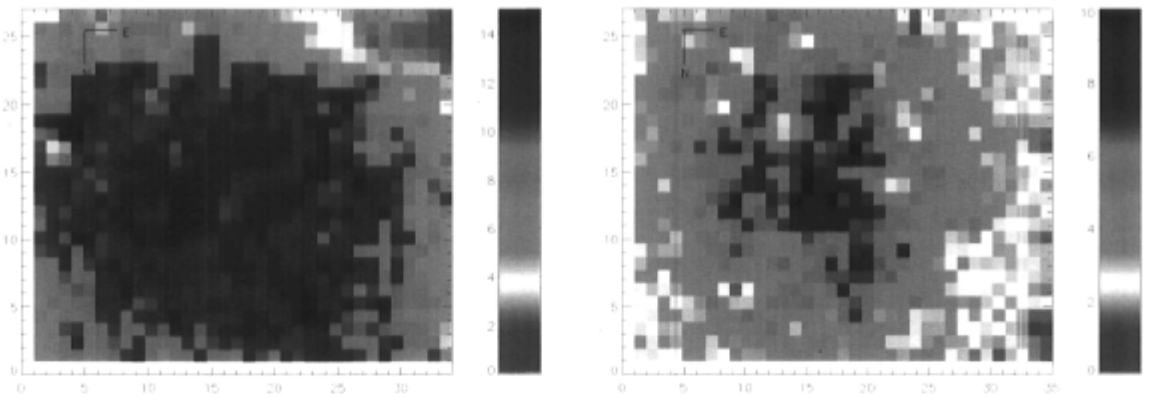

Figure 4.66: **S/N ratio of the continuum for NGC 6166 in Abell 2199.** *The S/N of the continuum around Hα is shown on the left, and the S/N of the continuum around Hβ is shown on the right. One pixel is ∼150 pc across.*

morphology of the continuum in the blue, between 5025 and 5100 Å (Figure 4.65) is similar to that seen for the red continuum, though it is less condensed. The individual pixels of the blue configuration show no strong Hβ or [O III] λ 5007 line emission.

Figure 4.66 shows that the S/N in the conitnuum of the individual pixels is in general at least 10 for the red spectra, though lower in the blue spectra, closer to $\simeq 6$.

Within each of nine regions, similar spectra are co-added increasing the S/N. Labeled on Figure 4.65, they are chosen for an investigation of several areas within the Hα emitting area. Regions 1, 3, 4, and 6 trace the lower Hα emission on the edge of the emitting area, Regions 2, 5, and 8 are at the Hα emission peak, Regions 7 and 9 gather spectra away from the Hα emitting area and thus represent the underlying cD galaxy.

All of the regions cover ∼630 pc on either side. The integrated spectra of these regions are presented in Figures 4.67 and 4.68, and are as previously labeled. Strong emission lines in the red spectral region are [O I] λ 6364, Hα, [N II] λλ 6548,6584, and [S II] λλ 6716,6731. However, the [S II] lines are not well separated. There is an emission feature at a wavelength of 6475 Å seen in all of the pixels. This is not at the wavelength of a strong known sky line, nor is it at the position of any well know emission lines for a typical LINER. When the spectrum of an individual pixel is examined, this feature shows three emission peaks with the same wavelength differences and flux ratios as the Hα-[N II] emission line complex. However, the difference in velocity is $\sim 5000\,\mathrm{km\,s^{-1}}$. This difference suggests that if the emission were real it would not be physically associated with the main Hα-[N II] system. There are several artificial spectral features in the region below 6400 Å in this dataset (which are not shown), and it is possible this too could be an artifact.

The blue spectra shown in Figure 4.68 are noisy. No evidence of [O III] λ 5007 emission or Hβ absorption or emission is seen except in Regions 2 and 8. The strong

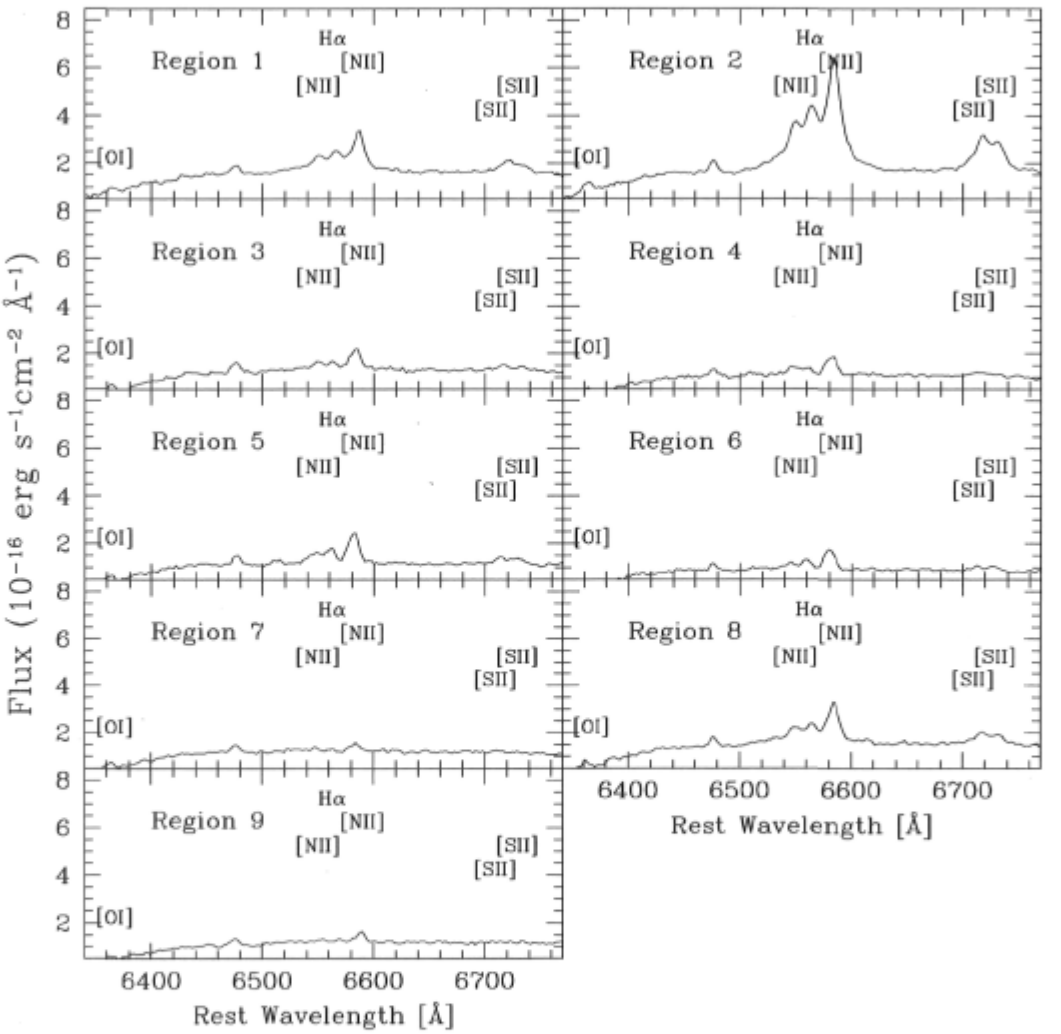

Figure 4.67: **Summed spectra of the 9 selected regions of the Hα image of NGC 6166 in Abell 2199.** *Prominent emission features are labeled.*

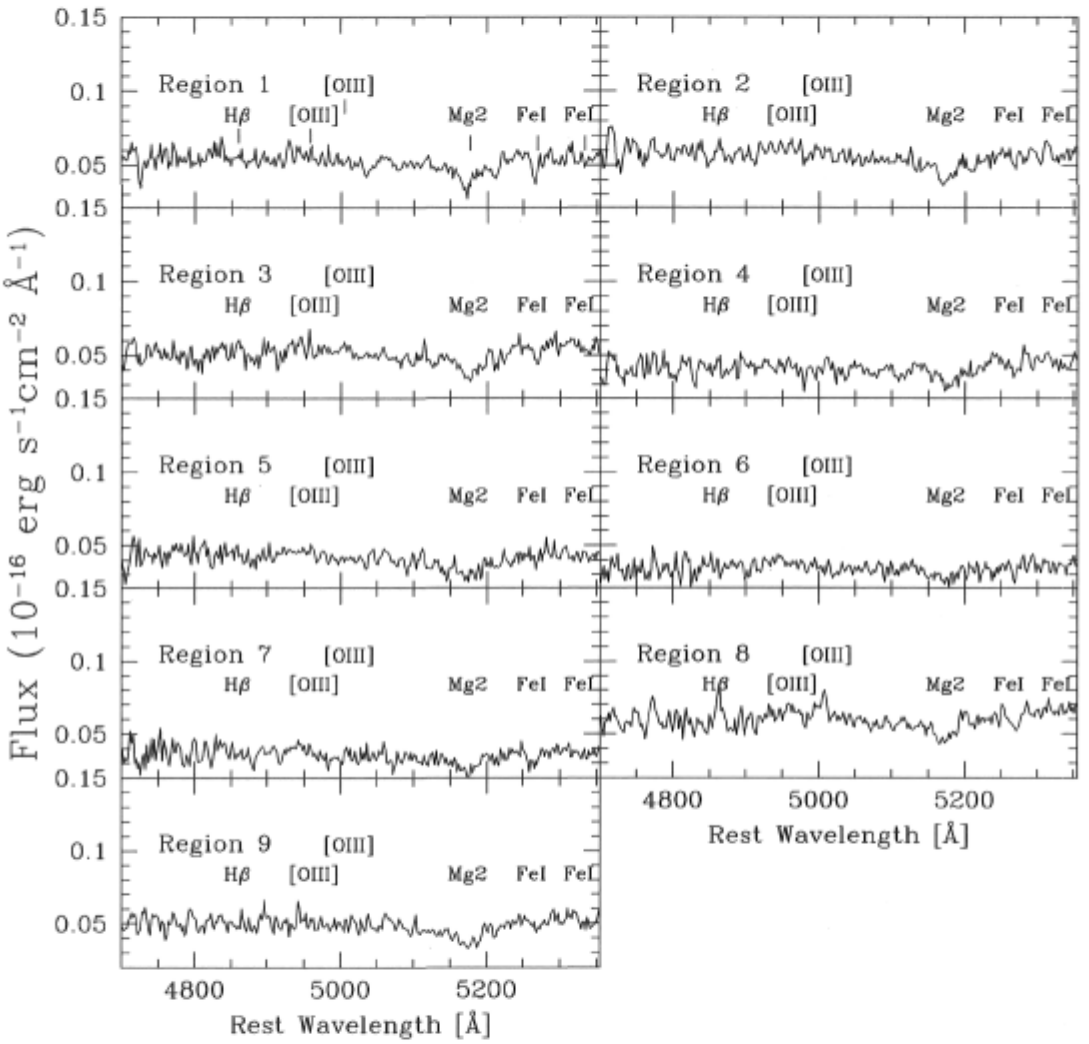

Figure 4.68: **Median combined spectra of the 9 selected regions of the Hβ image of NGC 6166 in Abell 2199.** *Prominent emission features are labeled.*

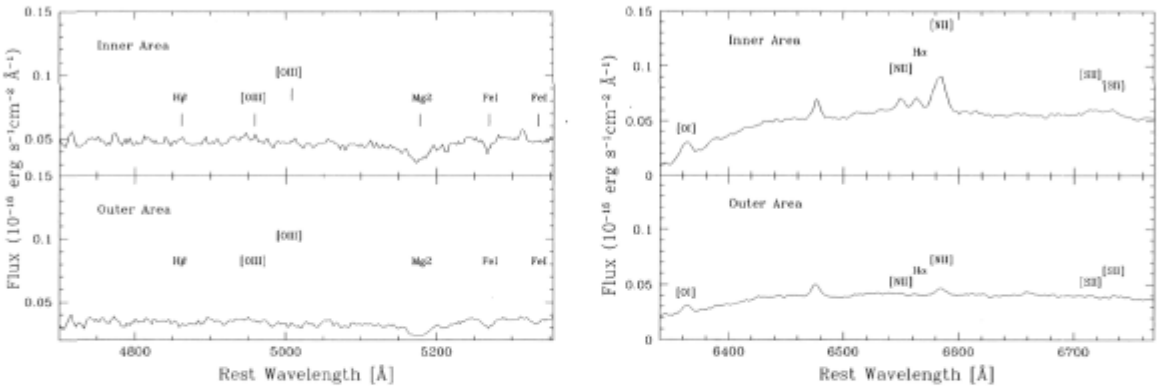

Figure 4.69: **Spectra for the center and outskirts of NGC 6166 in Abell 2199.** *The integrated spectrum of the central 230 pixels showed above the integrated spectrum of the outer 420 pixels. Left Panel: The blue portion of the spectrum. Right Panel: The red portion of the spectrum.*

absorption lines of Mg_2 λ 5177, Fe I $\lambda\lambda$ 5270, 5335 from the underlying galaxy are apparent in all regions.

4.11.2 The Underlying Population

Using the same method as for UGC 9799 of Abell 2052 in Section 4.10, the age of the underlying population is determined from the equivalent widths of Fe I $\lambda\lambda$ 5270,5335 and Mg_2 λ 5177 measured off of the median averaged integrated spectrum of 420 pixels on the outskirts (outside of the Hα emitting zone). This integrated spectrum is shown in Figure 4.69, alongside the corresponding integrated spectrum of 230 central pixels. The measured equivalent width for the outer spectrum of Fe I λ 5270 is 2.88 Å, of Fe I λ 5335 is 2.77 Å, and of Mg_2 is 6.94 Å. The equivalent width of the Mg_2 line is too large to agree with any of the calculated models from Mollá & García-Vargas (2000), and it is possible the nearby feature [N I] λ 5200 is affecting the measurement of Mg_2. The closest match using Mg_2, a supersolar metallicity of $2\,Z_\odot$ and an age of 20×10^9 yr, is therefore unreliable and I prefer to use the iron line measurements. Because of the age-metallicity degeneracy, the values for the Fe I lines agree both with a solar metallicity and an age of 10×10^9 yr, as well as a metallicity of $2\,Z_\odot$ and an age of $\sim 1.0 \times 10^9$ yr (Mollá & García-Vargas 2000). There is not a strong agreement between the indicators, but it is also possible that a single underlying population does not exist and that there is a superposition of very old and moderately old populations.

The continuum level of the outskirts gives the mass of the average pixel at this radius when compared to the theoretical continuum from a one solar mass star of this age. Again, there are some emission lines seen in the outskirts, so the derived values

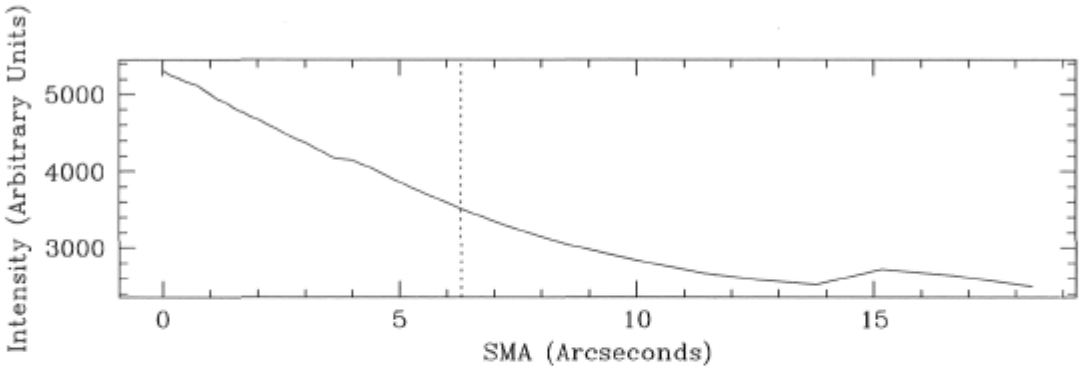

Figure 4.70: **Luminosity profile for NGC 6166 in Abell 2199.** *Measured from the Gemini GMOS acquisition camera using the i-filter. The vertical dotted line marks the extent of the OASIS field of view. The x-axis displays the Semi-Major Axis as calculated using the IRAF task, ellipse. Nearby galaxies show as bumps at 4 and 15″.*

mass are upper limits. The supersolar metallicity and oldest scenario from the Mg_2 absorption gives a mass of $3 \times 10^9\,M_\odot\,kpc^{-2}$, the solar metallicity and old age option from the Fe I λ 5335 lines gives a mass of $1 \times 10^9\,M_\odot\,kpc^{-2}$, and the alternate values of supersolar metallicity, but slightly younger ages from the Fe I λ 5335 lines gives a mass of $3 \times 10^8\,M_\odot\,kpc^{-2}$.

4.11.3 Line Measurements and the Ionization Mechanism

Examination of Figure 4.70 allows for a close inspection of the luminosity profile in the i-band image (from the archival Gemini GMOS acquisition camera image of Figure 4.64). It shows that the profile increases linearly towards the center and is actually quite piqued. It does not display the same $r^{1/4}$ shape as the other galaxies. This is mirrored in Figure 4.71, which shows a radial cut in the continuum emission surrounding Hα, across the center of the BCG. The footprint of the ionizing population is apparent in both emission lines and the continuum emission throughout all the pixels in the red spectra. Therefore, removing the underlying continuum using the methods from the previous galaxies introduces several uncertainties. Even before correcting the spectral ratios for the underlying galaxy (see below), it is clear that the ionization is from a hard ionizing source, like an AGN, and that the Hα emission cannot be used to identify a young population.

Figure 4.72 shows high [N II] λ 6584/Hα and ([S II] λ 6716 + [S II] λ 6731)/Hα ratios, signifying ionization by an AGN in all the emitting pixels. Furthermore, the Log([N II] λ 6584/Hα) ratios for the different regions in this galaxy vary from 0.24 to 1.0 and the Log([O III] λ 5007/Hβ) ratio (measurable only for Region 8) is 0.25. These

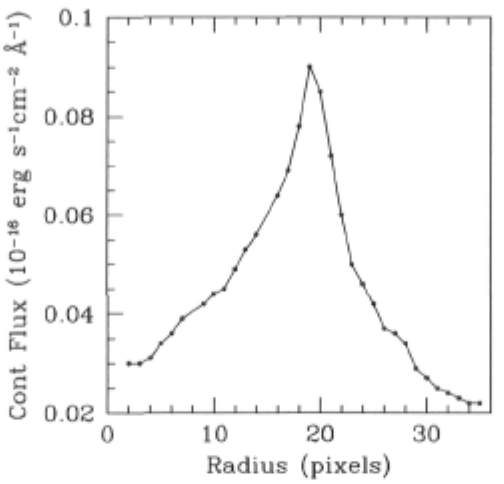

Figure 4.71: **Radial cut in the continuum for NGC 6166 in Abell 2199.** *This presents a horizontal cut across the central row of pixels in the continuum image.*

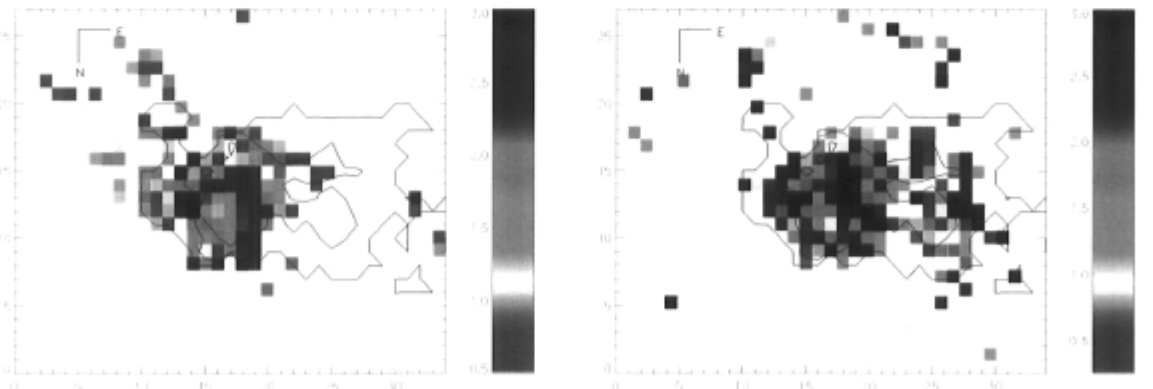

Figure 4.72: **Emission line ratio maps for NGC 6166 in Abell 2199.** *Left Panel: Map of the [N II] λ 6584/Hα ratio. Right Panel: Map of the ([S II] λ 6716 + [S II] λ 6731)/Hα ratio.*

are in line with the ratios from Crawford et al. (1999) derived from a 6″ long slit which was used here to correct for the internal extinction of the galaxy (0.36, for both ratios) and place the emission from each region in the LINER corner of the BPT diagram. It is possible that stellar absorption affecting Hα and Hβ could be artificially raising the ratios. However, this would not be by much since no absorption is seen in the integrated spectra from the outskirts (Figure 4.69). There are several examples of LINERs with similarly low values of [O III] λ 5007 emission such as Mrk 486 in Osterbrock & Ferland (2006) and other luminous infrared galaxies in Kewley et al. (2001b). Table 4.11 presents the measured center, flux, equivalent width, and FWHM (uncorrected for the instrumental profile) for the 9 regions after the underlying galaxy spectrum has been scaled (by the radial cut in the continuum, Figure 4.71) and subtracted.

The only region for which an Hβ emission strength is measurable is Region 8, which shows an Hα/Hβ ratio of 2.4. This is within the theoretical lower limit of 2.8 when considering the measurement errors ($\sim$10% for Hα and $\sim$30% for Hβ). It is also possible that some of the emission from the nearby nitrogen lines are contaminating the measurement of Hα (though the gaussian fits used by *deblend* appear to do a good job). The ratio is much lower than the integrated value of Crawford et al. (1999), Hα/Hβ = 9.3. However, as Hα is strong in several regions and Hβ is only present in Region 8, the integrated ratio is naturally much larger. Nevertheless Hβ is clearly detected in Region 8 which suggests that the extinction level is lower in this region, since to have an increased fraction for the integrated spectrum would require relatively less Hβ emission throughout. It is therefore reasonable to suggest that Region 2 may be closer to the dusty torus of the AGN.

4.11.4 Kinematics

The relative velocity map of Hα is shown in Figure 4.73 at the rest frame of the cluster. Clearly NGC 6166 is not at rest with respect to the cluster. Assuming the standard of rest of the galaxy to be at the position of the center of the continuum image, the velocity in the Hα emitting regions goes from $-200\,\mathrm{km\,s^{-1}}$ to $+200\,\mathrm{km\,s^{-1}}$. The low level flux of the Eastern side of the image has the largest relative velocities that increase quite quickly from the more moderate relative velocities of the very center. However, a relative velocity of only $200\,\mathrm{km\,s^{-1}}$ is quite small for an outflow. The pixels which have the most intense line emission are those with moderate velocities. The lowest velocities are in the Regions 5 and 6, just East of center. It could be that these regions, among, the brightest, are closer to us and hence subject to less extinction. If this were the case, one would then expect the Hβ line emission to be more smooth, however hardly any emission lines are seen in the image (only Region 8 has detectible emission). But, the Hβ emission lines are quite possibly effected by absorption which cannot be seen at the S/N level of this data. A higher S/N Hβ image would help verify this scenario.

Table 4.11: Spectral Line Values for Regions of NGC 6166 in Abell 2199

Measurement	Region 1	Region 2	Region 3	Region 4	Region 5	Region 6	Region 7	Region 8	Region 9
Hβ									
Center (Å)	-	-	-	-	-	-	-	4863.1	-
Flux	-	-	-	-	-	-	-	0.38	-
W_o (Å)	-	-	-	-	-	-	-	−12.4	-
FWHM (Å)	-	-	-	-	-	-	-	6.5	-
[O III] λ 5007									
Center (Å)	-	-	-	-	-	-	-	5006.3	-
Flux	-	-	-	-	-	-	-	0.67	-
W_o (Å)	-	-	-	-	-	-	-	−22.4	-
FWHM (Å)	-	-	-	-	-	-	-	16.3	-
[O I] λ 6364									
Center (Å)	-	-	6365.1	6356.0	6361.3	6360.2	6364.3	6360.9	6365.2
Flux	-	-	0.37	0.44	0.13	0.58	0.02	0.06	0.20
W_o (Å)	-	-	-	-	-	-	-	-	-
FWHM (Å)	-	-	13.2	50.5	8.7	12.4	1.3	2.8	17.7
[N II] λ 6548									
Center (Å)	6551.8	6550.6	6550.3	6548.1	6548.5	6545.1	6547.6	6550.0	6554.2
Flux	0.12	2.43	0.34	0.32	0.60	0.23	0.07	0.67	0.13
W_o (Å)	−48.1	-	−14.8	-	-	-	−6.2	−21.5	−9.2
FWHM (Å)	19.8	15.5	10.0	10.4	14.5	9.6	3.4	12.1	7.2
Hα									
Center (Å)	6568.3	6565.3	6563.3	6559.8	6561.6	6559.2	6561.3	6565.4	6569.2
Flux	0.98	2.69	0.30	0.27	0.54	0.40	0.05	0.92	0.12
W_o (Å)	−39.1	-	−12.7	-	-	-	−4.6	−29.8	−8.5
FWHM (Å)	12.9	12.2	8.9	10.0	9.1	9.5	7.1	12.7	6.5

Table 4.11: Continued

Measurement	Region 1	Region 2	Region 3	Region 4	Region 5	Region 6	Region 7	Region 8	Region 9
[N II] λ 6584									
Center (Å)	6586.5	6584.1	6583.0	6581.0	6581.3	6579.5	6582.3	6584.0	6589.8
Flux	1.94	6.04	0.86	0.776	1.35	0.84	0.20	1.84	0.27
W_o (Å)	−74.7	-	−34.8	-	-	-	−18.4	−60.6	−18.7
FWHM (Å)	13.1	14.9	11.6	11.3	11.3	10.2	10.2	12.4	6.6
[S II] λ 6716									
Center (Å)	6721.5	6718.5	6717.2	6710.0	6712.9	6711.9	6710.0	6718.5	6723.5
Flux	0.78	2.50	0.27	0.02	0.26	0.19	0.04	0.64	0.03
W_o (Å)	−31.7	-	−12.0	-	-	-	−4.9	−23.5	−2.1
FWHM (Å)	16.0	18.3	13.6	3.6	9.5	9.0	3.3	14.5	1.1
[S II] λ 6731									
Center (Å)	6734.6	6732.9	6732.1	6719.3	6727.4	6726.4	6729.9	6732.0	6732.4
Flux	0.17	0.91	0.11	0.35	0.41	0.28	0.03	0.27	0.02
W_o (Å)	−6.9	-	−4.8	-	-	-	−4.4	−10.1	−1.6
FWHM (Å)	9.6	10.6	6.1	25.7	14.0	11.4	1.9	8.2	1.1

Note: The central positions are given in terms of the rest wavelength. The flux is in units of 10^{-15} erg s^{-1} cm^{-2}. Errors in the flux measurements for the strong lines are of order 5-10%.The weak lines of Hβ, [O III], [O I] and [S II] have large errors of 20-30%.

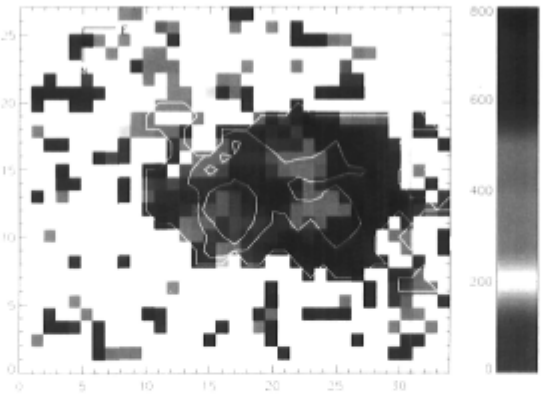

Figure 4.73: **Map of the Hα relative velocity for NGC 6166 in Abell 2199.** *The Hα flux is overlain as contours. The scale is in units of km s^{-1}. One pixel is ∼150 pc across.*

4.12 Cygnus-A

Cygnus-A is the most powerful narrow-line radio galaxy in the local Universe; it is often referred to as 3C 405. This AGN is in the BCG at the center of a poor cooling flow cluster (Reynolds & Fabian 1996). It is not easy to discriminate between the X-ray contribution of the AGN and the cluster X-ray gas itself (Molina et al. 2006) because in this case the AGN is so powerful it dominates the observed X-ray luminosity. No CO emission was detected by Salomé & Combes (2003) who quote an upper limit for the mass of $H_2 = 1.4 \times 10^9\,M_\odot$. This cluster therefore is not one where line emission would be presumed to be originating from the cooling flow, or to have a massive young stellar population. However, it is included in this sample so that the qualitative properties of this dataset can be compared to previous observations. Rigorous observations of this galaxy have been conducted in several wavebands, including optical HST line images (Jackson et al. 1998) and very high spatial and spectral resolution spectroscopy by Tadhunter et al. (1994, 2003). Nonetheless, this dataset improves upon existing observations threefold: First, the velocity maps produced here are full two dimensional relative velocities out to a larger spatial extent than those of Tadhunter et al. (2003), second, the Hβ emission maps are presented, and finally, the extinction correction is done on a pixel by pixel basis.

The previous observations from Jackson et al. (1998) of the line emission encompass the few central arcseconds of Cygnus-A, comparable to the OASIS field of view of $7.4 \times 10.3''$. The physical area is 7.7×10.8 kpc, and each pixel covers a distance of ∼220 pc on either side. Figure 4.74 shows the IFU field of view drawn on the center of Cygnus-A. The images of cluster center is from the F622W filter HST image (named U2920201B in the CADC archive), and mostly covers the BCG. The 1800s

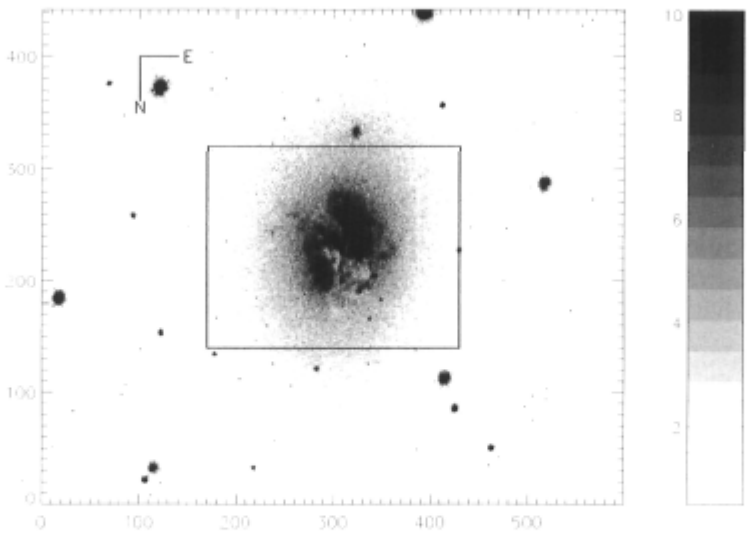

Figure 4.74: **Cygnus-A taken in the HST F622W filter.** *The IFU field is marked as a box with dimensions of 10.3 × 7.4″ (7.7 × 10.8 kpc) around the BCG. The background image is an 1800s exposure from HST with a resolution of 0.046″pix^{-1}. The scale is in arbitrary flux units.*

HST exposure has a very high spatial resolution of 0.046″pix^{-1}.

4.12.1 Line Images and Region Spectra

The continuum emission around Hα (between 6380 and 6430 Å) for Cygnus A is shown in Figure 4.75, with the continuum-subtracted Hα flux image, and the continuum-subtracted [N II] λ 6584 emission. The configuration does not allow for the observation of the [S II] emission lines. The continuum around Hβ (between 4720 and 4830 Å) is also shown in Figure 4.75 along with the continuum-subtracted Hβ flux image and the continuum-subtracted [O III] λ 5007 emission. The overall morphology of these images is consistent with those from Jackson et al. (1998). Within the red spectra, the brightest continuum emission is seen in three blobs: one central, one to the SE and another to the NW. In the line emission images, it is the NW and the central components that have the highest flux. Diffuse emission surrounds these blobs, and Jackson et al. (1998) deduce the morphology is associated to an opening cone which passes from the NE side of the image through the central blob to the SW side of the image. These authors also point out a jet that emanates from the center to the West, passing along south side of the NW blob. The blue continuum shows the SE and NW blobs, but the central peak is not seen, likely due to intense dust extinction (Jackson et al. 1998). The NW blob is present in both blue emission line images.

Figure 4.76 shows the S/N of the continuum in the red and blue. As also apparent

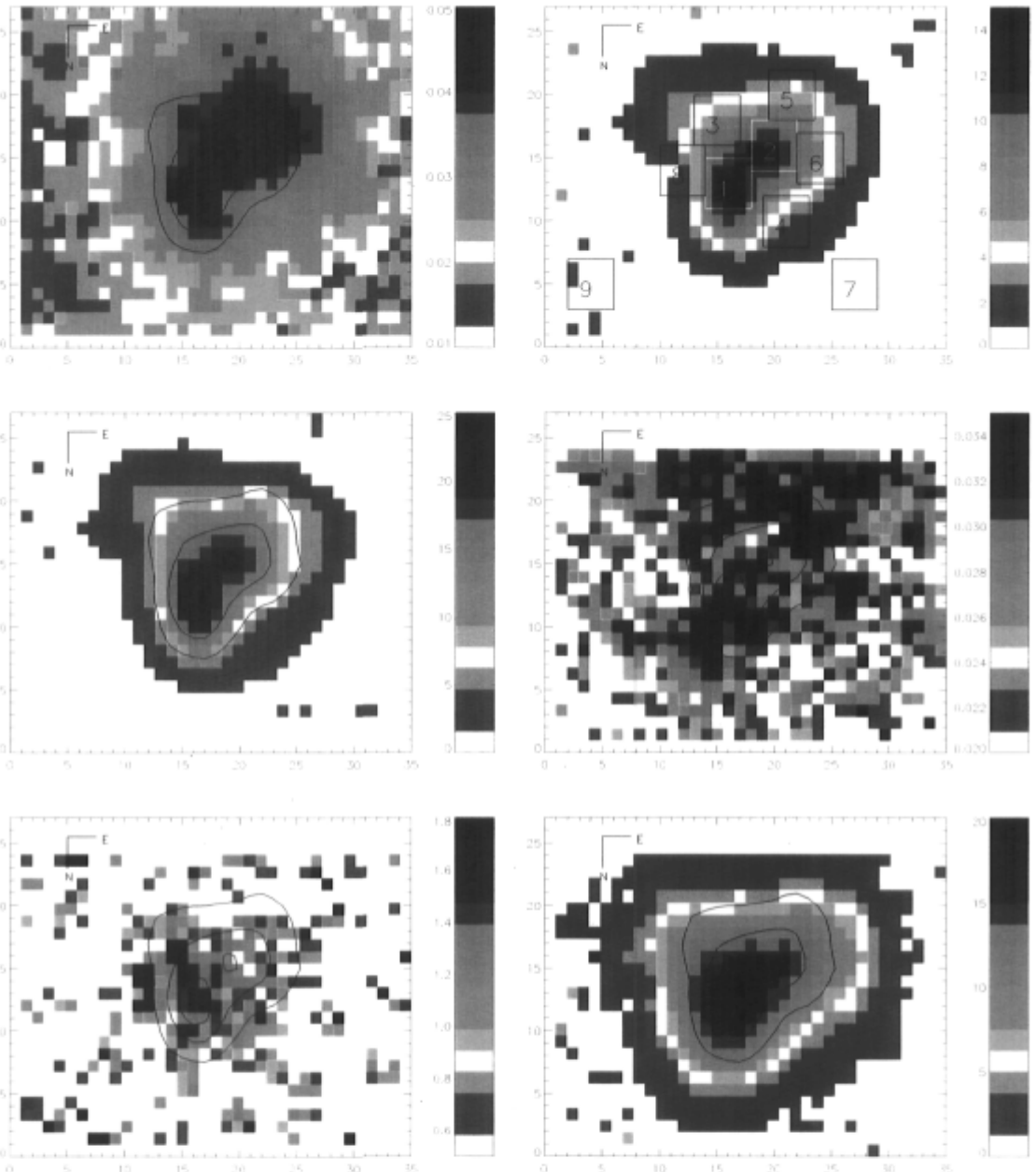

Figure 4.75: **Reconstructed images for Cygnus-A.** *Top Left Panel: The continuum surrounding the Hα emission line. Top Right Panel: The continuum-subtracted Hα image. The regions used in the subsequent analysis are represented as boxes. Middle Left Panel: continuum-subtracted [N II] λ 6584 image. Middle Right Panel: The continuum surrounding the Hβ emission line. Lower Left Panel: The continuum-subtracted Hβ image. Lower Right Panel: The continuum-subtracted [O III] λ 5007 emission flux image. All images are in reverse colour scale and units of* $10^{-16}\,erg\,s^{-1}\,cm^{-2}\,\AA^{-1}$. *Where present, contours illustrate the Hα emission morphology. One pixel is ∼220 pc across, for all panels.*

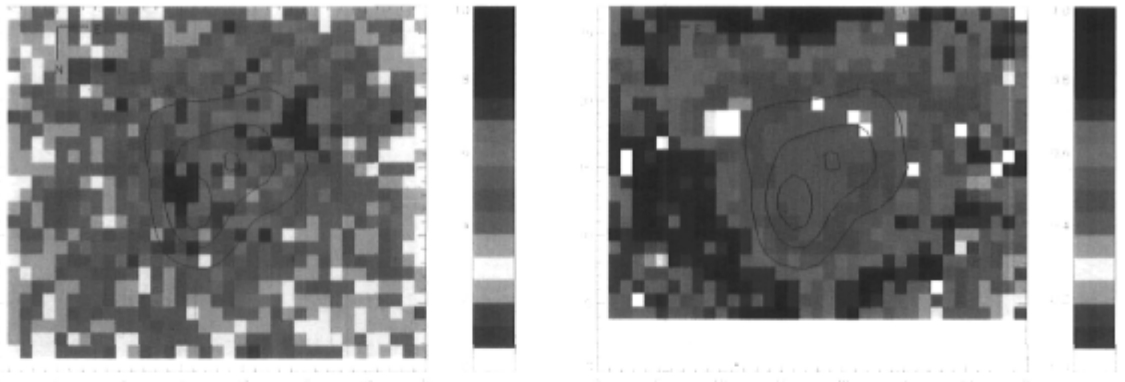

Figure 4.76: **S/N ratio of the continuum for Cygnus-A.** *The S/N of the continuum around Hα is shown on the left, and the S/N of the continuum around Hβ is shown on the right. One pixel is ∼220 pc across.*

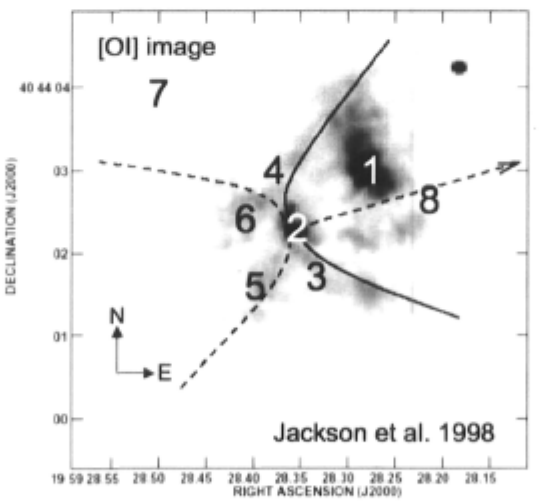

Figure 4.77: **Cygnus-A Geometry.** *This image is adapted from Figure 4 in Jackson et al. (1998) and shows the geometry of Cygnus-A. The position and direction of the opening cone and jet are shown on the a figure of the [OI] line emission. The numbers refer to the regions studied in this thesis. The scale is in arbitrary flux units.*

in the spectra, the S/N of the blue continuum is particularly low, and absorption lines are not resolved.

Within each of nine regions, similar spectra are co-added for further investigation. They are labeled on Figure 4.75 and Figure 4.77. The latter figure is adapted from Jackson et al. (1998). These regions include Region 1 which covers the NW blob, Region 2 which covers the bright central continuum emission, one region at each side of the ionization cone (Regions 3 and 4), one that covers the bright SE continuum blob (Region 5), one at the location of the blue condensations (Region 6) found by Jackson et al. (1998), two where there is an absence of strong line emission (Regions 7 and 9), and one at the location of the jet (Region 8).

All of the regions cover ~890 pc on either side. The integrated spectra of these regions are presented in Figures 4.78 and 4.79, and are as previously labeled. Strong emission lines in this spectral region are [O I] $\lambda\lambda$ 6300,6364, Hα, and [N II] $\lambda\lambda$ 6548,6584. The blue spectra of Figure 4.79 clearly show [O III] $\lambda\lambda$ 4959,5007 and Hβ emission. He II at 4686 Å and [NI] at 5199 Å are observable in the strongly line emitting Regions 1 and 2. The Fe I $\lambda\lambda$ 5270,5335 absorption lines are not observable in this configuration, and any Mg_2 λ 5177 absorption may be affected by the strong neighboring emission of [N I] at 5199 Å.

The AGN in this BCG dominates the spectra, therefore it is not possible to isolate any young populations from this data, if they are present. As well, the absorption lines of the underlying BCG are not resolved, so an age of the underlying galaxy cannot be estimated. The optical image is too affected by absorption to be able to extract a useful fit to a smooth any luminosity profile due to an old background population using IRAF's *ellipse*, and so this figure is not shown.

However, the emission lines are strong, and maps of both ratios of [N II] λ 6584/Hα and [O III] λ 5007/Hβ show interesting structure. The maps of these ratios are displayed in Figure 4.80. The first figure shows most pixels have ratios higher than $\sim$ 1.4, placing them on the AGN side of the BPT diagram. The highest ratios are in two clumps almost directly South and North of the center of the image. This is on the edge of the ionizing zone described by Jackson et al. (1998), and perpendicular to the direction of the jet. These clumps of high line ratios are ~1 kpc from the center, and so further out than the expected extent of the torus. However, if dust exists it could be scattering light from the central source. The lowest line ratios are East of the center, at Region 6. This is the location of the blue condensations seen previously. The spatial resolution here is not as high as for HST, and neighbouring pixels may be washing out signs of young stars, however Jackson et al. (1998) themselves saw no emission lines in the blue condensations. The [O III] λ 5007/Hβ map of Figure 4.80 is affected by the poorer quality of the Hβ image, but shows no clear structure immediately apparent in the map. However, all of the central pixels show ratios higher than ~8, disclosing the nature of this AGN to be more Seyfert-like than LINER-like. The BPT diagram shown

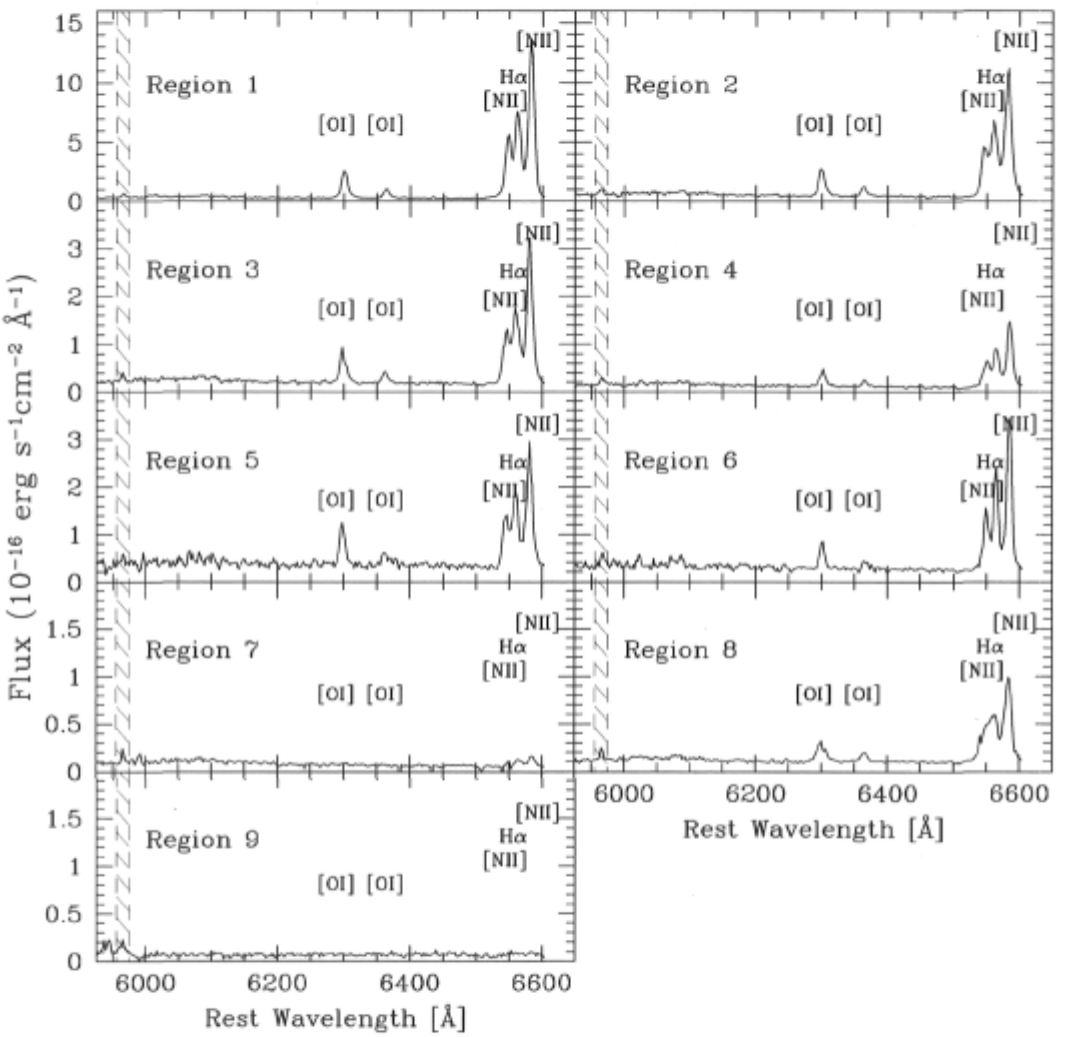

Figure 4.78: **Averaged red spectra of the 9 regions for Cygnus-A.** *Prominent emission features are labeled and the regions correspond to those labeled on the Hα image. The region hashed out shows where the strong sky lines have not been well subtracted.*

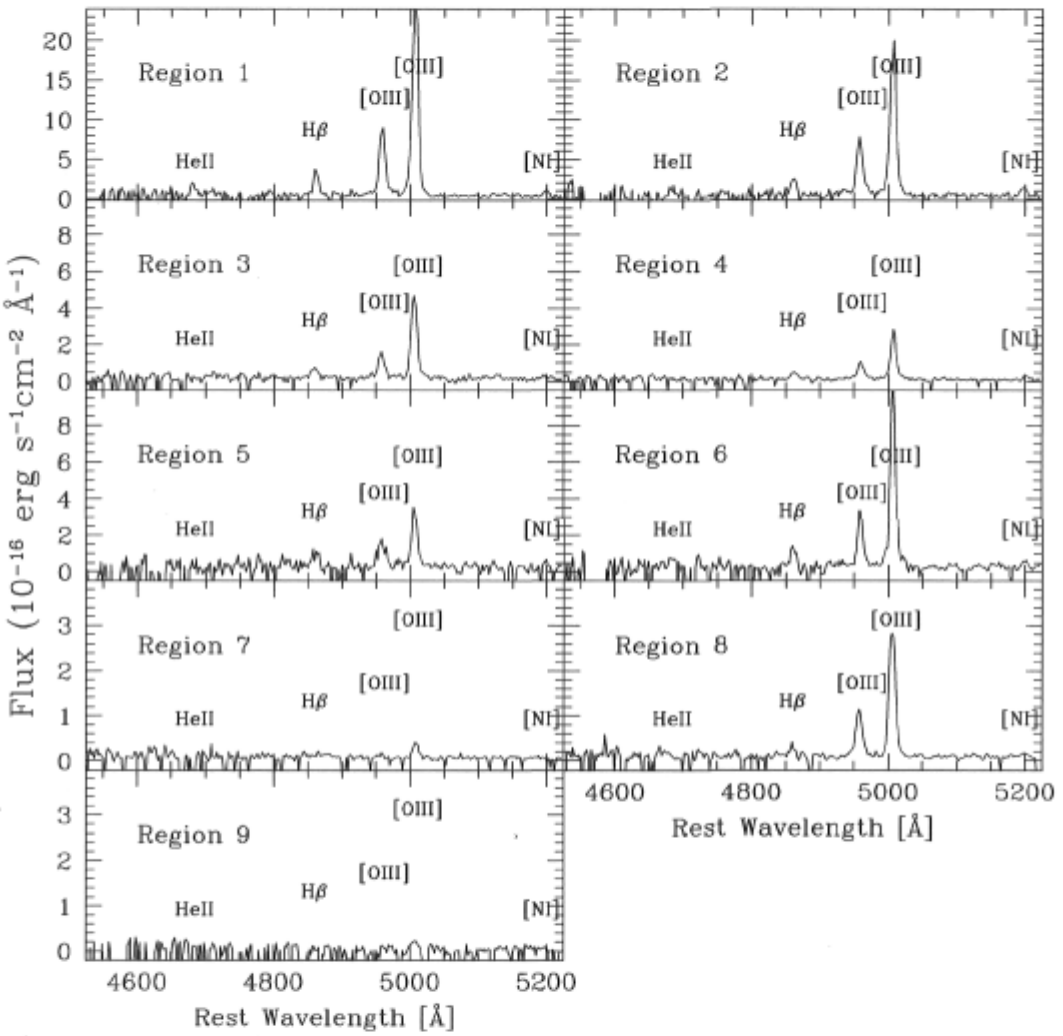

Figure 4.79: **Summed blue spectra of the 9 regions for Cygnus-A.** *Prominent emission features are labeled and the regions correspond to those labeled on the Hα image.*

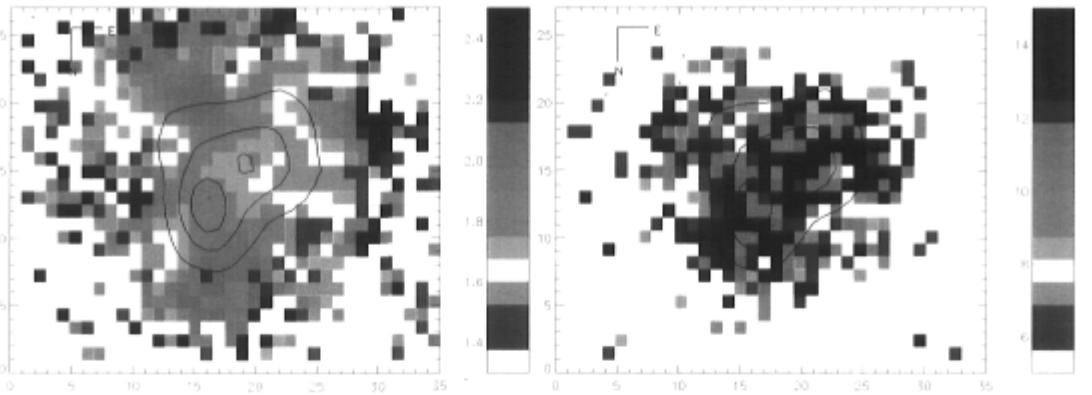

Figure 4.80: **Line ratio images for Cygnus-A.** *Left Panel: [N II] λ 6584/Hα map. Right Panel: [O III] λ 5007/Hβ map. The images are in reverse colour, uncorrected for internal extinction. The Hα flux is overlain as contours. One pixel is ∼220 pc across.*

in Figure 4.81 classifies virtually every pixel as ionized by AGN emission, and there is a smooth transition from pixels at the Seyfert corner down to the LINER side. This agrees with the well established classification of Cygnus-A being a narrow line radio galaxy.

4.12.2 Extinction

A map of the extinction can be created from the pixel to pixel values of the Hα and Hβ fluxes, after aligning the Hβ image to the Hα image. Because the continuum in the blue is not of terribly high S/N, and because corresponding continuum features are not immediately apparent in both the red and blue continuum, I align on the NW blob in the [O III] λ 5007 line image to that in the [N II] λ 6584 line image. These two lines are chosen since they are both very strong, and both are high ionization lines. The method is validated as the result is a good match to the NW continuum peak of both images. The extinction map is subsequently created using the following equation on a pixel by pixel basis:

$$\mathrm{E(B-V)}_{int} = \frac{2.177}{-0.37\mathrm{R}} \times \left(\mathrm{Log}\left\{\frac{\mathrm{I}_{o\mathrm{H}\alpha}}{\mathrm{I}_{o\mathrm{H}\beta}}\right\} - \mathrm{Log}\left\{\frac{\mathrm{I}_{\mathrm{H}\alpha}}{\mathrm{I}_{\mathrm{H}\beta}}\right\}\right). \tag{4.3}$$

Here, R = 3.1, $\mathrm{I}_{oH\alpha}/\mathrm{I}_{oH\beta}$ is 2.85, the theoretical ratio for Case B recombination, and $\mathrm{I}_{H\alpha}$ and $\mathrm{I}_{H\beta}$ are the observed values (Osterbrock & Ferland 2006; Kauffmann et al. 2003). The intrinsic Hα/Hβ ratio of 2.85 may not be the ideal value to use for known Seyfert galaxies, but the actual value is debated. It is often assumed that the Hα emission in these systems is enhanced due to collisional processes, and several authors use a value of 3.1 (Gaskell & Ferland 1984; Osterbrock & Ferland 2006), although other values have also been determined (Binette et al. 1990, calculate a value of 3.4). The

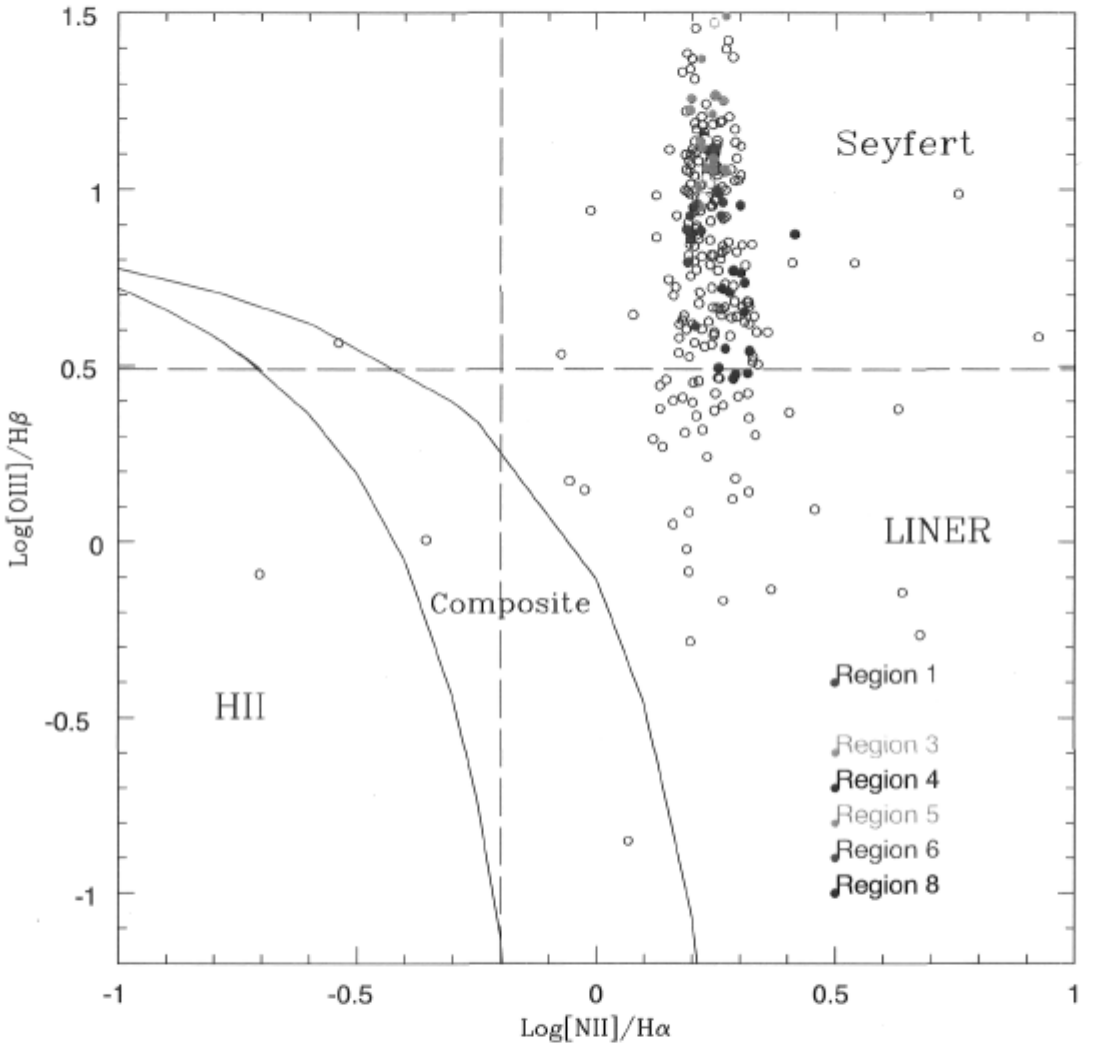

Figure 4.81: **BPT diagnostic diagram for Cygnus-A.** *Individual pixels are plotted as open circles and pixels within the analyzed regions are plotted as filled circles. This figure using the definitions of H II region, Composite and AGN ionizing sources from Kauffmann et al. (2003). The designations between LINER and Seyfert are from Osterbrock et al. (1996).*

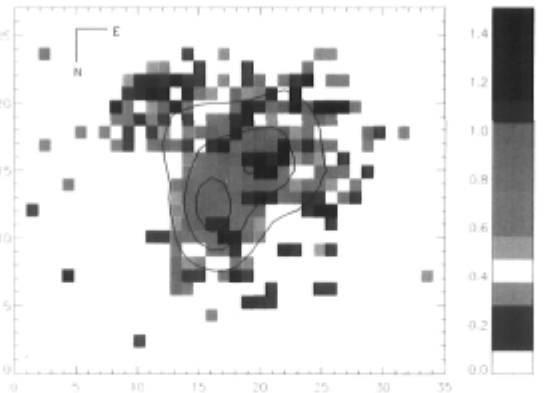

Figure 4.82: **Extinction map of Cygnus-A.** *The image is a reverse scale representation of E(B−V) derived from the Hα to Hβ line strengths, with the Hα emission overlain as contours. One pixel is ∼220 pc across.*

extinction map is presented in Figure 4.82 and shows very high values of $E(B-V)_{int}$ at the center, as well an extinction of ∼0.7 on the NW blob (Region 1). The low S/N of the Hβ emission in several pixels causes this map to be rather crude. Although the values of extinction determined here may be slightly overestimated due to the choice of intrinsic Hα/Hβ of used, the average value on the NW blob is 0.75±0.2, which is not far from the integrated value of 0.69±0.04 (Osterbrock & Ferland 2006) for Cygnus-A, also calculated using the Balmer decrement but using an intrinsic Hα/Hβ ratio of 3.08.

Figure 4.83 shows the ratios of differing ionization levels - [O I] λ 6300/[O III] λ 5007 and [O III] λ 5007/Hα. Because these are constructed from emission lines that are several hundred angstroms from each other, both components have been first corrected for extinction using the values from Figure 4.82. The ratio of [O I] λ 6300/[O III] λ 5007 is a good tracer of the ionization parameter (q) which itself is a measure of the number of ionizing photons per atom at the boundary layer. The figure shows both lower and higher ionization states are present. Typical values of the ionization parameter have been deduced by comparing galaxy observations with stellar synthesis models. Low values are $q \simeq 5\times10^6\,cm\,s^{-1}$ and high values are $q \simeq 8\times10^7\,cm\,s^{-1}$. The [O III] λ 5007/Hα also shows a region of higher ionization along the edge of emission, North of the NW blob (Region 1), which was noted in the observations of Jackson et al. (1998). However, this feature is on the edge of the Hβ emitting pixels, which define the useable extinction corrected values, and therefore suffers from low S/N pixels, and a high uncertainty.

4.12.3 Kinematics

The relative velocity maps of the Hα and [O III] λ 5007 emission lines are shown in Figure 4.84. The relative velocity map of the [N II] λ 6584 emission is not shown as it harbours very similar morphology and magnitude as to that for the Hα relative velocity

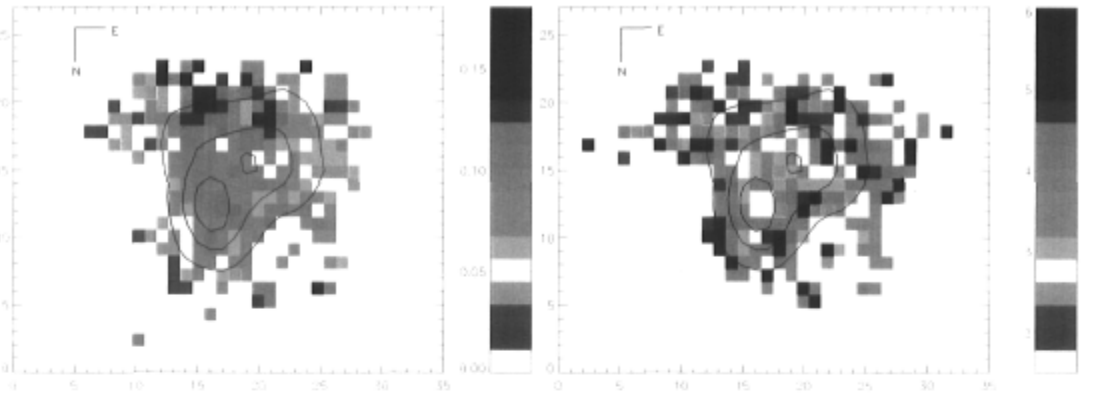

Figure 4.83: **Reconstructed images of Cygnus-A based on extinction maps.** *Left Panel: The [O I] λ 6300/[O III] λ 5007 ratio for Cygnus-A. Right Panel: The [O III] λ 5007/Hα ratio for Cygnus-A. The Hα flux is overlain as contours. One pixel is ∼220 pc across, for both panels.*

map. Large scale velocity gradients of $\pm 200\,\mathrm{km\,s^{-1}}$ are seen for Hα, and of $\pm 100\,\mathrm{km\,s^{-1}}$ for [O III] λ 5007, both in the SW and NE direction. This is perpendicular to the opening cone, and to the direction of the jet. On this scale, the velocity gradients in both lines are reminiscent of rotation.

The FWHM of the Hα emission line is also shown in Figure 4.84. It reveals large widths corresponding to the central continuum peak, the location of the central radio point source (Tadhunter et al. 2003). There is also an area of large width that extends west of this peak (that is, west of Region 2). This second area extends to Region 8, the direction of the jet. The large width could be caused by disturbance from the jet.

4.13 Summary of Results

Table 4.12 is presented as a summary of properties of the BCGs studied in this chapter. It shows the cluster name, richness, cooling flow designation, X-ray luminosity in the 0.1 - 2.4 keV band (Edge & Stewart 1991; Reynolds & Fabian 1996; Ebeling et al. 1996; Matsuura & et al. 1996; Sadat et al. 2004), whether the NRAO VLA Sky Survey images show radio emission, and the distance of the BCG from the X-ray peak (dR). The table also summarizes the results based on this work: the presence or absence of emission lines, if they are best characterized by ionization from hot stars or from an AGN, and the age and mass of the young and underlying old populations. Clear signatures of star formation are present in 2 BCGs, however only one is a cooling flow, and it harbours signatures of an AGN as well. The table also shows how AGN-ionized emission is present in both cooling flows and non-cooling flows, and how one cooling flow BCG shows a complete lack of emission lines.

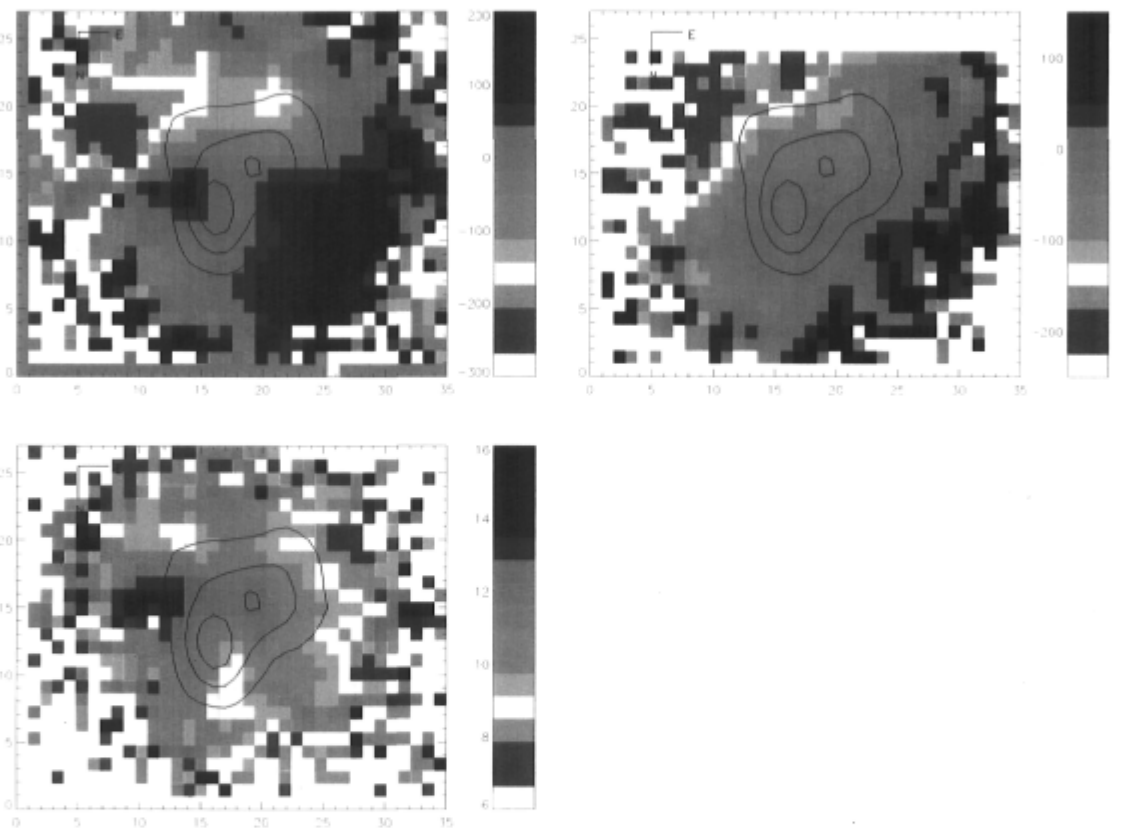

Figure 4.84: **Map of the Hα relative velocity in Cygnus-A.** *Upper Left Panel: Map of the Hα relative velocity. Upper Right Panel: [O III] λ 5007 relative velocity. Lower Left Panel: Map of the Hα FWHM . The Hα emission overlain as contours. The scale is in units of km s^{-1} for the relative velocities, and Å for the values of FWHM. One pixel is ∼220 pc across in all panels.*

Table 4.12: Summary of IFU Line Emission Properties

Cluster Name	Rich	CF	L_X 10^{37}W	Radio	dR kpc	Lines	Age_{young} Myr	Mass ρ_{young} $10^5\,M_\odot$	SFR Density $10^{-8}\,M_\odot\,yr^{-1}\,pc^{-2}$	Age_{old} Gyr	Mass ρ_{old} $10^8\,M_\odot\,kpc^{-2}$	Note
Abell 1060	Yes	No	0.47	Yes	30	SF	7	6	14	10	2	
Abell 1204	Yes	Yes	6.77	No	20	SF & AGN	8	1070	2	-	-	1
Abell 1668	Yes	No	1.61	Yes	30	AGN	-	-	-	5	60	
$Ophi_{BCG}$	Yes	No	> 4	Yes	4	No	-	-	-	10	600	2
MKW3s	No	Yes	2.68	Yes	0	AGN	-	-	-	20	2040	3
Abell 1651	Yes	Yes	8.25	some	-	No	-	-	-	-	-	
Abell 2052	Yes	Yes	2.52	Yes	38	AGN	-	-	-	8	0.1	
Abell 2199	Yes	Yes	3.70	Yes	7	AGN	-	-	-	> 1	> 3	
Cygnus-A	No	Yes	2.00	Yes	0	AGN	-	-	-	-	-	

Note 1: Possible companions near line emitting gas in Abell 1204.

Note 2: There is a clump of gas, Object B, near to the BCG in Ophiuchus showing AGN-like emission line ratios.

Note 3: Emission lines in MKW3s blueshifted with respect to underlying cD population.

Chapter 5

Discussion and Conclusion

In this chapter I present a discussion and an interpretation of the results from Chapter 4 and compare them to the results quoted in the current literature, especially to those of Wilman et al. (2006) and Hatch et al. (2007) who study integral field data of a similar sample of BCGs. This leads into a discussion of the complimentary nature of survey studies to the IFU observations, and a review of the major finds from Chapter 2. I close with general conclusions and remarks about future projects.

5.1 The IFU Study

By identifying the line emitting gas in each of the galaxies presented in the previous chapter, the regions that are consistent with excitation by hot stars were discriminated from those where emission by a harder source is required. Most of the BCGs studied in Chapter 4 do not show clear signs of recent star formation related to a cluster cooling flow (see Table 4.12). Here, I review the study and its main results. What becomes clear in looking at all 9 BCGs is that AGN signatures are evident and dominant in almost all cases, but otherwise the properties of the line emitting gas show little consistency between the BCGs.

5.1.1 Limitations and Expectations

This study is limited by a few observational and theoretical aspects. Primarily, it deals with a small sample size, and so assumptions on the population of all cooling flow BCGs is limited. But I continue in the spirit of increasing the total observed number of these objects, as this sample does significantly raise the number of cooling flow BCGs observed with an IFU. Also, this study chooses to look particularly at known line emitters, so a biased interpretation of the few cases of non-line emitters caught in the study is possible. To reiterate from Chapter 3, the cooling flow status of the cluster is a difficult parameter to gauge, and is certainly a part of the uncertainties of these results. The small field of view of the IFU observations allows only for an analysis

of the near nuclear regions, away from where much of the known activity occurs (eg. the regions of interplay between radio lobes and X-ray bubbles are out of the field of view). Additionally, the small bandwidth affords an analysis of only a small number of optical emission lines, several of which are interdependent on multiple and degenerate processes. Nevertheless, these emission lines are in general strong when present, and are so widely used that their interpretation remains useful.

Overall, I expected to see emission lines characteristic of a young stellar population throughout most of the sample of BCGs, as the majority were chosen a priori to be good candidates in which to expect young ionizing stars: several of the BCGs (those in Abell 1060, MKW3s, Abell 2052, and Abell 2199) have previous reports of a young stellar population either from long slit spectra, or observed UV excess. Chapter 2 showed that the presence of a radio source is common in emitting BCGs and that in general 10-20% of BCGs have line emission, thus those with radio emission are particularly targeted and non-cooling flow BCGs are also included in the sample (see Table 4.12). A strong correlation between the cooling flow status of the cluster and the presence of emission lines is obvious in Chapter 2, and so it is surprising that this is not mirrored in the results of Chapter 4. Although the sample size is small, it is not just the non-cooling flow radio quiet BCGs which lack lines in the IFU observations, and the two cases in which a young stellar population can be discriminated are not both cooling flows.

5.1.2 Overview of Results

The observations of this work allow for the description of the morphology, ionization mechanism, and relative velocity in the line emitting gas. After the production of maps of low (Hα) and higher ([N II]) ionization states the morphology was described, and this was seen to vary from system to system. Condensed (Abell 2052, Cygnus A), filamentary (Abell 1668, MKW3s), and extended (Abell 1204, Abell 2199) morphologies are observed and the Hα and [N II] emitting gas usually follows the same morphology. Also of note are two cases, Abell 1060 and Ophiuchus (both non-cooling flows), where the line emitting gas follows the morphology of prominent dust features seen in the acquisition images. Selected regions are then analyzed further by using BPT diagrams to diagnose the ionization mechanism. In two out of seven emitting BCGs, hot stars are likely perpetrators - NGC 3311 in the non-cooling flow cluster Abell 1060 and the BCG in cooling flow cluster Abell 1204. In these cases, SFRs and ages for the young populations are derived (see Table 4.12). Mostly however, the presence of an optical AGN was strong. But, this was found in cooling flows, as well as non-cooling flows. Two of the nine BCGs observed had no emission lines. This includes the BCG of the cooling flow cluster Abell 1651, and the BCG of the non-cooling flow cluster, Ophiuchus. Unexpectedly, it is a source other than the BCG in Ophiuchus (Object B, located at the X-ray peak) that shows line emission. In most cases, the relative velocities are in the

neighborhood of ± 100 - $200\,\mathrm{km\,s^{-1}}$, though some higher relative velocities indicative of large inflows (Object B in Ophiuchus) or outflows (MKW3s) are observed.

The properties and main results for each cluster BCG are highlighted in Table 4.12 and discussed briefly below.

- Abell 1060: Previous detections of star formation in this dusty (Laine et al. 2003) non-cooling flow (Hayakawa et al. 2006) BCG have been described by Vasterberg et al. (1991). I characterize several regions of star formation, note that the morphology of the star forming region follows that of the dust, and present a smooth velocity gradient reminiscent of rotation.

- Abell 1204: This cooling flow cluster (Bauer et al. 2005) has the highest redshift of our sample ($z = 0.1706$) and thus a larger extent of the cD galaxy is viewed. Regions of ionization due to AGN are separated from those indicative of a young stellar population. The latter are found further from the center in a plume that extends towards a chain of smaller cluster galaxies. The relative velocities are not large enough for an outflow ($\pm 200\,\mathrm{km\,s^{-1}}$), and show no signs of rotation, but an interaction with the nearby galaxies may be important.

- Abell 1668: This is a non-cooling flow cluster (Salomé & Combes 2003), yet strong lines are present. These appear in a filamentary distribution with line ratios signifying ionization from an AGN. The relative velocity of the line emitting gas shows that it is not at rest with the underlying cD.

- Ophiuchus: This non-cooling flow cluster BCG (White 2000) shows no emission lines. However, emission lines are seen in Object B, possibly a cloud of gas deposited by the cooling flow, and ionized by an AGN at a projected distance of $\sim 2\,\mathrm{kpc}$ away from the center of the BCG. Object B is cospatial with a dust feature seen on the acquisition image, and the emission lines have a relative velocity of $+750\,\mathrm{km\,s^{-1}}$ with respect to the BCG. I attribute this to infall onto the BCG.

- MKW3s: This cooling flow cluster (Kaastra et al. 2004) has previously been observed to have a UV excess and attributed star formation by Hicks & Mushotzky (2005). I find the emission lines in the IFU image to be filamentary in morphology, yet well described by ionization from an AGN. The lines are blueshifted by $+560\,\mathrm{km\,s^{-1}}$ with respect to the BCG, suggesting an outflow.

- Abell 1651: This cooling flow cluster (White 2000) BCG shows no emission lines.

- Abell 2052: This cooling flow cluster (Blanton et al. 2003; Kaastra et al. 2004) has patchy dust in the center of the BCG (Laine et al. 2003) and Hicks & Mushotzky (2005) and Blanton et al. (2003) have deduced star formation in the BCG from excess UV-IR and U-band continuum emission. I find that the AGN signature

overwhelms any star formation in the central few arcseconds of the BCG. The morphology of the emission lines here is point-like, in that it shows no asymmetric or extended features. The relative velocities vary on the scale of $\pm 250\,\mathrm{km\,s^{-1}}$, but are not smooth enough to warrant a classification of rotation.

- Abell 2199: Another cooling flow (Johnstone et al. 2002) BCG with previous calculations of star formation based on UV excess (McNamara & O'Connell 1989). Again, I find the AGN signature in the emission lines is dominant throughout the extent of the IFU image. The lines are brightest in the center, but exhibit an extended morphology towards the East. The relative velocities are similar to those seen in Abell 2199, but again the gradient is not regular enough to signify rotation.

- Cygnus A: This poor cooling flow cluster (Reynolds & Fabian 1996) is a well studied AGN (Jackson et al. 1998; Tadhunter et al. 1994, 2003). I find a morphology consistent with the images of Jackson et al. (1998), line ratios telling of an AGN, and a velocity gradient that suggests rotation. The FWHM of the emission lines traces the direction of the jet, as it becomes wider for the lines in that region.

Certainly gas exists and is excited, but the observations above show that many mechanisms are at play. The trends of line emission with cooling flow status that I was expecting based on the statistical study of Chapter 2 are not obvious here. For instance, signs of emission by hot stars are present in both cooling flow and non-cooling flow systems, and AGN-ionized gas is also present in both cooling flow and non-cooling flow systems. As found by several other authors (Wilman et al. 2006; Böhringer et al. 2002; Donahue et al. 2000), this data does not support a simple picture in which X-ray gas cools into molecular clouds subsequently forming stars. This is emphasized by the variation in morphology of the ionized nebula in these systems. The disturbed morphology of the non-AGN ionized gas of Abell 1204 extends towards the direction of several smaller galaxies, suggestive of an interaction with nearby companions. The spectrum of MKW3s is also interesting, with the Hα emission line shifted with respected to the underlying spectrum. Although for the majority of cases the line emission is stronger in the central regions of the BCG itself, in Ophiuchus at least, the line emission is localized North of the BCG center, at a distance of $\sim$2 kpc. Donahue et al. (2007) finds the emission lines in the cooling flow cluster 2A0335+096 are associated with the BCG, as well as a companion. In the case of 2A0335+096, the emission lines are described as dusty, and this is also the case in Ophiuchus and in NGC 3311 of Abell 1060 where the line emission is constrained by what appears on the acquisition images to be strong dust features.

5.1.3 A Working Scenario?

During the course of the work on this thesis, two other groups have presented integral field spectroscopic data, where observations of high spatial resolution of the very central regions of cooling flow BCGs were obtained. Wilman et al. (2006) observe the Hα-luminous cooling flow systems of Abell 1664, Abell 1835, Abell 2204, and Zw8193, and Hatch et al. (2007) studied Abell 262, Abell 496, 2A0335+096, Abell 1068, and Abell 2390.

An important and unique difference between this study and those of Wilman et al. (2006) and Hatch et al. (2007) is that non-cooling flow clusters are included here. Consequently I am able to begin to compare the characteristics of the line emitting gas in cooling flows with that in non-cooling flows. Also, the systems presented here are in general host to BCGs of much lower Hα line luminosity than those previously studied.

Wilman et al. (2006) find little variation of the emission line ratios across the emission nebulae in their high redshift and very luminous sample of 4 cooling flow BCGs, implying a uniform ionization state. They suggest the following single scenario to explain the line emission in all their galaxies: an interaction of smaller cluster galaxies triggers starbursts in cold gas reservoirs, presumably deposited from the cooling flow. This is supported by their observation that different ionization states of the gas vary little spatially, implying a single ionization source for the Hα emission. Intriguingly, the current observations for the modest cooling flow case of Abell 1204 support this idea (this is the only cluster in this sample where $z > 0.1$). In this case, the Hα, [N II] and [S II] emitting gas all share a similar morphology. I calculate a total SFR of $\simeq 7\,M_{\odot}\,yr^{-1}$ for this BCG, which is not inconsistent with the mass deposition rate as not all the molecular gas will convert to stars and as the current estimates of MDRs are an order of magnitude *below* the old *ROSAT* derived rate of $675\,M_{\odot}\,yr^{-1}$. Wilman et al. (2006) also reasoned that the Hα and CO gas are related as they share the same kinematics, and it is this CO gas, which is subsequently disturbed by the passing of nearby neighbors or by an AGN, which will emit the Hα line. The observations presented here for Abell 1204 show no hard evidence for an interaction with the nearby neighbors, but, it is tempting to speculate on the likelihood of an interaction with nearby galaxies seen on the acquisition image. It would be interesting to search for molecular gas in this BCG. This is the only cluster in the sample presented in this thesis which agrees with the Wilman et al. (2006) hypothesis.

However, the overall "mixed bag" of ionization scenarios seen throughout most of this sample is even more appealing when put into the context of the Hatch et al. (2007) observations. In opposition to the scenario put forth by Wilman et al. (2006), Hatch et al. (2007) find cases where the line emission properties in cooling flow BCGs suggest motions from strong AGN or starburst driven outflows (Abell 2390, Abell 1068), from galaxy passbys (2A 0335+096), and from rotation (Abell 262). They find that the ionization state is not uniform, and do not conclude that one scenario can account for

the emission lines seen in cooling flow BCGs, the results presented here are consistent with such conclusions.

There are of course many possible outcomes for any molecular gas that drops out of the cooling flow onto the BCG. In general, the observations from the dataset presented here, of an overwhelming influence of AGN signatures in most of the sample support the scenario currently put forth for the nature of cooling gas in X-ray clusters where AGN feedback is important. That is, part of the material condensing out of the cooling X-ray gas finds itself in the form of molecular reservoirs at the centers of the BCG, and part rains onto the central black hole. This could trigger an outburst from the AGN which turns on as a radio-mode AGN and then reheats the cluster enough to prevent any further cooling. Furthermore, our observations support this scenario as all the cooling flows with radio emission show lines that are indicative of AGN. This is important as the radio-mode happens after the star-forming mode and so star-forming lines would be difficult to explain in the picture above. The AGN could simultaneously ionize the molecular gas deposits and trigger starbursts. The molecular gas deposits would also be subject to flybys from companions, another mechanism which could trigger a starburst. This complex scenario does explain the observations of line emission resulting from the ionization of hot stars and AGN activity in cooling flows. It could also explain observations of AGN-ionized line emission in non-cooling flow, as the line emission could be triggered after the cooling cluster gas has been reheated by the AGN. It is however, somewhat more difficult to explain the observations of Ophiuchus, where the line emission is not localized in the BCG. But this non-cooling flow BCG could be a part of the nominal $\sim$15% of line emitting BCGs found in Chapter 2. The non-cooling flow BCG NGC 3311 of Abell 1060 may also be a part of this nominal $\sim$15% as it is a non-cooling flow and the emission lines show no evidence for AGN ionization, and thus perhaps the star formation is from a completely different process.

The variation in the host cluster properties of the line emitting BCGs needs to be explored further in order to discriminate between the line emission associated with cooling flows, and that which is part of the nominal $\sim$15%. Are the outliers of the proposed paradigm just part of the underlying $\sim$15% of BCGs with emission lines, separate from the X-ray properties of the host cluster? Or, are these cases which are in serious conflict with the big picture of what is happening to the cooling X-ray gas? These questions must be addressed before a complete understanding of the formation of large elliptical galaxies and their host clusters can be fully understood. Further experiments which can help elucidate these problems would include getting a better understanding of the time-scales involved in the various processes, such as infall onto the black hole, time between AGN outbursts, and condensation time for the molecular clouds.

5.2 Complementarity of the Surveys and IFU Study

Chapter 2 showed a correlation between an enhanced fraction of line emitting BCGs with the positive cooling flow status of the cluster, the presence of radio emission, and a close proximity between the BCG and the X-ray center. It also showed that a nominal fraction, ~15%, of emitting BCGs exists outside of these cases. These universal traits of emission lines in BCGs are validated because of the large sample size of both surveys from which the above results were derived.

One of the main problems with using the results of Chapter 4 to derive global characteristics of emission lines in cooling flow BCGs is the small sample size. With the 4 clusters from Wilman et al. (2006), the 6 from Hatch et al. (2007), plus Perseus (Conselice et al. 2002) and Centaurus (Crawford et al. 2005b), my additional 9 BCGs substantially increases the available data, however there are still only ~20 BCGs studied with the detail afforded by IFU observations. But, the detection and characterization of the emission lines in BCGs from the large surveys of Chapter 2 is based on data collected for hundreds of galaxies. Therefore, the results based on the NFPS and SDSS surveys are complementary to the IFU study as they permit an expectation for the overall properties of the BCG in relation to the cluster properties such as the cooling flow status and the presence of a radio source. Chapter 2 also helps in identifying those clusters in which the line emission might be most interesting to observe in detail. Thus BCGs in cooling flow clusters, with radio emission, and where the BCG is near to the X-ray peak are particularly targeted and non-cooling flows are also included.

A thorough investigation of emission lines from the cooling flow cluster BCGs, as well as the non-cooling flow cluster BCGs (and controls) is required in order to disentangle the nominal emission from the enhanced fraction. The studies of this thesis concentrated mainly on the emission mechanism, that is AGN versus ionization by a population of hot young stars. In the first study, AGNs were seen to be the dominant mechanism across most of the candidates. This is consistent with the IFU observations where for the most part, within the central few arcseconds of the center, the emission line ratios are indicative of a hard source (although regions indicative of star formation were found in addition to regions dominated by AGN ionization for the BCG of Abell 1204, a cooling flow cluster). It is also true that the AGN could be masking some star formation in the center, and that outside of the IFU image, there could be regions of star formation. That said, the fact that there is no immediate correlation between cooling flow status and emission line mechanism, does not disprove of one. It could also be a function of the small number of non-cooling flow BCGs so far observed. As an example, the non-cooling flow cluster Abell 1060, which shows emission in its BCG, may be a part of the nominal ~15%. This cluster is without bright nearby companions, but very dusty, and shows emission lines indicative of ionization by hot stars. On the other hand, Abell 1668 and Object B of Ophiuchus the two other non-cooling flow clusters show

lines indicative of AGN.

5.3 Conclusions

In closing, Chapters 2 and 3 demonstrated that the subset of cooling flow clusters show an important enhancement in the fraction of line emitting BCGs, regardless of the cooling flow definition used, and Chapter 4 shows the variety of processes at play which cause the lines. The two projects also show consistent results. Chapter 2 states that a higher fraction of line emitting galaxies are in cooling flow clusters, and Chapter 4 agrees with this as 5 of the 6 cooling flow clusters have emission lines. Chapter 2 states that a higher fraction of line emitting galaxies are in cooling flow clusters with radio emission, and in Chapter 4 all four cooling flows with radio emission have lines.

So far, no difference in the ionization mechanism has been found that clearly separates the cooling flow and non-cooling flow cluster BCGs. Neither has a consistent picture been developed to explain the origin of the line emission throughout the sample. Although, the emission line characteristics are consistent within each BCG and most systems show a hard ionizing source prominent throughout the central few arcseconds which is usually described by LINER emission line ratios.

From the analysis of the BCGs in the NFPS and SDSS surveys, it was shown that overall ∼15% of BCGs have emission lines, but that 71^{+9}_{-14}% of cooling flow cluster BCGs have emission lines, and 100^{+0}_{-15}% of cooling flow cluster BCGs within 50 kpc of the X-ray center are line emitting. Yet, it is not obvious how the action of the cooling flow plays a roll in terms of the optical line emission present in these systems.

The IFU observations have revealed a complex nature to the line emission in these galaxies, for which star formation, AGN, or both are important in several systems, but for which no consistency of the emission line characteristics and the cluster properties is seen. The line emission is point-like, filamentary, or extended; it exists in regions that are plagued with large patches of dust, and those that are relatively dust free. The AGN ionizes all of the gas within the image in some cases, whereas regions of star formation are discernible in others. Outflows are seen, as well as gas that has bulk rotations. And the emission could be associated with galaxy interactions in some, but not all cases. Each case with emission lines that is a cooling flow shows regions where the emission lines have AGN-like ratios.

Thus, it is still a mystery as to what the connection is between the line emitting gas, and the cooling flow. As well, the process that is fueling the nominal emission in the non-cooling flows and the other bright galaxies at the center of a cluster is still unknown. However, in cooling flows, the existence of an AGN is correlated with the presence of emission lines. As seen for example in Abell 1204 (this work), 2A0335+096 (Hatch et al. 2007), and Abell 2052 (Blanton et al. 2003), the ionization mechanism can change with the radial distance from the center, showing lines ionized by a hard

source at the center, and those ionized by hot stars further out.

This work supports the current ideas on the important role of a massive black hole in these galaxies, as much of the optical line emission is dominated by gas ionized by an AGN. The black hole may act as a sink for the cooling gas (Pizzolato & Soker 2005), may trigger a starburst (Wilman et al. 2006), and its energy output may prevent further cooling of the cluster gas (Best et al. 2005a; Croton et al. 2006; McNamara & Nulsen 2007). This last role is an important factor in our understanding of the building of large galaxies. The observed galaxy luminosity function undergoes a sharp cut-off at the high end. This cut-off can be explained with the inclusion of X-ray gas and AGN feedback, where the amount of cooling (and hence potential star formation) is regulated by heating from the AGN (Croton & et al. 2006).

5.3.1 Future Work

The main studies of Chapter 2, a determination of the fraction of star forming BCGs as a function of cluster and galaxy mass, should be repeated on cosmological simulations which include AGN feedback, such as those of Croton & et al. (2006) in order to test the models. The catalogue of SDSS BCG and controls I built in Chapter 2 can also be used to investigate the colours of the BCGs with respect to the controls using archival SDSS data. The catalogue should however be updated as the SDSS public release is now at DR6, in which many more of the cluster BCGs are observed spectroscopically.

In future studies regarding the results of Chapter 4, a field of view which encompasses regions further beyond the central few kpc should be examined. With information from the full optical spectrum (particularly the Hβ emission lines, the D4000 break, and the CaT), or observations further away from a hard central contaminating source, further constraints on the ionization mechanism and of the stellar populations can be deduced. A reconstruction of the star formation history of the galaxy could then be mapped out. Deep observations that encompass a larger physical scale, at the same level of detail, would be very helpful. In particular, a field of view large enough to encompass companion galaxies and regions that could be affected by radio emission should be covered. The large field of view imaging spectrograph, SPIOMM (Bernier et al. 2006; Grandmont et al. 2003), developed in large part at Université Laval, would be ideal for such studies.

Rich galaxy clusters are large systems with lots of ongoing and dynamically important processes occurring, and even in cooling flows the motion of the X-ray gas is but one such process. To obtain an idea of how important the cooling flow is in the big picture galaxy formation and cluster evolution, this process must be considered alongside other important phenomena. A study with the goal of determining how common companions are to BCGs, and to what degree they are causing activity in the central galaxies would especially be beneficial.

This study is the first in which non cooling-fow BCGs are examined next to cooling

flow BCGs, and more observations of non-cooling flow BCGs is necessary in order to discriminate between any difference in the emission line characteristics (magnitude, ionization mechanism) between the two samples. In fact, 10% of bright cluster galaxies (non-BCGs) show emission lines, and an inclusion of the study of this population would be prudent as well. Do these show only the signature of AGN, even out to large radii? Is it that cooling flow BCGs just have a larger reservoir of gas which is heated by the same processes present in the other systems, or is their line emission more special? Other current work which will have a strong effect on the interpretation of this work is that of Chris Bildfel, who is looking at line emission in high redshift cooling flow BCGs, and that of Pope (2007) who is determining AGN timescales.

Bibliography

Abazajian K., et al. 2005, AJ, 129, 1755

Allen S. W., et al. 1992, MNRAS, 259, 67

Allen S. W., Ettori S., Fabian A. C., 2001, MNRAS, 324, 877

Babul A., Balogh M. L., Lewis G. F., Poole G. B., 2002, MNRAS, 330, 329

Bacon R., et al. 2000, in van Breugel, W. and Bland-Hawthorn, J., eds., ASP Conference Series, Imaging the Universe in Three Dimensions. Vol. 195, Astron. Soc. Pac., San Francisco, p. 173

Baldwin J. A., Phillips M. M., Terlevich R., 1981, PASP, 93, 5 (BPT)

Balkowski C., Vollmer B., Cayatte V., 2001, Astrophysics and Space Science Supplement, 277, 393

Balogh M. L., Babul A., Voit G. M., McCarthy I. G., Jones L. R., Lewis G. F., Ebeling H., 2006, MNRAS, 366, 624

Bauer F. E., Fabian A. C., Sanders J. S., Allen S. W., Johnstone R. M., 2005, MNRAS, 359, 1481

Baum S. A., Heckman T. M., Bridle A., van Breugel W. J. M., Miley G. K., 1988, ApJS, 68, 643

Bautz L. P., Morgan W. W., 1970, ApJL, 162, L149

Bernier A.-P., Grandmont F., Rochon J.-F., Charlebois M., Drissen L., 2006, in McLean I.S. and Masanori I., eds., Proceedings of the SPIE, Ground-based and Airborne Instrumentation for Astronomy. Vol. 6269, p. 49

Berrier J. C., Bullock J. S., Barton E. J., Guenther H. D., Zentner A. R., Wechsler R. H., 2006, ApJ, 652, 56

Bertoldi F., McKee C. F., 1992, ApJ, 395, 140

Best P. N., Kauffmann G., Heckman T. M., Brinchmann J., Charlot S., Ivezić Ž., White S. D. M., 2005a, MNRAS, 362, 25

Best P. N., Kauffmann G., Heckman T. M., Ivezić Ž., 2005b, MNRAS, 362, 9

Best P. N., von der Linden A., Kauffmann G., Heckman T. M., Kaiser C. R., 2007, MNRAS, 379, 894

Binette L., Raga A. C., Calvet N., Canto J., 1990, PASP, 102, 723

Bîrzan L., Rafferty D. A., McNamara B. R., Wise M. W., Nulsen P. E. J., 2004, ApJ, 607, 800

Blanton E. L., Sarazin C. L., McNamara B. R., 2003, ApJ, 585, 227

Blanton E. L., Sarazin C. L., McNamara B. R., Clarke T. E., 2004, ApJ, 612, 817

Blanton E. L., Sarazin C. L., McNamara B. R., Wise M. W., 2001, ApJL, 558, L15

Böhringer H., et al. 2000, ApJS, 129, 435

Böhringer H., et al. 2001, A&A, 369, 826

Böhringer H., Matsushita K., Churazov E., Ikebe Y., Chen Y., 2002, A&A, 382, 804

Bower R. G., Benson A. J., Malbon R., Helly J. C., Frenk C. S., Baugh C. M., Cole S., Lacey C. G., 2006, MNRAS, 370, 645

Branchesi M., Gioia I. M., Fanti C., Fanti R., 2007, ArXiv e-prints, 706

Bridge C. R., et al. 2007, ApJ, 659, 931

Brough S., Collins C. A., Burke D. J., Lynam P. D., Mann R. G., 2005, MNRAS, 364, 1354

Carlberg R. G., Yee H. K. C., Ellingson E., 1997, ApJ, 478, 462

Carroll B. W., Ostlie D. A., 1996, An Introduction to Modern Astrophysics. An Introduction to Modern Astrophysics. Benjamin Cummings

Charlot S., Longhetti M., 2001, MNRAS, 323, 887

Chen Y., Reiprich T. H., Böhringer H., Ikebe Y., Zhang Y.-Y., 2007, A&A, 466, 805

Condon J. J., Cotton W. D., Greisen E. W., Yin Q. F., Perley R. A., Taylor G. B., Broderick J. J., 1998, AJ, 115, 1693

Conselice C. J., Gallagher III J. S., Wyse R. F. G., 2001, AJ, 122, 2281

Conselice C. J., Gallagher III J. S., Wyse R. F. G., 2002, AJ, 123, 2246

Cowie L. L., Binney J., 1977, ApJ, 215, 723

Cowie L. L., Hu E. M., Jenkins E. B., York D. G., 1983, ApJ, 272, 29

Crawford C. S., Allen S. W., Ebeling H., Edge A. C., Fabian A. C., 1999, MNRAS, 306, 857

Crawford C. S., Hatch N. A., Fabian A. C., Sanders J. S., 2005b, MNRAS, 363, 216

Crawford C. S., Sanders J. S., Fabian A. C., 2005a, MNRAS, 361, 17

Croton D. J., et al. 2006, MNRAS, 365, 11

De Lucia G., Blaizot J., 2007, MNRAS, 375, 2

De Lucia G., Kauffmann G., White S. D. M., 2004, MNRAS, 349, 1101

Donahue M., Mack J., Voit G. M., Sparks W., Elston R., Maloney P. R., 2000, ApJ, 545, 670

Donahue M., Sun M., O'Dea C. P., Voit G. M., Cavagnolo K. W., 2007, AJ, 134, 14

Dressler A., 1978, ApJ, 222, 23

Ebeling H., Edge A. C., Allen S. W., Crawford C. S., Fabian A. C., Huchra J. P., 2000, MNRAS, 318, 333

Ebeling H., Edge A. C., Bohringer H., Allen S. W., Crawford C. S., Fabian A. C., Voges W., Huchra J. P., 1998, MNRAS, 301, 881

Ebeling H., Voges W., Bohringer H., Edge A. C., Huchra J. P., Briel U. G., 1996, MNRAS, 281, 799

Ebeling H., Wiedenmann G., 1993, Phys. Rev. E, 47, 704

Edge A. C., Stewart G. C., 1991, MNRAS, 252, 414

Edge A. C., Stewart G. C., Fabian A. C., 1992, MNRAS, 258, 177

Edge A. C., Wilman R. J., Johnstone R. M., Crawford C. S., Fabian A. C., Allen S. W., 2002, MNRAS, 337, 49

Edwards L. O. V., 2004, in Reiprich, T. and Kempner, J. and Soker, N., eds., The Riddle of Cooling Flows in Galaxies and Clusters of galaxies. Charlottesville

Edwards L. O. V., Hudson M. J., Balogh M. L., Smith R. J., 2007, MNRAS, 379, 100

Edwards L. O. V., Robert C., 2007, in Boehringer H. and Schuecker P. and Pratt G.W. and Finoguenov A., eds., ESO Astrophysics Symposia, Heating vs. Cooling in Galaxies and Clusters of Galaxies. Springer-Verlag, Garching, in press

Eggen O. J., Lynden-Bell D., Sandage A. R., 1962, ApJ, 136, 748

Elmegreen B. G., 2000, ApJ, 530, 277

Evrard A. E., Metzler C. A., Navarro J. F., 1996, ApJ, 469, 494

Fabian A. C., 1994, ARA&A, 32, 277

Fabian A. C., Nulsen P. E. J., 1977, MNRAS, 180, 479

Fabian A. C., Sanders J. S., Ettori S., Taylor G. B., Allen S. W., Crawford C. S., Iwasawa K., Johnstone R. M., 2001, MNRAS, 321, L33

Fujita Y., Nagashima M., 1999, ApJ, 516, 619

Fujita Y., Sarazin C. L., Sivakoff G. R., 2006, PASJ, 58, 131

Gaskell C. M., Ferland G. J., 1984, PASP, 96, 393

Gómez P. L., et al. 2003, ApJ, 584, 210

Gonzalez A. H., Zabludoff A. I., Zaritsky D., 2003, Ap&SS, 285, 67

Goudfrooij P., Schweizer F., Gilmore D., Whitmore B. C., 2007, AJ, 133, 2737

Grandmont F., Drissen L., Joncas G., 2003, in Atad-Ettedgui, E. and D'Odorico, S., eds., Proceedings of the SPIE, Specialized Optical Developments in Astronomy. Volume 4842, p. 392

Gunn J. E., Gott J. R. I., 1972, ApJ, 176, 1

Hatch N. A., Crawford C. S., Fabian A. C., 2007, ArXiv e-prints, 706

Hayakawa A., Hoshino A., Ishida M., Furusho T., Yamasaki N. Y., Ohashi T., 2006, PASJ, 58, 695

Henry J. P., Finoguenov A., Briel U. G., 2004, ApJ, 615, 181

Hicks A. K., Mushotzky R., 2005, ApJL, 635, L9

Ho L. C., Filippenko A. V., Sargent W. L. W., 1997, ApJS, 112, 315

Horner D., Baumgartner W., Mushotzky R., Gendreau K., 2001, in Bulletin of the American Astronomical Society, X-ray Scaling Laws for Galaxy Clusters and Groups, 33, 1461

Hudson M. J., Ebeling H., 1997, ApJ, 479, 621

Inoue A. K., Hirashita H., Kamaya H., 2000, AJ, 120, 2415

Jackson N., Tadhunter C., Sparks W. B., 1998, MNRAS, 301, 131

Jaffe W., Bremer M. N., van der Werf P. P., 2001, MNRAS, 324, 443

Johnstone R. M., Allen S. W., Fabian A. C., Sanders J. S., 2002, MNRAS, 336, 299

Johnstone R. M., Fabian A. C., Morris R. G., Taylor G. B., 2005, MNRAS, 356, 237

Johnstone R. M., Fabian A. C., Nulsen P. E. J., 1987, MNRAS, 224, 75

Jones C., Forman W., 1999, ApJ, 511, 65

Kaastra J. S., et al. 2004, A&A, 413, 415

Kanov K. N., Sarazin C. L., Hicks A. K., 2006, ApJ, 653, 184

Kauffmann G., et al. 2003, MNRAS, 346, 1055

Kempner J. C., David L. P., 2004, ApJ, 607, 220

Kennicutt Jr. R. C., 1998, ARA&A, 36, 189

Kewley L. J., Dopita M. A., 2002, ApJS, 142, 35

Kewley L. J., Dopita M. A., Sutherland R. S., Heisler C. A., Trevena J., 2001a, ApJ, 556, 121

Kewley L. J., Groves B., Kauffmann G., Heckman T., 2006, MNRAS, 372, 961

Kewley L. J., Heisler C. A., Dopita M. A., Lumsden S., 2001b, ApJS, 132, 37

Laine S., van der Marel R. P., Lauer T. R., Postman M., O'Dea C. P., Owen F. N., 2003, AJ, 125, 478

Lake G., Moore B., 1999, in Barnes, J. E. and Sanders, D. B., eds., Proc. IAU Symp. 186, Galaxy Interactions at Low and High Redshift, p.210

Larson R. B., 1969, MNRAS, 145, 405

Leitherer C., Schaerer D., Goldader J. D., Delgado R. M. G., Robert C., Kune D. F., de Mello D. F., Devost D., Heckman T. M., 1999, ApJS, 123, 3

Lin Y.-T., Mohr J. J., 2004, ApJ, 617, 879

Lin Y.-T., Mohr J. J., 2007, ApJS, 170, 71

Lin Y.-T., Mohr J. J., Stanford S. A., 2004, ApJ, 610, 745

Mahdavi A., Böhringer H., Geller M. J., Ramella M., 2000, ApJ, 534, 114

Markevitch M., 1998, ApJ, 504, 27

Martel A. R., Sparks W. B., Allen M. G., Koekemoer A. M., Baum S. A., 2002, AJ, 123, 1357

Matsuura M., et al. 1996, ApJL, 466, L75

Matthews T. A., Morgan W. W., Schmidt M., 1964, ApJ, 140, 35

Mazzotta P., Brunetti G., Giacintucci S., Venturi T., Bardelli S., 2004, Journal of Korean Astronomical Society, 37, 381

Mazzotta P., Kaastra J. S., Paerels F. B., Ferrigno C., Colafrancesco S., Mewe R., Forman W. R., 2002, ApJL, 567, L37

McCarthy I. G., Balogh M. L., Babul A., Poole G. B., Horner D. J., 2004, ApJ, 613, 811

McNamara B. R., 2004, in Reiprich T., Kempner J., Soker N., eds, The Riddle of Cooling Flows in Galaxies and Clusters of galaxies Star Formation in Cluster Cooling Flows. p. 177

McNamara B. R., Nulsen P. E. J., 2007, ARA&A, 45, 117

McNamara B. R., O'Connell R. W., 1989, AJ, 98, 2018

McNamara B. R., O'Connell R. W., 1993, AJ, 105, 417

McNamara B. R., Wise M., Sarazin C. L., Jannuzi B. T., Elston R., 1996, ApJL, 466, L9

Miller C. J., et al. 2005, AJ, 130, 968

Miller N. A., Owen F. N., 2002, AJ, 124, 2453

Molina M., et al. 2006, MNRAS, 371, 821

Mollá M., García-Vargas M. L., 2000, A&A, 359, 18

Morgan W. W., Kayser S., White R. A., 1975, ApJ, 199, 545

Mulchaey J. S., Davis D. S., Mushotzky R. F., Burstein D., 2003, APJS, 145, 39

Mulchaey J. S., Zabludoff A. I., 1998, ApJ, 496, 73

Nagashima M., Lacey C. G., Okamoto T., Baugh C. M., Frenk C. S., Cole S., 2005, MNRAS, 363, L31

Navarro J. F., Frenk C. S., White S. D. M., 1995, MNRAS, 275, 720

Nelan J. E., Smith R. J., Hudson M. J., Wegner G. A., Lucey J. R., Moore S. A. W., Quinney S. J., Suntzeff N. B., 2005, ApJ, 632, 137

Oemler A. J., Dressler A., Butcher H. R., 1997, ApJ, 474, 561

Osterbrock D. E., Ferland G. J., 2006, Astrophysics of gaseous nebulae and active galactic nuclei, 2nd ed.. University Science Books, Sausalito, CA

Osterbrock D. E., Fulbright J. P., Martel A. R., Keane M. J., Trager S. C., Basri G., 1996, PASP, 108, 277

Ostriker J. P., Hausman M. A., 1977, ApJL, 217, L125

Owen F. N., Eilek J. A., 1998, ApJ, 493, 73

Peres C. B., Fabian A. C., Edge A. C., Allen S. W., Johnstone R. M., White D. A., 1998, MNRAS, 298, 416

Peterson B. M., 2006, in Alloin, D. ed., Physics of Active Galactic Nuclei at all Scales. Volume 693, Lecture Notes in Physics, Berlin Springer Verlag

Peterson J. R., Kahn S. M., Paerels F. B. S., Kaastra J. S., Tamura T., Bleeker J. A. M., Ferrigno C., Jernigan J. G., 2003, ApJ, 590, 207

Phillipps S., 2005, The Structure and Evolution of Galaxies. Wiley

Pizzolato F., Soker N., 2005, ApJ, 632, 821

Poggianti B. M., Smail I., Dressler A., Couch W. J., Barger A. J., Butcher H., Ellis R. S., Oemler A. J., 1999, ApJ, 518, 576

Poole G. B., Fardal M. A., Babul A., McCarthy I. G., Quinn T., Wadsley J., 2006, MNRAS, 373, 881

Pope E. C. D., 2007, ArXiv e-prints, 707

Popesso P., Böhringer H., Brinkmann J., Voges W., York D. G., 2004, A&A, 423, 449

Postman M., Geller M. J., 1984, ApJ, 281, 95

Rafferty D. A., McNamara B. R., Nulsen P. E. J., Wise M. W., 2006, ApJ, 652, 216

Reiprich T. H., Böhringer H., 2002, ApJ, 567, 716

Reynolds C. S., Fabian A. C., 1996, MNRAS, 278, 479

Romer A. K., et al. 2000, ApJS, 126, 209

Rosati P., Borgani S., Norman C., 2002, ARA&A, 40, 539

Rose J. A., Gaba A. E., Caldwell N., Chaboyer B., 2001, AJ, 121, 793

Rossetti M., Ghizzardi S., Molendi S., Finoguenov A., 2007, A&A, 463, 839

Sadat R., Blanchard A., Kneib J.-P., Mathez G., Madore B., Mazzarella J. M., 2004, A&A, 424, 1097

Sadler E. M., Gerhard O. E., 1985, MNRAS, 214, 177

Sakai S., Kennicutt Jr. R. C., van der Hulst J. M., Moss C., 2002, ApJ, 578, 842

Salomé P., Combes F., 2003, A&A, 412, 657

Sánchez S. F., 2004, in Ochsenbein, F. and Allen, M. G. and Egret, D., eds., ASP Conference Series, Astronomical Data Analysis Software and Systems (ADASS) XIII. Vol. 314, Astron. Soc. Pac., San Francisco, p. 517

Sanderson A. J. R., Ponman T. J., O'Sullivan E., 2006, MNRAS, 372, 1496

Sarazin C. L., 1988, X-ray emission from clusters of galaxies. Cambridge Astrophysics Series, Cambridge: Cambridge University Press

Schlegel D. J., Finkbeiner D. P., Davis M., 1998, ApJ, 500, 525

Schweizer F., Seitzer P., 2007, AJ, 133, 2132

Scott E. L., 1957, ApJ, 62, 248

Sharma M., et al. 2004, ApJ, 613, 180

Sijacki D., Springel V., 2006, MNRAS, 366, 397

Silk J., Rees M. J., 1998, A&A, 331, L1

Skrutskie M. F., et al. 2006, AJ, 131, 1163

Smith R. J., et al. 2004, AJ, 128, 1558

Sparke L. S., Gallagher III J. S., 2000, Galaxies in the universe : an introduction. Cambridge University Press, Cambridge, UK

Springel V., et al. 2005, Nature, 435, 629

Stoughton C., et al. 2002, AJ, 123, 485

Strateva I. Ivezić Ž., et al. 2001, AJ, 122, 1861

Tadhunter C., Dickson R., Morganti R., Robinson T. G., Wills K., Villar-Martin M., Hughes M., 2002, MNRAS, 330, 977

Tadhunter C., Marconi A., Axon D., Wills K., Robinson T. G., Jackson N., 2003, MNRAS, 342, 861

Tadhunter C. N., Metz S., Robinson A., 1994, MNRAS, 268, 989

Tran H. D., Tsvetanov Z., Ford H. C., Davies J., Jaffe W., van den Bosch F. C., Rest A., 2001, AJ, 121, 2928

Tremonti C. A., et al. 2004, ApJ, 613, 898

van den Bergh S., 1998, Galaxy Morphology and Classification. Cambridge Univ. Press, Cambridge, NY

Vasterberg A. R., Lindblad P. O., Jorsater S., 1991, A&A, 247, 335

Vazdekis A., 1999, ApJ, 513, 224

Vikhlinin A., McNamara B. R., Forman W., Jones C., Quintana H., Hornstrup A., 1998, ApJ, 502, 558

von der Linden A., Best P. N., Kauffmann G., White S. D. M., 2007, MNRAS, 379, 867

Watanabe M., Yamashita K., Furuzawa A., Kunieda H., Tawara Y., 2001, PASJ, 53, 605

White D. A., 2000, MNRAS, 312, 663

White D. A., Jones C., Forman W., 1997a, MNRAS, 292, 419

White R. L., Becker R. H., Helfand D. J., Gregg M. D., 1997b, ApJ, 475, 479

Wilman R. J., Edge A. C., Johnstone R. M., Fabian A. C., Allen S. W., Crawford C. S., 2002, MNRAS, 337, 63

Wilman R. J., Edge A. C., Swinbank A. M., 2006, MNRAS, 371, 93

Yamasaki N. Y., Ohashi T., Furusho T., 2002, ApJ, 578, 833